Collision Dynamics as a Probe of Gas−Liquid and Related Interfaces

Carla Waring

A thesis presented for the degree of Doctor of Philosophy

Heriot-Watt University

School of Engineering and Physical Sciences

April 2011

Abstract

This thesis presents a body of work aimed at increasing the current understanding of the dynamics of collisions at the gas-liquid and related interfaces. In particular, collisions of open-shell radicals (oxygen atoms in the electronic ground state and hydroxyl radicals) with hydrocarbon surfaces have been investigated. Translationally hot radicals were scattered from liquid hydrocarbons and related surfaces. The products of inelastic scattering and hydrogen abstraction reactions (OH radicals) were detected, with translational and internal-state resolution, by laser-induced fluorescence (LIF).

The radicals were used as a 'chemical probe' of the interface, providing unique information on the structure and reactivity of the surface, and how this relates to the bulk composition. Key results include the establishment of the relative reactivity towards oxygen atoms of liquid hydrocarbons and alkylthiol SAMs and the penetration depth of O atoms into the SAM surfaces. This was achieved through systematic studies involving custom-synthesised site-selectively deuterated SAMs. It was found that hydrogen abstraction can occur deeper within the monolayer than previously believed but still emerge as OH (or OD) without reacting further to form water.

The reactivity of $O(^3P)$ atoms towards a technologically important family of ionic liquids ($[C_n mim][Im]$) was measured. It was found that the reactivity increased non-linearly as a function of alkyl chain length, to an extent which far exceeded any anticipated increase in reactivity based on stoichiometry alone. The interface in this case was found to differ greatly from the bulk composition, with preferential occupation by the alkyl units at the surface.

The energy transfer and reactive uptake of OH radicals at a variety of hydrocarbon surfaces was investigated. There was significant transfer of the initial translational energy to all the surfaces as well as substantial translational-to-rotational energy conversion. This energy conversion was dependent on the functional groups present in the liquids as was the reactive uptake of OH. Reactive uptake coefficients (γ) were obtained for alkane, alkene and carboxylic acid-containing organic liquids. The results are discussed in terms of the relevance to the aging of organic particles in the troposphere.

Acknowledgements

In the first instance I would like to thank my primary supervisor, Professor Kenneth G. McKendrick. I appreciate in particular the vast investment of his time into my education. I would like to thank him for his open door policy (whether he liked it or not), allowing me to interrupt him to share my exciting or upsetting news about the experiment on at least a weekly basis.

Huge thanks are owed to Dr Matthew L. Costen, who was a daily fixture in the lab, imparting a great deal of (mostly) welcome practical advice. He too had an open door policy (I am noticing a trend here...) and always gave his time willingly when I was confused, which was quite often.

I appreciate the input of Dr Paul A. J. Bagot who worked alongside me on the gas-liquid experiment. In addition to the practical help and guidance Paul was great company and made my time in the lab very enjoyable. So too did Dr Grant Paterson. We, as a 'team', were so productive we even managed to find time for side projects. I wonder if 'Phys Chem - The Musical' will ever see the light of day! I Hope so.

Thanks are also owed to all the previous and current members of the group, including the project students, who have helped me with experiments and contributed to a great working environment. Thanks also to Iain Drummond for building the new wheel and SAM holder and for being a general Mr fix-it.

Thanks to my parents for giving me absolute freedom to carve my own path in life, without pressure or judgement.

Finally, thanks to my husband Sam, for a decade of support and encouragement. Long may it continue and here's to the next adventure...

Table of contents

Chapter 1

Introduction

1.1 Objectives

At its most fundamental, the goal of studying chemistry is to understand molecular change. This begins on a molecular level with a detailed understanding of the transfer of energy when two bodies collide and ultimately form a new chemical species. A detailed understanding of collision dynamics is essential to unlocking the forces and energetic factors which govern reactivity. The study of dynamics has been applied most rigorously to gas-phase elementary processes, although in recent years, this has begun to extend to gas−surface and solution-phase processes.

The work presented in this thesis aims to improve the current understanding of collision dynamics at the gas−liquid and related interfaces. A central goal is to use collision dynamics as a probe of a liquid or self-assembled monolayer (SAM) surface. Where possible, the results have been interpreted in terms of what they tell us about the chemical and structural landscape of the interface.

Specifically, a program of work has been carried out, building on previous work on the dynamics of hydrogen abstraction reactions by O(^{3}P) atoms at liquid hydrocarbon surfaces. Hydrogen abstraction reactions have been studied at the surface of a technologically important class of ionic liquids and alkylthiol self-assembled monolayers (SAMs). The collision dynamics of the closely related hydroxyl (OH) radical has also been investigated at a range of liquid hydrocarbons of varying functionality. The aim is to establish how the functional groups influence energy transfer and reactivity.

1.2 Motivation

The driving force of this work is to gain further insight into reaction and collision dynamics at the gas—liquid interface and to reveal what the dynamics can tell us about the chemical and structural nature of the interface. This is important from a fundamental point of view, as processes at the gas—liquid interface are less well understood than their gas-phase and gas-solid counterparts. They are however, vital to a number of applications including respiration, distillation, technological applications, catalysis and heterogeneous atmospheric chemistry.

The work presented in this thesis is broadly centred around the initial hydrogen abstraction reaction in the oxidation of hydrocarbon surfaces by ground state oxygen atoms ($O(^3P)$) and hydroxyl radicals (OH). An example of the technological importance of these reactions is in the degradation of polymeric materials on spacecraft and satellites by atomic oxygen in low earth orbit (LEO). The LEO environment is located at altitudes of 200 to 700 km above the Earth's surface where the atmosphere is composed primarily of atomic oxygen (~80%)[1], the remainder being molecular nitrogen. The orbital motion of the space vehicles travelling in this altitude region can result in speeds as high as 8 km s^{-1}[1] which leads to effective collision energies between the spacecraft and the atomic oxygen of ~5 eV (480 kJ mol^{-1}); leading to degradation of certain components of the spacecraft, such as solar panels and polymer heatshields[2]. As such, there is much interest in producing corrosion and degradation-resistant materials for this application. It follows therefore that the degradation mechanism be well understood to form part of the feedback loop. The degradation reaction of any hydrogen containing polymeric material, designed for this purpose will likely begin by a hydrogen abstraction reaction by atomic oxygen. It is therefore crucial as an initial starting point that the dynamics of this reaction are well known.

In atmospheric chemistry also, the reaction of OH radicals with organic liquids is important in the processing of organic aerosols. Organic aerosols are complex with a wide range of functionality including alkyl, unsaturated, aromatic and acid groups as well as highly oxidized multifunctional compounds[3]. The general consensus is that structurally the organic (hydrophobic) matter coats an inorganic/aqueous (hydrophilic) core in an inverted micellular structure[4,5], this makes organic liquids and surfaces an ideal proxies for atmospheric aerosols.

Aerosols, both organic and inorganic, are thought to affect the Earth's energy budget and influence cloud formation. Chemical aging by OH and other atmospheric oxidants is widely thought to activate the organic coating to allow for greater water uptake as depicted in figure 1.1. This process will also alter the optical properties of the aerosol particle. Deciphering the direct and indirect effects aerosols have on climate are 'amongst the largest uncertainties in the current understanding of regional and global environmental change'[6]. A detailed understanding of the heterogeneous interaction of OH radicals with a variety of organic liquids is clearly essential to further understanding of these processes.

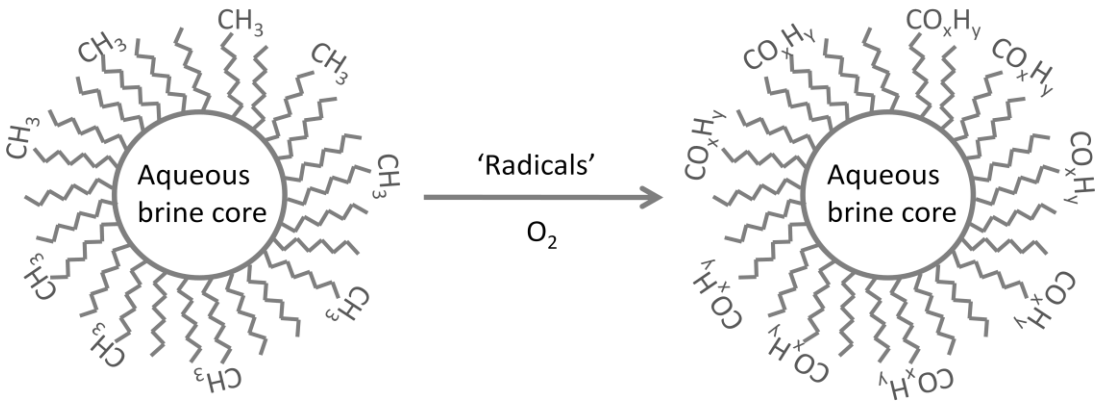

Figure 1.1: Schematic representation of the proposed inverted micelle structure of organic atmospheric aerosols which when processed by OH and other oxidants is thought to affect the optical and cloud condensation properties of the aerosol particle. Figure adapted from reference[4].

1.3 Previous experimental work on collision dynamics at the gas—liquid and related interfaces

1.3.1 Inelastic scattering at the gas—liquid interface

The majority of work in this field has been carried out by the Nathanson group[7-16], who have developed a molecular-beam approach to studying inelastic scattering dynamics at the gas—liquid interface. Central to their methodology was a liquid covered wheel housed within a vacuum chamber with detection of the scattered species by mass spectrometry. Over the last two decades they have studied a vast array of systems, investigating the effects of incident species mass[9], chemical nature[8], incident energy[8], incident and detection angle[12,13], liquid type[8,9,14] and liquid temperature[10] on the scattering dynamics. They have also carried out work on molten metals[11] and more recently on energy transfer and isotope exchange reactions at sulphuric acid[17] and salty glycerol surfaces[14] to better understand solvation processes.

These experiments presented for the first time concepts which are now commonplace in the field of gas—liquid scattering dynamics. The time-of-flight (TOF) profiles obtained were distinctly bimodal in nature. The extremes in scattering behaviour were described by two limiting mechanisms. The first was direct or *impulsive* scattering (IS) which was described as being the result of a single hard-sphere type collision where the scattered species rebounds maintaining a significant fraction of its initial energy. The second was a *trapping-desorption* (TD) mechanism where the gas is temporarily trapped at the liquid surface, thermally equilibrating with it, before desorbing back into the gas phase.

It was found that energy transfer (from the incident E_{trans} to the surface) in the IS channel was greater, the larger the mass of the incoming gas-phase atom. The IS:TD ratio was lower for higher mass projectiles as shown in a comparative study of Ne, Ar and Xe[9] at a perfluorinated surface (PFPE). This suggests that heavier species are more effectively trapped at liquid surfaces than lighter ones. The chemical nature as well as the mass of the incoming gas was also a factor, especially when comparing hydrogen-bonded liquids (glycerol, $C_3H_5(OH)_3$) with non-hydrogen-bonded ones (squalane, 2,6,10,15,19,23-hexamethyltetradodecane, $C_{30}H_{62}$).

A series of gases of increasing polarity (Ne, CH_4, NH_3 and D_2O) were scattered from glycerol and squalane surfaces[8]. Nathanson and co-workers found that the apolar gases (Ne, CH_4) were accommodated on squalane more effectively than on the hydrogen bonded liquid glycerol. The most protic gas (D_2O) accommodated most readily on the glycerol surface, showing the influence of intermolecular forces; polar gases being more attracted to the hydrogen bonded liquid. This is important in terms of solubility and is an extension of the 'like dissolves like' principle as polar gases are more likely to be trapped (and ultimately dissolve) in polar (hydrogen bonded) liquids. Nathanson and co-workers concluded however, that in the absence of strong attractive intermolecular forces, squalane accommodates gases more readily than a H-bonded surface reflecting the *softer* and *rougher* squalane surface.

The nature of the liquid also influences collisions of noble gases[9]. A comparison of the scattering dynamics of Ne, Ar and Xe from squalane and PFPE found that energy transfer was more efficient with squalane than PFPE, reflecting the relative masses of the CH_x and CF_x groups present and therefore the ability of squalane to 'absorb' more energy during the collision.

The molecular beam setup also allowed for the incident and scattering anglular dependence to be investigated[12]. The experiments showed that the IS:TD ratio was dependent on the angle of deflection (χ) rather than either discrete incoming (θ_i) or final (θ_f) angle as defined in figure 1.2. Head on collisions, with small θ_i and large χ, result in significant energy transfer and a high trapping probability where as glancing collisions, large θ_i, small χ, skim the surface and transfer less of the initial energy to it[12].

Another factor influencing the IS:TD ratio was the liquid temperature[10]. The IS channel was largely unaffected by the liquid temperature (suggestive of single hard-sphere collisions) but the TD component was more prevalent at higher liquid temperatures for Ar atoms at a PFPE surface. This suggests that the *dominant* effect is not that the liquids are softer at higher temperatures but that they are rougher on a macroscopic scale.

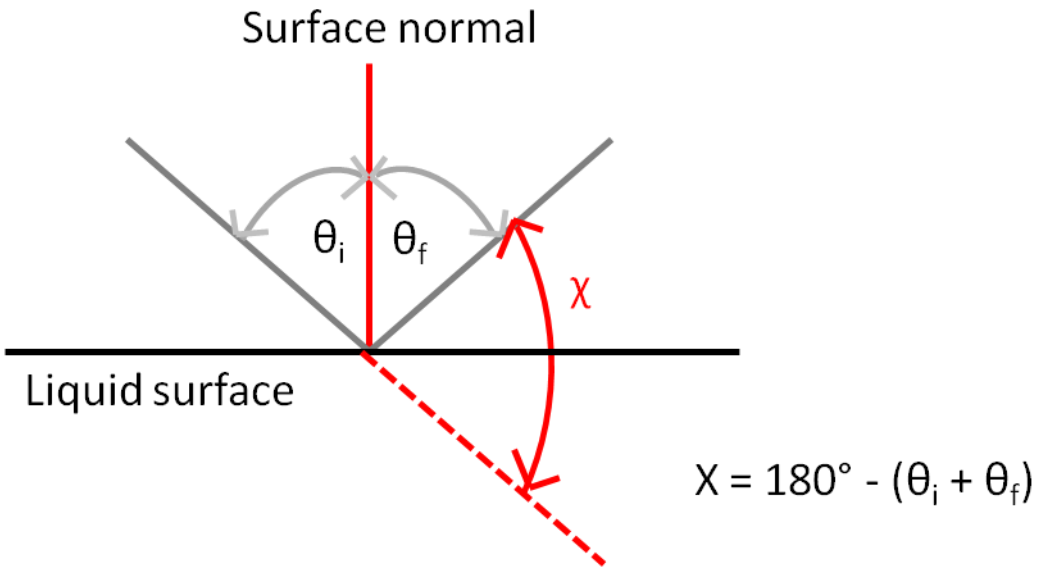

Figure 1.2: Figure showing the relationship between incidence angle θ_i, final angle θ_f and angle of deflection, χ, in molecular beam scattering experiments. Adapted from reference [12].

The work of the Nathanson group has provided a wealth of information on the translational energy transfer at the gas—liquid interface and the factors that affect it. However, the molecular beam experiments with mass spectrometric detection are unable to provide information on the internal state distribution of scattered molecular species. A limited number of studies with spectroscopic detection and hence quantum state resolution have been developed. The work of McCaffery and co-workers on I_2 scattering from squalane, a perflouorinated polyether (PFPE), polydimethylsiloxane (PDMS) and liquid and solid metal gallium surfaces is the earliest example[18-20].

A molecular beam of I_2 was scattered from the surface and I_2 was detected by laser induced fluorescence (LIF) as a function of time. The incoming I_2 beam was translationally hot, with a vibrational temperature T_{vib} of 100 K and a rotational temperature T_{rot} of 10 K. The scattered I_2 was detected by varying the molecular beam pulse-probe laser time delay. The beam pulse-probe laser delays were chosen to sample the two extremes in scattering behaviour: First, the direct IS channel, probed at early delay times and the second, the TD channel probed at longer times.

McCaffery and co-workers observed slight rotational warming in the IS channel in the order PMDS>PFPE>squalane, with an increase in rotational temperature of only 10 K for PFPE. This modest change reflects what must be weak translational to rotational (T→R) energy transfer in the I_2 molecules. There was modest vibrational warming from squalane and also from PFPE. I_2 from PDMS showed vibrational cooling which

was interpreted as PDMS having surface modes more available to absorb energy from the incident molecules[18] compared with the other liquids. This vibrational cooling is a questionable result, particularly as the magnitude of the 'cooling' was ~20% of the original vibrational temperature and the temperatures were quoted without statistical uncertainties.

The TD channel showed more significant internal state excitation compared to the incident beam. This is consistent with initially cold incident molecules undergoing collisional thermalisation at the liquid surface. The trend in internal energy in the desorbing species was PMDS>squalane>PFPE, reflecting the liquids' differing abilities to activate the trapped species to overcome the activation barrier to desorption. It is interesting that for all liquids, the assigned TD channel never achieves full thermalisation, with a rotational or vibrational temperature equivalent to the liquid surface temperature. This could be a result of inefficient energy transfer from the liquid to the I_2 molecules, or could be due to an oversimplification of the assigned scattering mechanism; not all I_2 molecules detected at the later time delay may have been collisionally thermalised at the liquid. Some may have undergone a direct-type process (one or a limited number of collisions) with part of the liquid surface which resulted in significant translational energy transfer, but retains some memory of the initial rotational distribution.

The work of McCaffery and co-workers highlights that for each of the liquids, a combination of *acceptor-donator* ability (accepting energy from incident beam, donating energy to trapped molecules to overcome the desorption barrier) and the kinematics of the collision (CF_x groups in PFPE vs. CH_x in squalane) can be used to explain the energy transfer trends. This is reminiscent of the terms introduced by Nathanson, of *softness, roughness* (squalane) and *stiffness* (PFPE) used to describe energy transfer as a function of liquid.

More recently Nesbitt and co-workers have carried out a comprehensive quantum-state-resolved study of CO_2 molecules scattering from PFPE[21-25] and squalane[26] liquid surfaces. They used a 10.6 kcal mol^{-1} (44.4 kJ mol^{-1}) molecular beam at normal incidence and detected the scattered species by high-resolution infrared spectroscopy, yielding the translational and internal energy distribution. The CO_2 molecules were characterised pre- and post-collision and a dual component scattering mechanism was identified. Boltzmann analysis of the scattered CO_2 was not represented by a linear fit

in either the ground or vibrationally excited state. It was found that the data could be fit by a sum of two Boltzmann-like temperatures; one defined as IS scattering and the other as TD.

Nesbitt and co-workers found that there was significant rotational warming in the direct IS channel, with a rotational temperature T_{rot} increase from ~15 K in the incident beam (pre-collision) to ~600 K post-collision. This was found to be independent of the liquid used[26]. The TD component was characterised by a rotational temperature approximately equal to that of the liquid surface. The vibrational temperature remained at or slightly below the liquid surface temperature in all cases, reflecting the differences in T→R and T→V energy transfer. A more subtle point is the increase in post-collision rotational temperature with an increase in surface temperature, from 600 to 800 K following a liquid temperature rise of only 91 K[21]. The interpretation of this was that at higher temperatures the *rougher* surface provides 'more local structure to torque CO_2 into higher rotational states'. The temperature variation also had an influence on the TD component. The IS:TD ratio was found to decrease with increasing temperature as a rougher surface is more effective at trapping incident molecules.

The above section is a review on the state of the art in inelastic scattering dynamics at liquid surfaces. The molecular beam experiments with mass-spectrometric detection of Nathanson and co-workers have elucidated a great deal of information about the factors which influence energy transfer between particles at the gas—liquid interface. The field has also clearly opened up in recent years and novel developments using quantum-state-resolution detection methods provide additional information which was previously unavailable.

In parallel to the inelastic scattering experiments at the gas—liquid interface, investigations were carried out at the closely related gas—SAM interface. This is described in more detail in the following section.

1.3.2 Inelastic scattering at the gas—SAM interface

Self-assembled monolayers (SAMs) are formed by the attachment of amphiphillic molecules to a suitable substrate. The most common is the alkylthiol SAM which is formed from the spontaneous adsorption of thiols onto gold substrates. A specific introduction to the structure and preparation of SAMs is provided in chapter 4, the focus here is on the dynamics of collisions at the gas—SAM interface. There are examples of studies of the structural changes to SAMs following exposure to high energy beams of inert gases[27-29]. This introduction however, will focus on the work carried out on the collision dynamics at the gas—SAM interface presuming sufficiently low gas dosage that the surface remains unchanged over the course of the experiments.

SAMs, despite having numerous practical applications in their own right, are often used as proxies for liquid surfaces in experimental and theoretical dynamical scattering studies as well as in atmospheric oxidation studies to mimic organic aerosols. This is due in part to their structural definition. In comparison to a liquid, SAMs are very structured and the interface is well defined and characterised. It can be argued, though, that an incoming projectile *sees* a SAM surface in the same way it sees a liquid hydrocarbon. The alkyl chains of a SAM, although structured, have additional liquid-like degrees of freedom not available in a solid. The comparison of gas—SAM and gas—liquid collision dynamics is therefore a particularly interesting field of study.

The first experiments primarily designed to investigate collision dynamics at the gas—SAM interface were carried out by Naaman, Cohen and Sagiv[30] over two decades ago. They studied the translational energy transfer of a series of gases (He, Ar, O_2 and NO) from fluorine (PTFE) and alkyl terminated (OTS) SAMs with mass spectrometric detection of the gas-phase products.

The incoming atoms underwent a high degree of thermalisation with the SAM surfaces compared with collision with a bare substrate. Some particularly interesting trends were observed. For He, Ar and O_2, there was more kinetic energy transfer from the impinging gas to the surface when the surface was alkylated rather than fluorinated. This is correlated with the findings of Nathanson[9] and McCaffery[18,19] at the gas—liquid interface. In contrast to the work of Nathanson, however, they found when comparing collisions of He and Ar with fluorinated SAMs that the kinetic energy transferred was greater for the lighter atom (He ~28 % transferred, Ar ~ 4% transferred).

NO was found to behave differently to the other projectiles, with energy transfer fractions that were the same for both fluorinated and alkylated SAMs. The authors suggested that the (unknown) internal state distribution of the scattered NO could account for this. It may also be the case, although steps were taken to avoid it, that the anomalous results could be due to contamination. This is particularly important in gas—SAM experiments as the surfaces cannot be refreshed, unlike their gas—liquid counterparts. Structural characterisation methods such as scanning tunnelling microscopy (STM) which have become widely available since the work of Naaman, Cohen and Sagiv are exceptionally important for monitoring the surface to ensure the surface is a true, uncontaminated, pristine monolayer.

A decade later, following the experiments of Nathanson and co-workers, motivated in part by the recent move to use SAM surfaces as proxies for liquid surfaces in theoretical simulations, a comprehensive program of gas—SAM scattering experiments was carried out by the Sibener[31-33] and Morris groups[34-45]. Sibener and co-workers (alongside a complementary theoretical effort) investigated noble gases scattering from 1-decanethiol SAM surfaces. The initial energy, impact angle, final angle and surface temperature dependence of the scattered Ne[32], Ar[33] and Xe[31] was investigated by mass spectrometry.

The resulting translational energy distributions revealed similarities and differences compared to work at the gas—liquid interface. In all cases, a fast IS component was observed (most prevalent at grazing angles) and a slower Maxwell-Boltzmann (TD) component. In the case of Ne, interestingly, the slower (TD) component was found to be hotter than the liquid surface. It was also not well described by a cosθ angular distribution. Both these observations clearly indicate that the Ne atoms are not trapped sufficiently long to thermalise efficiently. The slow Ne atoms detected were proposed to be due to high-energy-transfer events resulting from single ‘hard’ collisions. This was not the case in the gas—liquid experiments, where Ne was interpreted as having a formal TD component[9], perhaps reflecting the comparative roughness of a liquid surface compared with the more atomically smooth SAM surface. The heavier Ar atoms behaved more as would be expected on the basis of the gas—liquid experiments. The TD channel was described by a cosθ angular distribution at the surface temperature[33].

In the experiments with Xe[31], an interesting third channel was proposed. It arose from an increase in fast superthermal Xe atoms being detected at more normal angles. This is the opposite of what had ever been observed previously. This channel, exclusive to Xe was named *directed ejection* and was thought to be specific to those atoms which had penetrated deeply pushing the alkyl chains apart. The subsequent ejection (of the Xe atoms) at high energy was the result of the alkyl chains returning to their equilibrium positions. This process, it was argued, is more likely for heavier atoms on account of their larger momentum.

At around the same time the Morris group carried out a wide range of gas—SAM scattering experiments using a similar molecular beam and mass spectrometry detection setup[34-45]. To investigate the influence of SAM structure on the scattering dynamics, a series of experiments was initiated using beams of Ar at fixed incident and detection angles. The effects of alkyl chain length[36] and chain packing density[35] were investigated. It was found that sequentially increasing the alkyl chain length from $n = 2$ to $n = 6$ (where n represents the number of carbons in the alkyl chain) shifted the impulsively scattered Ar to later detection times as it transferred more of its initial energy to the surface.

Interestingly, as the chain length was increased from $n = 6$ to $n = 8$ the scattered Ar dynamics was independent of an increase in chain length, leading the authors to the conclusion that up to six carbon atoms are directly involved in a collision. The TD fraction was also found to increase with chain length suggesting that the longer chains are more able to dissipate enough of the initial energy to trap the incoming atoms. The authors reflect that these effects could be the result of increased degrees of freedom in the longer chains making energy transfer more facile.

A curious pattern was observed at chain lengths $n > 7$. The IS channel exhibited an even-odd effect where the IS intensity was higher for odd chains than even ones. This reflects the well defined structure of SAM surfaces and is a result of the fixed impact and detection angles and their relative orientation to the methyl groups of the surface. This type of effect would obviously never be observed in gas—liquid experiments but shows how very subtle structural effects can influence the dynamics in gas—SAM systems.

The influence of chain-packing density was investigated by comparing alkyl thiols on Au and Ag surfaces[35]; with SAMs on Ag substrates having a higher packing density and shallower tilt angle than those on Au substrates. There was less TD and lower energy transfer overall for the higher density Ag monolayer, suggesting that the tighter packing impeded the chains' acceptor modes.

Further SAM structural effects were investigated by Morris and co-workers by varying the terminal group[34,40]. Methyl (CH_3-), alkene (C=C-), hydroxyl (OH-) and carboxylic acid (COOH-) terminated monolayers were compared. It was found that Ar thermally accommodated most readily on the alkyl monolayers (CH_3-, C=C-) and that both methyl and alkene monolayers resulted in similar scattering dynamics overall. This indicates that the terminal C-C bond exerts little influence on the energy transfer. The hydrogen-bonded monolayers produced faster IS products and less TD; an effect which is not due to surface roughness as in the work of Nathanson in gas—liquid experiments[8] using squalane and glycerol. Instead, Morris and co-workers observed that the IS channel is largely unaffected by surface roughness. It was, instead attributed to kinematics. The hydrogen bonded surfaces are more rigid, and the H-bonding network provides a greater effective mass than an alkyl monolayer.

The polar molecule HCl[37,44] accommodated as efficiently on the H-bonded surface as on the alkyl surface. This was proposed to be the result of strong intermolecular forces between the polar HCl and the H-bonded surface, which is reminiscent of the strong interaction between the protic D_2O and H-bonded glycerol in the Nathanson gas—liquid experiments[8]. Morris and co-workers assigned the scattered HCl to three distinct mechanisms, IS, TD, and also a third mechanism due to the temporary trapping of HCl (by HCl-OH hydrogen bonding) and subsequent *prompt desorption*. This mechanism was favoured over TD at higher surface temperatures as the barrier to desorption is overcome by the available thermal energy. At low temperatures, more of these would presumably remain trapped (full TD).

A more complete study on the effects of surface and projectile polarity followed[43]. Polar (ND_3, D_2O) and non-polar gases (Ne, CD_4) were scattered from polar (OH-, NH_2-terminated) and non-polar (CH_3-terminated) SAMs. In general the non-polar gases transferred more energy to the non-polar alkyl monolayer than the polar surfaces. The polar surfaces were more rigid, an effect that was most extreme for Ne, where thermal accommodation was rare, if present at all. Sibener and co-workers[32] identified a

greater degree of accommodation for Ne than Morris[43] (although fully thermalised Ne wasn't present in either study). The greater degree of accommodation in the Sibener experiments is likely to be a collision-energy effect; partial accommodation was observed when lower energy Ne (<10 kJ mol^{-1}) was used[32] compared with the higher energy beam (60 kJ mol^{-1}) of Morris and co-workers[43]. The polar gases in contrast, were thermally accommodated readily on all surfaces as a result of the increased attractive forces and polarisability of the polar gases compared to the non-polar ones. This work illustrates how the IS channel provides information on the rigidity of the surface and the TD channel provides information on the potential well depth.

Motivated in part by the experiments of Nesbitt and co-workers, the most recent work by Morris and co-workers has been a comparative study, with accompanying theoretical simulations on the dynamics of Ar and CO_2 scattering from OH-, CH_3- and fluorinated CF_x- SAMs[46]. Ar transfers less energy to the OH- and CF_x-SAMs than the alkyl CH_3-SAMs; a kinematic effect resulting from the H-bonding network for the OH-SAMs and the high effective mass of the CF_x groups. CO_2 conversely, accommodates more readily on all the surfaces. In this case the attractive intermolecular forces are more dominant on account of CO_2 molecules being larger and more polarisable than Ar atoms.

Nevertheless, IS dominates for both gases; more initial energy is dissipated at the CH_3-SAMs surface and the translational energy distribution of the IS channel is similar for both gases. This was also observed in their combined theoretical and experimental effort on CO scattering from alkyl and fluorinated SAMs[45]. This is an interesting comparison to the work of Nesbitt who found that when scattering CO_2 from a fluorinated liquid surface[22,24], translational to rotational energy transfer plays an important role in the scattering dynamics. For SAMs, this appears not to be the case, if it is right to assume that rotation comes at the expense of translation. A significant contribution into rotation should have resulted in a difference in the translational distribution between Ar and CO_2 as Ar has no internal states in which to deposit energy.

It is clear that the work highlighted above has provided a great deal of information on gas—SAM scattering dynamics. It has been shown that, although relevant to the gas—liquid interface; there are many discrepancies between the two systems. This ultimately must be considered when using SAMs as model systems for liquids in theoretical scattering simulations (see section 1.4.1.). Section 1.5 also clearly identifies a need for

the field to extend beyond mass-spectrometric detection methods as the field develops beyond atomic into molecular and ultimately reactive scattering; to account for the changes in internal energy. The relatively few reactive studies at the gas—SAM interface will be reviewed in section 1.3.4. First, the gas—liquid interface will be revisited where the field of reactive scattering has been more widely investigated.

1.3.3 Reactive scattering at the gas—liquid interface

The majority of reactive scattering experiments carried out at the gas—liquid interface have involved the reactions of $O(^3P)$ atoms and liquid hydrocarbons. This is primarily due to the motivational factors described in section 1.2 but experimental practicalities must also be taken into account. A pre-requisite for dynamical investigations is a low pressure environment where the products can be detected under single collision conditions. Liquid hydrocarbons such as squalane are well suited to this environment by account of their low vapour pressures. The gas—liquid interfacial reaction of $O(^3P)$ atoms and liquid hydrocarbons has its roots in the equivalent gas-phase reactions, the fundamentals of which are described briefly here.

The dynamics of the reaction between ground-state atomic oxygen $O(^3P)$ and saturated hydrocarbons (equation (1)) have been studied extensively over the last three decades and are the subject of a recent review[47].

$$O(^3P) + RH \rightarrow OH\ (^2\Pi) + R\cdot \qquad (1)$$

The reaction is thought to proceed via a direct abstraction mechanism with the $O(^3P)$ atom approaching the C-H unit in near collinear geometry as shown in figure 1.3. The barrier heights have been derived from kinetic measurements and are dependent on the C-H bond-type. They increase in the order tertiary<secondary<primary<methane and have typical reported values of ~21 kJ mol^{-1}, ~22 kJ mol^{-1}, ~34 kJ mol^{-1} and ~42 kJ mol^{-1} respectively[47]. As will be shown in the following sections, the OH reaction products formed lend themselves to spectroscopic detection techniques such as LIF. The resulting quantum state resolution achieved allows significant dynamical information to be extracted.

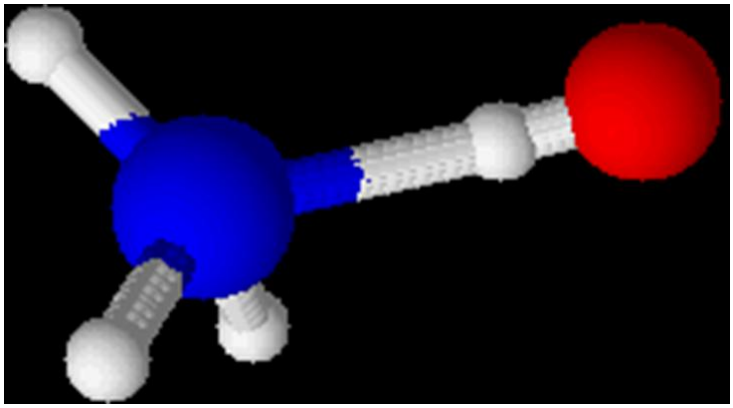

Figure 1.3: Collinear geometry of the C-H-O transition state for the reaction of $O(^3P)$ with methane. Atoms shown are carbon (blue), oxygen (red) and hydrogen (white).

The interesting general features of the internal state distribution of the OH products from the gas-phase reaction are[47]: that there is modest rotational excitation, often characterised as a (slightly) superthermal Boltzmann distribution. This is in agreement with the collinear transition state picture; primary C-H groups produce OH products exclusively in $v' = 0$, while secondary and tertiary C-H lead to some occupation of $v' = 1$; the vibrational branching ratios show that < 10% will be formed vibrationally excited; the OH formed from secondary C-H groups is rotationally colder than those from primary units, which is opposite to that expected based on the exothermicity of the reaction; finally, the vibrationally excited OH is rotationally colder than thermal in all cases, regardless of the hydrogen environment.

One of the key developments in these experimental studies beyond the early pioneering experiments by Andresen and Luntz in the late 1970s[48] and Whitehead and co-workers[49] was the use of photolytic precursors. Whitehead and co-workers developed the technique of using NO_2 as a precursor for $O(^3P)$ for studying the reaction of $O(^3P)$ with GeH_4[50]. This made it possible to study reactions of $O(^3P)$ atoms with higher translational energies (through laser photolysis in the UV region) than was possible using the previous molecular beam experiments. As a result it was possible for the reaction of $O(^3P)$ with methane (CH_4) and ethane (C_2H_6) to be investigated for the first time by McKendrick and co-workers[51]. This was closely followed by a more detailed evaluation of OH (or OD) product fine structure and internal energy distributions[52].

Kajimoto and co-workers were the first to investigate the stereodynamics of such reactions using photolytically generated $O(^3P)$ and detection by Doppler-resolved polarization spectroscopy allowing for the measurements of the differential cross section (DCS)[53]. The long standing direct mechanism via a collinear transition state

would have resulted in predominantly backscattered reaction products. Kajimoto and co-workers however found that as the collision energy was increased (12 - 33 kJ mol^{-1}) there was an increase in intensity (eventually matching the backscattered intensity at high collision energy) in the forward scattered direction. They proposed that as the collision energy was increased an additional 'stripping' pathway, with a larger impact parameter, became available leading to forward scattered products.

Suits and co-workers have more recently used velocity map imaging (VMI) to investigate the stereodynamics of reactions between $O(^3P)$ atoms and cyclohexane[54] and a range of saturated hydrocarbons[55] at various collision energies. They found that a large fraction of the reaction exothermicity presents itself in alkyl fragment internal modes rather than translation which could reflect more complex dynamics than a simple direct rebound process. In contrast to Kajimoto, backwards scattering was found to dominate in all cases, broadening in the sideways direction at higher collision energy but at no point significantly forward scattered. This was described as being characteristic of an H-O-R collinear transition state and a direct mechanism.

A combined experimental and theoretical approach by the Minton and Schatz groups was used to study the reactions of $O(^3P)$ atoms with saturated hydrocarbons at collision energies representative of oxygen atoms in low Earth orbit (LEO)[56,57]; at energies *far* in excess of what had been used previously (~300 kJ mol^{-1}). In contrast to the majority of the lower collision energy work the favoured mechanism for both inelastic scattering of the O atoms and reaction to form OH was a large impact parameter 'stripping' mechanism[57] with the majority of the available energy being present in product translation. A minor small impact parameter H-atom elimination channel was also observed and predicted; thought to proceed through the formation of OC_2H_5 + H from the original HOC_2H_5 transition state.

More recent experimental developments, such as the work of Liu and co-workers, are designed to test the theoretical prediction that by preferentially exciting bending or stretching modes in the hydrocarbon reactant, reactivity will be increased[58]. They selectively excited the bending modes of CH_4 and CD_4 by altering the temperature of the molecular beam source. This reactant beam was crossed with a beam of $O(^3P)$ atoms. The alkyl reaction products were probed by resonance-enhanced multiphoton ionization (REMPI) and velocity map imaging. The resulting DCS were predominantly backscattered, in agreement with the majority view above and supporting the direct-

rebound mechanism. Liu and co-workers found that reactant vibration did not influence the reactivity of the system in contrast to Polanyi's rule that reagent vibration is effective at enhancing late-barrier reactions for atom + diatomic systems.

The thorough body of work carried out in the gas phase encouraged what is a significant experimental advancement, the progression to the reaction of $O(^3P)$ with liquid hydrocarbons. These experiments present significant challenges compared to the gas-phase counterparts. The low pressures necessary for dynamical investigations place obvious vapour pressure constraints on the available liquids. This makes the liquid hydrocarbon, squalane, with its vapour pressure of ~10^{-7} Torr, an ideal candidate.

There have been a limited number of early higher-pressure experiments carried out, most notably by Hori and co-workers[59] and Zadok and Mazur[60]. Zadoc and Mazur, when studying the γ-radiolysis of liquid solutions of carbon dioxide and cycloalkanes identified $O(^3P)$ as the major oxidant. They found that the C-H bonds were regioselectively attacked in the order tertiary>secondary>primary in agreement with the gas-phase measurements being carried out at a similar time by Andresen and Luntz[48]. Five years later, Hori and co-workers also proposed that $O(^3P)$ was the dominant oxidising species and that the primary step is a hydrogen abstraction reaction[59].

The first truly dynamical investigations of the $O(^3P)$ + HR (liq) (where HR was the benchmark liquid hydrocarbon squalane ($C_{30}H_{62}$)) systems were not carried out until the late 1990's by Minton and Cassavechia[61,62] and the early 2000's by McKendrick and co-workers[63]. Using liquid covered wheels of the type developed for inelastic scattering Minton[61,62,64,65] and McKendrick[63,66-70] established two independent but complementary techniques for studying these systems in unprecedented detail. Minton adopted a molecular-beam approach with detection of the inelastically and reactively scattered products by a rotatable quadrupole mass spectrometer. Their unique $O(^3P)$ beam source (a CO_2 laser photolysis (of O_2) plasma source) generated a range of hyperthermal collision energies up to to 5 eV (~480 kJ mol^{-1}). The detection method allowed for the angular and velocity distributions of the scattered products to be measured.

McKendrick and co-workers utilised a photolytic source of O(^{3}P) atoms giving mean superthermal collision energies of ~16 kJ mol^{-1}[63] and the OH reaction products were detected by LIF. The use of a photolytic source to generate the O(^{3}P) atoms above the liquid surface and the wide range of scattering angles sampled in the detection method provides poorer velocity resolution than the molecular beam approach. The advantage of the LIF detection method however, is that it allows the internal states of the scattered OH to be interrogated. These two techniques are closely related to the work described in this thesis, which is a continuation of the previous work by McKendrick and co-workers. The major findings from both are therefore summarized below.

The first experiments carried out by Minton and Cassavechia used a radio-frequency discharge of O_2 to form the molecular beam of O(^{3}P) with centre-of-mass collision energies of approximately 21-47 kJ mol^{-1}[62]. Time-of-flight profiles (TOFs), where flight time is proportional to speed of the scattered species, were recorded for the inelastically scattered O and reactively scattered OH and H_2O species; no volatile organic reaction products suggestive of C-C breaking reactions were observed at these energies.

It was identified that the TOF profiles were a bimodal fit to two separate components: direct and trapping desorption. At an incidence angle (θ_i) of 60°, the direct OH reaction products peaked at a final scattering angle (θ_f) of 37°. The angular distribution was narrow and best described by a $\cos^4(\theta_f - 37°)$ function. The thermal (TD) OH was found to desorb with a $\cos\theta$ distribution with respect to the surface normal.

The work of Minton and co-workers was refined[61,64,65] following the development of a plasma source of O(^{3}P) atoms. This allowed for the generation of higher energy O(^{3}P) atoms with no significant contribution from electronically excited oxygen atoms. These were more comprehensive studies and Minton and co-workers identified superthermal (direct) and thermal (TD) contributions to both inelastically (O) and reactively (OH, H_2O) scattered products. Oxygen atoms were the most abundant products, meaning the reaction probability must be less than 0.5. It is surprising that thermal O was observed. This highlights that even high energy particles, when trapped can quickly lose sufficient energy and fall beneath the reaction barrier.

Of the reaction products, OH was the most abundant. Representative TOF profiles are shown in figure 1.4. The profiles were sensitive to incident collision energy. At higher

energy, larger signals were observed. The fastest (direct OH) were scattered at more grazing incidence angles (relative to the surface normal) and the TD component was most obvious when the detector was placed at normal incidence to the surface (0°). The observation of a (minor) TD component is important as this implies that OH is able to reside on the surface for long enough to collisionally thermalise without reacting further to form H_2O.

The H_2O reaction products were also found to be bimodal. A superthermal H_2O component is counter-intuitive since H_2O cannot be formed by a single, simple direct process. The minor H_2O superthermal component was interpreted as being the result of two direct processes, an initial direct reaction to form OH followed by a subsequent direct reaction to form H_2O. The majority of the H_2O detected was consistent with having been thermalised at the liquid surface before being detected in the gas-phase.

Newton diagrams were constructed to extract the effective surface mass experienced on average by the incoming O atoms. This was inferred to be ~76 atomic mass units (mu), roughly consistent with a C_5H_{11} (mass = 71 mu) portion of the surface. This is important since it shows that the squalane surface is not infinitely massive compared to the incoming O atoms, rather the O atoms are coming into contact with discrete units of the surface which will ultimately affect the scattering dynamics.

The experiments at the highest collision energies (~500 kJ mol^{-1}) were carried out with the aim of identifying products indicative of H-elimination and C-C bond breaking reactions[64]. These channels had been predicted theoretically but never experimentally observed. The H-elimination channel was not identified due to it being a minor pathway and problems associated with detecting H by mass spectrometry. There was however, a C-C bond breakage product isolated (OCH_3) which was not observed in the earlier lower-energy work[61,62,65].

Minton and co-workers estimated the relative probabilities of the formation of OH, H_2O and OCH_3 as being 77%, 20% and 3% respectively. The OH and OCH_3 angular distributions were found to be essentially the same; a direct mechanism was favoured in both cases. It was proposed that the O atoms *abstracts* a CH_3 unit through a very 'hard hit' at the C-C bond. Translationally, the OH and OCH_3 products were less similar. The OCH_3 product was found to be travelling much slower and with a broader angular distribution than its OH counterpart. This reflects the increased mass of the CH_3

fragment and the increased energy loss in the 'hard hit' resulting in reaction. The effective mass of the collision partner for the O in the reaction for CH_3O formation is 124 mu compared with ~76 mu for OH.

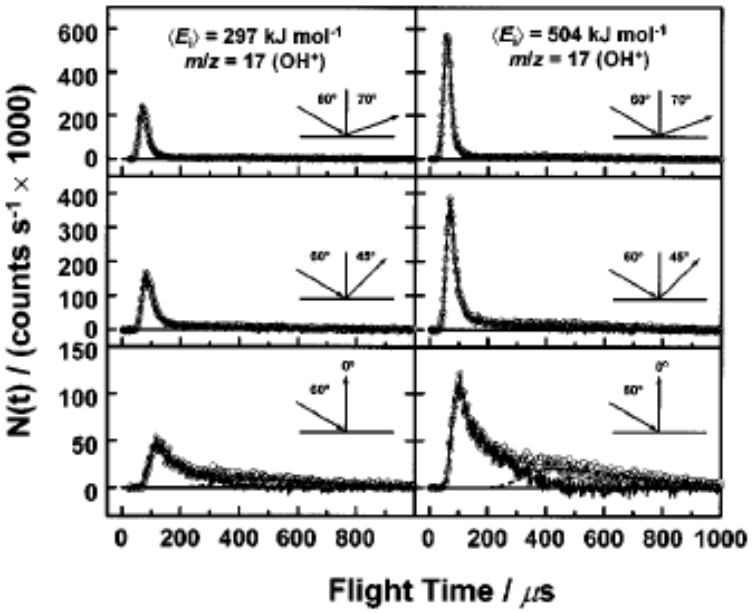

Figure 1.4: OH time of flight (TOF) profiles following reaction of $O(^3P)$ at a squalane surface at incident energies of 297 kJ mol^{-1} and 504 kJ mol^{-1}. The profiles show the increased OH yield at higher energy, the favouring of direct reactions at grazing incidence angles and the emergence of a slower TD component at more normal detection angles. Reprinted from reference[65].

The first proof-of-concept study carried out by McKendrick and co-workers on the reaction between $O(^3P)$ atoms and the liquid hydrocarbon squalane[63] highlighted the viability of the photolytic precursor and LIF detection method. They showed that the translational energy and internal distributions of the OH reaction products could be measured by recording appearance profiles (analogous to TOF profiles in molecular-beam experiments) and LIF excitation spectra. This was developed and they subsequently published their first unequivocal detection of a thermal (TD) reaction mechanism as revealed in the internal product state distribution[69].

The OH/OD vibrational branching ratios were measured for both squalane and its deuterated analogue. A minor vibrationally excited ($v' = 1$) component was identified, with a $\frac{v'=1}{v'=0}$ branching ratio of 0.07 for OH. McKendrick and co-workers concluded that OH detected in $v' = 1$ must originate specifically from reaction at the secondary and tertiary groups; these groups must therefore, be present at the interface. This conclusion

is borne out of the fact that reaction at primary groups does not lead to vibrationally excited OH, if a comparison to gas-phase reactions is valid[51]. The surface composition of the squalane interface was subject to theoretical simulation by McKendrick and co-workers and others and will be discussed in section 1.4.3.

The rotational temperatures of the OH reaction products were found to partially reflect the liquid surface temperature, this can only be interpreted in terms of the OH having a *memory* of the liquid surface; it had resided on the surface long enough to at least partially thermalise with it. The OH detected was not fully thermalised. This was proposed to be a result of the photolysis-probe laser time delay at which the spectra were recorded; a delay consistent with the peak in an appearance profile. At this time the OH was interpreted as being a combination of both direct and TD-type encounters.

The direct component was isolated and characterised by recording LIF excitation spectra at short time delays, corresponding to the fastest (direct) OH products[66]. It was found that the rotational distribution of the fastest OH products was not affected by the liquid-surface temperature. This is as would be expected for a direct reaction mechanism based on a single collision event. The temperatures assigned to the rotational distribution of this direct component were very similar to those in the gas-phase reactions[51]. Similar trends with vibrational state were observed also, OH in $v' = 1$ was consistently rotationally colder than OH in $v' = 0$. This suggests that the direct reaction mechanism is analogous to the gas-phase mechanism; it proceeds through a collinear geometry.

The liquid-temperature dependence of the appearance profiles showed a number of interesting features[67]. The appearance profiles were recorded for a given rotational state in both $v' = 0$ and $v' = 1$ at a series of liquid temperatures from 263 K to 333 K. In $v' = 0$, the shapes and magnitudes of the appearance profiles were unaffected by the temperature increase. Those measured in $v' = 1$, however, showed an increase in average recoil speed (earlier peak in appearance profile) and an increase in OH yield. A number of possible reasons for this interesting behaviour were considered. McKendrick and co-workers concluded ultimately that the differences do not reflect an increase in $v' = 1$ production with an increase in temperature but rather an increase in OH $v' = 1$ survival probability. OH in $v' = 1$ is presumably more likely to be trapped at the liquid surface on account of it being slower than OH in $v' = 0$. Higher liquid temperatures could lead to an opening of the squalane structure, allowing for more of the OH $v' = 1$ to

escape. This could in theory be tested in a Minton-style molecular beam experiment by monitoring the relative OH and H_2O yields as a function of liquid temperature.

McKendrick and co-workers extended the O(^{3}P) + HR series for the first time beyond squalane and studied a range of branched and linear liquid hydrocarbons[68]. Similar internal state distributions were observed for OH from each of the liquids. The major differences were in the relative OH yield (quantified by the area under the appearance profiles) from each of the liquids. Two branched hydrocarbons were used, squalane ($C_{30}H_{62}$) and pristane ($C_{19}H_{40}$). Pristane was less reactive by a fraction consistent with the relative amounts of primary, secondary and tertiary hydrogens in each molecule.

The relative reactivity of the branched and linear hydrocarbons was compared. The linear hydrocarbons were found to be *less* reactive than their branched counterparts, despite having fewer of the least reactive primary units per molecule. There was also a curious trend that the shorter the linear hydrocarbon, the lower the reactivity, to an extent that far outweighed any differences in primary and secondary hydrogen availability.

McKendrick and co-workers postulated that the *surface-freezing* phenomenon could explain this behaviour. Surface-freezing is a process whereby linear hydrocarbons spontaneously align at the vacuum-liquid interface at temperatures close to their melting points[71,72]. The result would be that the least reactive primary end groups preferentially occupy the interface, resulting in a reduction in reactivity. This postulate was part of the motivation behind the experimental work included in chapter 4. A self-assembled monolayer could be considered as the ultimate extreme of this surface freezing behaviour, so comparing the reactivity of a liquid hydrocarbon to a SAM is an interesting test of the explanation for the reduced reactivity. The concept of surface-freezing in linear hydrocarbons has been investigated by molecular dynamics simulations and will be revisited in section 1.4.3.

Aside from the reactions of O(^{3}P) and liquid hydrocarbons, an experimental study by Nesbitt and co-workers on reactions of F atoms with the liquid hydrocarbon squalane[73] is also relevant here. They used a F atomic beam and detected the HF products by high resolution infrared spectroscopy. The HF ($v' = 2$) product rotational distribution was also characterised by a bimodal fit. As with their CO_2 work, the products were found to be a combination of two components; a direct process resulting

in rotationally superthermal HF products (~1000 K) and a TD-type process with a thermal rotational temperature.

Although a TD-type component was identified in the rotational distribution, Nesbitt and co-workers state that this collisional relaxation did not extend to vibration. The products were detected in a vibrationally excited (non-thermal) state, $v' = 2$. This reflects well-known differences in the efficiency of T→R and T→V energy transfer in TD-type processes. This is an example of how IS/direct and TD are convenient shorthand labels for describing scattering mechanisms but are an oversimplification. Something which has truly 'thermalised' with the liquid surface should emerge with thermal translational, rotational and vibrational distributions. A possible explanation as to why full rotational but not vibrational thermalisation is observed could be due to the timescales of the experiment. Those molecules which are detected must have remained close to the interface to be able to escape. In contrast, it is possible that those molecules which have suffered enough collisions to fully thermalise (rotationally and vibrationally) are no longer located near the interface (have dissolved) and do not emerge on the timescale of the experiments.

1.3.4 Reactive scattering at the gas—SAM interface

The situation as it stands is that reaction dynamics at the gas—liquid interface has been more widely investigated experimentally than at the gas—SAM interface. Theoretically, the situation is reversed, with the majority of realistic dynamical simulations having been carried out at the gas—SAM interface. The reasons for this are partly motivational, and partly due to convenience. Reactions at the gas—liquid interface are less difficult to study experimentally than those at a SAM surface; the liquid surface is continually refreshed, eliminating any complications from modification of the surface during the experiments. Conversely, liquids (particularly long chain hydrocarbons) are extremely difficult to treat theoretically, making SAMs ideal model systems for liquid hydrocarbons. Clearly, there is a need for experimental and theoretical advancements to balance this situation. This disparity is evident in the summary provided in section 1.5.

There have been a number of kinetics experiments at the gas—SAM interface motivated by their attractiveness as proxies for organic aerosol particles. The proposed inverted micelle structure (figure 1.1) of organic aerosols[4] is well replicated by a SAM surface.

The organic matter in atmospheric aerosols is processed by gas-phase oxidants (aged) altering the chemical and physical properties of the aerosols. Finlayson-Pitts and co-workers, for example, have investigated the oxidation of unsaturated, vinyl terminated SAMs by OH[74] and O_3[75-77] as summarised in a recent review article[78].

These experiments are useful for identifying reaction products and intermediates, both of which contribute towards an understanding of the oxidation reaction mechanism. They also are carried out in atmospherically realistic environments, at ambient pressures and temperatures. This however, adds to their complexity and as the work of Finlayson-Pitts shows, elucidation of the kinetics and mechanisms of these reactions is difficult. This, in turn, highlights the importance of the development of heterogeneous reaction dynamics studies to understand more fully the individual steps in these reactive processes. A particular difficulty and one which is often overlooked in the kinetics experiments is the structural changes which take place at the SAM surface during the reaction. A recent study by Finlayson-Pitts and co-workers, utilised atomic force microscopy (AFM) to monitor the SAM surfaces during O_3 exposure[76]. They observed the formation of large aggregates of polymeric carbonaceous material, suggestive of highly complex reactions.

Aside from the work of Finlayson-Pitts and co-workers described above[74], Molina and co-workers[79,80] and the Naaman group[81,82] have also investigated the kinetics and reactive uptake of OH radicals at SAM surfaces[79,80], with a similar atmospheric motivation. In each case oxidation at these surfaces was found to be efficient compared to equivalent gas-phase reactions. These experiments are discussed in detail in the introduction to chapter 5 (section 5.1.2).

Motivated by the LEO environment described in section 1.2, Fairbrother and co-workers have studied reactions of thermal $O(^3P)$ atoms[83,84] and atomic hydrogen[85,86] at a variety of SAM surfaces including alkylthiol SAMs[85], partially fluorinated SAMs[84,86] and X-ray modified, cross-linked SAMs[83]. The experiments were designed to investigate what type of materials would best suit technological applications in LEO and by what mechanism degradation and erosion takes place. In each case the SAM surfaces were exposed to the reactive gas, formed by the thermal cracking of molecular oxygen or hydrogen and the SAM was monitored by X-ray photoelectron spectroscopy (XPS) as a function of time.

Integration of the XPS signals allowed for the quantification of carbon, sulfur and fluorine loss as well as the identification of changes in the chemical environment of the sulphur and carbon atoms. A comparison of CF_3-SAMs ($CF_3(CH_2)_7(CH_2)$-SAM) and CH_3-SAMs ($CH_3(CH_2)_{11}$-SAM) under exposure to $O(^3P)$ and O_2[84] showed that the two systems undergo very different reactions. The CF-SAMs were found to be inert for reasonable exposure times (up to 1 hour at a pressure of 6 10^{-7} Torr). At longer times, carbon and fluorine were lost and Al_2O_3 and RSO_3 reaction products were observed. This led the authors to the conclusion that reaction was occurring at the film—substrate interface.

The reaction was thought to be initiated by $O(^3P)$ penetrating to the substrate, bypassing the C-F sections as F abstraction or C-C insertion would not be possible at the energies used. The $O(^3P)$ atoms would also be unlikely to abstract a hydrogen from the base of the chain; the barriers for these reactions are high (20-30 kJ mol^{-1} [47]) compared to the energy of the thermalised O atoms.

In contrast, the CH_3-SAM reaction was reported as being initiated at the gas—surface interface. The proposed mechanism proceeds via a hydrogen abstraction reaction and subsequent reaction of the alkyl radical with oxygen immediately after exposure begins. The surface is then thought to undergo etching and fragmentation as carbon is lost. This erosion was found to be slowed by the presence of carbon cross-links in the CH_3-SAMs formed by X-ray irradiation of the samples[83].

Similar reactions between CF_3-SAMs and CH_3-SAMs were carried out using atomic hydrogen[86]. In this case there are more available reaction channels such as F-abstraction, H-abstraction and H/F substitution. Although F-abstraction is thermodynamically favoured, according to theoretical simulations it is kinetically hindered. As a result H-abstraction is predicted to be the dominant channel[87]. Fairbrother and co-workers found this to be the case[86]. The reaction was initiated by a H-abstraction close to the film/substrate interface. Subsequent C-C bond breakage by the alkyl radical formed following H-abstraction was believed to be the source of C and F being lost at the same rate.

Atomic hydrogen reacting with CH-SAMs of various chain lengths was also investigated[85]. The short- (C_9 and C_{12}) chain SAMs were found to behave very differently than the long- (C_{16} and C_{18}) chain SAMs. Firstly, the short chain CH_3-SAMs

were very quickly destroyed by exposure to atomic hydrogen (<10 min at 6×10^{-7} Torr), revealed by the rapid loss of both sulfur and carbon. It was proposed that the reaction was initiated at the film—substrate interface, although it seems unlikely that there would be no H-abstraction to form H_2 further up the chain. Regardless, reaction certainly takes place at the film—substrate interface as reduced sulphur is observed (R-S-H) and there is, according to the authors, complete desorption of the alkyl chains. The long-chain SAMs, in contrast, appear to be less vulnerable to attack. The carbon desorption rate is far slower. Unlike for the short-chain SAMs, penetration to the film—substrate boundary is much more difficult. As a result the alkyl radical formed in the initial H-abstraction step subsequently undergoes C-C bond breaking and forming reactions. The result is a cross-linked polymeric structure (much like that formed from X-ray modification[83]) which protects the surface further. The differences between the two mechanisms are depicted in figure 1.5.

The experimental studies which are most pertinent to the work in this thesis and chapter 4 in particular, are those of Jacobs and co-workers on reactions of O^+ ions with alkylthiol SAMs[88-90].

A monoenergetic, hyperthermal beam (5-40 eV) of O^+ ions was directed at various SAM surfaces at fixed incident angle of 45° with respect to the surface normal. The reactivity was investigated initially using XPS to monitor the loss of carbon and corresponding growth of oxygen as a function of O^+ dosage and subsequently by mass spectrometry[90] to identify reaction products[88,89]. The initial study[90] using 5 eV O^+ ions found that the monolayer was efficiently etched by the O^+ atoms, removing carbon atoms and becoming incorporated in the chains as either -C-O-H or -C-O-C- functionality. The carbon atoms were interpreted as being stripped sequentially from the surface, as opposed to desorption of the entire chain as was observed by Fairbrother and co-workers[83]. It was inferred that four carbon atoms were removed for every ten O^+ ions hitting the surface.

The authors also state that a comparison between the reactions of O^+ ions and $O(^3P)$ atoms is valid as the O^+ ions are thought to neutralise efficiently immediately prior to impact[89]. On this proviso it would be appropriate to compare these observations with those for $O(^3P)$ atoms at the gas—liquid interface. The removal of four carbon atoms per 10 O^+ ions would translate to a C-C bond breaking reaction probability of 0.4. In contrast, however, Minton and co-workers[64] observed only a very minor C-C bond

breakage channel in the reaction of $O(^3P)$ atoms (5 eV) with the liquid hydrocarbon squalane, quoting an approximate reaction probability of 0.03.

The difference in reaction probability here is surprisingly large. Of course, the experiments are very different; one at a liquid and one at a SAM surface. The XPS detection method was also noted by the authors to cause additional (minor) degradation of the SAMs[90]which could account for the large amount of C-C bond breakage. A possible source of the difference lies in the inability of the SAM surface to refresh itself. As a result radical chain reactions would be more destructive at SAM surfaces than in liquids where multiple encounters per molecule are far less probable.

Jacobs and co-workers subsequently developed an isotopic labelling method to isolate the contribution that individual carbon atoms along the alkyl thiol chain make to the overall OH (OD) formed [88]. The XPS detection was replaced by mass spectrometry and the OH (OD) reaction products were directly detected. Dodecylthiol SAMs (C_{12}-SAMs) were synthesised with isotopically labelled C_1, C_2 and C_3 positions, where the numbering C_1 originates at the terminal methyl (CH_3) group. Again using 5 eV O^+ ions with low dose rates to avoid damage, the OH (OD) reaction products were detected as negative (OH^-/ OD^-) ions and their relative yields were used to determine the relative contribution from each carbon. A direct comparison between OH^- and OD^- proved difficult, with the relative contributions from OH^- being larger than expected.

A number of possible explanations for this were discussed, including differences in OH^- and OD^- detection and survival probabilities, reactions at domain boundaries and kinetic isotope effects. A simpler explanation could be that the there are spurious sources of hydrogen, even at ultrahigh vacuum pressures which could result in artificially high OH levels; this would not be an issue for deuterium. The comparative OD^- signals from the three SAMs gave relative contributions of 75%, 22.5% and <2.5% for C_1, C_2 and C_3 respectively. The outer methyl group was found to contribute most to the observed signal, and very little H abstraction occured beyond C_2. Any reaction occurring deeper in the chains, if occurring at all, was not contributing to the overall OH^- (or OD^-) signal.

This was revisited in a more detailed study comparing collisions of O^+ and Ne^+ ions with a series of alkylthiols (fluorinated, deuterated and non-deuterated) SAMs at a range of extreme collision energies from 5-40 eV[89]. There was still a clear preference for abstraction at the terminal methyl group (C_1) but there were problems with the OD^-

detection from further down the alkyl chains. It was found that the D atoms down the chains were becoming scrambled as the reaction proceeded. This was particularly prevalent at the higher collision energies. This coincided with structural damage to the SAM, corroborated by scanning tunnelling microscopy (STM) images of the surface. The higher energy O^+ ions (E > 10 eV), also gave rise to the detection of significant alkyl fragments such as $C_2H_5^+$and $C_3H_5^+$ unlike the sequential removal of carbon one atom at a time as was observed at 5 eV[90].

As was the case in the previous isotropic labelling work, there was a surprisingly large OH^- signal from a fluorinated $CF_3(CF_2)_7(CH_2)_2$-SAM, surprising in as much as this would involve reaction from deep within the monolayer (whilst also escaping for detection as OH^- without neutralising or reacting further). It was speculated that this was the result of reaction occurring at the domain boundaries, although the percentage of the surface occupied by such defects should be low in SAMs of high quality. This highlights the importance of detailed structural analysis alongside these experiments as the SAM surfaces are inherently susceptible to damage when subject to bombardment by reactive atoms.

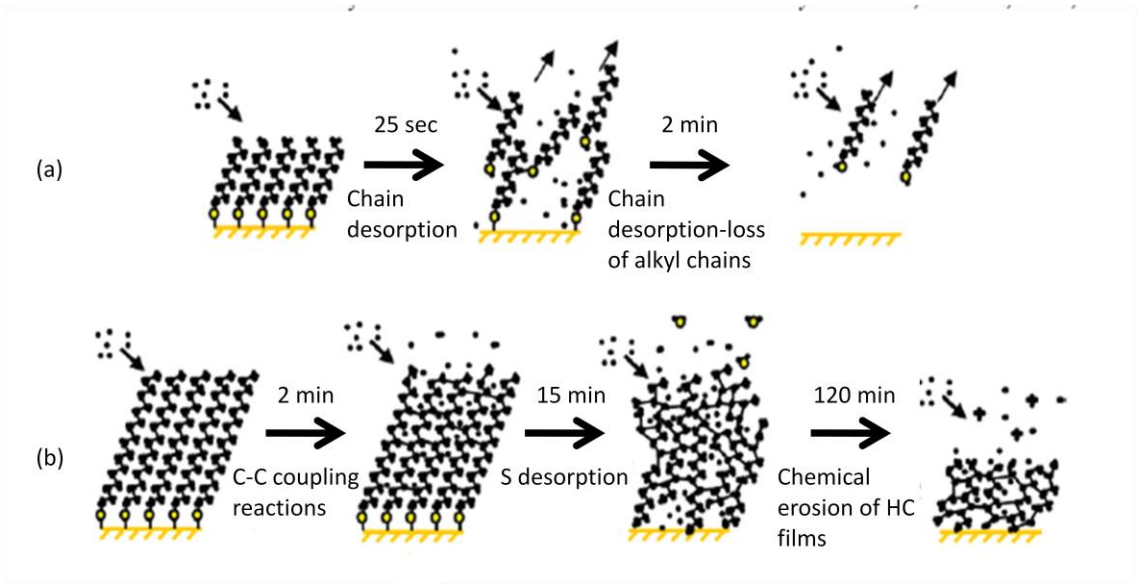

Figure 1.5: Diagram depicting the mechanistic differences in atomic hydrogen reacting at (a) short-chain and (b) long chain alkyl thiol SAMs. Figure adapted from reference [86].

1.4 Previous theoretical work on collision dynamics at the gas—liquid and related interfaces

1.4.1 Inelastic scattering at the gas—SAM interface

Theoretical scattering simulations have developed extensively in accuracy over the last decade motivated by a desire to understand energy transfer at the gas—SAM and closely related gas—liquid interface. Within this context SAMs are considered a reasonable proxy for liquid surfaces, decreasing the computational complexity which would be necessary for the detailed treatment of liquids. The field of inelastic scattering simulations at SAM surfaces has been dominated by the Hase and Troya groups, who have investigated independently a wide range of systems both inelastic and reactive.

Hase and co-workers began by simulating the interaction of Ne atoms with alkylthiol SAMs[32,91-93]. The model system for the SAM surface was originally a united atom (UA) model, including realistic bond lengths, angles, torsional and bending motions but treating each CH_3 and CH_2 group as pseudo atoms and the Au surface as rigid[91]. The Ne-SAM interaction was derived from *ab initio* calculations for the Ne + CH_4 system. The authors found that the Ne atoms did not penetrate deeply into the surface, regardless of initial energy. The majority scattered from the terminal CH_3 unit and a minor fraction from the subsequent CH_2 group (C_2). A number of trends were identified such as a preference for impulsive scattering at high energy and grazing incidence and a TD component consistent with thermally desorbing at a $\cos\theta$ angular distribution.

The model for Ne + alkylthiol SAMs was developed and tested by Hase, and they found that the energy transfer was independent of the analytical function applied to the *ab - initio* potential (whether two- or three-body terms were included). Energy transfer was more efficient in a UA model than an explicit atom (EA) model due to the lower barrier for conformational change with UA treatment, but the overall energy transfer trends from a UA and EA model were the same; the dynamics were insensitive to the size of the model SAM (35 chains vs. 100 chains) and to the Au substrate (whether it was treated as rigid or a thermal bath)[93]. As a result they had shown that a simpler and therefore computationally less expensive model, was effective at simulating these processes and subsequently used the UA model with the *ab initio* interaction potential to investigate the effects of intramolecular dynamics on energy transfer[92].

Hase collaborated with Sibener (experimentalist) to further understand the mechanistic details of Ne + SAM collisions[32]. It was found that the internal modes of the alkyl chains, particularly bending and torsional modes, were an efficient sink for dissipating energy during collisions[92]. The authors identified that certain direct trajectories, closely coupled to these modes, were able to dissipate sufficient energy in a *single* collision to appear in the TD channel (i.e. travelling slowly) in an equivalent experiment[32]. It was found, both theoretically and experimentally that Ne thermally accommodates only very rarely on SAM surfaces and the majority of slow trajectories are the result of deformation of the SAM surface in a single encounter.

These effects, although hard to distinguish experimentally, have been suggested by both Morris[43] and Sibener[32] through Ne + SAM experiments. A more dominant, formal TD mechanism was inferred in the Ne + liquid experiments of Nathanson and co-workers[8], perhaps reflecting the structural differences between SAM and liquid surfaces. Liquids would be rougher on a molecular level than SAMs, making accommodation and hence true TD more likely. Sibener and co-workers carried out complementary simulations on Ar[33] and Xe[31] scattering from alkylthiol SAMs in addition to their experimental molecular beam studies. The simulations showed that TD was more prevalent in the heavier and more polarisable noble gases and that once accommodated on the surface, thermalisation was rapid.

An interesting third mechanism was also identified for Xe, named directed ejection as described in section 1.3.2. In an extension to their previous work on Ne, the Hase group investigated collisions of Ar atoms with fluorinated (CF_3-SAMs) and hydrogenated (CH_3-SAMs) SAMs[94]. They were able to identify three limiting mechanisms, direct, physisorption and penetration. Those undergoing a physisorption mechanism had undergone two or more collisions but remained at the surface; they could then desorb at thermal (TD) or superthermal energies depending on the amount of energy transferred. Those which penetrated would emerge with typical TD characteristics, speeds dependent on the liquid temperature and a $\cos\theta$ angular distribution about the surface normal. The actual penetration depths were not reported. A trajectory was assigned to the penetration channel once it had reached any depth beyond the terminal CH_3 group.

Hase and co-workers' more recent work on Ar scattering from alkylthiol (CH_3-SAMs) and hydroxyl terminated (HO-SAMs) analysed the penetration depth more fully[39]. As had been observed previously in experiments, energy transfer was less efficient to

the hydrogen-bonded OH-SAM. The simulations uniquely revealed that the CH_3-SAMs were penetrated more deeply than the OH-SAMs, sometimes reaching as deep as the final carbon atom before the sulphur tether (C_{10}), before emerging at a range of speeds dependent on residence time and consequently the number of collisions. The H-bonding network in the OH-SAMs acted as a barrier to penetration. Physisorption, however, was more prevalent in OH-SAMs than CH_3-SAMs. As a result, the CH_3-SAMs could be described as being better at thermalising Ar and the OH-SAMs appeared more rigid and sticky to the incoming Ar atoms. An interesting development would be to extend the simulations beyond noble gases to the polar diatomic, HCl, experimental work has shown increased accommodation of HCl on OH-SAMs compared to Ar[37,44].

Simultaneously, Troya and co-workers simulated collisions of Ar at SAM surfaces[38]. They developed a hybrid explicit atom/united atom (EA/UA) force field to describe the SAM surfaces. The outer 2 carbons and associated hydrogens were treated explicitly (EA), while the remainder of the CH_2 units in the chain were treated as pseudo atoms (UA). The Ar-SAM interaction was modelled by an accurate all-atom potential derived from first principles. The inter-chain separations were adjusted to mimic the Ag and Au substrates used in the experiments of Morris and co-workers to study the effects of chain packing density on the collision dynamics[35]. In good agreement with the experiments it was found that the less dense (Au analogues) monolayers were more efficient at dissipating the initial energy and promoting trapping of the Ar atoms.

The trajectories were analysed and three distinct mechanisms were interpreted, direct (IS), trapping-desorption (TD) and direct penetration. Direct collisions were single bounce events, at the terminal CH_3 group. TD was defined as having undergone several collisions at the surface or in the surface interior before desorbing. Direct penetration was a single bounce encounter but at a point *below* the outer CH_3 group. These direct penetration events lost more initial energy than their direct counterparts but weren't fully thermalised either. A similar mechanism has been inferred experimentally with Ne[32], where true thermalisation was not observed. Distinguishing between mechanisms experimentally is difficult as most methods rely on the detection of scattered species travelling at a particular speed. In molecular beam experiments there will be some overlap between different collision mechanisms resulting in scattered products travelling at the same speed. Future developments combining translational

energy and internal energy detection methods could help isolate the predicted mechanisms.

Troya and co-workers extended their work beyond atoms to diatomics, specifically CO, scattering from alkyl (CH_3-) and fluorinated (CF_3-) SAMs. The motivation was to begin to predict the influence of internal energy transfer during collisions. The simulations were designed to investigate the energy transfer[45] and stereodynamics[42]. The work was carried out in collaboration with the experimentalists Morris and co-workers[45] although their molecular beam setup is incapable if internal state resolution. To this end direct experimental comparisons are, as yet, unavailable, but ultimately achievable given recent advancements in gas−surface scattering with internal state resolution.

In general terms, on translational energy transfer, the experiments and simulations are in agreement[45]. The CO transfers more of its initial translational energy to the CH_3-SAM than the more massive CF_3-SAM based purely on the kinematics of the collision. This echoes what has been previously observed experimentally at the gas-liquid interface[9,18,19,30] and the gas-SAM interface[46]. The simulations go beyond current experiments in the prediction of the collisional influence on the internal energy states of the CO. There is predicted to be an overall rotational warming (T→R energy transfer) post-collision with the SAM surface, which is more extreme in the CF_3-SAM than the CH_3-SAM. This is in contradiction to the work of Nesbitt on CO_2 scattering from PFPE and squalane surfaces[26], who found that the degree of rotational excitement (in the IS channel) was independent of the liquid. This could be indicative of differences in the surfaces, or in the projectile (CO_2 vs. CO). Troya and co-workers postulate that the differences in the efficiency of T→R energy transfer between the alkyl and fluoro SAMs is a structural quality of the surface (resulting from the molecular orientation with respect to the direction of rotation of CO at the moment of impact) in that CF_3-SAM surfaces exert more torque on the CO than CH_3-SAM surfaces.

CO vibration was also investigated and it was found that the collisions were ‘vibrationally adiabatic’. There was no net gain or loss of vibration as a result of collision, and the translational and rotational energy transfer was unaffected by the initial vibrational state of the CO (whether it was in $v' = 0$ or $v' = 1$). This was attributed to the timescales of the encounters, the collisions sampled were deemed to be of

insufficient duration to influence CO vibration. Interesting stereodynamical features were also predicted[42], whether starting with a random or oriented and aligned (in terms of rotational angular momentum) initial geometry, there was a rotational orientation and alignment preference in the scattered CO (figure 1.6). This was particularly evident in collisions that resulted in a large degree of rotational excitation. The *cartwheel topspin* motion was preferred from both SAMs but the extent to which it was favoured was greater in the CF_3-SAM. This was suggested to be a result of increased corrugation of the CH_3-SAM compared to the CF_3-SAM. Gas−SAM experimental work is currently behind theory in reaching the level of sophistication necessary to observe these subtle effects, but the promise of interesting properties will doubtless encourage development in these areas.

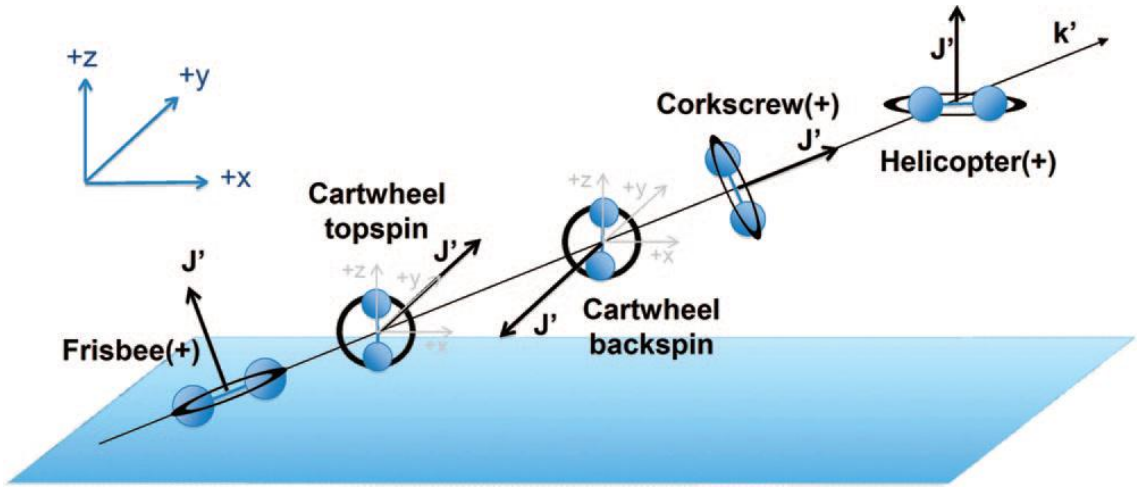

Figure 1.6: Schematic representation of the limiting rotational motions of a diatomic molecule scattering from a liquid surface. Reprinted from reference[42].

Hase and co-workers have recently carried out simulations of CO_2 scattering from F-SAM surfaces comparing an EA and UA model and using a CO_2 + CF_4 potential function to model the gas—SAM interaction[24]. As was the case in various gas—SAM and gas—liquid systems the energy transfer was more efficient at the CH_3-SAM surface. Their calculations show that this is indeed a result of mass and chain flexibility effects rather than the interaction potential. This is perhaps further evidenced by the fact that this effect has been observed experimentally using a range of different projectiles including noble gases[9], CO[42], CO_2[26] and HCl[37,44] at both gas—SAM and gas—liquid interfaces. The UA model would be advantageous to use, if it were effective, to save on computational costs. It was however, found to overestimate energy transfer and penetration compared with the EA model. At present there are no equivalent gas—SAM experiments to compare the theoretical simulations to; in

comparison to the work of CO_2 scattering from PFPE surfaces however, there is reasonable agreement.

These simulations further unravel the intricacies of the gas—SAM scattering mechanism. Here, four discrete mechanisms are predicted: direct (IS), resulting from a single collision; physisorption, resulting from 2 or more encounters at the SAM surface and desorbing at thermal or superthermal energies depending on the number of encounters; direct penetration, where the incoming projectile penetrates beneath the terminal layer and is subsequently thermalised; and physisorption-penetration, where the surface-physisorbed species, penetrate below the outer layer and are subsequently thermalised.

1.4.2 Reactive scattering at the gas—SAM interface

As was the case in the experimental studies described in section 1.3.3, the majority of reactive simulations at the gas−SAM interface have focussed on the reaction of $O(^3P)$ atoms at hydrocarbon surfaces. As such, the development of models is rooted in previous gas-phase work. This review will therefore commence with a brief review of these simulations.

Andresen and Luntz carried out the first theoretical investigation of $O(^3P)$ + HR reactions[95] alongside their experimental work[48]. They performed quasiclassical trajectory (QCT) calculations on a simple R-H-O triatomic model potential surface with a collinear approach geometry, where R was treated as being structureless. The London-Eyring-Polanyi-Sato (LEPS) potential energy surface (PES) was optimised to match the experimental results for a secondary hydrocarbon encounter. The experimental parameters included in the model were the vibrational branching ratio, the ground state rotational distribution and the barrier height. The primary and tertiary surfaces were not adjusted. When run, all three accurately reproduced the experimental observations; although there is circularity in that the trajectories on the secondary PES replicated the experimental parameters on which they were based.

The modestly superthermal rotational distributions observed experimentally (section 1.3.3) were replicated, including the narrower distribution in $v' = 1$ compared to $v' = 0$, as were the vibrational branching ratios. The calculations also predicted predominantly backscattered OH, in agreement with Suits[54,55] and co-workers experimental

observations but in contrast to those of Kajimoto and co-workers[53]. These first calculations proved successful at reproducing experimentally observed phenomena and were suggestive of the accuracy of the pseudo-triatomic-collinear-approach geometry and the direct mechanism.

The validity of the QCT calculations was confirmed following the work of Clary and co-workers[96] who carried out vibrationally adiabatic distorted wave (VADW) calculations. The VADW had been a tried and tested method for Clary and co-workers for triatomic systems such as $O(^3P) + H_2$ and was adapted for the $O(^3P)$ + HR system using the same LEPS potentials used in the QCT calculations. The results were in good agreement with experimental results and the previous QCT calculations.

The first rigorous calculations of potential energy surfaces from first principles (*ab initio)* were carried out by Walch and Dunning[97] on the $O(^3P) + CH_4$ system in the same year as Andresen and Luntz's QCT scattering calculations. These calculations, carried out using polarisation configuration interaction (POL-CI) wavefunctions, confirmed what had been inferred indirectly in the experimental results for higher hydrocarbons. The barrier height was calculated as being 42.7 kJ mol^{-1} in excellent agreement with the experimentally derived value[47]. The transition state (saddle point) was found to have C_{3v} symmetry with a preferred 180° collinear R-H-O geometry with elongated R-H and H-O bonds. The $O(^3P) + CH_4$ system was subsequently tackled by Schlegel and co-workers[98] during a comparative study of reactions of H, OH and $O(^3P)$ with methane. They accurately predicted the collinear transition state geometry but the barrier height was over-estimated compared to both the previous calculations by Walch and Dunning[97] and the experimental measurements. This over estimation was attributed to the single reference fourth order Moller-Plosset (MP4) basis set used to predict the barriers and heat of reaction. This was subsequently corrected by scaling to the POL-CI barrier calculated by Walch and Dunning.

There has been a revival in recent years of theoretical activity in these reactions, motivated in part by increased computational capabilities and the desire to more accurately predict the nature of the PES. Corchado and co-workers[99] implemented a more extensive dual-level calculation. They found reasonable agreement with the experimental rate constants and inferred transition-state geometry. They predict that quantum mechanical tunnelling effects are important in these reactions. The PES used by Corchado and co-workers was found to be antisymmetric (APES) with respect to the

four methane hydrogens by Espinosa-Garcia and co-workers[100]. They developed a new symmetrical analytical PES and went on to use it to examine dynamical features of the $O(^3P) + CH_4$ system, finding good agreement where comparable experimental data was available.

Clary and co-workers simultaneously used the less accurate but still realistic APES to carry out the first state-to-state scattering calculations on the $O(^3P) + CH_4$ system[101]. They investigated the influence of selectively exciting the vibrational modes of the CH_4 and found that excitation of the local C-H stretching and umbrella modes leads to significant increases in reactivity. This is contrary to what was later observed experimentally by Liu and co-workers[58]. These calculations also showed that certain initial states led to interesting and selective preferences for the rotational states of the final CH_3 radical.

Such dynamics would be interesting to probe experimentally but as yet this has not been attempted. Clary and co-workers continued to improve the construction of their Hamiltonians, extending to a more general $X + YCZ_3 \rightarrow XY + CZ_3$ system[102] including terms for the relative velocities of the reacting pair, a C-H stretch in the reactants and an O-H stretch in the products; defined as a 3DF (three degrees of freedom) model. This was followed by a yet more rigorous 4DF model[103] which defined for the first time the symmetric and asymmetric C-H stretch. In all cases, there was evidence that CH_4 vibrational excitement should lead to enhanced reactivity. In particular, the symmetric C-H stretch was predicted to be more efficient at promoting reaction than the asymmetric stretch[103].

In parallel Yu and Nyman used the symmetric PES corrected by Espinosa-Garcia and co-workers[100] and applied the rotating umbrella (RBU) model to perform time-independent quantum scattering calculations on the $O(^3P) + CH_4$ system. The RBU model is four-dimensional, including terms for stretching, bending and umbrella modes in the reactants. For the first time, product stretch, rotations and CH_3 umbrella motions were predicted for the scattered products. As observed previously, the excitation of the reactant modes led to increased reactivity and the CH_3 rotational distribution was correlated with the degree of excitation in the reactant CH_4.

Recent advancements have led to the progression from methane (CH_4) to ethane (CH_3CH_3) in higher-energy systems more representative of LEO by Schatz and

Troya[104,105] and Hase and co-workers[106,107]. At these higher collision energies (1-5 eV) alternative reaction pathways became available such as H-elimination and C-C bond breakage, in addition to the hydrogen abstraction channel. The differential cross sections show an increase from backward to forward scattering at the high collision energies[105], which was interpreted as being consistent with a direct collinear approach. It should be pointed out that this is not in agreement with the experimental work of Kajimoto and co-workers[53] who observed forward scattering at collision energies far lower (~0.34 eV) than those sampled by Schatz. The rotational energy distributions were calculated for the H-abstraction channel and were found to be more rotationally excited than those measured experimentally[51]. The experimental measurements were, however, carried out at substantially lower collision energy. High-level *ab initio* calculations have now advanced beyond ethane to larger hydrocarbons containing up to five carbon atoms. The result is that theoretical reaction barriers, reaction energies and thermal rate constants are now available for a wide range of $O(^3P)$ + HR systems of increasing complexity as is summarised in a recent broad study by Troya[108].

Extending theoretical treatments such as those described above to larger systems such as SAMs presents a considerable challenge. The complexity of such calculations scales as a power of the number of atoms in the system. As a result, the simulations are often a compromise between the accuracy of the model potential and the computational expense of running the calculations. Typically, in scattering simulations at the gas−SAM interface, less (computationally) expensive semi-empirical Hamiltonians are used in the place of rigorous quantum treatments to model the dynamics of the interaction of the $O(^3P)$ with the surface. In addition to this quantum mechanical/molecular mechanics (QM/MM) force fields have been developed for the treatment of the SAM surface as depicted in figure 1.7. An outer, QM, region is defined as being that involved in reaction. The remainder of the surface is treated by the simpler MM model and is assumed not to contribute to reaction. The position of the QM/MM boundary is a variable quantity, typically the outer two or four carbon atoms (of the alkyl chain) are defined as 'active' and are treated quantum mechanically.

The first scattering simulations of this type were carried out by Hase and co-workers[109] and the outer two carbon atoms formed the QM region. Semi-empirical PM3 electronic structure calculations were used for the $O(^3P)$ + SAM interaction potential based on high-level *ab initio* calculations of the $O(^3P)$ + C_2H_6 system. The

PM3 calculations were improved through re-parameterisation with experimentally and theoretically derived specific reaction parameters (PM3-SRP).

These simulations, despite their compromises, were able to predict a number of experimentally observed features for the hydrogen abstraction reaction: direct and thermal reaction channels, as had been inferred previously in the gas−liquid experiments of Minton[62,64,110] and McKendrick[63,66,68-70] and those in the gas phase (section 1.3.3); the majority of OH products occupying the ground vibrational state; and a modestly superthermal rotational distribution for direct products.

The system was revisited by Hase and co-workers several years later in more detailed simulations for the *non*-reactive encounters of $O(^3P)$ at a SAM surface[111]. The energy transfer for a wide range of initial energies and incident angles was calculated. A key difference over the earlier study was that the azimuthal angle was randomised which is a closer approximation of what would occur in an equivalent experiment. As a result it was predicted that, unlike in their early study (where the QM region was smaller), penetration and abstraction from the surface interior would occur (even at low collision energy).

Troya, in collaboration with Schatz simulated the reaction of *hyperthermal* (~5 eV) $O(^3P)$ atoms and alkylthiol SAMs motivated by the LEO environment[112]. They used the MSINDO (modified symmetrically orthogonalised intermediate neglect of differential overlap) semi-empirical Hamiltonian to treat the QM part of the system. In addition to inelastic scattering of the $O(^3P)$ atoms, three reactive channels were identified. H abstraction to form OH, O addition (into a C-H bond) resulting in H-elimination and O addition (to a C-C) bond resulting in the formation of CH_3O and CH_3CH_2O fragments. The MSINDO Hamiltonian is useful for predicting potential reaction channels available at the higher collision energies.

These simulations confirmed some experimentally observed quantities (from gas phase and gas−liquid experiments), although directly comparable reactive studies at the gas−SAM interface have not been carried out as yet. For example, it was predicted that the OH formed in the H-abstraction channel would be vibrationally cold, with less than 10% being in the first vibrationally excited state. The product rotational distribution was mechanism dependent. The direct reaction products were found to be rotationally hot (~5 kJ mol^{-1} in rotation). The TD component (in the H-abstraction channel) was

thermalised in as much as it was described by a Boltzmann distribution but the distribution was hotter than the surface temperature suggesting incomplete thermalisation. This could be a consequence of the very large collision energy or a result of the trajectories with residence times > 3 ps being discounted to save on computational cost. Alternatively, the model potential may be responsible for this over prediction.

In all experimental cases to date, only modestly superthermal rotational distributions have been observed in the direct OH reaction products. The simulations of Troya and Schatz predict up to 0.3 eV (30 kJ mol^{-1}) to appear in product rotation. This is equivalent to a rotational temperature in excess of 3000 K. McKendrick and co-workers in contrast, measured a rotational temperature of ~370 K[66] in the direct reaction products. The difference could be a consequence of the far higher collision energies in the simulations although a similar study carried out independently by Schatz[113] with 1 eV O(^{3}P) also significantly over predicted energy in internal modes, compared to experiment. This suggests that amount of energy in the internal states is insensitive to collision energy and that it is the simulation that is quantitatively inaccurate.

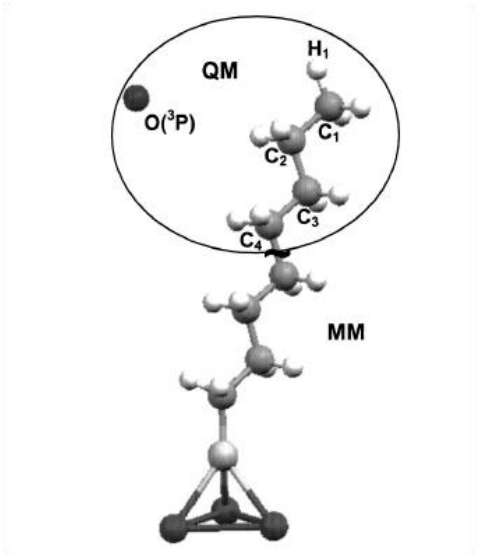

Figure 1.7: Schematic representation of the QM and MM regions of the QM/MM hybrid model. Reprinted from reference[114].

There is clearly a requirement to improve the accuracy of the calculations described above. This challenge has, at least partially, been met recently by Troya and co-workers[115] who investigated the reactions of F atoms at alkylthiol SAM surfaces. Their approach was to compare a number of semi-empirical Hamiltonians with more rigorous quantum calculations for a gas-phase system (O + CF_4/C_2F_6) to allow them to

select the most accurate interaction potential possible (ultimately selecting the MSINDO Hamiltonian). A specific-reaction-parameter (SRP) approach, similar to that used by Hase[109] was also included. As a result of these measures, Troya and co-workers achieved far greater agreement with the available experimental work than was previously obtainable.

The model predicted that the HF products were: vibrationally excited (distribution peaking in $v' = 2$); had an inverted vibration-to-collision energy dependence; were rotationally superthermal (peaking at J = 3-4 and extending out to ~J = 15); and had a rotational distribution which was colder that the vibrational distribution. All of the above are in agreement with the experimental findings of Nesbitt and co-workers[73] from the reaction of F atoms and a liquid squalane surface.

It is clear that there has been significant development in the theoretical treatment of gas−SAM interactions. There is now a requirement for these improvements to be applied more widely, to different reactive systems and to investigate effects such as: collision energy dependence; angular randomisation (as would be the case in any complimentary experiments at the gas−SAM interface); location of the QM/MM boundary (to account for potential reactions deeper in the chain); and ultimately to extend these methods to the more complicated liquid hydrocarbon environment.

1.4.3 Molecular dynamics simulations of liquid hydrocarbon surfaces

The development of the theoretical treatments described in section 1.4.2 to the gas−liquid interface, would require a significant leap in complexity. The liquid hydrocarbon, with additional degrees of freedom and more atoms than a SAM proxy presents a significant computational challenge. In order for such simulations to be attempted (section 1.4.4), a suitable model for the liquid hydrocarbon structure must be developed to accurately portray the chemical, physical and interfacial properties of liquid hydrocarbons. What follows is a description of the recent developments in the field of molecular dynamics (MD) simulations, as applied to liquid hydrocarbons.

Harris was the first to carry out MD simulations of linear liquid hydrocarbons[116] using a UA approach where the methyl (CH_3) and methylene (CH_2) units were treated as pseudoatoms (the hydrogen atoms were not explicitly represented). The UA approach was necessary to reduce the associated computational cost but realistic bond

lengths, angles and torsional potentials were included in the simulation. Some 300 decane ($C_{10}H_{22}$) and eicosane ($C_{20}H_{42}$) molecules were included in a 'box' with periodic boundary conditions in all directions, assigned random velocities from a Maxwell-Boltzmann distribution and allowed to equilibrate.

The simulations broadly replicated most of the physical and interfacial properties of the liquids; although some physical properties, such as surface tension, were found to be over-estimated with respect to experimental measurements. This was due to the limits of the accuracy of the Lennard-Jones based model and could be corrected for by introducing terms for three-body interactions in the potential. The structural predictions were particularly interesting. It was found that at temperatures well above their melting points the liquids exhibit a significant degree of defined interfacial structure. At 400K (melting points < 300 K) both $C_{10}H_{22}$ and $C_{20}H_{42}$ had methyl (CH_3) groups preferentially exposed at the interface. The methyl units were described as tending to protrude from the interface at an angle perpendicular to it and the methylene units were found to lie preferentially, on average, parallel to the interface.

Yamamoto and co-workers, motivated by peculiar structural effects predicted at the gas—liquid interface, carried out similar simulations on n-alkanes[71,72]. The UA method was adopted here also, but a simplified bead-spring system was employed neglecting bond angles and torsional motions, allowing for faster and larger simulations to be carried out. They simulated the gradual heating of a frozen crystalline sample and observed preferential melting in the bulk while the interface remained frozen[72]. This was found to persist over a wide temperature range (385-410 K) around the melting point of the liquids[71]. The surface freezing was described as a monolayer structure and according to the simulations even exhibited the hexagonal packing known for SAMs.

This has important experimental implications as surface freezing was proposed as an explanation for the reduced reactivity of linear hydrocarbons, compared with branched ones, towards $O(^3P)$ atoms[68]. McKendrick and co-workers repeated the simulations of Yamamoto, replicating hydrocarbons and experimental conditions used in their experiments and found that the interfacial freezing was observed (figure 1.8). In contrast to the thermally equilibrated simulations of Harris and co-workers[116], the simulations carried out by Yamamoto are more comparable to the experimental conditions used by McKendrick and co-workers. Due to vapour-pressure constraints

the experiments were limited to temperatures just above the melting points making surface freezing a viable explanation for the observed trend in reactivity. Harris' simulations predict the opposite trend for thermally equilibrated liquid samples; this would be interesting to test experimentally.

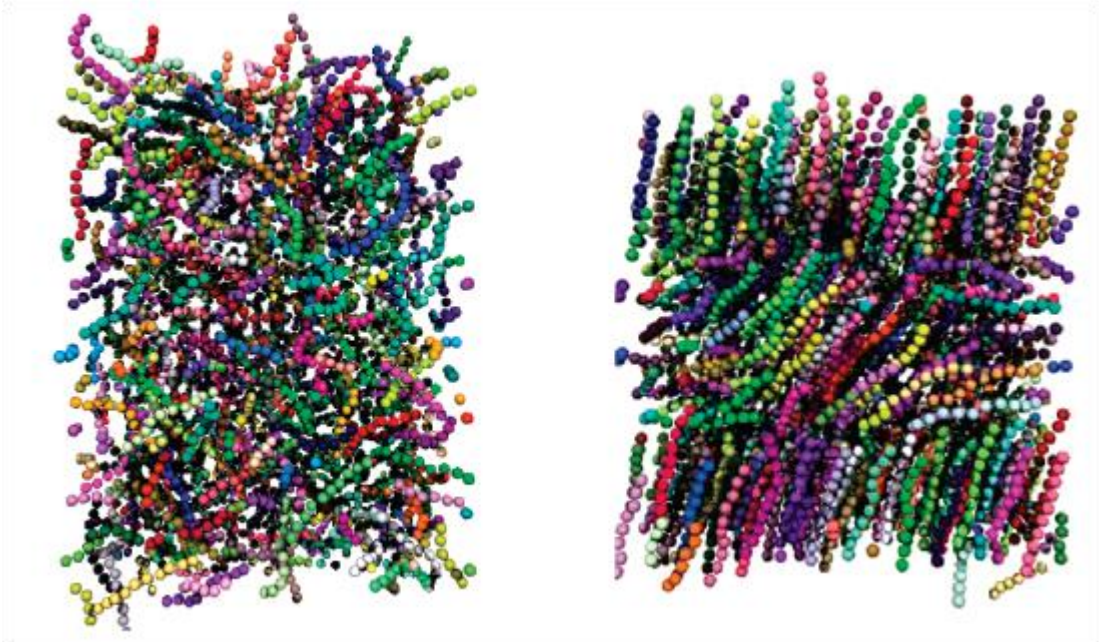

Figure 1.8: Molecular dynamics simulations of a $C_{10}H_{21}$ linear hydrocarbon. Interfaces with vacuum are located on the top and bottom of the slab. Left view is a snapshot of the thermally equilibrated 400 K simulation and right view follows rapid cooling to 240 K showing the monolayer-type interfacial structure. Reprinted from reference[68].

Mondello and Grest[117] carried out the first MD simulations on the branched liquid hydrocarbon, squalane. It was a development of the UA model used by Harris and the methyl (CH_3), methylene (CH_2) and methine (CH) units were treated as three distinct pseudo-atoms. The simulations were designed to test transport properties such as the diffusion coefficients of complex fluids and were a test for the applicability of the potentials to branched hydrocarbons compared with linear ones. The simulations reproduced with reasonable accuracy some experimentally derived properties, but the simulations were regarded as a preliminary study and not fully developed to correctly represent branched hydrocarbons.

This challenge was met by Siepmann who developed a transferable potential for phase equilibria united atom (TraPPE-UA) force field with a Monte Carlo (MC) simulation method to study the liquid-vapour phase behaviour of squalane[118-120]. In Siepmann's initial work[118,119], the squalane molecules (~200) were given the initial conformation of a layered crystal and cycled through several thousand MC cycles at an

elevated temperature, defining the melt system. The MC cycles represent random selections (from a defined range) of *moves* such as translation, rotation and conformational change applied to each of the individual molecules. The melt system was then cooled to the desired temperature, equilibrated through a further 25000-100000 MC cycles[119] and subsequently analysed. The simulations gave excellent agreement with experimentally established properties such as critical and boiling temperatures, reflecting the ability of the model to simulate a branched liquid hydrocarbon.

A subsequent study by Siepmann and co-workers[120] was focussed more on the interfacial structural properties of squalane. The chemical structure of the interface was investigated by plotting Z-density profiles of the individual pseudo-atoms, which reflect the probability of finding a particular pseudo-atom (or corresponding CH_x unit) at a certain distance from the bulk through the interface to the vacuum. They found that the interface was very *rough* on a molecular level but no individual group was preferentially exposed at the interface, unlike in the linear hydrocarbons[116]. This was of interest to McKendrick and co-workers who set out to use Siepmann's MC method and (TraPPE-UA) force field to generate Z-density profiles which could in turn be used to predict the probability with which an oxygen atom approaching a squalane surface will hit a particular type of CH_x group[121]. The method was extended to 288 squalane molecules (96 for Siepmann[120]) and the simulations almost exactly replicated experimental surface tension measurements.

McKendrick and co-workers found a modest but clear preference for CH_3 primary units to occupy the interfacial region for the branched hydrocarbon squalane. They argue that this is also the case in the work by Siepmann if their Z-density profiles were scaled to the relative amounts of CH_3, CH_2 and CH groups present. McKendrick and co-workers showed that an O atom approaching a squalane surface would be slightly more likely to hit a CH_3 unit than predicted by stoichiometry but all three hydrogen environments are available at the interface for abstraction, corroborating their earlier experimental findings[51].

1.4.4 Inelastic scattering at the gas—liquid interface

To date, there has only been a very limited number of theoretical simulations on inelastic scattering at the gas—liquid interface. Nathanson and co-workers

complemented their experimental work on collisions of Xe atoms at a squalane surface with molecular dynamics simulations. The squalane $C_{30}H_{62}$ structure was treated simply as a large soft sphere[16]. This early study, taking into account the obvious structural oversimplifications, was designed to investigate whether simple models could effectively reproduce the experimentally observed scattering behaviour.

The model was accurate at reproducing certain aspects of the experiment, such as a bimodal translational distribution in the scattered products. It was unsuccessful at replicating the energy transferred in the collisions, largely due to the neglect of any internal modes of the liquid. The trapping desorption component was particularly underestimated. TD events are influenced by the projectile-surface intermolecular potential (represented in the model by a Lennard-Jones potential for Xe + CH_4). It is therefore natural that this is where the model was most limited; as a sphere-type model for a liquid hydrocarbon cannot accurately portray these interactions.

Over a decade later, Hase and co-workers carried out classical chemical dynamics simulations of Ne scattering from a squalane surface[122]. The treatment of the squalane molecules remained classical and was developed from a UA approximation. The remainder of the structure was represented by realistic bond lengths, angles, torsion and stretching modes. The interaction potential between the Ne and the CH_3 and CH_2 units in squalane was developed from high-level electronic-structure calculations similar to those used in simulations of Ne and self-assembled monolayers (section 1.4.1). This gave much better agreement with experiment in terms of energy transfer[8] than Nathanson's earlier model[16]. The simulations of Hase and co-workers also allowed for the correlation of Ne final energy and number of collisions (kicks) to be investigated. It was found that those trajectories which were thermalised at the surface (TD) had undergone multiple collisions at the surface but were not dissolved in it (as they had relatively short residence times).

There is clearly disparity between the volumes of experimental and theoretical studies of gas—liquid scattering dynamics, favouring experimental work at the present time (section 1.5). The following section will describe recent theoretical advancements towards the accurate simulation of hydrogen abstraction reactions at the gas—liquid interface.

1.4.5 Reactions at the gas—liquid interface

The MD simulations discussed in section 1.4.3 detail the development of accurate models to describe a liquid hydrocarbon surface. The ultimate challenge is in using these models to advance the complex scattering calculations described in section 1.4.2 beyond the SAM, to a liquid surface. The complexity arises from the molecular dynamics used to simulate the liquid surface, and the electronic structure calculations necessary to model the interaction of the incoming atom and the surface. For these reasons this field is very much in its infancy, as highlighted in table 1.1 (section 1.5). The situation is beginning to change and Schatz and co-workers have recently carried out the first such simulations[113,123] for the $O(^3P)$ + squalane system.

The liquid surface was treated with an explicit atom force field (OPLS-EA), explicitly defining the hydrogen atoms because they are involved in the reactions. The liquid surface was treated in two portions. The part of the surface involved in the collision was treated quantum mechanically (QM) and the rest of the molecule by simpler, classical molecular mechanics (MM) methods. The beauty of these simulations is that the positions of the QM/MM boundaries were able to change throughout the encounter and need not be defined beforehand. The QM section is defined by a sphere around the open shell projectile and therefore follows it throughout the trajectory, modelling the most realistic interactions on-the-fly. The MSINDO semi empirical Hamiltonian was used, similar to the more recent work of Troya at the gas−SAM interface[115]. The specific-reaction-parameterisation refinement employed by Troya is currently not being included in these preliminary studies on gas−liquid systems.

The energies simulated by Schatz and co-workers were high, 1-5 eV, to mimic conditions in LEO and to complement the experiments of Minton[64]. An H-elimination and a C-C bond breaking channel were predicted, the H-elimination channel remains to be observed experimentally[64]. At these high energies, the H-abstraction channel was found to be the dominant. The probability of the OH reaction products entering the gas-phase was very high (> 80%), suggesting that, at these high energies at least the majority of H-abstraction products will be scattered away from the liquid surface. The direct channel in the simulations was shown not to reflect the strong specular scattering observed in the analogous experiments[62,64].

This was interpreted as being a problem in experimental studies in defining what is truly direct and what is TD. The simulations predict that some of the trajectories travelling with speeds consistent with a direct mechanism will have had a number of encounters at the surface. The reverse was predicted also; that slow products may arise from single encounters at the surface. The binary separation between direct and TD events in experimental studies represents extremes in mechanistic behaviour. The true picture appears to be far more complex.

The internal energy, particularly OH rotation, was over-predicted at the lowest[123], and highest[113], collision energies sampled compared with experimental observations[66,67,124]. This is a similar problem to that described in section 1.4.2, and is likely a result of compromises in the Hamiltonian accuracy which were necessary for these complex calculations. Previous developments at the gas–SAM interface suggest that re-parameterisation (SRP) of the model could improve the accuracy[115]. Clearly, there is room for improvement, but the achievements to reach this point should not be underestimated. Schatz and co-workers have made a major development in extending scattering simulations of this type beyond the SAM proxy to liquid surfaces. This will hopefully encourage further progress in this field.

1.5 Summary of the field of scattering dynamics at the gas—liquid and related interfaces

This chapter has reviewed the field of scattering dynamics at the gas—liquid and related interfaces. Table 1.1 summarises the systems which have been studied up to this point in time, with their respective references. Inelastic and reactive collisions at gas—liquid and gas—SAM interfaces have been included. The investigations have been separated according to the detection method used and whether experimental or theoretical. In general, those with mass-spectrometric detection are molecular beam experiments providing information on the translational energy of the scattered species. Those listed as spectroscopic methods utilise detection with quantum state resolution and hence information on the internal energy distribution. The table clearly shows that some areas are less developed than others: experiments using spectroscopic detection methods, reactive scattering studies (at both interfaces) and the theoretical treatment of processes at liquid surfaces are currently less well studied.

The experimental work in this thesis aims to improve this situation and its relevance is shown in table 1.1. Presented in the following chapters is a body of work composed of three separate but closely linked studies. First, hydrogen abstraction reactions at ionic liquid surfaces by $O(^3P)$ atoms have been investigated, in tandem with complementary molecular beam experiments by the Minton group (chapter 3)[125]. These experiments are the first examination of the reactivity of a technologically important class of liquids towards $O(^3P)$ atoms. Second, the reactivity of $O(^3P)$ towards alkylthiol SAMs has been established (chapter 4). The OH reaction products were detected by LIF making this the first dynamical investigation of reactions at the gas—SAM interface with internal state resolution. Finally, the inelastic scattering and reactive uptake of OH radicals at a range of liquids of atmospheric interest has been investigated (chapter 5). This is the first experimental study of the collisions of an *open-shell* molecule at the gas—liquid interface.

Scattering type (interface)	Mass spectrometric detection method	Spectroscopic detection method	Theoretical scattering simulations
Inelastic (gas—liquid)	Ne[7-10], Ar[9,10,13], Xe[7,9,10], SF_6[7], CH_4[8], NH_3[8], H_2O[126] and D_2O[8].	I_2[18-20], CO_2[21-26] **OH(chapter 5)**	Xe[16] and Ne[122]
Inelastic (gas—SAM)	He[30,127], Ne[32,43], Ar[30,33-36], Xe[31], NO[30], O_2[30] ,CO[42,45] HCl[37,44], ND_3[43], CD_4[43], D_2O[43], and CO_2[46].	NO[128]	He[127], Ne[32,92,93,129] , Ar[33,38,39,41,130], Xe[31], CO[42,45] and CO_2[24,131]
Reactive (gas—liquid)	$O(^3P)$[61,62,64,65] and Cl[61]	$O(^3P)$[63,66-69,124] and F[73], **OH(chapter 5), $O(^3P)$(chapter 3)**	$O(^3P)$[113,123] and F[123]
Reactive (gas—SAM)	H[85,86], $O(^3P)$[83,84], O^+ [88-90]	**$O(^3P)$(chapter 4)**	$O(^3P)$[109,111,112] and F[132]

Table 1.1: Summary of the current 'state of the art' of scattering dynamics at the gas—liquid and related interfaces. Contributions to the field included in this thesis are highlighted in bold.

Chapter 2

Experimental

The general experimental approach is outlined in the following section. The experimental methodology is a continuation of the previous work carried out by McKendrick and co-workers on the dynamics of reactions between $O(^3P)$ atoms and liquid hydrocarbons[63,67-70] (chapter 1 section 1.3.3). A number of additional experimental advancements were made. These will be highlighted in this chapter as well as in the introduction to each relevant chapter as necessary.

The surface was at the heart of all the experiments, whether it was a liquid or self-assembled monolayer. In all cases a laser-based pump-probe method was employed. Potentially reactive radicals were generated by photolysis of a low pressure (normally ~1 mTorr) of a suitable precursor at a fixed distance above the surface. A fraction of those generated travelled to the surface, interacted with it and returned to the laser axis where they were detected by LIF.

2.1 The liquid surface

For all experiments at liquid surfaces (chapters 3, and 5) the central feature of the experimental set-up was the liquid-coated wheel. Pioneered by Lendovich and Fenn[133], this method has been widely used to provide evenly covered and continually refreshed liquid surfaces for a variety of experimental approaches.

The stainless-steel 5 cm diameter wheel (figure 2.1 (a)) was immersed in a custom-made copper bath filled with approximately 2 ml of the desired liquid. The wheel was rotated at 0.5 Hz, driven by an external motor, turning an axle connected to the wheel. A copper spacer was placed between the wheel and the front of the bath as this was found to give more uniform coverage. The temperature of the bath was controlled by a Peltier heating element and monitored by a thermocouple. This allowed for

temperature-dependent measurements to be taken from 0 °C to +70 °C (± 1 °C). Figure 2.1 (a) i and ii shows the second-generation wheel set up. The first generation was identical in terms of the liquid wheel but the re-designed version had additional features for ease of liquid exchange.

The first-generation wheel (used previously by McKendrick and co-workers and in chapter 3 and part of chapter 5) had a bath whose distance relative to the laser axis was varied by adjusting a series of bolts on the outside of the chamber. Each time a different liquid was used the entire wheel assembly was removed, the bath was cleaned and re-assembled, filled with a new liquid, put back inside the chamber and the distance would be set again. The second-generation wheel (used for the majority of chapter 5) was designed so that the distance was set and the wheel assembly was fixed permanently in place, whilst three interchangeable wheels (figure 2.1 (a) i) and their baths could be removed easily and quickly via the front access port. This resulted in shorter turnaround times when changing liquids and improvement in reproducibility in terms of wheel-to-laser-axis distance.

2.2 Chemical and physical properties of liquids used

Various liquids were used during the course of this work. The major practical constraints when selecting suitable liquids were the vapour pressure and melting points. Squalane ($C_{30}H_{62}$, 2,6,10,15,19,23-hexamethyltetradodecane) was used throughout as a reference as it has a convenient combination of a low melting point (-38 °C) and a vapour pressure of 1×10^{-7} Torr at room temperature. A summary of the liquids used, along with relevant physical properties, is given in table 2.1. The corresponding molecular structures are provided in figure 2.2. Most liquids were purchased and used directly without further purification. The ionic liquids were custom-synthesised by collaborators at the University of York[134].

The ionic liquids used were a family of 1-alkyl-3-methylimidazolium bis(trifluoromethylsulfonyl)imide based molten salts, each with a similar structure (figure 2.3) except for the length of the alkyl chain R. This class of ionic liquids are generally named [$C_n$mim] [NTf_2], where *n* refers to the chain length of the alkyl chain R. The smaller members of the series are commonly referred to as [emim] [NTf_2] and [bmim] [NTf_2] with chain lengths of $n = 2$ and $n = 4$ respectively. The ionic liquids were thoroughly de-gassed at 10^{-6} mbar and 70 °C for 24 hrs before use.

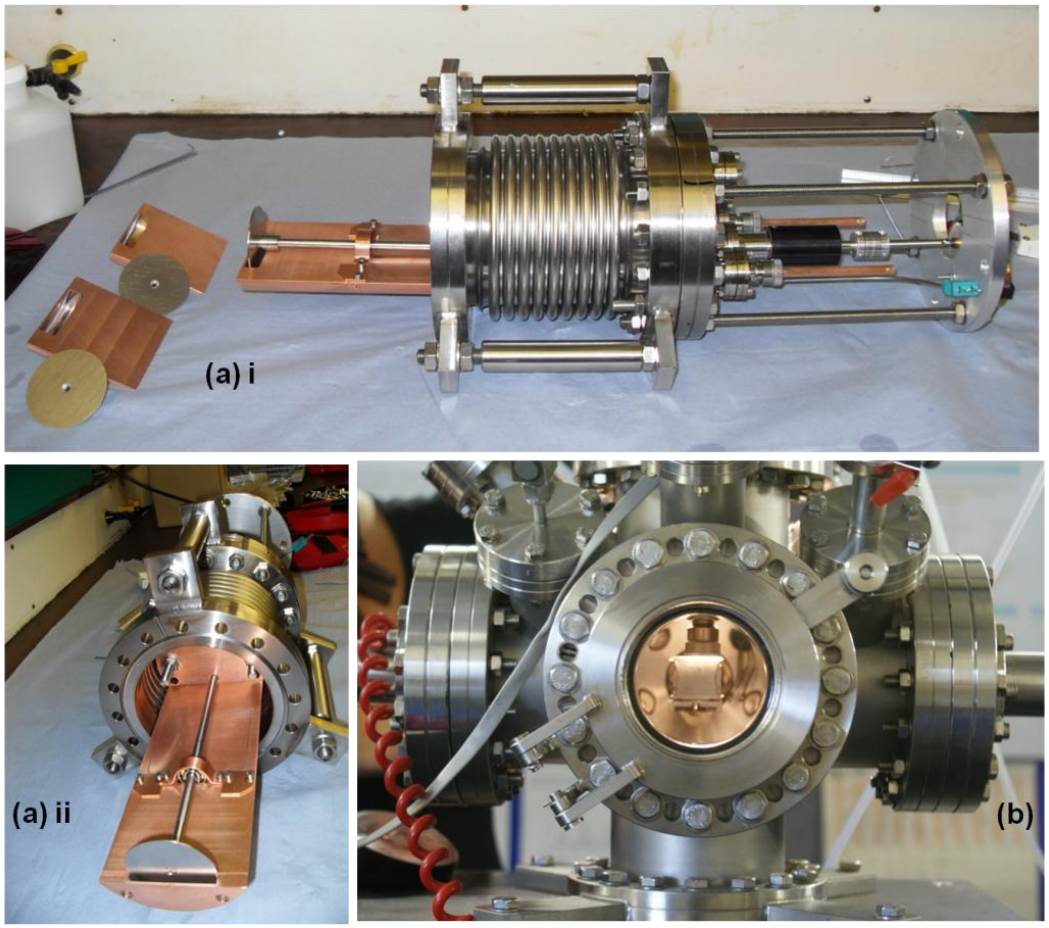

Figure 2.1: Photographs of the second generation wheel assembly (a) i and (a) ii showing the interchangeable bath, axle and external motor and (b) the custom made SAM holder located within the experimental vacuum chamber.

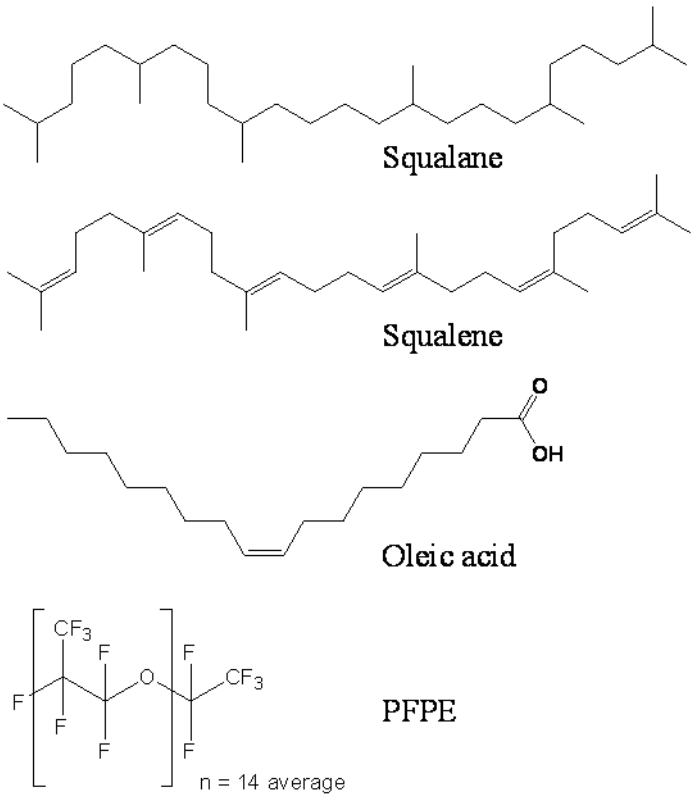

Figure 2.2: Chemical structures and common names for the organic liquids used.

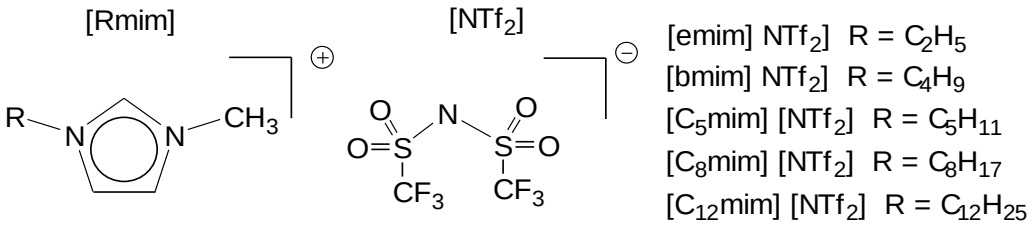

Figure 2.3: Chemical structures and nomenclature for the 1-alkyl-3-methylimidazolium-based ionic liquids

Liquid	Chemical formula	Source	Purity	Vapour Pressure/ Torr (at 298 K)	Melting Point / K	Relevant Chapter
Squalane	$C_{30}H_{62}$	Sigma-Aldrich	≥ 99%	~10^{-7}	235	3, 4and 5
PFPE (Krytox 1506)	F-[CF(CF_3)-CF_2O]-CF_2CF_3	DuPont	-	~10^{-7}	213 (pour point)	3 and 5
Ionic Liquids [Rmim] [NTf_2]	R=C_2H_5, C_4H_9, C_5H_{11}, C_8H_{17}, $C_{12}H_{25}$.	Custom synthesis	Halide <100 ppm Water <50 ppm	Negligible	< 288	3
Squalene	$C_{30}H_{50}$	Sigma-Aldrich	≥ 98%	~10^{-7}	198	5
Oleic acid	$C_{18}H_{34}O_2$	Sigma-Aldrich	≥ 99%	~10^{-8}	288	5

Table 2.1: Key properties and chemical formulae of the liquids used.

2.3 Self-assembled monolayer preparation and surface characterisation

The substrates for the SAMs were atomically flat 20 mm 20 mm gold (111) thin films (200 nm thick), deposited onto freshly cleaved Mica substrates (Phasis Sárl, Geneve). The desired thiol (table 2.2) was dissolved in appropriate quantities of analytical reagent grade absolute ethanol (or tetrahydrofuran for C_{18}) (Fisher Scientific) to give a 1 mmol L^{-1} solution. The gold slides were immersed in the ethanolic solutions at room temperature for a minimum of 6 hours, although normally overnight. The SAMs were then removed from the solutions, rinsed with ethanol and dried with research grade nitrogen (BOC) and used immediately. The SAMs were placed on custom-built holders (figure 2.1 (b)), held in place by stainless-steel clips and placed in the vacuum chamber through an access window attached to an x,y,z translation stage. The stage allowed reproducible three-dimensional positioning of the SAM. The distance from the SAM surface to the laser axis was accurately known (± 0.5 mm) through a series of calibration tests. The SAMs were characterised at different stages (specific details provided in chapter 4) by scanning-tunnelling microscopy (STM)[135] and X-ray photoelectron spectroscopy (XPS)[136].

Thiol	Chemical formula	Source	Purity
Fully hydrogenated	$C_6H_{12}SH$, $C_8H_{17}SH$, $C_{12}H_{25}SH$, $C_{18}H_{37}SH$	Sigma-Aldrich	≥98%
Fully deuterated	$C_6D_{12}SH$, $C_{12}D_{25}SH$	CDN-isotopes Cambridge	≥99%
Partially deuterated	$CD_3(CH_2)_{11}SH$, $CD_3CD_2\ (CH_2)_{10}SH$	Custom synthesis	-

Table 2.2: Summary of thiols used for self-assembled monolayer preparation

2.4 Vacuum system

Photographs of the second-generation wheel assembly, SAM holder and reaction chamber are shown in figure 2.1 ((a) and (b)). In either case the surface was held inside a six-armed stainless-steel reaction chamber (Vacuum Generators) of volume approximately 12 L. In the gas-liquid experiments the chamber was evacuated by a cryo-cooled diffusion pump (Edwards Diffstak) and an air-cooled turbomolecular pump (Edwards EXT 75DX) backed by rotary pumps. Foreline traps containing activated alumina (Edwards) for hydrocarbon capture were placed between the rotary pumps and their respective diffusion and turbo pumps to minimise backflow of pump oil into the chamber. This system resulted in typical base pressures of 1×10^{-6} mbar.

For the gas-SAM experiments, the turbomolecular pump backed by a rotary pump was used in isolation. In this case a liquid nitrogen trap was added to the fore-line as cleanliness of the chamber was of paramount importance during these experiments. As the overall volume was lower and the surface assembly more leak tight in the gas-SAM experiments, the turbopump alone was sufficient to give superior base pressures (typically 1×10^{-7} mbar) and reduced the risk of contamination from pump oils. The pressure in the chamber was monitored using an inverted magnetron ion gauge (Edwards) in the region 10^{-2} to 10^{-9} mbar and a capacitance manometer (Edwards Barocel 0-1 Torr) for higher pressures.

2.5 Photolytic precursors

The scattered species in all experiments was formed by laser-photolysis of a suitable precursor. Precursors were selected on the basis of a number of considerations, such as availability, ease of preparation where necessary, sufficiently high photolytic quantum yields and having an acceptable absorption cross section at a wavelength accessible by commercially available lasers. The photolytic precursors used are summarized in table 2.3.

2.5.1 Precursor pressure and single collision conditions

A low pressure, typically 1 mTorr, of a given precursor was admitted into the chamber where it was photolysed. This pressure was chosen specifically because it was important that the experiments were carried out under ‘single-collision’ or nascent

conditions. That is a situation where the majority of molecules detected have been unaffected by any secondary encounters. This is an important prerequisite when studying collision dynamics as only under single-collision conditions does the scattered species have a reliable *memory* of the encounter of interest. If the proportion of molecules in a sample which have undergone more than one collision on average is high, then this information will be lost as the sample moves toward a collisionally thermalised distribution.

The average number of collisions suffered by the scattered products was estimated using a typical gas-kinetic collision rate constant of 1×10^7 collisions $Torr^{-1}$ s^{-1}. At a pressure of 1 mTorr and a typical photolysis-probe delay time of 15 μs, the average number of collisions was therefore 0.15, sufficiently low to assume that the detected products were in fact nascent. A further check that is not dependent on the gas-kinetic collision rate constant and therefore the assumption of thermal velocity distributions (which are not in general produced in the photolysis) was to calculate the average distance between collisions. The mean free path (λ) was calculated according to equations 2.1 and 2.2. Treating them as hard spheres, typical radii for NO_2 and OH are 1.46 Å[137] and 0.48 Å[138] respectively. The collision cross section, σ (equation 2.1), was determined for a collision between NO_2 (precursor) and OH (product) to be 1.18×10^{-19} m^2. At a pressure of 1 mTorr the resulting mean free path, λ, is ~19 cm. In comparison, typical distances travelled (a return trip from the laser axis to the surface and back) in the experiments varied from 1 cm up to a maximum of 1.8 cm. As the average distance travelled by the scattered products was considerably shorter than the average distance between collisions it can again be assumed that the overwhelming majority of products detected were nascent.

$$\sigma = \pi(r_1 + r_2)^2 \quad \text{Equation 2.1}$$

$$\lambda = \frac{k_B T}{\sqrt{2}\sigma P} \quad \text{Equation 2.2}$$

Precursor	Species	Photolysis wavelength / nm (and lab-frame polarisation)	Absorption cross section (σ) / cm^2	Anisotropy parameter (β)	Source	Relevant chapter
Nitrous acid (HONO)	OH	355 (vertical)	6×10^{-19} [139]	-1 [140]	Reaction ($NaNO_2 + H_2SO_4$)	5
Deuterated nitrous acid (DONO)	OD	355 (vertical)	6×10^{-19} [139]	- 1 [140]	Reaction ($D_2O + NO_2 + NO$)	4 and 5
Nitrogen dioxide (NO_2)	$O(^3P)$	355 (horizontal)	5×10^{-19} [139]	+ 0.7 [141]	BOC ≥ 98% purity	3 and 4

Table 2.3: Summary of photolytic precursors used to generate the relevant scattering species.

2.5.2 Nitrous acid precursor formation

The OH and OD radicals were generated from a nitrous acid precursor (HONO/DONO). The HONO was generated in a reaction between sulfuric acid and sodium nitrite solution. H_2SO_4 (100 ml, 2 mol L^{-1}) was placed in a three-necked flask within an ice bath. $NaNO_2$ (200 ml, 2 mol L^{-1}), held in a dropping funnel above, was added slowly to the acid at a constant drop rate of around 0.25 drops/second. This yields HONO according to reaction (1).

$$2NaNO_2(aq) + H_2SO_4(aq) \rightleftharpoons 2HONO(g) + Na_2SO_4(aq) \quad (1)$$

$$NO_2(g) + NO(g) + H_2O(l) \rightleftharpoons 2HONO(g) \quad (2)$$

$$NO_2(g) + NO(g) + D_2O(l) \rightleftharpoons 2DONO(g) \quad (3)$$

The reaction was left to stabilize for 1 hr before use. The HONO gas evolved was extracted from the flask by a constant flow (70 sccm) of high purity nitrogen. As a safety precaution, to avoid a buildup of pressure in the flask, most of this flow was directed to an exhaust, apart from a small fraction which was extracted via a metering valve to the vacuum chamber. The pumping of the chamber was balanced to give a precisely controlled pressure (1 mTorr). The nitrogen flow rate and salt drop rate were set to maximize HONO concentration, monitored by LIF signal intensity of the OH formed by HONO photolysis and to minimize the formation of NO_2 through HONO decomposition (reaction (2)).

The minimization of NO_2 formation was a crucial factor. The HONO was used as a precursor to OH in the *inelastic* scattering experiments (chapter 5), it was therefore important to ensure that any OH from alternative sources such as *reactive* processes was minimized. At the wavelength used for HONO photolysis (355 nm), NO_2 is also photolysed to give ground state oxygen atoms ($O(^3P)$). It was a concern that any significant concentration of NO_2 in the gas flow could result in OH formed from reaction between the $O(^3P)$ atoms and the liquid hydrocarbons used. The amount of NO_2 formed in the HONO generator was quantified using the reaction of $O(^3P)$ with deuterated squalane ($C_{30}D_{62}$). The OD yield from $O(^3P)$ atoms formed by photolysis of 1 mTorr of 'pure' NO_2 (BOC) reacting with the deuterated liquid squalane was compared with the OD yield (as measured via LIF where signal intensity is proportional to OD number density) from $O(^3P)$ atoms from 1 mTorr of the HONO-containing gas

mixture from the precursor generator. This is described in more detail in chapter 5 (section 5.3.1)

A second method of nitrous acid preparation was used to prepare the deuterated analogue, DONO. The DONO was used as a convenient source of OD radicals; to optimize the experiment for OD detection. The DONO was formed by adding heavy water (D_2O, Sigma-Aldrich) to a 12 L glass bulb filled with 1 atm of NO_2. The NO_2 contains NO as an impurity and therefore facilitates the formation of DONO according to reaction (3).

2.6 Optical system

2.6.1 Photolysis laser

As already summarized in table 2.3, a number of photolytic precursors were used during the course of this work, each requiring a photolysis wavelength of 355 nm. This was achieved by using the third-harmonic output of a Nd:YAG laser (Continuum Surelite SL-II-10) resulting from the sum-frequency mixing of the fundamental wavelength (1064 nm) and the frequency-doubled second harmonic (532 nm) in a KDP crystal. The triggering of the flashlamp and Q-switch was controlled externally by a four channel delay and pulse generator (Stanford Research Systems, DG535). The flashlamp was triggered at a repetition rate of 10 Hz and the Q-switch trigger pulse was typically sent 191 μs after the flashlamp pulse. This resulted in pulses of horizontally polarised 355 nm light, of length 5-6 ns and of energy approximately 100-110 mJ. When vertically polarised light was required, in the DONO and HONO experiments, the beam was passed through a λ/2 waveplate.

The beam size was restricted by an iris of diameter 5-6 mm which resulted in typical photolysis energies of 80-90 mJ measured upon entry to the reaction chamber. The beam entered the chamber through fused silica, 40 mm diameter, 5 mm thickness and λ/4 flatness windows (Apex Optical Services) set at Brewsters' angle to minimise reflection at the entry window. Scattered light from the photolysis beam was reduced by a series of black Teflon baffles of 5-7.5 mm diameter placed in the photolysis arm of the reaction chamber.

2.6.2 Anisotropy considerations

At thermal equilibrium in the gas phase, molecules are oriented randomly i.e. they have an isotropic distribution of molecular or rotation axes. The optical absorption process is most favourable when the transition dipole moment is aligned with the electric vector of the light. The transition dipole moment must be located along or perpendicular to one of the symmetry axes of the molecule. This is defined by the fact that under the action of light the electrons in a bond can be set in motion either along the transition dipole moment or perpendicular to it[142]. As a result the recoil direction of photofragments formed may be in the same direction as the electric vector (parallel transition) or perpendicular to it (perpendicular transition).

From an isotropic distribution in the gas phase, the selection of a specific subset of the randomly oriented molecules can be achieved using linearly polarised laser light. Since an anisotropic sample of the precursor is excited by absorption, it follows that the recoil direction of the fragments formed by photodissociation will also be anisotropic. The extent of anisotropy in a photodissociation process is defined by the anisotropy parameter β (equation 2.3) where P_2 is the second Legendre polynomial (equation 2.4) and θ is the angle between the electric field vector of the light and the recoil direction of the fragments.

$$I(\theta) = \frac{[1 + \beta P_2(\cos\theta)]}{4\pi} \quad \text{Equation 2.3}$$

$$P_2(\cos\theta) = \frac{(3\cos^2\theta - 1)}{2} \quad \text{Equation 2.4}$$

The extreme allowed limits of equation 2.3 occur when β = +2 and β = -1. In the first case, when β = +2, the intensity for a given θ is proportional to $\cos^2\theta$ (parallel transition). Second, when β = -1, the intensity for a given θ is proportional to $\sin^2\theta$ (perpendicular transition). A value of β = 0 is representative of an isotropic distribution.

The anisotropy parameters (β) for the photolytic precursors used in this work are included in the previously presented, table 2.3. The linear polarisation of the photolysis beam was adjusted in order to maximize the amount of scattered species directed at the surface (either liquid wheel or SAM) to increase signal intensities. For NO_2, with a positive β parameter, horizontally polarised laser light was used, whereas for HONO

and DONO with a negative β parameter, vertically polarised light was used. This is illustrated in figure 2.4.

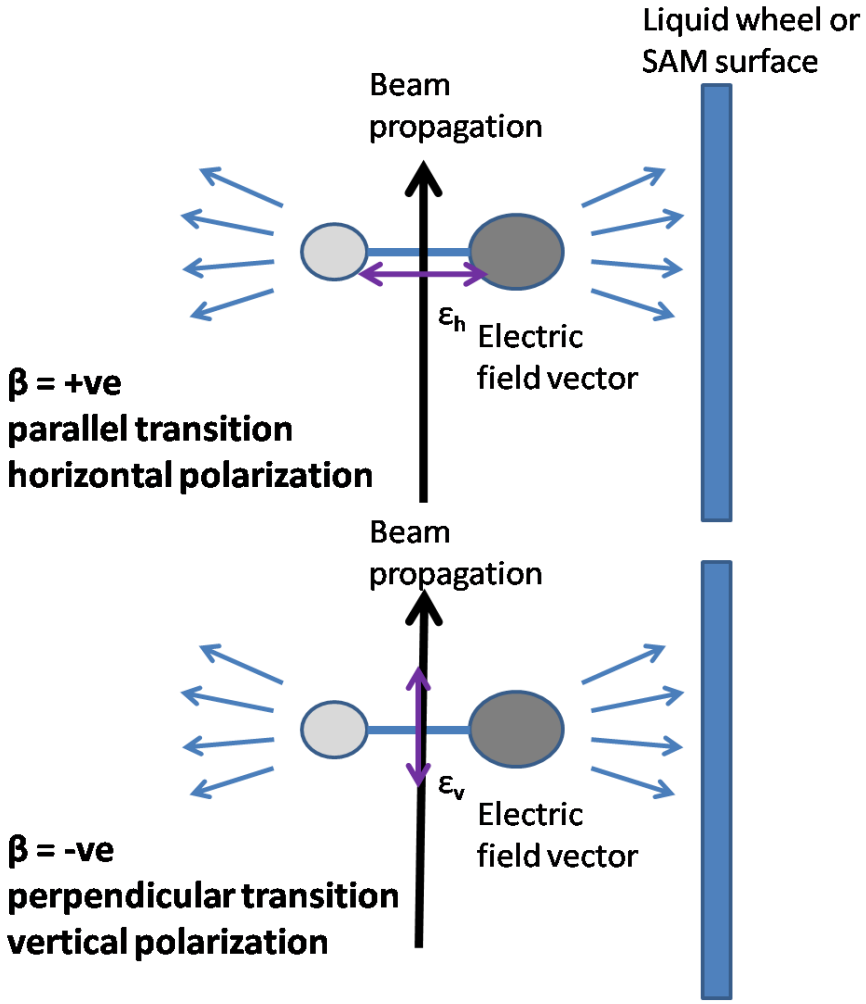

Figure 2.4: Schematic illustrating the ability to preferentially direct the scattering species toward the surface by tailoring the photolysis lab-frame polarization to the anisotropy parameter of the precursor.

2.6.3 Probe laser

The probe laser was used to detect the products (OH and OD radicals) by LIF. It was necessary that the probe laser provided a tuneable source of laser light and was capable of generating a variety of wavelength ranges as outlined in table 2.4. To fulfil these requirements a Nd:YAG (Continuum Surelite II-10) pumped dye laser (Sirah Pulsed Dye Laser, CSTR-LG-24) was used (figure 2.5).

The dye laser system consisted of four major components; the resonator, pre-amplifier, amplifier and a frequency conversion unit (FCU). In the resonator, a fraction of the pump beam (separated by a beam-splitter and mirror combination) is used to stimulate

emission from a continually refreshed solution of organic dye molecules inside the oscillator cavity. The stimulated emission then illuminates a grating and is reflected off a mirror, this process is responsible for the wavelength selection. Some of the laser light from the resonator leaks out (through the output coupler) and is turned through 180° (inverting the lab-frame linear polarization of the pump light), by a combination of Brewster's-angle plates and a turning prism.

The beam then passes back through the oscillator cuvette, albeit through a different volume than the resonator beam, where it is amplified in the pre-amplification stage. Further amplification takes place in the main amplifier when the pre-amplified beam passes through a second larger dye cuvette, pumped by the remainder of the pump beam. The final stage is the FCU where harmonic generation and sum-frequency generation can be carried out on the laser output to give the required wavelength.

The dye laser was pumped by the vertically polarised, second harmonic output (532 nm) of the Nd:YAG laser at a typical energy of 250 mJ $pulse^{-1}$. The grating in the resonator had a groove density of 2400 lines/mm which provides a tuning range between 350 and 740 nm. Details of the dyes used and wavelengths obtained are summarized in table 2.4. Second harmonic generation was achieved by passing the beam through a KDP doubling crystal, a quartz compensator and a Pellin-Broca unit for wavelength separation resulting in horizontally polarised, UV light (2-4 mJ) in the region of 260-380 nm.

The energy of the probe laser was attenuated either by adjustment of the pump laser energy, via its Q-switch delay (for laser energies ~1 mJ, see table 2.4) or by a combination of a polariser and a $\lambda/2$ waveplate (for energies in the μJ range). Consistent energies across a wavelength range were achieved by 'learning' a calibration curve for a given dye. FCU motor positions for a given wavelength range were recorded to give a selected energy (arbitrary energy but always above that required for experiment) and used by the software running the laser to give reproducible and reasonably constant energy across a range of wavelengths. The probe laser was under full experimental control via a custom written LABVIEW program as described in section 2.7.4.

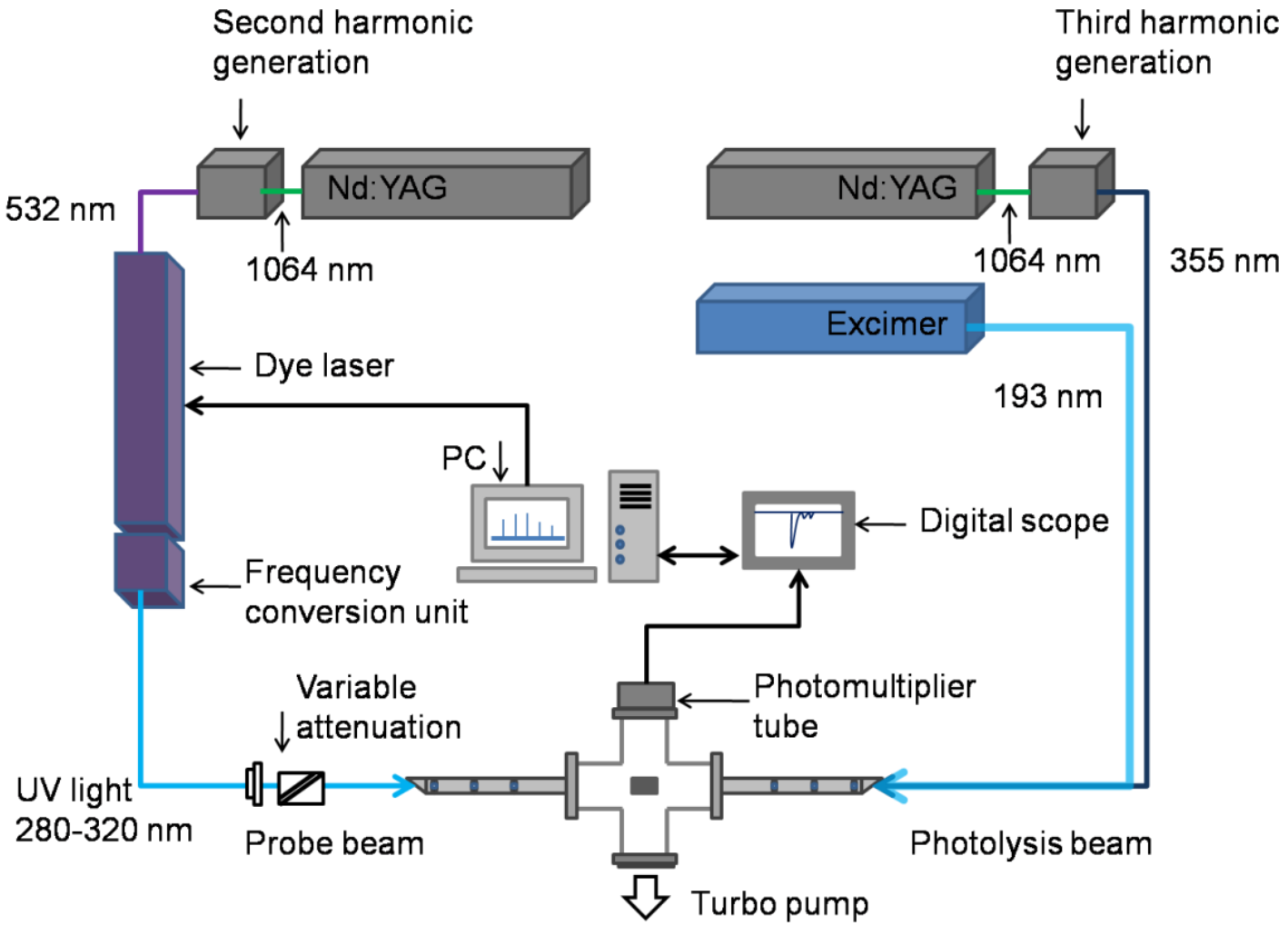

Figure 2.5: Schematic of the optical and data acquisition system.

Species	Transition (electronic (vibrational))		λ range / nm		Typical pulse energy / mJ	Filter centre λ ± FWHM /nm	Laser dye
OH off diagonal absorption	absorption A-X (1,0)	emission A-X (1,1)	absorption 281-285	emission 312-318	1	315±8	Rhodamine 6G
OD off diagonal absorption	absorption A-X (1,0)	emission A-X (1,1)	absorption 286-291	emission 312-318	1	315±8	Rhodamine 6G and Rhodamine B mixture
OH/OD diagonal absorption	absorption A-X (0,0)	emission A-X (0,0)	absorption 306-312	emission 306-312	0.02	311±12	DCM(Oscillator) Rhodamine 101(Amplifier)
OH/OD diagonal absorption	absorption A-X (1,1)	emission A-X (1,1)	absorption 310-318	emission 310-318	0.02	311±12	DCM(Oscillator) Rhodamine 101(Amplifier)

Table 2.4: Summary of spectroscopic transitions used and the appropriate dye laser wavelengths and interference filters used.

2.7 Product detection and data acquisition

2.7.1 Laser induced fluorescence

The OH and OD products were detected by LIF, first developed by Zare and co-workers[143], it has since become a standard technique for monitoring a wide variety of atomic, neutral, and ionic molecular species[144]. The basic requirements for LIF are: a molecule with a strong electronic absorption band; a finite fluorescence quantum yield; and a tuneable laser capable of producing the wavelengths required for absorption. While scanning the laser across this electronic absorption band, there will be specific wavelengths at which the laser light is resonant with a rotational-vibrational transition and the molecule will be excited to a specific rotational-vibrational level in the excited electronic state. As depicted for a generic diatomic molecule in figure 2.6, it is this excited rovibronic state that then spontaneously emits a fluorescence photon which can be detected. The result is an 'excitation spectrum' of fluorescence intensity as a function of laser wavelength, which essentially mirrors an absorption spectrum. With adequate resolution the internal state distribution of the ground electronic state is observed. One of the advantages of LIF over other traditional absorption spectroscopies is its sensitivity; it is technically a zero background technique.

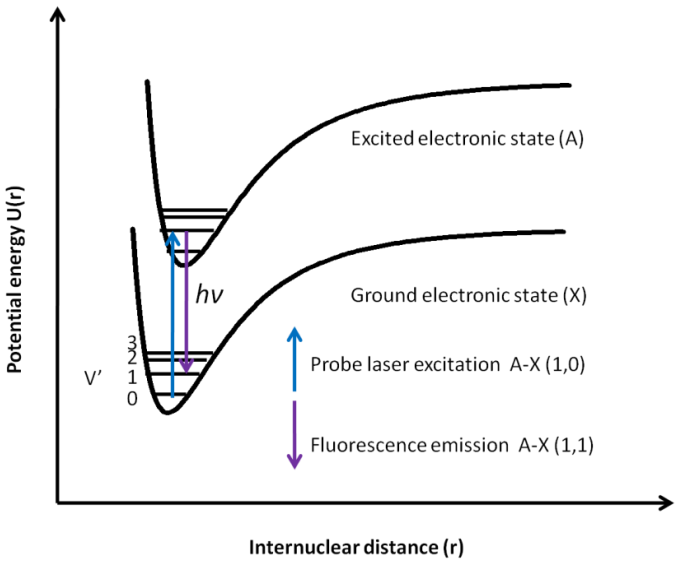

Figure 2.6: Potential energy diagram for a generic diatomic molecule highlighting the basic principles of LIF detection. A typical off-resonant combination of absorption and emission bands is illustrated.

2.7.2 OH spectroscopy

OH in the ground electronic state (X) has an electronic configuration of $(1\sigma)^2(2\sigma)^2(3\sigma)^2(1\pi)^3$ and a corresponding molecular term symbol of $^2\Pi_i$ (as $\Sigma = \pm 1/2$ and $\Lambda = \pm 1$). In low rotational levels, OH $^2\Pi_i$ can be thought of as an intermediate case between Hund's case (a) and (b), while in higher rotational levels it is best described as Hund's case (b). Therefore both coupling cases must be considered when interpreting the spectroscopy. For Hund's case (a), the symbol Ω represents the sum of the projection of the orbital angular momentum, Λ, and the electronic spin, Σ, on the internuclear axis. As a result Ω can take values of $\pm 3/2$ and $\pm 1/2$ from the four possible combinations of $\Sigma = \pm 1/2$ and $\Lambda = \pm 1$.

Consequently, the rotational levels are split into two spin-orbit manifolds $^2\Pi_{3/2}$ and $^2\Pi_{1/2}$, where the $^2\Pi_{3/2}$ manifold starts lower in energy by 125 cm^{-1}. The two spin-orbit manifolds, also labelled F_1 and F_2, are shown schematically in figure 2.7. The consequence of the spin-orbit splitting is that there are equivalent transitions originating from both manifolds. Because the $^2\Pi_{3/2}$ spin-orbit manifold is lower in energy, for a sample in thermal equilibrium lines originating from the F_1 manifold will be more intense that their F_2 counterparts. At 300 K the lower energy state is more heavily populated by a factor of 70:30[145].

A further splitting called Λ-doubling also occurs in the $^2\Pi_i$ state. It is caused by the coupling of the orbital angular momentum to the molecular rotation. The result is the splitting of each rotational level into two closely spaced 'Λ-doublets' with an energy gap that increases with increasing J. In the high J regime, where Hund's case (b) applies, the Λ-doublets correspond to extremes in orientation of the unpaired electron orbital lobe either in (labelled A') or out of (A") the plane of rotation. As shown in figure 2.7, each Λ-doublet is defined by a parity label +/f or -/e. Only transitions between states of opposite parity are allowed according to spectroscopic selection rules.

The first excited electronic state of OH, the A state, has the term symbol $^2\Sigma^+$ resulting from an electronic configuration of $(1\sigma)^2(2\sigma)^2(3\sigma)^1(1\pi)^4$. A Σ state has no projection of orbital angular momentum along the nuclear axis ($\Lambda = 0$). As a result Hund's case (b) is appropriate and the electronic spin is coupled to the angular momentum of the rotating nuclei and each level is split into two spin-rotation doublets (p-type splitting). Main branch transitions from the $^2\Pi_{3/2}$ (F_1) spin orbit manifold in the ground state to their

counterparts in the excited state are characterised by J=N+1/2 and those from $^2\Pi_{1/2}$ (F_2) manifold are characterised by J=N-1/2.

The selection rules for allowed transitions for OH are summarised in table 2.5. Application of these selection rules results in six main branches; Q_1 ($\Delta J/\Delta N$ = 0 from F_1), Q_2 ($\Delta J/\Delta N$ = 0 from F_2), P_1 ($\Delta J/\Delta N$ = -1 from F_1), P_2 ($\Delta J/\Delta N$ = -1 from F_2), R_1 ($\Delta J/\Delta N$ = +1 from F_1) and R_2 ($\Delta J/\Delta N$ = +1 from F_2). There is the possibility for six further satellite branches where, as a result of OH being intermediate in the coupling cases, the selection rule $\Delta N/\Delta J = 0, \pm 1$ loses validity and transitions where $\Delta N \neq \Delta J$ and $\Delta N = \pm 2$ become allowed. The transitions (figure 2.7) are labelled according to the convention, ${}^{\Delta N}\Delta J_{f'f''}$, where the superscript is the change in *N*, the main character is the change in *J*, *f'* denotes the spin-rotation coupling in the upper state and *f''* the spin-orbit manifold of the lower level. For the main branches, where $\Delta N = \Delta J$ and $f' = f''$ the nomenclature is simplified to $\Delta J_{f''}$.

ΔJ	ΔN	$\Delta \Lambda$	$\Delta \Sigma$	$\Delta \Omega$	Parity
0, ±1	0, ±1	0, ±1	0	0, ±1	+ ↔ - - ↔ +

Table 2.5: General and specific selection rules applicable to the spectroscopy of OH radicals

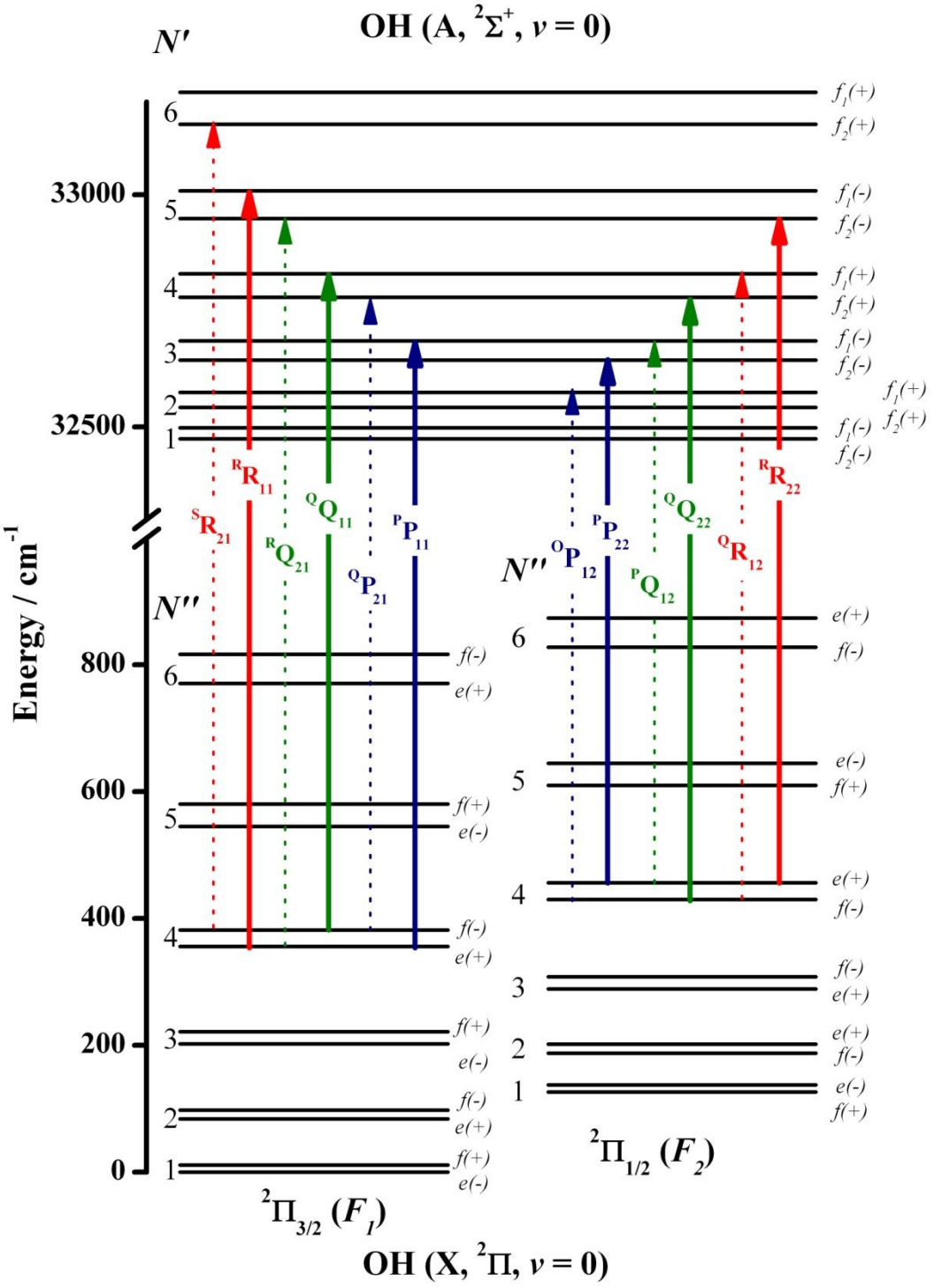

Figure 2.7: Energy level diagram for the A-X band of the OH radical, showing the six main branches and six satellite branches. Re-printed from reference[146]. Main branches are represented by solid lines and sub branches by dashed. Λ- doublet and spin-orbit splitting are exaggerated.

2.7.3 Fluorescence detection

The OH and OD radicals were probed on the A-X band and the subsequent fluorescence was detected. Depending on the specific experiments the radicals were probed on either diagonal ($\Delta v = 0$) or the off-diagonal ($\Delta v = +1$) bands, with fluorescence from the diagonal bands detected, as summarized in table 2.4. Probing on the diagonal and off-diagonal bands presented different advantages and disadvantages. Diagonal transitions are more intense (have a higher transition probability) than their off-diagonal counterparts as a result of increased Frank-Condon overlap between ground and excited state wavefunctions. As a result, when probing diagonal transitions, lower probe laser energies were used to avoid saturation (saturation being a product of the transition probability and the pulse energy), resulting in greater spectroscopic resolution. Conversely, when probing off-diagonal higher probe laser energies were required to achieve the same signal heights.

A disadvantage of probing the diagonal bands was that the probe laser wavelengths and the fluorescence wavelengths were coincident; meaning the scattered probe laser light could not be discriminated against by a filter. The pros and cons for each probe and detection method were considered and as a result experiments were carried out on both diagonal and off-diagonal transitions. Further details are given in each specific experimental chapter as appropriate.

The fluorescence was collected perpendicular to the laser axes using a liquid light guide (Ultrafine Technology Ltd. Series 300, length 500 mm, width 8 mm) situated 20 mm above the laser axis. The photons collected in the liquid light guide were directed through filters that discriminated against the photolysis and probe laser wavelengths (where possible), to a photomultiplier tube (PMT, Thorn EMI 9813QB) operating at typical gain voltages of 1.3-1.9 kV.

2.7.4 Experimental control – timing and data acquisition

The experimental control and data acquisition system was under the full control of custom written LABVIEW software[147]. The timing and triggering of the lasers was controlled by a 4-channel delay generator (SRS DG535). The primary trigger originated from the delay generator, operating at 10 Hz. The flashlamps and Q-switch were independently triggered for both lasers. A digital storage scope (LeCroy,

Wavesurfer, WS434) was also triggered synchronously with the Q-switch of the probe laser. The PMT signal (section 2.7.3) was passed to the scope for the data acquisition.

A fluorescence waveform was captured (by the scope) from the PMT output for each laser shot. The waveform was acquired over a timebase of 10 μs, including a probe laser pre-trigger of 5 μs. The scope operated at a sample rate of 2×10^9 samples s^{-1}. The waveforms were averaged within the scope for a software controlled number of laser shots (typically 20 – 30). The averaged waveforms were subsequently passed to a data-acquisition computer via an Ethernet connection (TCP/IP) where they were processed further.

The averaged waveforms were collected in a signal gate of length approximately 1.5 μs starting approximately 200 ns after the probe laser was fired. A pre-trigger gate started 1200 ns before the probe fired and finished 200 ns before it fired. This was used to establish the electronic baseline. The information in the pre-trigger gate was subtracted form that collected in the signal gate. The resulting average signals were then stored on the hard drive. There were two separate custom written[147] data-acquisition programs used. The first allowed the fluorescence signal as a function of photolysis-probe delay time to be measured. The second recorded the fluorescence signal variation as a function of probe wavelength (which was also under full software control as described in section 2.6.3) for a fixed photolysis-probe delay. These experimental outputs are described in more detail in the following section.

2.8 Experimental outputs

2.8.1 Appearance profiles

One output of the experiment using the custom written LABVIEW software described in section 2.7.4 are OH appearance profiles. These give information on the translational distribution of the inelastically scattered or reactively generated OH radicals. The probe laser wavelength was fixed on an OH $A^2\Sigma^+ - X^2\Pi$ rovibrational transition and the time delay between the firing of the photolysis and probe lasers was varied in 1 μs increments. The results were typical of those observed previously by McKendrick and co-workers[63,66-70,121,124]. The OH appearance reflects the wave of returning OH from the surface and the peak arrival time is correlated to the most probable speed of the returning OH.

To unambiguously confirm the effects of secondary collisions on the appearance profiles, it was necessary to establish the range of photolysis-probe delay times over which truly nascent OH is detected for a given precursor pressure. OH appearance profiles were measured at a variety of precursor pressures following reaction at a squalane ($C_{30}H_{62}$) liquid surface. The results are shown in figure 2.8. The peak intensity (proportional to the amount of OH formed at the surface) increases approximately linearly with precursor pressure. However, the ratio of the signal at longer times to that at the peak increases as the pressure increases (figure 2.8 (b)).

This is due to a higher proportion of OH molecules suffering secondary gas-phase collisions after exiting the liquid surface. The result is a build up of translationally thermalised OH in the probe region; an effect which is more prevalent at longer time delays at higher pressure. A hypothetical 'zero-pressure' profile was also constructed by linear extrapolation of the normalised signals at each time delay. It is clear that on the falling edge the difference between the hypothetical zero-pressure profile and that at 1 mTorr is non negligible. Careful consideration should therefore be made when interpreting mechanistic information from appearance profiles beyond photolysis-probe delay times of ~30 μs.

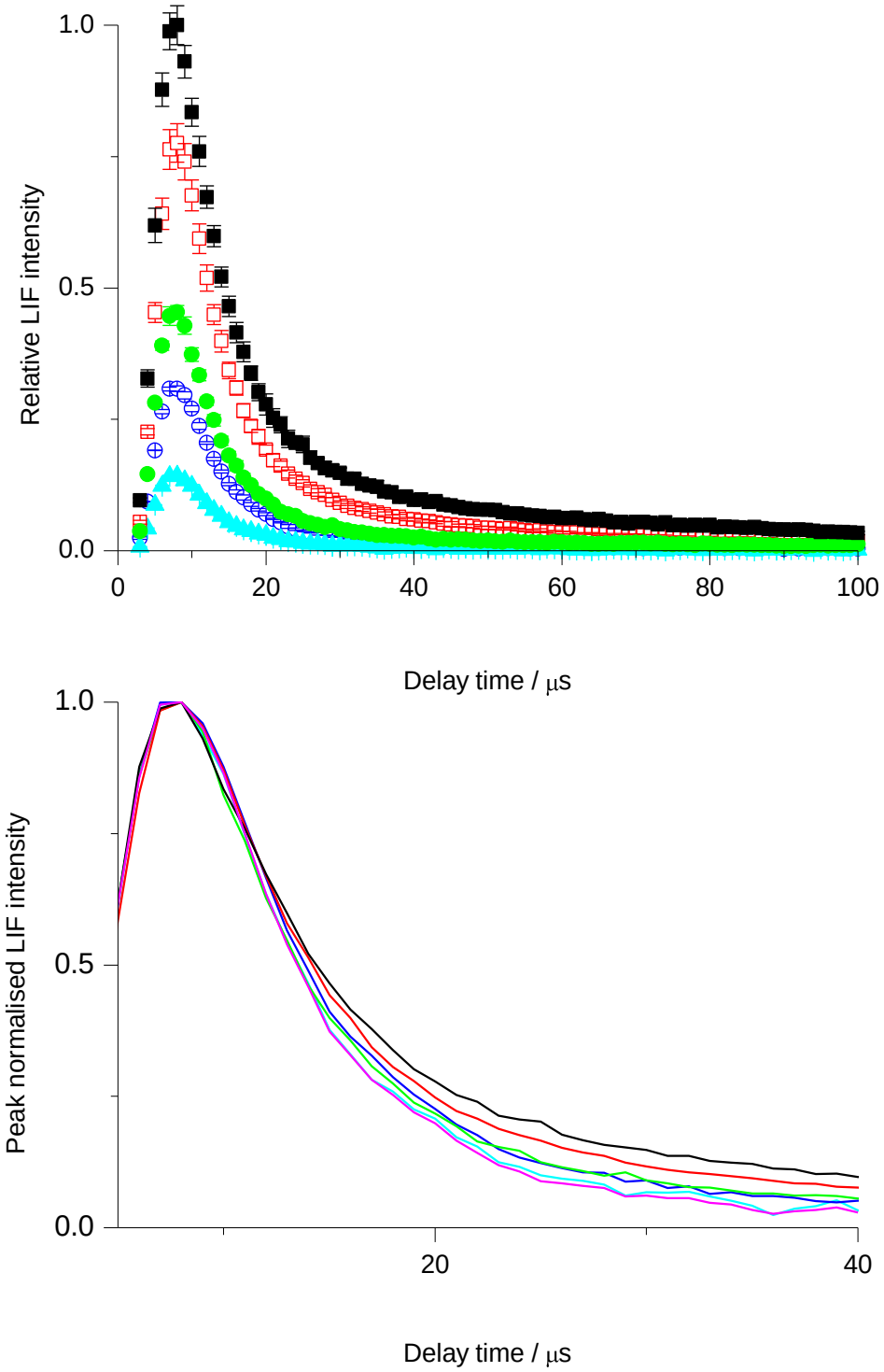

Figure 2.8: Representative appearance profiles recorded on the $Q_1(1)$ line of the OH *A*-*X* (1,0) band, from squalane. **(a)** Recorded at $p(NO_2)$ ~ 4 mTorr (black closed squares), ~ 3 mTorr (red open squares) ~ 1.5 mTorr (green filled circles), ~1 mTorr (blue open circles) and ~0.5 mTorr (cyan filled triangles). **(b)** Data re-presented having been peak normalized, $p(NO_2)$ ~ 4 mTorr (black line), ~ 3 mTorr (red line) ~ 1.5 mTorr (green line), ~1 mTorr (blue line) and ~ 0.5 mTorr (cyan line), profile at a hypothetical zero pressure (magenta line). Bath temperature = 298 K; surface-probe laser distance = 4 mm.

2.8.2 Excitation spectra

Excitation spectra were the second experimental output. They were recorded by scanning the probe laser wavelength with a fixed delay between the photolysis and probe lasers. The rotational populations were generally extracted from the measured spectra using a thermal calibration method. Thermal spectra (recorded at higher pressures and longer delays) were recorded alongside the nascent spectra. The measured thermal populations were compared to the 'real' thermal distribution at 300 K (from the spectral simulation program LIFBASE[145]) to give a calibration factor for each rotational level (equation 2.5). This calibration factor was then applied to the measured nascent populations, yielding the real nascent populations. This thermal calibration method was used to correct for a number of factors such as: spectral line saturation, variation of probe laser energy with wavelength and variation of detection sensitivity with wavelength.

$$\frac{PN'_{thermal}}{PN'_{LIFbase}} = f_{calibration} \qquad \text{Equation 2.5}$$

The rotational populations (extracted from several spectra and averaged) were often presented in the form of a Boltzmann plot. The Boltzmann equation (2.6) describes the relationship between the population in a given level and the energy of that level for a thermal sample. A Boltzmann plot comprises the natural log of the population divided by the degeneracy for a given rotational level against the energy of that level. The rotational temperature, T, can then be extracted, given that the gradient is equal to $-\frac{1}{k_B T}$.

$$P \propto g \exp^{-\frac{E}{k_B T}} \qquad \text{Equation 2.6}$$

The rotational temperature is a convenient method for characterising the rotational distribution and can be useful for comparative studies, but it relies on the assumption that the rotational distribution is thermal. A dynamical process may not result in a rotational distribution which can be characterised by a rotational temperature. As was described in the introduction for Nesbitt and co-workers[21,22,26], the rotational

distribution from a dynamical process may be the sum of two Boltzmann-type temperatures or may not be a temperature at all (i.e. not a linear fit to a Boltzmann plot).

2.8.3 Monte Carlo simulations

In order to gain mechanistic insight from the appearance profiles, Monte Carlo simulations were carried out[148], similar to those used previously by McKendrick and co-workers[66,67]. The simulations were designed to replicate what the appearance profiles would look like if a single defined reaction mechanism was responsible for the OH products. In all experimental chapters (3, 4 and 5) a Monte Carlo simulation of a 300 K thermal distribution was used. This thermal simulation is representative of what would be observed if a TD-type mechanism were responsible for the observed profiles. The simulations include all experimental variables such as: the $O(^3P)$ velocity distribution, the laser polarisation, the laser-surface distance and the size of the detector.

The procedure involves sampling at random initial positions within the photolysis beam volume and assigning an $O(^3P)$ velocity from the known distribution for 355 nm photolysis of NO_2[140] (or HONO as applicable). Of these, a trajectory is deemed successful if it intercepts the surface volume and will subsequently be randomly assigned a speed and direction based on the thermal (TD) mechanism. That velocity vector will then be propagated and counted as contributing towards the observed signal if it re-enters the probe laser volume within the detection zone of the light guide. The signal is counted for each time-delay it remains in the detection volume. The thermal (TD) velocity distribution is assumed to be a Maxwell-Boltzmann distribution at the surface temperature with the appropriate $\cos\theta$ angular distribution about the surface normal (as was described in chapter 1, this distribution is well known and is generally surface and projectile independent).

The simulation of a direct component (chapter 3 and 4) required further assumptions to be made about the velocity distribution of the scattered OH. The direct velocity distribution was chosen to mimic that observed by Minton and co-workers scattering $O(^3P)$ from liquid squalane surfaces[62,64,110]. This included the $\cos^4(\theta_f - 37°)$ angular distribution and an effective surface mass of 76 mu (chapter 1, section 1.3.3). The simulations suggest that changing the angular distribution has little effect on the shape of the simulated profiles for the direct channel. This is likely to be due to the wide

range of possible initial and final angles in these experiments compared with equivalent molecular beam experiments.

Shown in figure 2.9 is an example of the simulated profiles. Once a simulated trajectory 'hits' the surface, the program assigns from these either a direct or TD mechanism with 50:50 probability. The profiles shown are the result of: 1×10^6 Monte Carlo cycles; a laser-surface distance of 5 mm; photolysis beam diameter of 5 mm; a photolysis beam length of 10 mm; a liquid-light guide diameter of 10 mm: and a probe diameter of 4 mm. From the starting point of a 50:50 direct-to-thermal probability the simulations imply that the experimental setup will favour the detection of slow OH. There are two main reasons for this. The first is that the slower OH will spend more time in the probe beam, making it more likely to contribute to the observed signal. The second is a result of the angular distribution of the scattered OH. Direct trajectories scatter in a specular fashion. Hence ingoing OH trajectories that are away from the surface normal lead to scattered return IS trajectories that are also away from the surface normal, and are on average unlikely to encounter the probe volume. In contrast the TD mechanism scatters with a $\cos\theta$ distribution regardless of the initial impact angle. As a result, there is a contribution from trajectories that originate off-axis with the lasers in the TD channel.

Figure 2.9 shows the predicted relative intensity and shape of a direct and thermal appearance profiles from a start point of equal direct and thermal probability. Also shown is the sum of the two simulations which would be the overall predicted appearance profile.

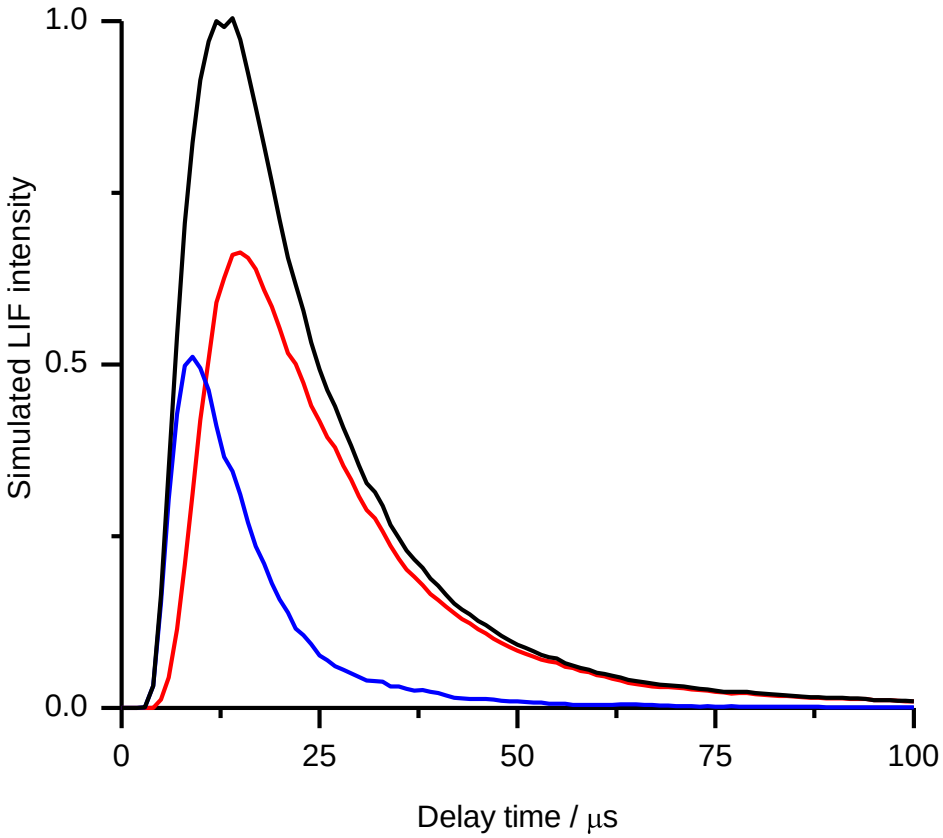

Figure 2.9: Monte Carlo simulations of direct IS (blue) and thermal TD (red) OH following reaction of $O(^3P)$ at a liquid surface. Included is the predicted appearance profile (black) which is the sum of the two simulations.

Chapter 3

Reactions of O(^{3}P) atoms at ionic liquid surfaces

3.1 Introduction

Ionic liquids (ILs) comprise a diverse range of molten salts with melting points below ~100 °C. They are composed solely of ions, with large organic cationic and anionic components being responsible for their unique physical and chemical properties such as negligible vapour pressure, low volatility and high thermal stability. The complexity and potential for tunability of ILs have resulted in them being earmarked as having great potential in a wide range of applications including catalysis[149], fuel cells[150], electrospray thrusters[151,152], nanoparticle formation[153] and vapour detection[154]. They are also attractive as green solvents[155] (replacing the dependence on traditional organic solvents), as their wide-ranging functionality promotes solvation of a wide variety of compounds and their physical properties encourage beneficial solvent recycling and recovery behaviour.

Each of the applications above is dependent on a detailed understanding of the molecular composition of the interface and relating this to the bulk. A widely studied 'family' of ILs receiving recent attention are those based on the 1,3-dialkylimidazolium cation (figure 3.1). The alteration of the length of the alkyl chains offers a convenient method of tuning the properties of the IL. Chain lengths up to C_{12} are routinely studied[156]. A number of experimental techniques have been employed with this in mind including direct recoil spectroscopy (DRS)[156,157], sum-frequency generation vibrational spectroscopy[158], Rutherford backscattering[159], X-ray photoelectron spectroscopy (XPS)[160-162] and neutron reflectivity[163]. In addition there has been a theoretical effort simulating the bulk and interfacial properties of 1,3-

dialkylimidazolium cations with a variety of anionic partners using molecular dynamics simulations[164-176].

An interesting common observation from these studies is that the interfacial structure of this IL family does indeed appear to differ from the bulk composition. In particular, the longest alkyl chain on the cation has been found to be preferentially located at the interface, projecting out into the vacuum[173,177-179]. It has also been suggested that the alkyl chains segregate into complex lamellar-type structures[163]. There is, however, some disagreement about this phenomenon, with some studies reporting no ion segregation or even that the alkyl groups are pointing down into the bulk[156,157]. Possible explanations for this disparity may arise from recent work suggesting that the surface structure can be influenced by the presence of water[180] or the anion used[162]. The accurate theoretical modelling of these systems also depends on how refined the model is. Ignoring polarisation effects, for example, can affect the proposed interfacial structure. This was demonstrated specifically by Voth and co-workers for a [1,3-ethylmethylimidazolium][NO_3] IL, finding better agreement with experimental values when polarisation effects were included[168].

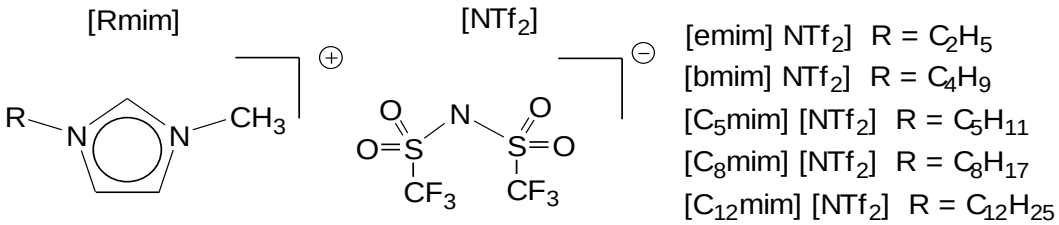

Figure 3.1: Chemical structures and nomenclature for the 1-alkyl-3-methylimidazolium-based ionic liquids

In this chapter, the interfacial reactivity of a family of 1-alkyl-3-methylimidazolium bis(triflouromethylsulfonyl)imide ([$C_n$mim][NTf_2]) ILs (figure 3.1) towards gas-phase, ground state atomic oxygen ($O(^3P)$) has been investigated and interpreted in terms of interfacial structure. The lower members of the family, [mmim][NTf_2], and [emim][NTf_2], have been highlighted as potential candidates for use in electrospray thruster systems for spacecraft propulsion[151,181]. This reaction is of particular importance with this technological application in mind. Since $O(^3P)$ is the majority species in the low earth orbit environment (see introduction, chapter 1, section 1.2), the

thruster constituents (including the expelled IL propellant) will be subject to reaction with hyperthermal $O(^3P)$ atoms.

With similar motivations, a complementary, hyperthermal collision energy (~520 kJ mol^{-1}) study was carried out by Minton and co-workers[125]. Following their earlier work on the reaction dynamics of $O(^3P)$ with liquid hydrocarbons (chapter 1, section 1.3.3), they studied the reaction with the longest and shortest members of the IL family ([emim][NTf_2] and [C_{12}mim][NTf_2]) with O, OH and H_2O detection by rotatable quadrupole mass spectrometry. The results were co-reported alongside all-atom molecular dynamics simulations of the liquid surfaces carried out by Schatz and co-workers. The work presented in this chapter will be closely compared to that work.

3.2 Experimental summary

As was described in chapter 2, the experimental setup has been adapted directly from the previous work of the McKendrick group on the reaction dynamics of $O(^3P)$ atoms and liquid hydrocarbons[63,66-70,124]. The experiment is depicted schematically in figure 3.2. A series of 1-alkyl-3-methylimidazolium ($[C_nmim][NTf_2]$) based ionic liquids (figure 3.1) were custom-synthesized by collaborators at the University of York[134] using modified literature procedures[182]. Prior to use, the ionic liquids were de-gassed under vacuum (10^{-6}-10^{-7} mbar) at 70 °C (±1 °C) for 24 hours. $O(^3P)$ atoms were generated by photolysis of NO_2 at a fixed distance above the liquid surface.

A fraction of the $O(^3P)$ atoms formed travel to the liquid surface, react with any available C-H units and return to the laser axis as OH. The resultant OH was detected by LIF, in the ground vibrational state, following excitation on the $A^2\Sigma^+ - X^2\Pi$ (1,0) band by a second variable wavelength laser beam at the same carefully controlled distance above the liquid surface. Appearance profiles and excitation spectra were recorded (chapter 2, section 2.8) to elucidate the translational and internal energy distribution of the OH reaction products. The measurement of appearance profiles allows for the relative yield from a given liquid to be quantified; since the OH yield is proportional to the integrated appearance profile. As such, the relative reactivity of a family of ionic liquids was measured in comparison to the benchmark liquid hydrocarbon squalane ($C_{30}H_{62}$).

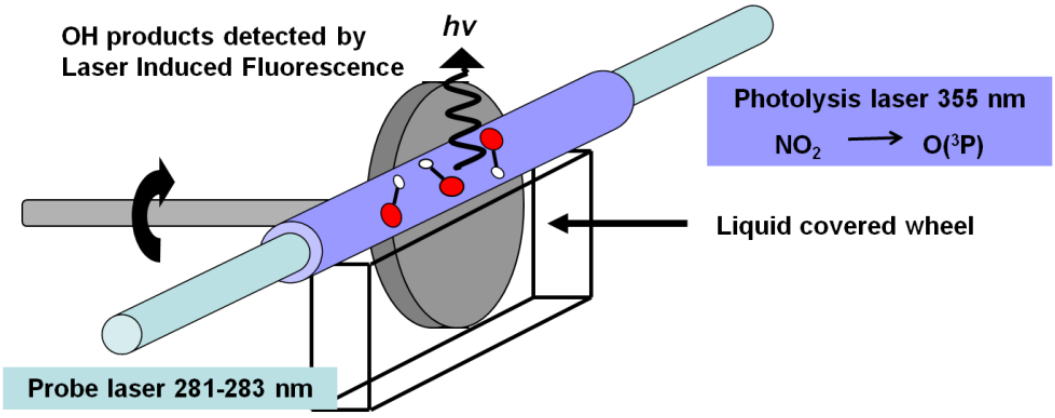

Figure 3.2: Schematic representation of the photolytic-spectroscopic method used to probe liquid surfaces by reactive scattering of atoms.

3.3 Experimental Results

3.3.1 Appearance profiles – relative reactivity measurements

In the first instance it was necessary to establish that the observed OH signals were free from artefacts due to spurious OH-producing processes. For this purpose, a liquid free from any abstractable hydrogen atoms was required. The perfluorinated polyether (PFPE) Krytox 1506 (DuPont, F-[$CF(CF_3)$-CF_2O]$_{14ave}$-CF_2CF_3) (chapter 2, section 2.2) was used as an inert 'blank' liquid. It was pre-heated under vacuum for 24 hrs in a manner identical to that used for the ionic liquids. The resulting OH appearance profiles, alongside those measured for the reference liquid squalane, are shown in figure 3.3 (a).

The profiles for squalane are characteristic of those measured by McKendrick and co-workers previously[63,66-70,124] and of those shown in chapter 2 (section 2.8.1). There is an initial 'dead time' as $O(^3P)$ atoms travel to the liquid surface and OH returns to the laser axis for detection. The OH signal then rises sharply, reaching a peak at a time delay consistent with the 4 mm distance between the beam axes and liquid surface and the known average $O(^3P)$ speed of 1340 m s^{-1} following NO_2 photolysis[140].

Underlying the raw profiles was a background signal originating from two sources. The first was caused by the photolysis laser pulse, present as a large apparently negative going signal, only present at the very earliest of delays (before the onset of the LIF signal from the returning OH) appearing in the background data acquisition gate. This signal was genuine, with a finite lifetime of ~500 ns as opposed to a scattered light spike. A possible source is fluorescence of electronically excited NO_2* as it required the presence of both NO_2 and the photolysis laser. The second source was a small photolysis-probe delay independent signal caused by probe-beam scatter and probe-induced photolysis of a minor OH-containing impurity in the NO_2 (such as HONO). These background sources were eliminated by systematically blocking the photolysis and probe lasers in sequence and subtracting the resulting background signals from the raw profiles. All appearance profiles presented within this chapter have been subjected to this background subtraction.

It is clear (figure 3.3 (a)) that no perceptible OH was detected from the PFPE liquid, within the achievable signal to noise, verifying that spurious OH production is

negligible. The experimental procedure was therefore extended to the family of ionic liquids shown in figure 3.1. The OH signal intensity was measured from each member of the IL family and compared with the signal intensity from squalane recorded immediately afterwards. Figure 3.3 (b) is an example of a typical data set for $[C_{12}mim][NTf_2]$ and squalane and highlights the reproducibility achieved when recording multiple profiles. Three independent measurements of OH appearance were recorded for each liquid compared to the benchmark squalane. The resulting ~20 individual appearance profiles were averaged and are shown in figure 3.4.

The profiles have been truncated at 30 μs to minimise any contribution from OH having undergone secondary collisions, as described in chapter 2 (section 2.8.1) based on the pressure dependence of the OH signal following reaction of $O(^3P)$ with squalane. The error bars represent the 1σ standard error in the mean of the resulting ~20 measurements, showing the excellent reproducibility. The order in which appearance profiles for each of the liquids were measured was randomised day-to-day. For each ionic liquid, squalane reference profiles were measured as closely in time as was practically possible (always on the same day).

Figure 3.4 shows that, as was the case for PFPE, only trace amounts of OH (if any) were detected from $[emim][NTf_2]$, comparable to the overall sensitivity of the measurements. The very small, apparently negative signals at early times for PFPE (figure 3.3 (a)) and $[emim][NTf_2]$ (figure 3.4) are the result of the imperfect subtraction of the background due to the photolysis laser. The size and scatter in this artificial signal is the major source of statistical and systematic uncertainty in any genuine OH signal observed. As such, only an upper limit on reactivity of $[emim][NTf_2]$ compared to squalane can be established.

This was determined to be 0.0014:1 (table 3.1) and was the ratio of the maximum possible OH signal from $[emim][NTf_2]$ (average + error) to the signal from squalane. The relative reactivities of the intermediate ionic liquids, compared to the squalane reference, were also measured (on three separate occasions) and are summarised in table 3.1. The results clearly show that the reactivity of the ionic liquids increases as the alkyl chain length in the $[C_nmim]$ cation is increased.

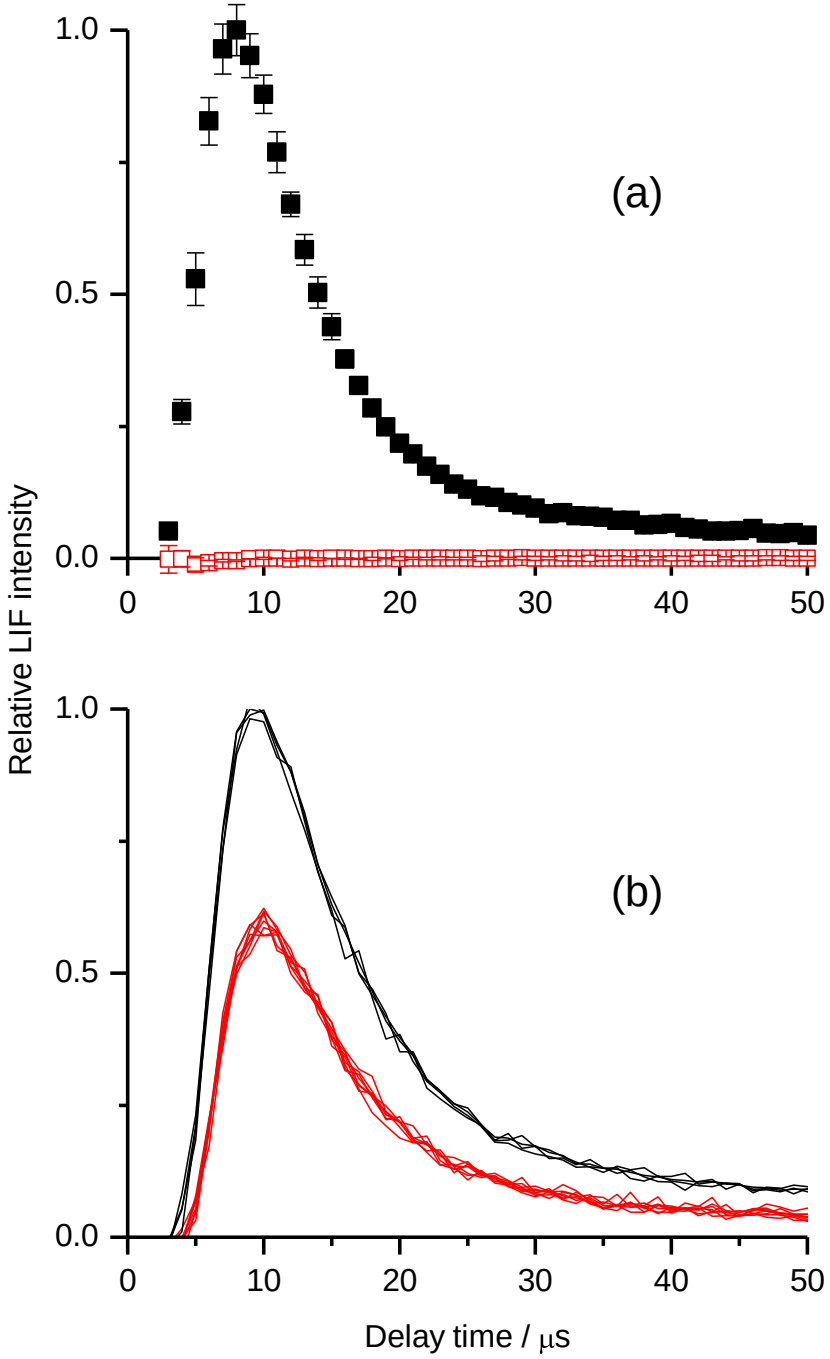

Figure 3.3: (a) Representative appearance profiles recorded on the $Q_1(1)$ line of the OH *A*-*X* (1,0) band. Photolysis and probe-laser background signals have been subtracted, as described in the text. Liquids used were the squalane reference (black filled squares) and the inert 'blank' PFPE (red open squares). **(b)** A series of OH appearance profiles measured following reaction at a squalane (black lines) and $[C_{12}mim][NTf_2]$ (red lines) surface. Figure (b) shows the excellent reproducibility achieved when recording multiple profiles. Bath temperature = 298 K; *p*(NO2) ~ 1 mTorr; surface-probe laser distance = 4 mm.

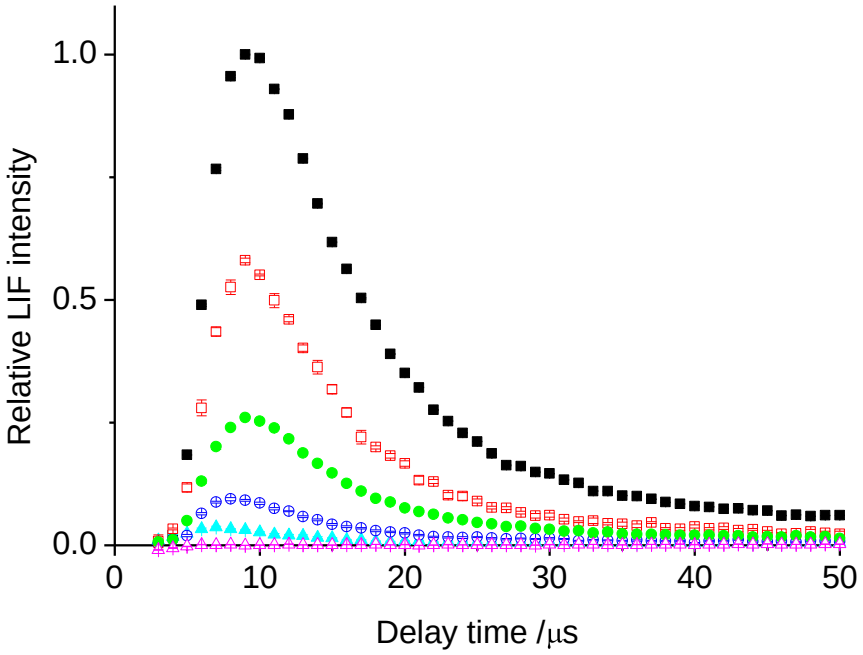

Figure 3.4: Representative appearance profiles recorded on the $Q_1(1)$ line of the OH *A*-*X* (1,0) band. Background signals resulting from the photolysis and probe lasers have been subtracted, as described in the text. Squalane (black filled squares) was used as the reference in each case. Ionic liquids were [emim][NTf_2] (magenta open triangles), [bmim][NTf_2] (cyan closed triangles), [C_5mim][NTf_2] (blue open circles), [C_8mim][NTf_2] (green filled circles), [C_{12}mim][NTf_2] (red open squares). Bath temperature = 298 K; $p(NO_2)$ ~1 mTorr; surface-probe laser distance = 4 mm. Error bars reflect the 1σ standard error in the mean.

Cation	Sq:ionic liquid Run 1	Sq:ionic liquid Run 2	Sq:ionic liquid Run 3	Sq:ionic liquid average
[emim]	1:0.00125	1:0.00153		1:0.00139†
[bmim]	1:0.037	1:0.036	1:0.041	1:0.038±0.003
[C_5mim]	1:0.092	1:0.094	1:0.095	1:0.094±0.002
[C_8mim]	1:0.259	1:0.283	1:0.271	1:0.27±0.01
[C_{12}mim]	1:0.58	1:0.60	1:0.67	1:0.62±0.05

Table 3.1: Summary of three repeated independent measurements of relative reactivity ratios of the series of [$C_n$mim][NTf_2] ionic liquids with O(^{3}P), each compared to a squalane reference. Error quoted is the 2σ standard error in the mean. †Estimated upper limit on reactivity.

3.3.2 Liquid temperature dependence

For the longest-chain ionic liquid, [C_{12}mim][NTf_2], OH appearance profiles were recorded at three bulk liquid temperatures of 298, 323 and 343 K. [C_{12}mim][NTf_2] was chosen for this more extensive investigation due to its optimum achievable signal-to-noise. The resulting profiles are shown in figure 3.5. Great care was taken to ensure that experimental parameters such as precursor pressure, photolysis and probe laser energy and laser axis-surface distance were kept constant between measurements. It is clear that neither the absolute signal intensity nor shape of the profile is influenced significantly by the liquid temperature, with any subtle differences lying within the statistical uncertainties.

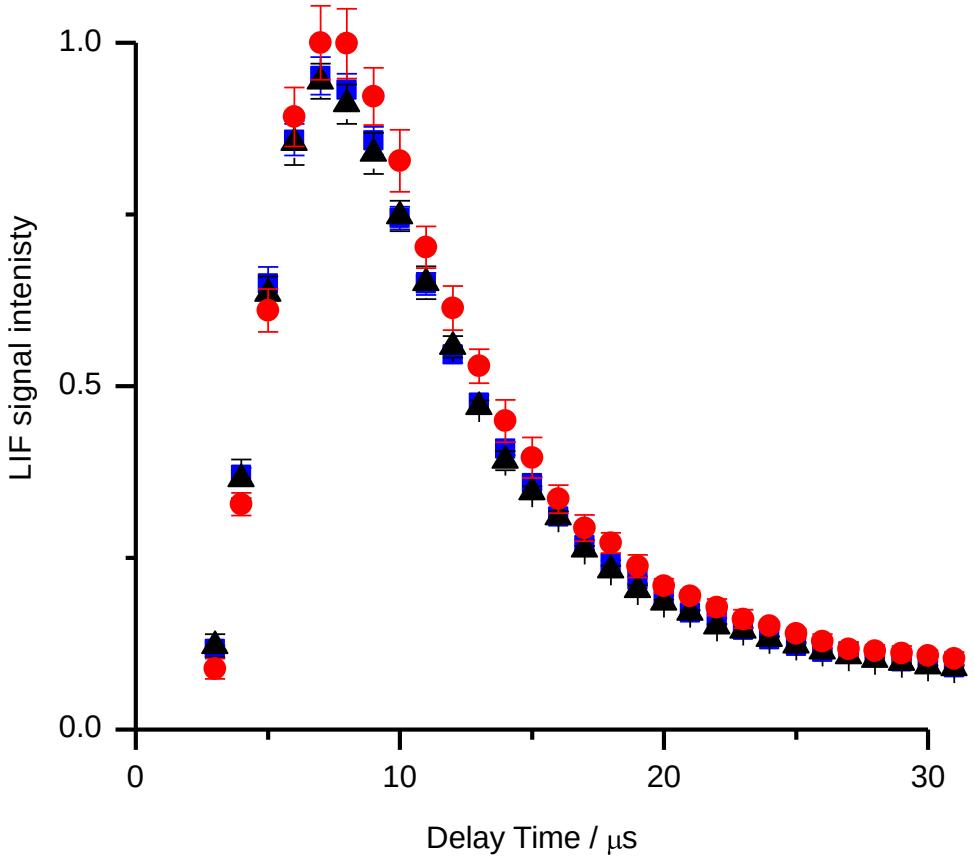

Figure 3.5: Measured appearance profiles of OH (v' = 0) LIF signals for [C_{12}mim][NTf_2] recorded at 298 K (blue squares), 323 K (black triangles) and 343 K (red circles). Profiles recorded on $Q_1(1)$ line of the OH A-X (1,0) band, shown following background subtraction as described in the text. Error bars represent the 1σ standard error in the mean of several profiles recorded at each liquid temperature. $p(NO_2)$ ~ 1 mTorr; surface-probe laser distance = 4 mm.

3.3.3 LIF excitation spectra – internal state distribution

Excitation spectra of the nascent OH reaction products in the ground vibrational state ($v' = 0$) were measured from the $[C_{12}mim][NTf_2]$ ionic liquid (figure 3.6). The probe laser wavelength was varied across the $A^2\Sigma^+ - X^2\Pi$ (1,0) band. The photolysis-probe laser delay was set at 5, 9 and 23 μs, corresponding to the rising edge, peak and tail of the appearance profile respectively. Corresponding thermal spectra were also recorded, at a pressure of 100 mTorr (1 mTorr NO_2 and 100 mTorr N_2) and a time delay of 130 μs. Assuming a typical gas-kinetic collision rate of 10^7 collisions $Torr^{-1}s^{-1}$, this would be equivalent to OH radicals having undergone 30 gas-phase collisions, making them sufficiently collisionally thermalised.

As described in chapter 2 (section 2.8.2), a calibration factor (obtained by comparing the measured thermal populations with the known thermal population distribution at 300 K[145] for a given rotational state) was then applied to the nascent rotational populations and Boltzmann plots were constructed. A representative Boltzmann plot is shown in figure 3.7. The rotational temperature is extracted from the gradient of the linear fit to the experimental points (chapter 2, section 2.8.2).

Rotational temperatures were determined for the Q_1, R_1 and R_2 spectroscopic branches; these were then averaged according to their relative populations in a 300 K sample, 70% F_1 and 30% F_2. Seven independent measurements were made at each delay and the resultant rotational temperatures for each photolysis-probe delay were averaged (table 3.2) and the scatter in the seven independent measurements was carried through as the error in the average. There is a clear correlation between rotational temperature and the photolysis-probe time delay at which they were measured, with colder rotational temperatures at longer delays. Despite this, even those measured at the longest times were hotter than thermal, albeit modestly so.

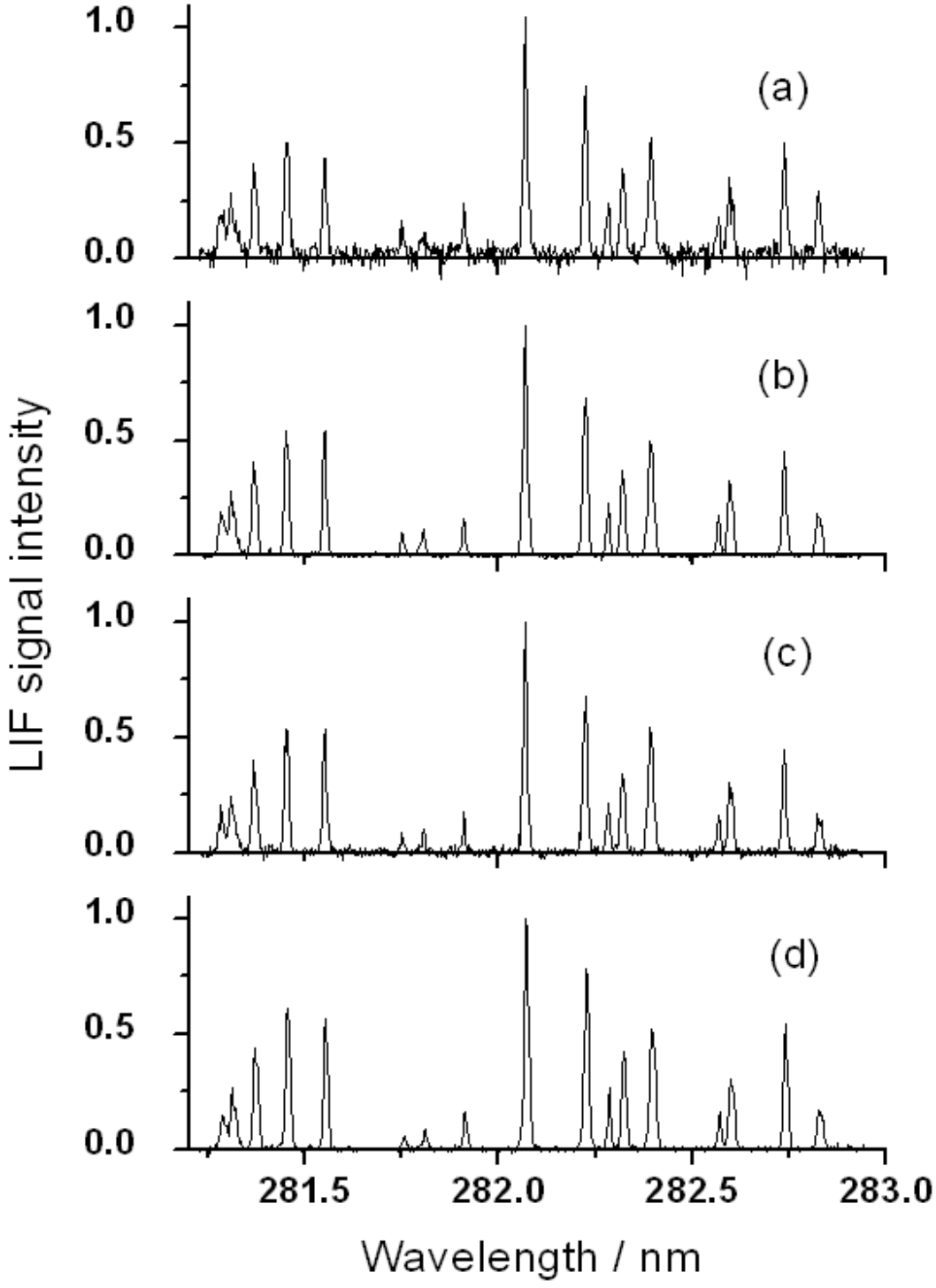

Figure 3.6: Representative OH *A*-*X* (1,0) LIF excitation spectra from $[C_{12}mim][NTf_2]$. Nascent spectra recorded at photolysis-probe laser delays of **(a)** 5 μs, **(b)** 9 μs, **(c)** 23 μs. **(d)** Thermal spectrum at a photolysis-probe laser delay of 30 μs, $p(NO_2)$ ~ 1 mTorr and $p(N_2)$ ~ 0.1 Torr. Probe laser-liquid surface distance = 4 mm.

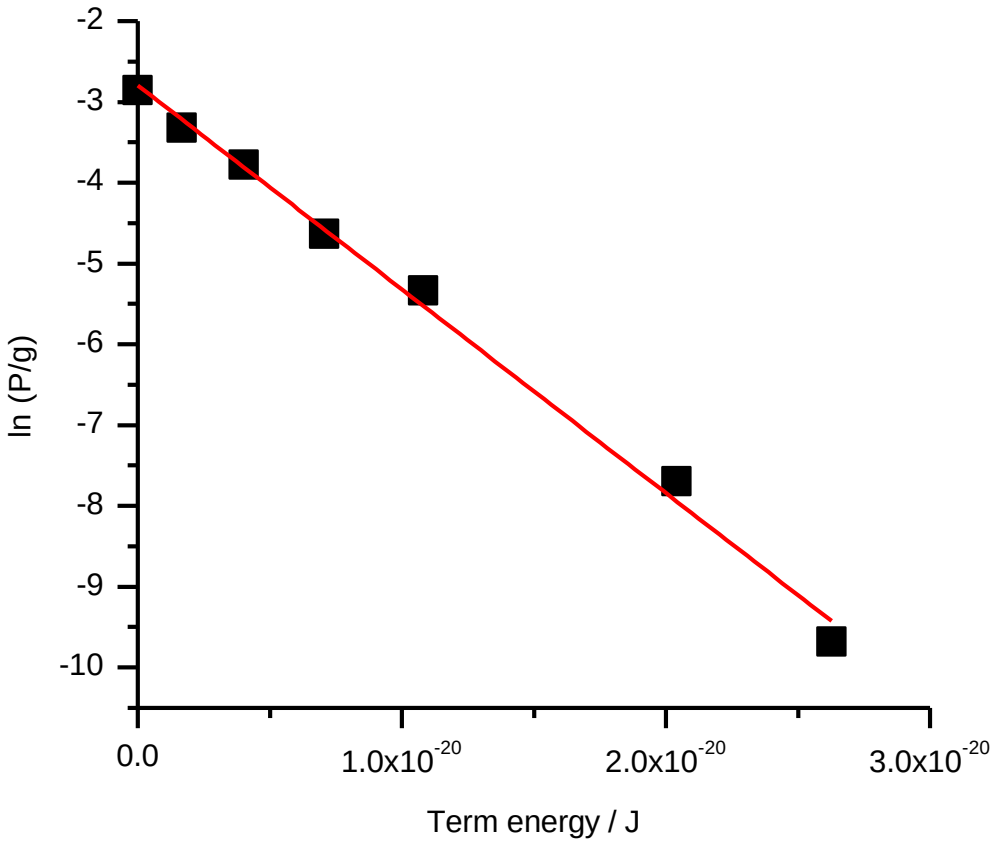

Figure 3.7: Representative Boltzmann plot for OH (v' = 0) recorded on the Q_1branch following reaction with [C_{12}mim][NTf_2]. $p(NO_2)$ ~ 1 mTorr. Probe laser-liquid surface distance = 4 mm. Photolysis-probe laser time delay = 9 μs.

	Rising edge 5 μs	Peak 9 μs	Tail 23 μs
Rotational temperature/ K	372±16	340±5	333±4

Table 3.2: Rotational temperatures of nascent OH (v' = 0) formed by reaction of (O^{3}P) atoms with [C_{12}mim][NTf_2], measured at different photolysis-probe delays. Error quoted is the 1σ standard error in the mean of seven independent measurements per liquid.

3.4 Discussion

3.4.1 Reaction mechanism

Only the secondary CH_2 units are considered reactive based on the well known relative bond strengths of primary and secondary C-H bonds of ~34 and ~22 kJ mol^{-1} respectively[47], compared to the average collision energy of 16 kJ mol^{-1} (FWHM 26 kJ mol^{-1}) for $O(^3P)$ atoms following NO_2 photolysis[140]. The aromatic hydrogen atoms can be completely discounted energetically with barriers in excess of ~100 kJ mol^{-1}[183]. It can therefore be assumed that the hydrogen abstraction reaction is taking place exclusively at the secondary C-H environments on the longer alkyl chain (C_n) on the cation.

The resulting OH reaction products can also be assumed not to have undergone secondary collisions with the liquid to any great extent. This is reasonable as the barriers to abstraction of a second H atom (to form H_2O) are much lower (typically 3-10 kJ mol^{-1})[184] than for the initial hydrogen abstraction reaction by $O(^3P)$. Therefore the detection of OH as a reaction product is evidence that the reaction must be taking place only at the outermost regions of the IL surface. Any OH products which find themselves deeper within the liquid would react to form water and therefore would not be observed in this experiment.

The OH appearance profiles for the longer chain liquids $[C_8mim][NTf_2]$ and $[C_{12}mim][NTf_2]$ have been re-presented, peak normalised alongside that for the benchmark liquid hydrocarbon squalane in figure 3.8. Also included is a Monte Carlo[148] simulation of a 300 K thermal distribution representative of what would be observed for OH having undergone a TD mechanism (chapter 2, section 2.8.3).

The profiles (figure 3.8) show that the OH detected from the ionic liquids has a translational distribution similar to that from squalane. It is also clear that the appearance profiles are not well replicated by a TD distribution; the majority of OH detected is travelling too fast (detected at early photolysis-probe time delays) to have undergone sufficient secondary collisions at the surface to have thermalised with it. There is however, a subtle difference between the profiles from the ILs and the liquid hydrocarbon squalane, particularly at the longer photolysis-probe delays. There is less slow OH returning from the ILs than from squalane. This is unlikely to be a

consequence of small discrepancies in the surface-laser beam distance as the rising edges of all the appearance profiles are coincident.

This was pursued more quantitatively by extending the Monte Carlo simulations to include a direct process. As described in chapter 2, section 2.8.3, the simulation of a direct component requires the assumption that the angular distribution of the OH products from the ILs is the same as from squalane. However, the simulations suggest that the experimentally observed signal is largely independent of the angular distribution used for the direct channel. This is likely to be due to the wide range of possible initial and final angles in these experiments compared with equivalent molecular beam experiments.

A χ^2-minimising, linear-least-squares fitting routine was applied to fit the simulations to the experimentally derived profiles from $[C_{12}mim][NTf_2]$ and squalane (figure 3.9). As was deduced in chapter 2 (section 2.8.1) the appearance profiles and corresponding fits were truncated at 30 μs to minimise any influence from OH having undergone secondary gas-phase collisions. The resulting direct-to-thermal (IS:TD) ratios are provided in table 3.3. It is clear that the direct simulation reproduces the experimental profiles well, particularly on the rising edge, with only a very minor TD component being necessary to improve the fit at longer delay times. As a result it can reasonably be concluded that the majority of OH products from reaction between $O(^3P)$ and the ionic liquid are the result of a *direct abstraction reaction*.

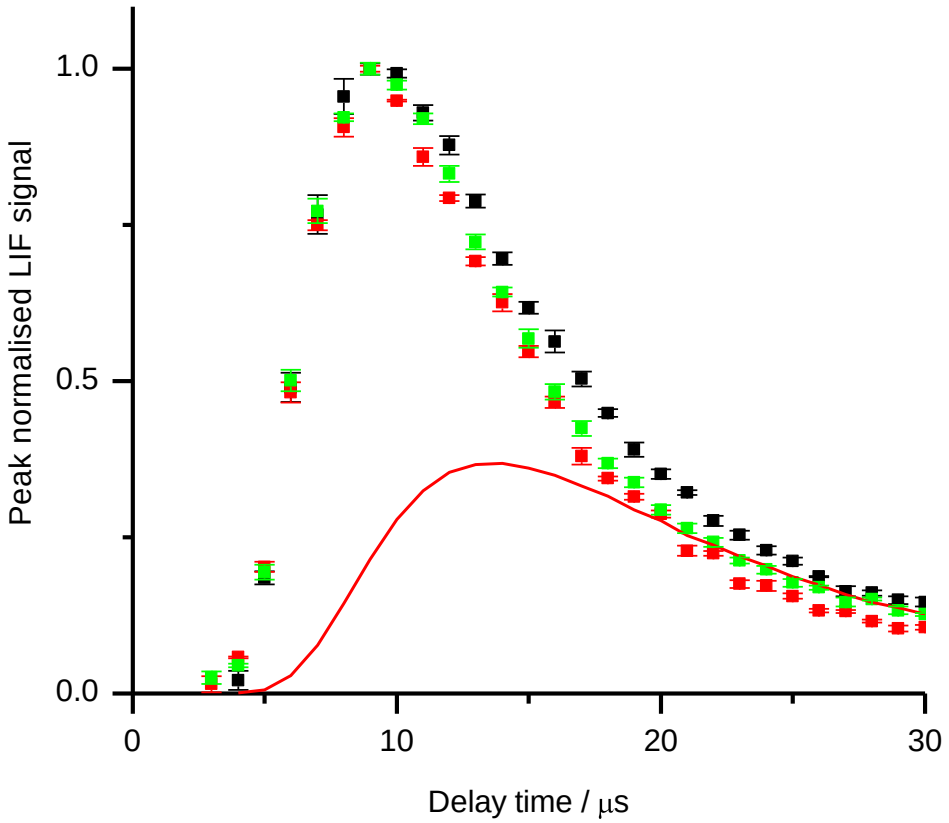

Figure 3.8: Representative peak normalised OH *A*-*X* (1,0) LIF appearance profiles recorded on the $Q_1(1)$ transition, from squalane (black closed squares), $[C_{12}mim][NTf_2]$ (red closed squares) and $[C_8mim][NTf_2]$ (green closed squares). Background signals from the probe and photolysis lasers have been subtracted. Probe laser-liquid surface distance = 4 mm, $p(NO_2)$ ~ 1 mTorr. Also included is a Monte Carlo simulation of a thermal 300 K Maxwell-Boltzmann distribution (red line) as described in the text.

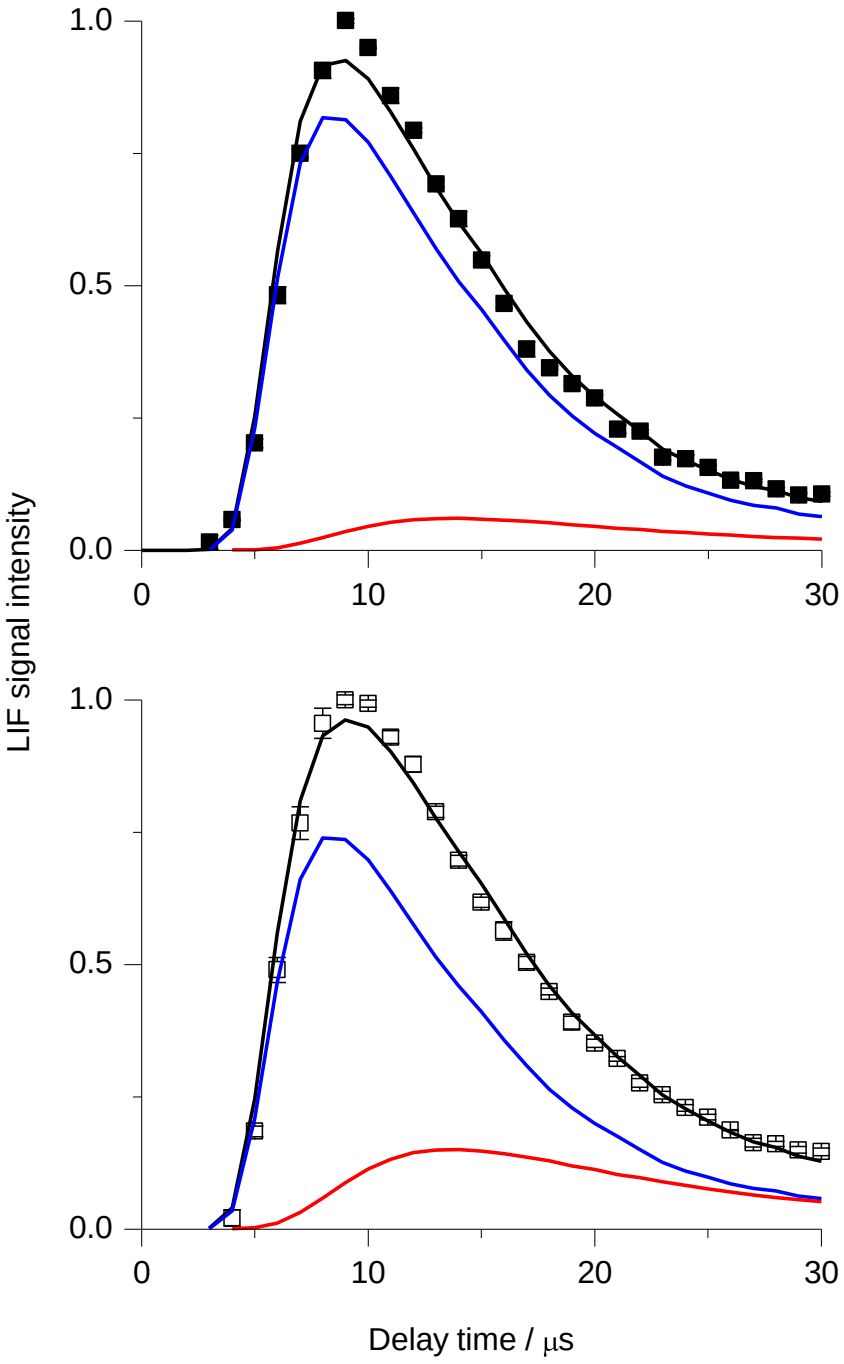

Figure 3.9: Representative peak normalised OH *A*-*X* (1,0) LIF appearance profiles recorded on the $Q_1(1)$ transition, for (a) $[C_{12}mim][NTf_2]$ (black closed squares) and (b) squalane (black open squares). Also included are the Monte Carlo simulations of a direct, impulsively scattered (IS) component (blue line) and a thermal (TD) component (red line). The black solid line in each case represents a linear least-squares fit to the experimental data. Probe laser-liquid surface distance = 4 mm, $p(NO_2)$ ~1 mTorr.

Figure 3.9 shows that squalane requires a larger nominal TD component to replicate the broader experimental appearance profiles but as was the case for the ILs, the dominant reaction mechanism is also direct (IS). The minor TD component from squalane may not be the result of truly collisionally (with the surface) thermalised OH. As was discussed in the introduction (chapter 1, section 1.4.2), theoretical simulations have predicted that direct processes can on occasion result in slow moving OH which will arrive at time delays consistent with thermal OH. As such, an overly literal interpretation of the nominal IS:TD ratio should be avoided.

Regardless of this, the simulations corroborate that the dominant (almost exclusive) mechanism from the ILs is a ballistic direct process that *must* take place at the extreme outer layers of the liquid, and that there is more slow travelling OH from squalane than the IL. A true TD component to the mechanism from squalane was previously, unambiguously interpreted by McKendrick and co-workers for the reaction of O(^{3}P) with squalane through the liquid surface temperature dependence of the rotational distribution of OH (chapter 1, section 1.3.3)[67].

The modest differences between the IL profiles and those from squalane are significant and reproducible. They suggest that the [C_{12}mim][NTf_2] surface is microscopically smoother than that of squalane, making the OH less likely to suffer secondary dissipative encounters before escaping into the gas phase. The squalane surface being rougher is plausible as molecular dynamics simulations of a squalane surface[121] predict considerable roughness on the molecular scale as a consequence of its branched structure. Squalane has been described by experimentalists as rough previously[8,10,21]; where a rough liquid is one that promotes secondary collisions and trapping. Squalane was found to produce more slow travelling scattered products (protic and aprotic gases) compared to the hydrogen bonded liquid glycerol[8] and has been interpreted as becoming *rougher* when heated (thermal roughening)[10,21].

An alternative explanation for differences in the shape of the appearance profiles from the ILs compared with squalane could be that the effective collision mass of the squalane and IL surface are different, which would in turn influence the recoil speed of the scattered products. The coincidence of the profiles at the rising edge however, suggests that this is not the case as differences in the effective mass of the surface would be obvious here where single, direct, hard collisions dominate. This suggests that the

portions of the IL surface where OH products originate (CH_2 groups of the long 1-alkyl chain) have a similar effective surface mass to a liquid hydrocarbon.

There would of course presumably be regions of the surface occupied by the counterion or non-alkyl segments of the cation which would therefore have different effective surface mass to a liquid hydrocarbon. However, this would not influence the OH translational distribution; it would be present in the inelastic scattering dynamics of the O(^{3}P) atom, which is not probed in this work. This effect was observed in the complementary experiments of Minton and co-workers[125].

Minton and co-workers found (through detection of the O and OH products by TOF mass spectrometry) that more energy was lost (as a fraction of the initial energy) during the direct H-abstraction reaction to form OH than in the direct impulsive, inelastic scattering of O. For the squalane reference the energy transfer for O and OH was essentially the same. Figure 3.10 clearly shows that the inelastically scattered O atoms retain more of their initial energy post-collision than the OH reaction products. As evidenced by a higher $\frac{E_f}{E_i}$ ratio for the inelastically scattered O (compared to reactively formed OH) at all incident angles for O atoms from both [emim] and [C_{12}mim] based ionic liquids.

Liquid	Squalane	[C_{12}mim][NTf_2
IS:TD	0.85:0.15	0.94:0.06

Table 3.3: Impulsively scattered (IS) to thermal (TD) ratios obtained from linear least-squares fits of Monte Carlo simulations to the experimental appearance profiles. Purely statistical errors are likely to be in the region of 1% percent but are likely to be outweighed by systematic errors in the modelling.

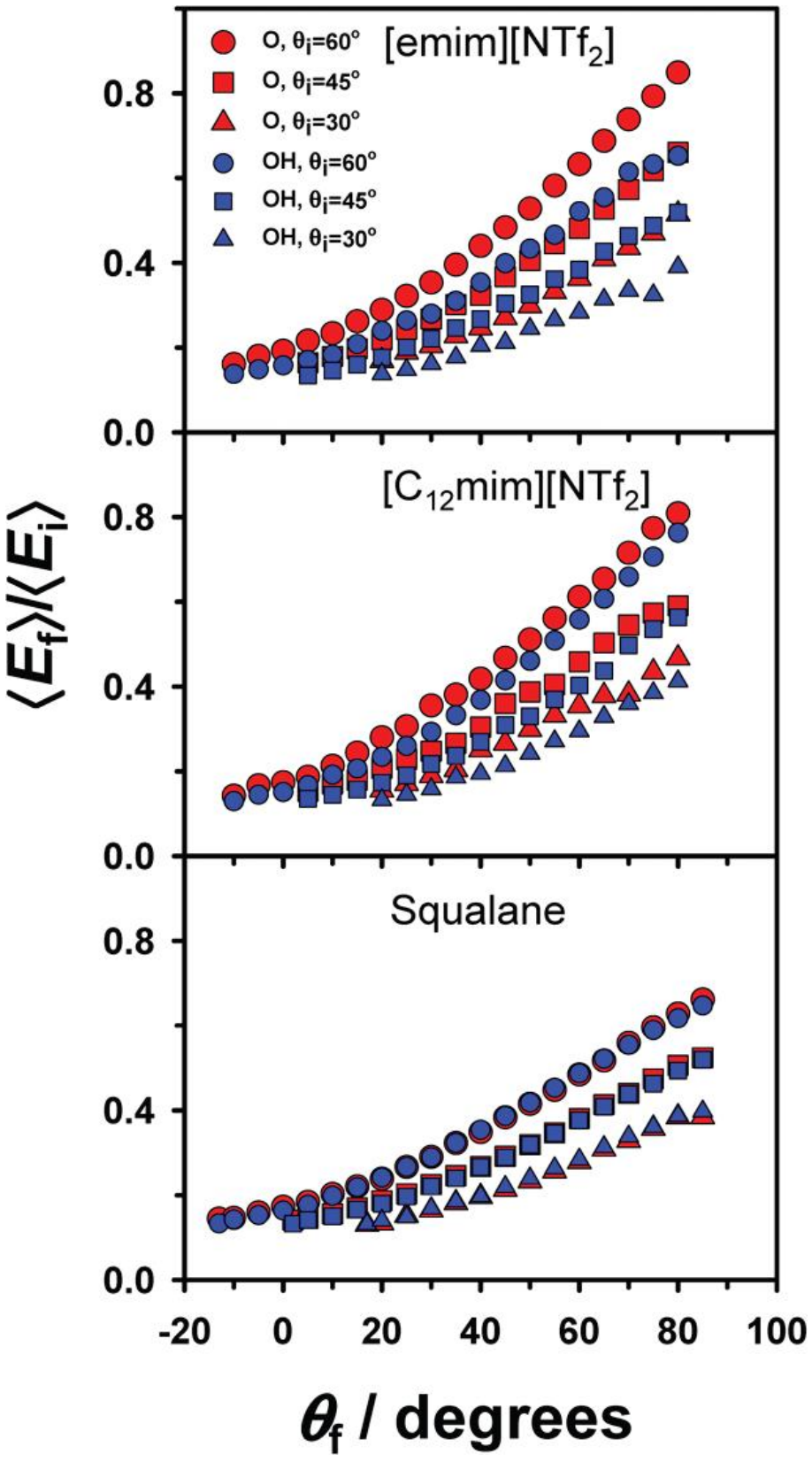

Figure 3.10: Ratio of average final translational energy of hyperthermal O or OH to average incidence translational energy, following interactions of O atoms with [emim][NTf_2], [C12mim][NTf2], and squalane surfaces, as a function of the final angle at incidence angles of 60, 45, and 30°. The surface temperature of [emim][NTf_2] and [C_{12}mim][NTf_2] was 323 K, and the surface temperature of squalane was 298 K. Reproduced from reference[125].

The temperature dependence of the OH yield (figure 3.5) also contains subtle evidence of the directness of the reaction. The appearance profiles as a function of liquid temperature are re-presented in figure 3.11, where Monte Carlo simulations at the corresponding temperatures are also included. The 298 K simulation has been peak normalised and all the others have been normalised relative to it, to correctly reflect the predicted differences in signal size at each temperature. The simulations show that as temperature is increased, the OH products move to earlier delay times, as evidenced by the rising edge and peak arrival times in the simulated profiles.

The predicted small drop in OH number density (proportional to the area under the profiles) with increased temperature represents the decrease in detection sensitivity with OH speed, due to the faster products spending less time in the probe region. It is clear in the first instance that the measured appearance profiles do not follow this trend as the rising edges and peak arrival times are coincident (within the associated errors) at all three temperatures. In fact the opposite trend is present if any, as the highest temperature appears to be very slightly broader. This may reflect an increase in surface roughness with increased temperature (thermal roughening), promoting multiple collisions of the escaping products and consequently the detection of more slow OH. Alternatively, the extremely subtle difference may simply reflect the limits of reproducibility of the experiments; slight probe laser-surface distance discrepancies or inaccuracies in the background subtraction would lead to a similar outcome. What is certain however, is that the appearance profiles show no evidence of the speed variation which would be expected were a significant amount of trapping present.

The lack of temperature dependence also suggests that there are no thermally activated reaction channels available, at least at the temperature range sampled. Any $O(^3P)$ atoms translationally accommodated on the surface would quickly collisionally thermalise and subsequently fall well below the reaction barrier (~22 kJ mol^{-1}[47], chapter 1 section 1.3.3). It could be envisaged that as the temperature of the liquid is increased, some of these trapped atoms could acquire enough energy to surmount the reaction barrier by some thermally activated reaction mechanism. This would lead to Arrhenius-type temperature dependence which would lead to an increased OH yield over the temperature range sampled.

A temperature increase of 45 K would result in approximately a three-fold increase in the rate coefficient under the Arrhenius regime. This was clearly not observed as it

would manifest in an increase in the area beneath the appearance profiles. A similar lack of temperature dependence was observed previously by McKendrick and co-workers for the reaction with squalane[67]. The implication is that the O(^{3}P) *must* react on the first, or at least a very early encounter, promoted by its incoming superthermal energy.

The final corroborating evidence of a dominant direct reaction mechanism is the rotational temperatures (table 3.2) derived from the measured excitation spectra (figure 3.6). It is clear that in all cases the rotational temperature of OH reacting with [C_{12}mim][NTf_2] is significantly above the bulk liquid temperature of 298 K. The rotational temperature measured at the rising edge of the appearance profile (5 μs) of 372±16 K is similar to that observed in previous gas-phase reactions between O(^{3}P) and hydrocarbons[47]. This reaction has been shown to proceed via a direct mechanism, through a collinear transition state (chapter 1, section 1.3.3). The previous work by the McKendrick group at liquid hydrocarbon surfaces also results in similar modestly superthermal rotational temperatures[66,67,69,124] (chapter 1, section 1.3.3).

It is interesting that the OH rotational temperature declines as the photolysis-probe time delay is increased. This has been observed previously by McKendrick and co-workers at a squalane surface[66] and was attributed to an increasing TD component resulting in a lower average rotational temperature as the time delay was increased. This could also be the case for the [C_{12}mim][NTf_2] IL, some secondary encounters could lead to a colder rotational temperature for the slower OH. In the absence of rotational distributions as a function of liquid temperature it is impossible to know whether the observed rotational cooling is an effect of a TD component influencing the rotational temperature of the slower OH. However, it should be noted that the Monte Carlo simulations predict only a very minor TD component making this proposal unlikely.

Another possible explanation for the slower OH having a lower rotational temperature is a dynamical, rotational-translational correlation, whereby the fastest OH products are formed in such a way that they are also the most rotationally excited. This is not obvious in the appearance profiles from [C_{12}mim][NTf_2]. Figure 3.12 shows profiles, recorded on the $Q_1(1)$ and $R_1(5)$ transitions respectively. The profiles have been peak normalised and they are very similar in shape.

A strong rotational-translational correlation would result in the more rotationally excited OH travelling faster. This would translate in the observed data as the $R_1(5)$ profile peaking earlier or being steeper on the rising edge than the $Q_1(1)$ transition; this is clearly not observed. The large errors associated with the $R_1(5)$ measurement on the rising edge make any comparison at these points unreliable. The breadth of the appearance profiles is largely governed by the $O(^3P)$ ingoing velocity distribution and the physical geometry of the experiment. As such, the translational energy resolution of the appearance profiles in this work is limited. Therefore the excitation spectra (figure 3.6) can be considered a more reliable measure of the variation of rotational temperature with delay. Figure 3.12 does however, show that as time delay is increased (from peak to tail) the $N' = 1$ ($Q_1(1)$) profile gains over the $N' = 5$ ($R_1(5)$) profile which is consistent with a modestly decreasing rotational temperature with delay.

The experimental data and Monte Carlo simulations overwhelmingly support the dominance of a direct hydrogen abstraction mechanism. The appearance profiles show that the majority of OH formed is travelling too fast to have been thermalised at the surface; the appearance profiles are well replicated by a simulation of a direct component; the observation of OH as a reaction product means the reaction must be taking place at the extreme outer layers of the liquid; the rotational temperatures at all delays measured were found to be superthermal in agreement with previous gas-phase measurements; the shape of the appearance profiles and OH yield was found to be insensitive to temperature over the range sampled.

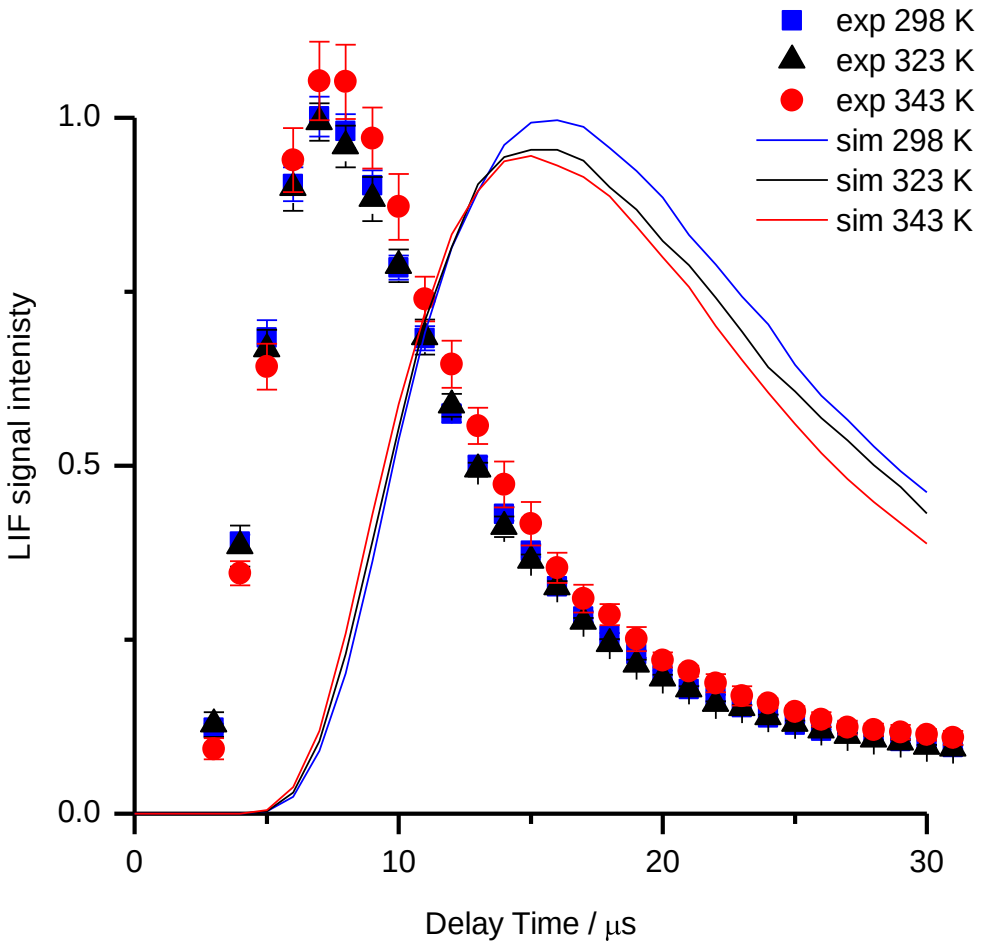

Figure 3.11: Measured appearance profiles of OH (v' = 0) LIF signals for [C_{12}mim][NTf_2] recorded at 298 K (blue squares), 323 K (black triangles) and 343 K (red circles). Profiles recorded on $Q_1(1)$ line of the OH *A*-*X* (1,0) band, shown following background subtraction as described in the text. Error bars represent the 1σ standard error in the mean of several profiles recorded at each liquid temperature. $p(NO_2)$ ~ 1 mTorr; surface-probe laser distance = 4 mm. Also included are Monte Carlo simulations of a thermal TD component at 298 K (blue line), 323 K (black line) and 343 K (red line). The 298 K simulation has been peak normalised and all other simulations have been normalised relative to it to reflect the predicted differences. Likewise the 298 K measured appearance profile has been peak normalised and the others have been correctly weighted relative to it to reflect the real measured relative signal sizes.

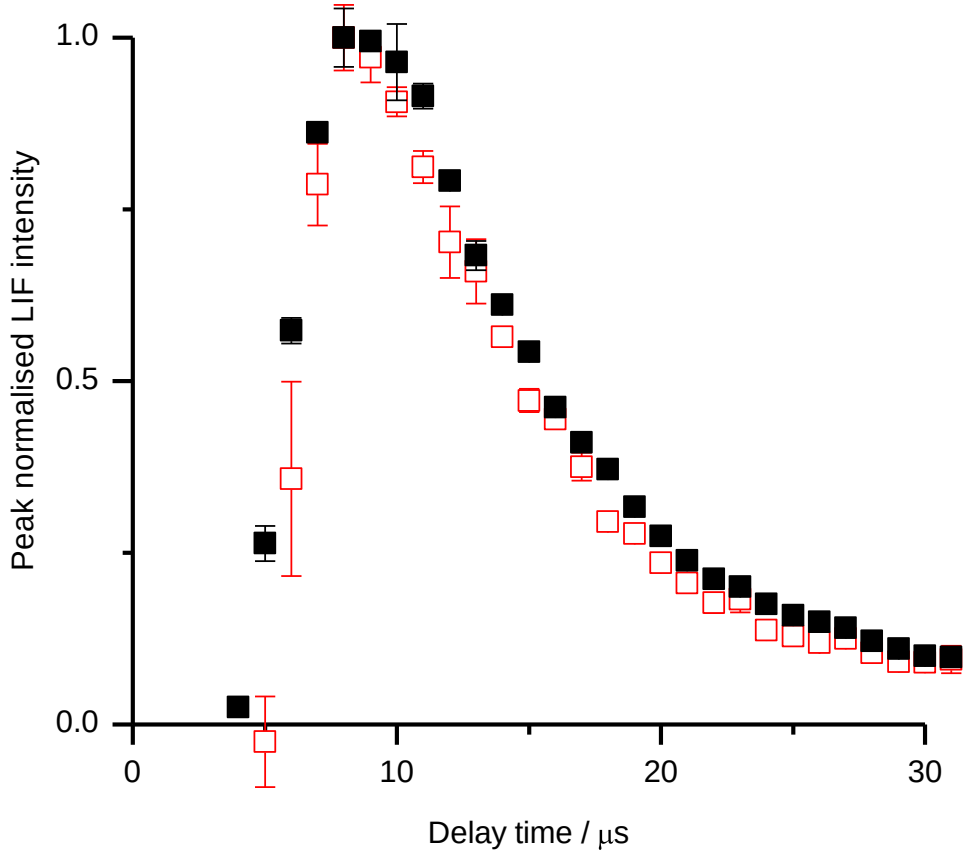

Figure 3.12: Measured appearance profiles of OH (v' = 0) LIF signals for [C_{12}mim][NTf_2] Profiles recorded on $Q_1(1)$ (black closed squares) and $R_1(5)$ (red open squares) transitions of the OH *A*-*X* (1,0) band, shown following background subtraction as described in the text. Error bars represent the 1σ standard error in the mean of several individual profiles. $p(NO_2)$ ~1 mTorr; surface-probe laser distance = 4 mm. Liquid temperature ~298 K.

3.4.2 Reactive scattering as a chemically specific analytical probe of liquid surfaces

The arguments outlined in section 3.4.1 point strongly to a predominantly direct reaction mechanism. Consequently, it can safely be assumed that the reaction observed is occurring at the extreme outer layers of the liquid surface, as any trapped OH would be expected to react further to form H_2O, given the modest reaction barriers for this reaction. The direct reaction at the interface can therefore be used as a new type of analytical tool to characterise the ionic liquid surface. It can be assumed, based on reaction barrier heights (section 3.4.1), that the $O(^3P)$ atoms react exclusively at the secondary CH units. As such, the $O(^3P)$ atoms act as a site-specific probe of the interface, providing information on the extent to which the interface is occupied by the C_n alkyl chain of the cation.

The observation of OH is, in itself, evidence of the presence of alkyl units at the interface. Figure 3.4 clearly shows substantially different OH yields from the family of ionic liquids. The integrated appearance profiles are proportional to the OH yield. The differences in OH yield, relative to the reference liquid squalane (table 3.1) are too extreme to be accounted for by differences in molecular stoichiometry. This is emphasised in figure 3.13 where the OH yield per reactive hydrogen atom is plotted. This was calculated by dividing the area under the appearance profile (proportional to amount of OH formed) by the number of 'reactive' hydrogen atoms present in the liquid. In this work, only the secondary CH units on the C_n alkyl chain on the cation were assumed to be reactive.

A purely stoichiometric dependence would correspond to a horizontal line on figure 3.13. Instead, there is a dramatic, non-linear chain length dependence with a significant enhancement in OH yield with increasing chain length. The results show that [emim][NTf_2] is the least reactive towards $O(^3P)$. In the context of the applicability of this family of ILs being used in thruster systems for spacecraft it is clear that, all other factors being equal, [emim][NTf_2] would indeed be the best candidate of those studied. It can also be predicted, on the basis of these results that the shortest member of the family, [mmim][NTf_2], which was not included in this work, would be a good candidate also. From a defence point-of-view it would be important to establish which ILs used might produce an OH plume which could be detected by an enemy. Conversely, it

would be useful to detect the presence of an enemy's satellites by knowing that an OH plume might be suggestive of ILs being used in their thrusters.

Included in figure 3.13 is the reactivity per reactive hydrogen observed in the complementary molecular beam experiments of Minton and co-workers[125]. The reactivity has been normalised with respect to the peak signal from $[C_{12}mim][NTf_2]$ in both the molecular beam (Minton) and photolytic (this work) experiments to allow for direct comparison. In the molecular beam case, the terminal CH_3 groups are also presumed to be reactive as a result of their increased collision energy (~520 kJ mol^{-1}); the barrier to abstraction for a primary C-H is ~42 kJ mol^{-1}[47].

In this case, there is clearly still a distinct, non-stoichiometric variation in the OH yield for the more restricted measurements on the first and last members of the series ($[emim][NTf_2]$ and $[C_{12}mim][NTf_2]$). There is agreement therefore between the two studies that the availability of the aliphatic chains at the interface increases dramatically with chain length. There is a less extreme suppression of reactivity towards $[emim][NTf_2]$ in the molecular beam experiments (figure 3.13). This suggests that the higher energy probe (520 kJ mol^{-1}) used in the molecular beam experiments samples a different range of depths than the lower energy probe (16 kJ mol^{-1}) used in the photolytic experiments presented here. In the higher energy case, it is more likely that OH formed at greater depth will be able to escape before reacting to form water on account of it having sufficient energy to overcome the attractive projectile-surface interactions.

The conclusions of both experimental scattering studies are further strengthened by the molecular dynamics simulations, carried out by Schatz and co-workers, co-reported with the Minton experimental results[125]. The simulations predict little preference for the ethyl groups in $[emim][NTf_2]$ to occupy the surface. For the $[C_{12}mim][NTf_2]$ surface on the other hand, there is a clear selectivity towards the alkyl groups preferentially occupying the interface. This is shown in the representative snapshots of the $[emim][NTf_2]$ and $[C_{12}mim][NTf_2]$ surfaces shown in figure 3.14. The final six carbon atoms are predicted to project out, above the surrounding anion density.

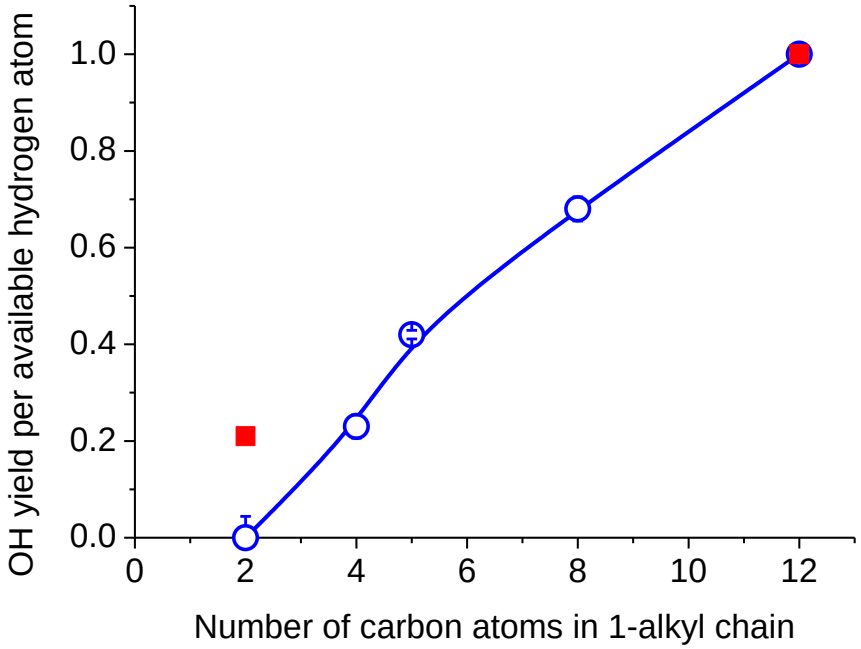

Figure 3.13: Relative OH yield per available hydrogen as a function of alkyl chain length for a series of $[C_n mim][NTf_2]$ ionic liquids as measured by photolytic-spectroscopic experiments (blue open circles with 2σ error bars) and the complimentary molecular beam approach (red closed squares)[125]. Yields per atom are normalised for n = 12 for both experiments. The available hydrogen atoms are assumed to be restricted to CH_2 groups in the photolytic experiments but include CH_3 and CH_2 groups in the molecular beam experiments. This reflects the relationship between collision energies and barrier heights for the different C-H bond types.

The authors[125] go further and predict that the alkyl chains (or the outer 6 carbon atoms) lie, on average, parallel to the plane of the surface. This is consistent with the photolytic experimental results presented here. A chain lying parallel to the surface would expose the secondary C-H units. A chain perpendicular to the surface in a monolayer-type structure would preferentially expose the least reactive primary groups. This might be expected to result in a suppression of reactivity in the photolytic experiments described here. Some clustering of the chains is predicted also for the longer chain IL, at the interface and the bulk (figure 3.14).

It has clearly been established here that there is preferential occupation of the interface by alkyl groups as the chain length is increased. This is in agreement with the majority view from many of the more traditional experimental surface analysis techniques described in the introduction (section 3.1)[160,161,177,178,180] and theoretical studies[166,168,169,175,176]. A discrepancy remains with the direct recoil spectroscopy measurements of Seddon and co-workers[156,157] who predict no ion segregation. This may be a consequence of the photolytic method presented here (and

even the molecular beam) being 'gentler' than direct recoil spectroscopy as previously implemented with higher energy particles such as Ar^+ and Ne^+ ions[156]. There is evidence that there is a critical chain length of $n \geq 4$ carbon atoms, beyond which chain segregation is more pronounced [161,179]. The results presented here (figure 3.13) would be consistent with this, although in the absence of data for $[C_3mim][NTf_2]$ it is impossible to conclude whether this onset is sudden above $n = 3$. There is however, clear preferential occupation of the interface by alkyl units above $n = 4$.

The advantage of using chemical 'probes' such as this to interrogate the chemical nature of the interface is that specific target groups can be identified; such as the alkyl segment in this case. A consequence of this is that the absolute surface coverage by the target alkyl groups can also be estimated. The difference in the energy transfer between the O and OH impulsively scattering from the liquid surface (described in section 3.4.1) in the Minton experiments confirms that the $[C_{12}mim][NTf_2]$ surface is not saturated with alkyl groups.

The surface coverage was estimated in this work by comparing the OH yield from each IL to that of the reference liquid hydrocarbon squalane. McKendrick and co-workers previously used molecular dynamics simulations to predict the fraction of the squalane surface at which H-abstraction reactions could take place[121] i.e. the fraction of the surface which is occupied by secondary and tertiary C-H units. They predicted that 60% of the squalane surface was potentially reactive; a fraction which is close to the bulk composition of squalane but with a slight preference for primary CH_3 units to occupy the surface.

The OH yield from each IL relative to squalane is known (table 3.1), and this relative yield as a fraction of the potentially reactive surface coverage of the squalane reference gives an estimated surface coverage (by alkyl CH_2 units) of ~35% for $[C_{12}mim][NTf_2]$, ~16% for $[C_8mim][NTf_2]$, ~5% for $[C_5mim][NTf_2]$, ~2% for $[bmim][NTf_2]$ and ~0.2% for $[emim][NTf_2]$. These surface coverage estimates agree qualitatively with the majority of previous experimental and theoretical work (that there is a preference for the alkyl chains to occupy the surface). Although direct quantitative comparison is not possible at this time it would be an interesting and reasonably straightforward quantity to test in future MD simulations.

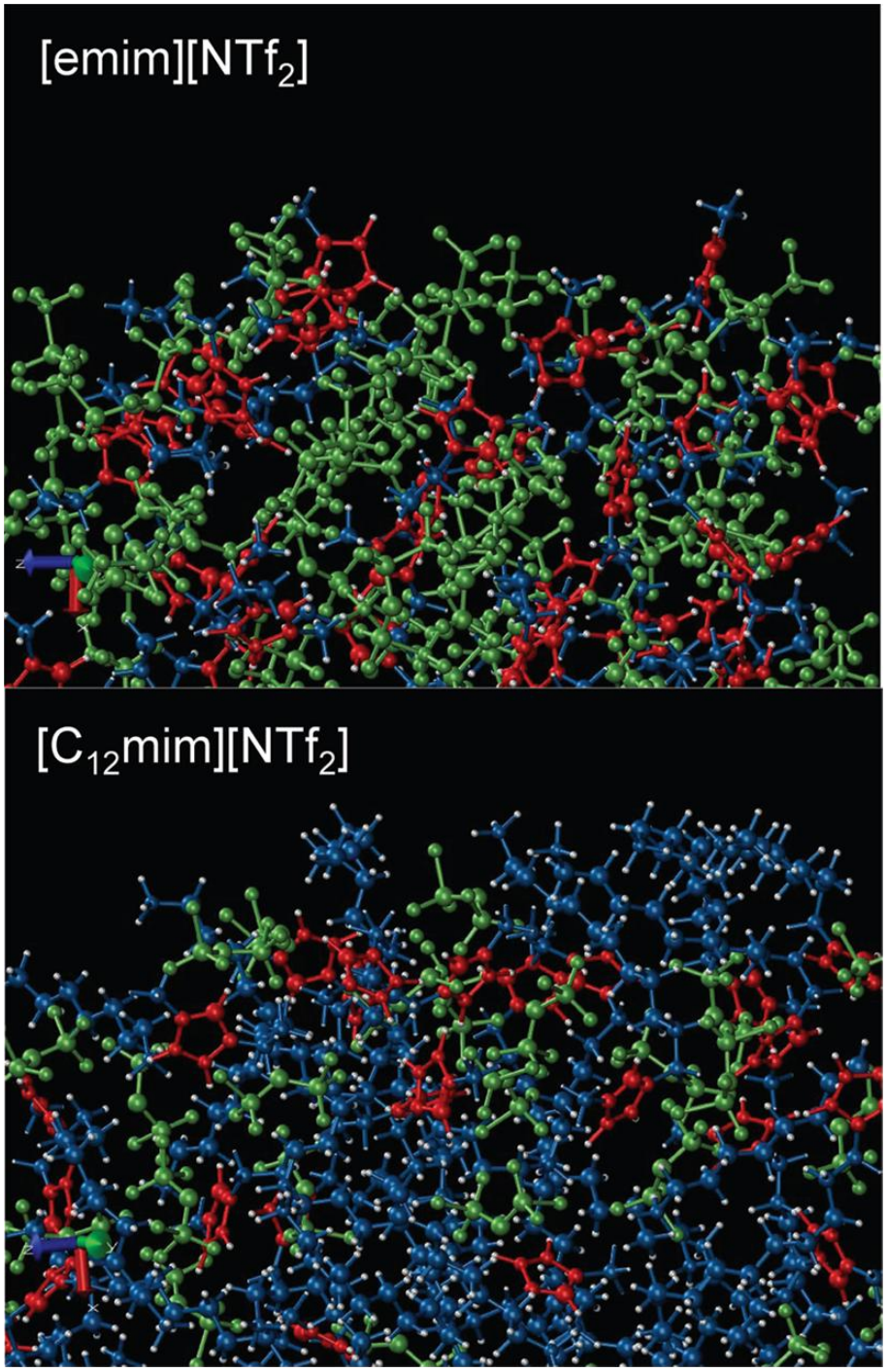

Figure 3.14: Representative snapshots from molecular dynamics simulations of the surfaces (at 323 K) of [emim][NTf_2] (top) and [C_{12}mim][NTf_2] (bottom) ionic liquids, showing the anion (green), imidazolium ring (red), alkyl chains (blue) and hydrogen atoms (white). Reproduced from reference[125].

3.5 Conclusions

- Photolytically generated O(^{3}P) atoms have been shown to be a sensitive surface-and chemical-target-group-specific, probe of the surface structure of a family of [$C_n$mim][NTf_2] ionic liquids.
- The translational and internal energy distribution of the OH products of the hydrogen abstraction reaction taking place at the 1-alkyl chain has been determined and the dominant reaction mechanism has been shown to be a direct, impulsive abstraction with little if any thermalised (TD) OH products.
- The OH yield and translational distribution was found to be independent of liquid temperature (across the range sampled). This is further evidence of a very dominant direct reaction mechanism and no thermally activated reaction channels being available.
- The rotational distribution was found to be (modestly) superthermal at all delay times probed, supporting the conclusion of a predominately direct mechanism. There was some translational-rotational correlation observed, where the rotational temperature was found to 'cool' with increasing photolysis-probe time delay. This could be the result of a small TD component being present, or a dynamical effect whereby the fastest OH products are also the most rotationally excited.
- The OH yields were found to be a strong function of the 1-alkyl (C_n) chain length, with reactivities far exceeding any stoichiometric increase in the available hydrogens. This reveals that the interface is preferentially occupied by alkyl units in the higher members of the IL family. This is in agreement with some but not all of the existing surface analysis techniques used to study ionic liquids and corresponding molecular dynamics simulations. The results are also in good agreement with the less comprehensive, complimentary experimental and theoretical study carried out by Minton and co-workers[125].
- The results are consistent with previous experimental and theoretical predictions of a threshold at $n \geq 4$ beyond which the surface segregation increases dramatically; although in the absence of data for $n = 3$ it is not possible to state the position of this threshold definitively.
- The surface coverage (by alkyl groups) has been estimated by comparison of the OH yields to that from the benchmark liquid squalane. From this, it is clear that the surfaces of the ionic liquids are not saturated with alkyl chains.

3.6 Future work

The main aim of the work presented in this chapter was to investigate the relative reactivity of a family of ionic liquids towards $O(^3P)$ and determine the extent to which this reaction is an effective probe of the liquid surfaces. There are certain specific dynamical questions which could be addressed by a direct continuation of this work. First, it is unclear at the present time whether a true thermal TD component is present in the OH products. The appearance profiles suggest there is only a very minor TD component, if present at all. This could in principle be resolved by a more systematic investigation of the rotational distribution, particularly as a function of liquid temperature. This was carried out previously by McKendrick and co-workers when studying the dynamics of the reaction between $O(^3P)$ and squalane[67] who observed that the rotational temperature of the OH products formed in $v' = 0$ was influenced by the surface temperature. This is evidence that the OH products had resided at the surface long enough to (at least partially) thermalise with it.

In section 3.4.1, an alternative interpretation of the rotational temperature of the OH products 'cooling' with increased time delay (alternative to the presence of a TD component) is presented. It is proposed to be a dynamical effect whereby the fastest OH are formed in such a way that they are also the most rotationally excited. The extent to which this was observed in the appearance profiles (figure 3.12) was limited. This could in principle be investigated further by improving the translational resolution of the experiment. This could be achieved by using a molecular beam source of $O(^3P)$ atoms or using a photolytic precursor with a narrower translational energy distribution. There are no obvious replacements for the NO_2 precursor for clean $O(^3P)$ production at the available wavelengths of commercial lasers. The molecular-beam approach is something which could be attempted with a considerable rebuild of the experiment, although $O(^3P)$ is difficult to form cleanly and at low collision energy by the methods employed in molecular beam experiments.

Dynamical questions aside, the technique has been shown to be an effective probe of the surface composition of this family of ionic liquids. This method can in principle be used to investigate any IL family containing abstractable hydrogen atoms. The influence of the anion would also be an interesting parameter to vary, to establish any effect it might have on the surface composition. In a wider context, 'reactive probes'

could be applied more generally, alongside traditional surface analysis techniques to probe interfacial structure. The results presented here show that varying collision energy could be used to sample different depths of the interface and different reactive probes could be used to target specific chemical groups (if the higher collision energy results of Minton and co-workers are comparable to the lower energy work in this thesis). The interfacial reaction of Cl has already been demonstrated with squalane[61] but not pursed in any analytical sense, as is the case with F atoms[73]. Recent scattering calculations of the reaction of F atoms with hydrocarbon surfaces predict they undergo essentially a barrierless reaction with the first group they encounter[132] and in that sense they would also reflect reaction at the outermost portions of the liquid.

Chapter 4

Reactions of O(^{3}P) atoms with alkylthiol self-assembled monolayers

4.1 Introduction

The preparation and structural analysis of self-assembled monolayers (SAMs) is a vast field in its own right, with a wealth of available literature. Only a brief introduction to SAM properties and structure will be provided here. The focus of this chapter is the elucidation of the reaction dynamics of O(^{3}P) atoms with alkylthiol SAMs and its importance within the gas—surface scattering field specifically. As such, the general introduction in chapter 1, (particularly sections 1.3.2, 1.3.4, 1.4.1 and 1.4.2) is of particular importance here.

4.1.1 Self-assembled monolayers – preparation and structure

Self-assembled monolayers (SAMs) are formed by the spontaneous chemisorption of amphiphillic molecules to a substrate. Their nature is defined by the adsorbate-substrate interaction. The most widely studied and utilised are alkylthiol SAMs formed by the chemisorption of alkylthiols (RSH) onto gold (Au(111)) substrates. Alkylthiol SAMs can be prepared by adsorption from a dilute (millimolar) ethanolic solution of alkylthiol molecules (solution deposition) or by adsorption via the vapour phase in a vacuum environment[185]. SAMs were first used to control wettability in steam engines in the 1930's[186] but their wide variety and tunability (through adsorbate/substrate variation) has led to applications in a number of fields such as corrosion protection[187], molecular recognition[188], photolithography[189] and biocompatibility[190]. Within the context of this thesis, they are also useful proxies for liquid hydrocarbons and have

been used as such in theoretical scattering simulations as was described in chapter 1 (sections 1.4.1 and 1.4.2).

Alkylthiols chemisorb with an enthalpy of reaction of ~-126 kJ mol^{-1}, irrespective of alkyl chain length (in the region $4 > n < 10$)[191]. The stability of alkylthiol SAMs is the result of the strong thiolate (Au-S) bond formed and complimentary van der Waals interactions between the alkyl chains. They have been found to be reasonably resilient in air and under vacuum, and can be heated to 350 K without showing damage or alkyl chain loss[186]. A recent study by Sampath and Subramanian[192] on the adhesion behaviour of alkylthiol SAMs in air and water, found that there was no substantial chain length effect ($4 > n < 16$) on SAM stability. The shorter chains (n = 4-8) appeared to be slightly less stable but suffered from comparably large associated errors making absolute conclusions difficult[192].

Air stability is dependent on a number of factors such as chain length, atmospheric O_3 concentration and initial film quality[193]. Alkylthiol SAMs can be damaged by exposure to atomic oxygen and ozone in ambient air[193,194]. Short chained alkylthiol SAMs ($n < 6$) were found, by a variety of surface analysis techniques to be least resilient[193]. The attack was proposed to occur at the sulphur atoms. This was inferred through the removal of features typical for SAMs in the XPS spectra (thiolate signals, Au-S-R where R is the alkyl chain), and the emergence of oxidized sulfur groups such as sulphates and sulphonates ($X\text{-}SO_4^{2-}$ or $X\text{-}SO_3^{2-}$ where X = Au or the alkyl chain R)[193]. This degradation of SAMs in ambient air has implications on their practical uses as it occurs within several hours (in air and exposed to daylight)[194]. Within the context of this work, it was therefore important that the samples were used freshly prepared from solution and weren't stored for any prolonged period.

Surface analysis techniques are clearly critically important in deciphering and monitoring the structure of alkylthiol SAMs and a vast array of techniques have been employed with this in mind. Examples, but by no means an exhaustive list include: X-ray photoelectron spectroscopy (XPS)[195,196]; atomic force microscopy (AFM)[197]; thermal programmed desorption (TPD)[198]; Fourier-transform infrared spectroscopy (FTIR); and low-energy electron diffraction (LEED)[199]. Arguably the most important technique is scanning tunnelling microscopy (STM), a non destructive technique which is able to generate images of SAM surfaces with atomic-scale

resolution. The combination of surface analysis techniques mentioned above has resulted in the structure of alkylthiol SAMs being very well characterised[196].

The alkyl chains and a gold adatom occupies the threefold hollow sites in the Au sub-layer and form a hexagonally packed $(\sqrt{3}\times\sqrt{3})$R30° overlayer[196,200,201]. The chains are separated by a distance of 5 Å which is $\sqrt{3}x$, where x is the atomic spacing of the Au sub-layer (x = 2.88 Å) and the alkyl over-layer is rotated 30° with respect to the Au sub-layer. This is shown schematically in figure 4.1. At full monolayer coverage the chains stand upright with a tilt angle of ~34° with respect to the surface normal[202]. At lower surface coverage (sub-monolayer) alkylthiol SAMs have been shown to adopt *striped* structures where the alkyl chains are thought to be lying flat on the substrate[203]. This low coverage can be the result of desorption of the chains, through heating of the SAM for example, or by incomplete monolayer adsorption in the preparation stage. The kinetics of adsorption are thought to proceed through several steps including this low-coverage striped phase before the full monolayer is achieved[204]. For this reason, SAMs are generally prepared by immersion in solution for several hours to ensure high quality standing-up phase SAMs are formed.

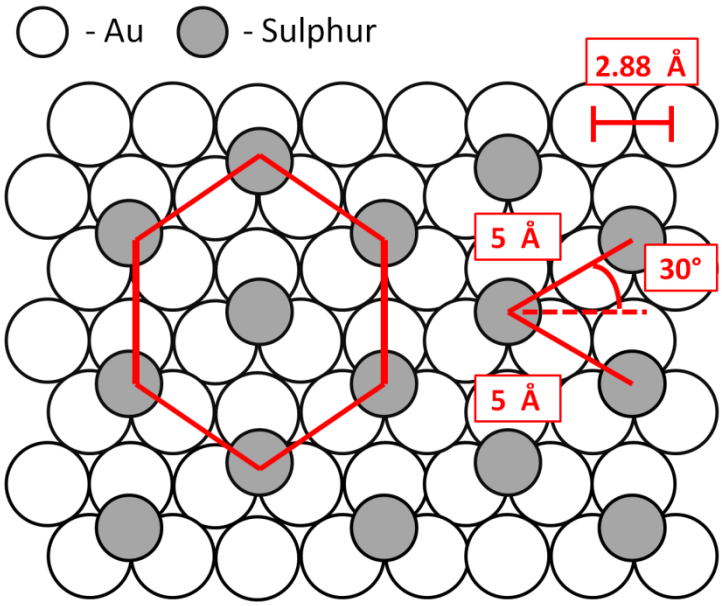

Figure 4.1: Schematic representation of the hexagonal packing of alkyl chains in alkylthiols SAMs and description of the $(\sqrt{3}x\sqrt{3})$ R30° over-layer with respect to the Au(111) sub-layer. Adapted from reference [205].

4.2 Experimental summary

As described in chapter 2 (section 2.3), a variety of alkylthiol SAMs (hydrogenated, deuterated and partially deuterated) were prepared by immersing Au(111) slides in millimolar ethanolic solutions of the desired thiol. The SAMs were removed from solution, rinsed with ethanol, dried with nitrogen and used immediately. The SAMs were placed in a vacuum chamber, held at a base pressure of ~1×10^{-7} Torr. $O(^3P)$ atoms were generated above the SAM surface by 355 nm laser photolysis of an NO_2 precursor (1 mTorr). This results in a broad superthermal $O(^3P)$ speed distribution with an average lab-frame kinetic energy of 16 kJ mol^{-1} (FWHM = 26 kJ mol^{-1})[141]. A fraction of the $O(^3P)$ atoms formed collide with the SAM surface where they can undergo hydrogen abstraction reactions at the alkyl chains to generate OH (or OD) reaction products. Only the most energetic $O(^3P)$ atoms have sufficient energy to surmount the reaction barriers of 34 kJ mol^{-1} and 22 kJ mol^{-1} for primary (CH_3) and secondary (CH_2) C—H bonds respectively. A fraction of the OH (OD) reaction products return to the laser axis where they are detected by laser induced fluorescence (LIF) on the OH/OD A-X (1,0) band.

4.3 Experimental Results

4.3.1 Signal verification and implications for the experimental procedure

The primary objective was to detect OH radicals from the reaction of $O(^3P)$ with the SAM surface. Initial tests were carried out using a $C_{12}H_{25}$-SAM. The presence of OH products was verified by scanning the probe laser across the $Q_1(1)$ transition of the A-X (1,0) band at an appropriate photolysis-probe laser delay (consistent with a realistic round trip time to and from the surface). Subsequently, the OH signal as a function of delay time was measured by fixing the probe laser wavelength and varying the time delay between the photolysis and probe laser. The appearance profiles were typical of what had previously been measured by McKendrick and co-workers in related gas-liquid experiments[63,67-70]. They had an initial dead-time, consistent with the time required for the $O(^3P)$ atoms to travel to the surface, followed by a rise in intensity of OH reaction products which reach a maximum before dropping off again.

The appearance profiles recorded in the initial stages of the experiments are shown in figure 4.2. Several individual profiles have been averaged and their dependence on SAM surface-laser axis distance is shown. As distance is increased, the signals peak at later times (a result of the longer round-trip distance travelled) and are smaller in intensity (a result of decreased detection sensitivity with increased distance due to geometric factors). This behaviour is consistent with the OH observed being formed at the surface.

Having confirmed that the OH signal originated from the *surface*, the next step was to confirm that it was coming from the *SAM layer* specifically. This was achieved using per-deuterated SAMs (C_6D_{13}-SAM) and detecting the OD reaction products. If an OD signal were to be detected this would be unequivocal proof that the reaction was taking place at the SAM surface; it is reasonable to assume that there are no spurious sources of OD in the vacuum chamber. Initially, though, this proved very difficult and no OD was detected from the C_6D_{13}-SAM. A further complication was that *OH* was detected from the per-deutero SAM and also even from a bare gold substrate.

The OH appearance profiles for the C_6D_{13}-SAM, bare gold substrate and a corresponding $C_{12}H_{25}$-SAM are shown in figure 4.3. These profiles have had no relative normalisation factor applied and it is clear that the OH signal from each of the three surfaces is similar in magnitude and in shape. Figures 4.2 and 4.3 show that the OH signal *is* coming from the SAM substrate but not from the monolayer explicitly. The detection of OH could therefore be a result of a monolayer preparation problem or originate from a contaminant, containing abstractable hydrogen atoms, which is present on all surfaces placed in the vacuum chamber.

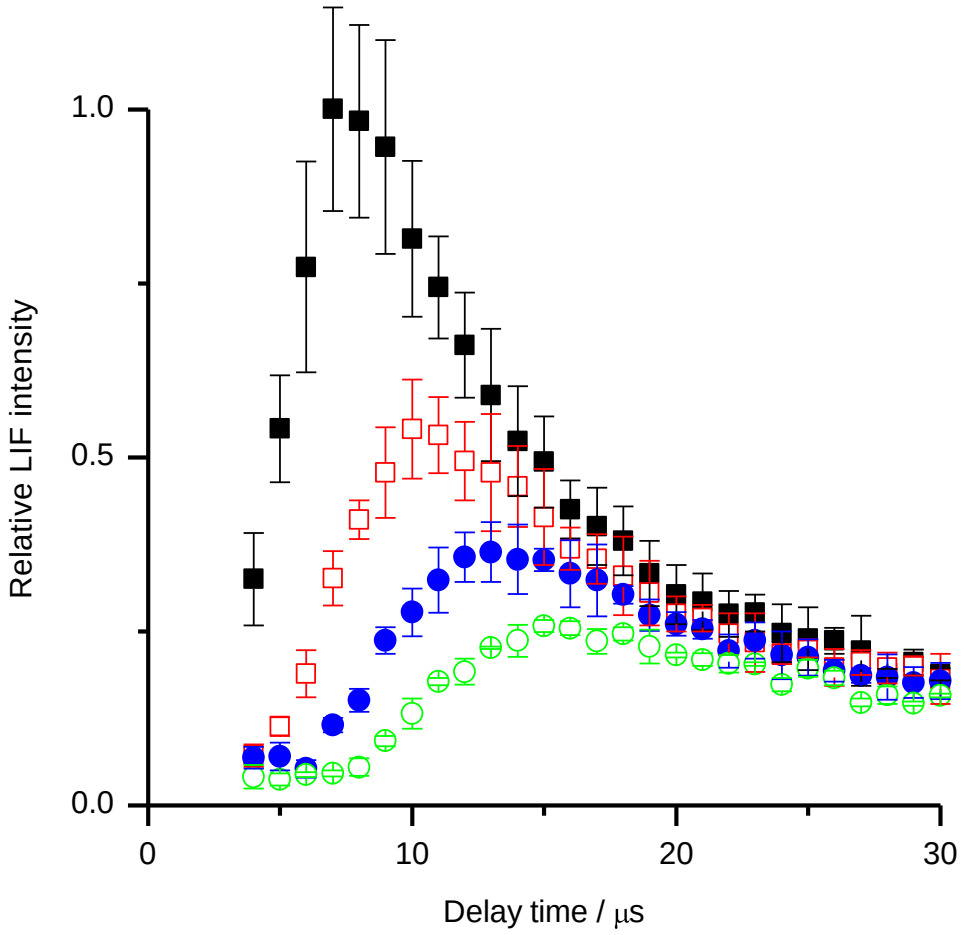

Figure 4.2: Measured appearance of the OH *A*-*X* (1,0) $Q_1(1)$ LIF signal as a function of photolysis-probe delay time from a $C_{12}H_{25}$-SAM. Nominal probe-laser beam to SAM distance of 4 mm (black filled squares), 5 mm (red open squares), 6 mm (blue closed circles) and 7 mm (green open circles). $p$$NO_2$ ~1 mTorr.

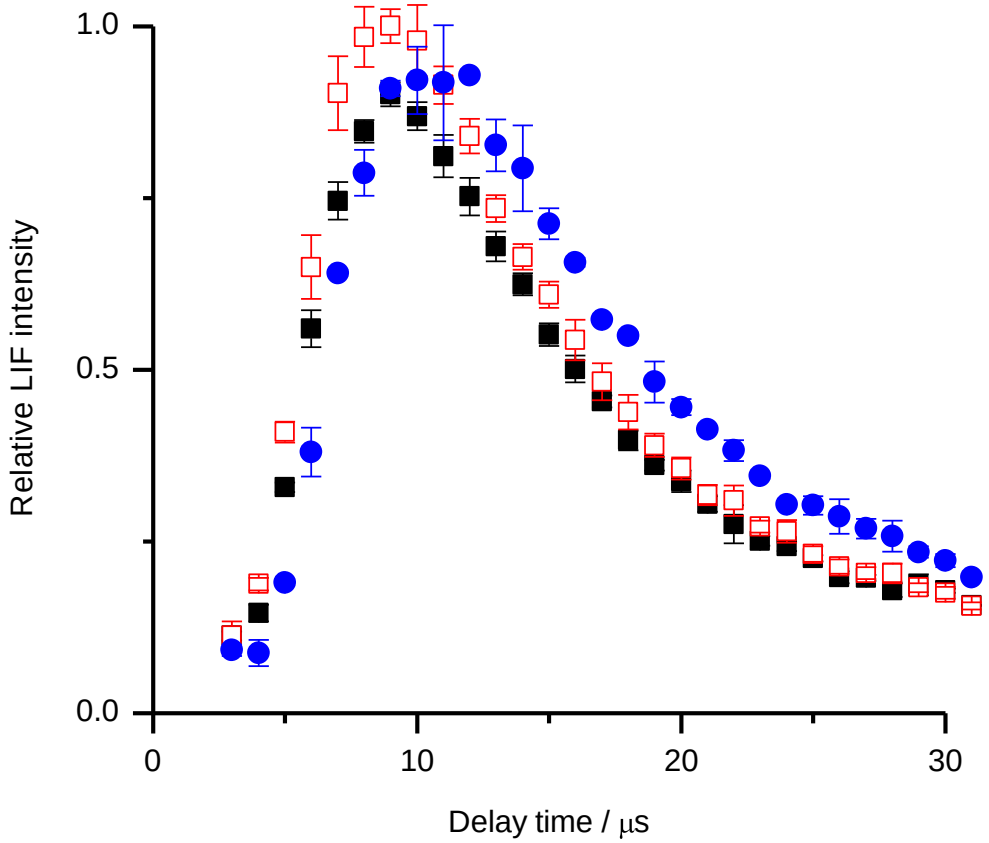

Figure 4.3: Measured appearance of the OH *A*-*X* (1,0) $Q_1(1)$ LIF signal as a function of photolysis-probe delay time from a $C_{12}H_{25}$-SAM (black closed squares), C_6D_{13}-SAM (red open squares) and bare Au substrate (blue closed circles). Nominal probe-laser beam to SAM distance of 5 mm. $p$$NO_2$ ~1 mTorr.

A series of experiments was devised to locate the source of the problem, first of which was the evaluation of the SAMs preparation method. It was important to ensure that the Au(111) substrates purchased were atomically flat and that self assembly was occurring when the substrates were exposed to solutions of the alkylthiols. Scanning-tunnelling microscopy (STM) was used to analyse the gold substrates before and after exposure to the thiol solutions. This was carried out in collaboration with researchers at the University of St Andrews[135].

The STM images of the clean gold substrate and equivalent SAM formed after exposure to the $C_6D_{13}SH$ solution are shown in figure 4.4. There is an obvious difference between the two samples. First, the Au substrate is atomically smooth and shows the *herringbone* structure which is a signature for Au(111). Second, following exposure to the thiol, the herringbone structure of the Au substrate is no longer visible and the surface is covered in small domains with visible order and the characteristic *pitted* structure of SAMs[196]. The pits are Au vacancy islands (0.24 nm deep) and are well reported in the literature as being the result of surface reconstruction of the Au substrate as a result of the self-assembly process[206]. The STM images revealed that the purchased substrates and SAM preparation method were producing reasonable quality monolayers. As a result it was assumed that the contamination problem was most likely occurring in the vacuum chamber rather than in the SAM preparation stage.

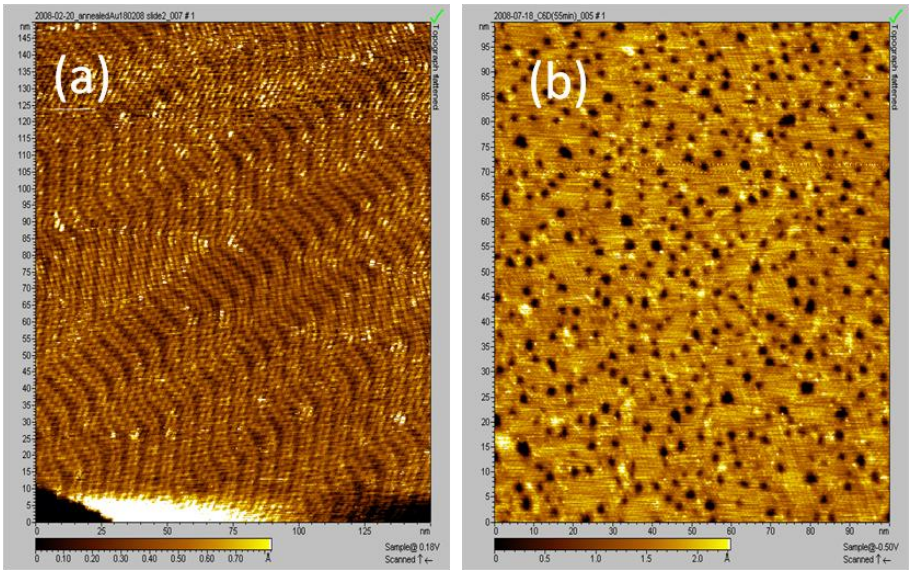

Figure 4.4: STM images of (a) the Au(111) substrate showing the atomically resolved herringbone structure and (b) C_6D_{13}-SAM showing the pitted structure and molecular domains characteristic of SAM formation. The images were recorded in constant current mode under ambient conditions using a PicoPlus (Molecular Imaging) instrument by collaborators at the University of St Andrews[135].

The most obvious and probable source of an abstractable hydrogen containing impurity associated with the vacuum chamber was pump oil. The diffusion pump was replaced by a turbomolecular pump (oil free and faster pumping speed) and liquid nitrogen and zeolite hydrocarbon traps were added to the backing pump line. The chamber was rigorously cleaned also. Despite these changes, an OH signal from the per-deutero SAM persisted.

To further investigate the source of these problems, the C_6D_{13}-SAMs were analysed by XPS immediately out of solution, after 2 hours in the chamber with 1 mTorr N_2 and after 2 hours in the chamber with 1 mTorr NO_2. The resulting spectra are shown in figure 4.5. The spectra show that the SAM surface composition is largely unaffected after being placed in a vacuum chamber under N_2. Both spectra in figure 4.5 (a) are dominated by the Au (4f) peak which would be expected for monolayer coverage. The carbon and sulfur peaks are present also. The spectrum following NO_2 exposure in the vacuum chamber (figure 4.5 (b)) is clearly different. The dominant peak in this case is carbon, the sulfur peaks are more pronounced also, and the Au peak is less intense than carbon. This is suggestive of the surface being covered with a carbon containing multi-layer. The XPS and LIF measurements combined show the existence of a carbon containing impurity, with abstractable hydrogen atoms, which is present only when NO_2 is present.

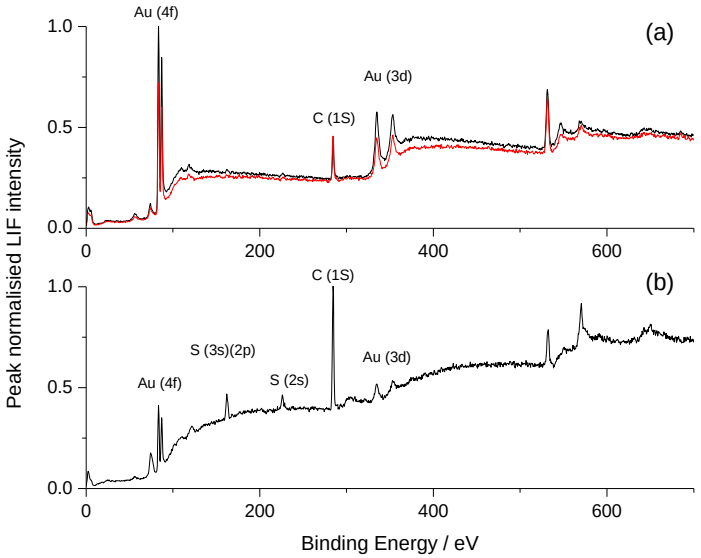

Figure 4.5: Peak normalised XPS spectra of C_6D_{13}-SAMs. (a) Freshly removed from solution (red line) and following 2 hours in the vacuum chamber under N_2 (1 mTorr) (black line). (b) Exposed to NO_2 (1 mTorr) for 2 hours.

The timescale on which the impurity grew in was established by recording OH appearance profiles from the C_6D_{13}-SAM as a function of NO_2 exposure time. The replacement of the diffusion pump with a turbomolecular pump allowed for data to be acquired much more quickly after the SAM was placed in the reaction chamber. Previously, the diffusion pump would take at least 20 minutes to reach a base pressure of 1×10^{-6} mbar. With the turbomolecular pump, this pressure could be achieved in approximately 5 minutes. OH appearance profiles could then be recorded as soon as the NO_2 was admitted to the chamber.

Appearance profiles were recorded at different NO_2 pressures and the peak OH LIF intensity was plotted as a function of NO_2 exposure time (figure 4.6 (a)), illustrating the clear OH growth from the per-deutero C_6D_{13}-SAM. The use of the turbomolecular pump and other improvements in efficiency of the procedure for mounting the samples meant that OD signals could now be observed from the C_6D_{13}-SAM. Previously, no OD had been observed because the NO_2 exposure time at which this was attempted had been too long. In a similar manner to that for OH, the OD intensity as a function of NO_2 exposure time was measured as shown in figure 4.6 (b). The OD decay and OH growth curves are complementary. At 2 mTorr NO_2 there is an initial period (~10 min) where the OD signal appears to be at least approximately constant, and the OH signal is negligible. The OD signal then decays and the OH signals grow rapidly until OD is no longer observable and the OH signal (from the contaminant) reaches a maximum. The OD decay and OH growth rates are enhanced at higher NO_2 pressure, confirming that the NO_2 is (at least partially) responsible for the destruction.

Any corresponding structural changes were examined by STM analysis of the SAMs[135]. Images were recorded of C_6H_{13}-SAM (assumed to be structurally identical to C_6D_{13}-SAMs) samples freshly out of solution, and following either 10 minutes or 1 hr of NO_2 exposure in the vacuum chamber. Large scale images (250 nm $\times$ 250 nm) of a freshly prepared SAM (figure 4.7 (a)) show structures typical of SAMs formed at room temperature. A separate SAM sample which had been exposed to NO_2 (and $O(^3P)$) in the reaction chamber for 10 minutes showed the same characteristics (figure 4.7 (c)). On both substrates a full monolayer is observed with small low-crystallinity domains.

Inset in figure 4.7 (a) is a fast-Fourier transform (FFT) of the data which brings out the symmetry in the structure. The FFT shows the hexagonal packing arrangement of the alkyl chains. This hexagonal packing is a result of the alkyl chains occupying the three-

fold hollow sites of the gold substrate as shown in figure 4.1. High resolution images (figure 4.7 (b) and (d)) show the molecular-level definition of the technique and that there are some areas of high crystalinity.

In marked contrast, a large scale image of a C_6H_{13}-SAM that was exposed to NO_2 for 1 hour is distinctly different and damaged (figure 4.7 (e)). There are smooth and rough areas on the surface and the gold vacancy islands are not as pronounced. A high resolution image (figure 4.7 (f)) reveals that the smooth areas consist of a *striped phase* with an inter-row periodicity of 1.3 nm[207].

The XPS, STM and LIF data all show that the SAMs lose their structural integrity after ~10 minutes of NO_2 exposure in the chamber. This has been shown for the C_6-SAMs and was assumed to be the case for other chain lengths. As the NO_2 precursor is intrinsically necessary to generate $O(^3P)$ atoms, the only option was to ensure that all data were collected within the 10 minute window where the SAM structures appear to be intact. This was experimentally challenging, involving multiple repeat measurements, but was ultimately essential. The major constraint was on the data acquisition time. Approximately three appearance profiles could be recorded in this 10 minute window, but excitation spectra, which generally take over 1 hour to record, could not be recorded in their entirety.

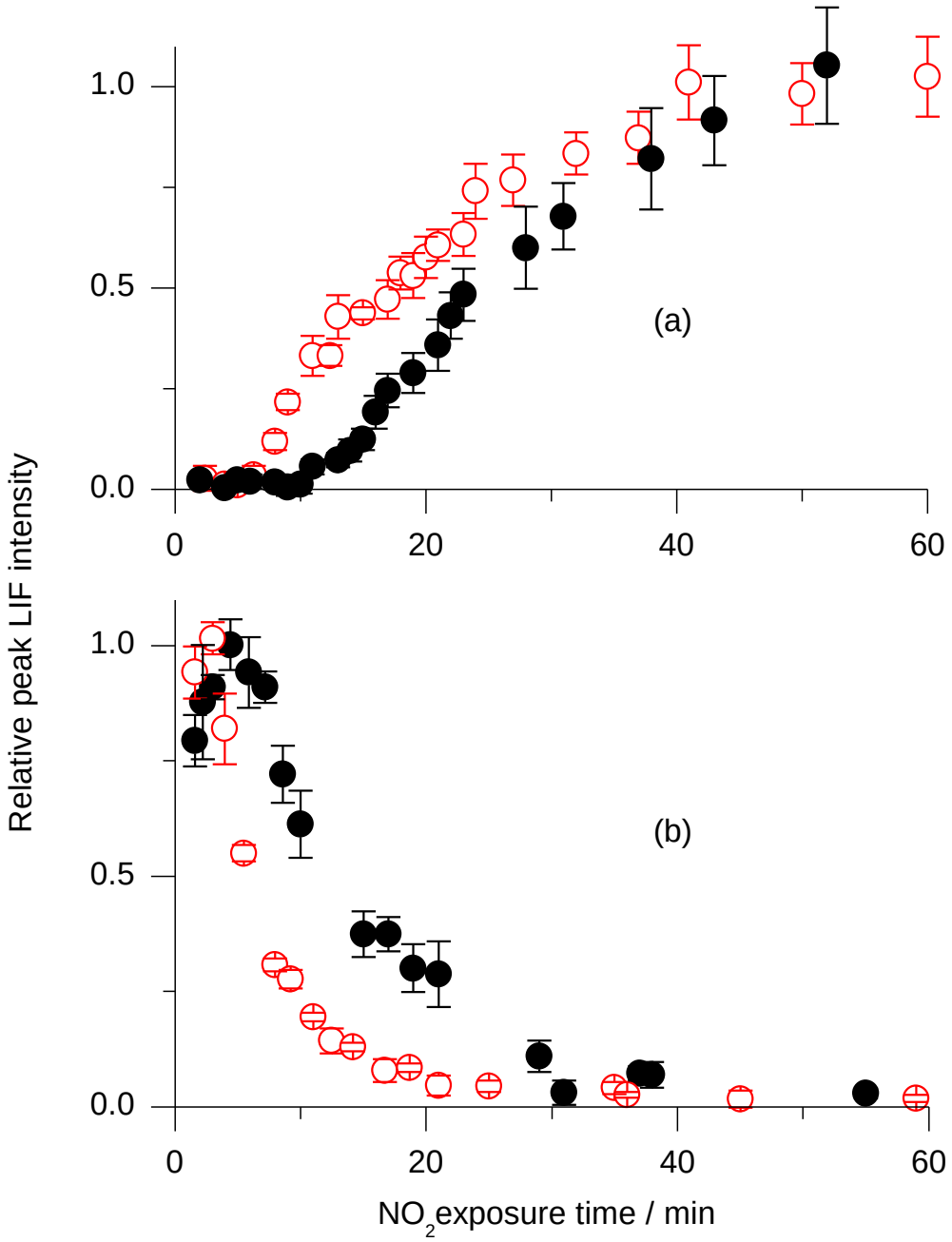

Figure 4.6: Intensity of LIF signals for (a) OH and (b) OD from reaction of O(^{3}P) with a C_6D_{13}-SAM as a function of NO_2 exposure time. NO_2 pressures of 2 mTorr (black closed circles) and 6 mTorr (red open circles) are shown. Each point represents the peak height in an appearance profile. Data were recorded on the OD/OH *A*-*X* (1,0) $Q_1(1)$ line at a probe laser-SAM distance of 4 mm. Relative intensities for OD and OH have been arbitrarily normalised at short and long exposure times respectively.

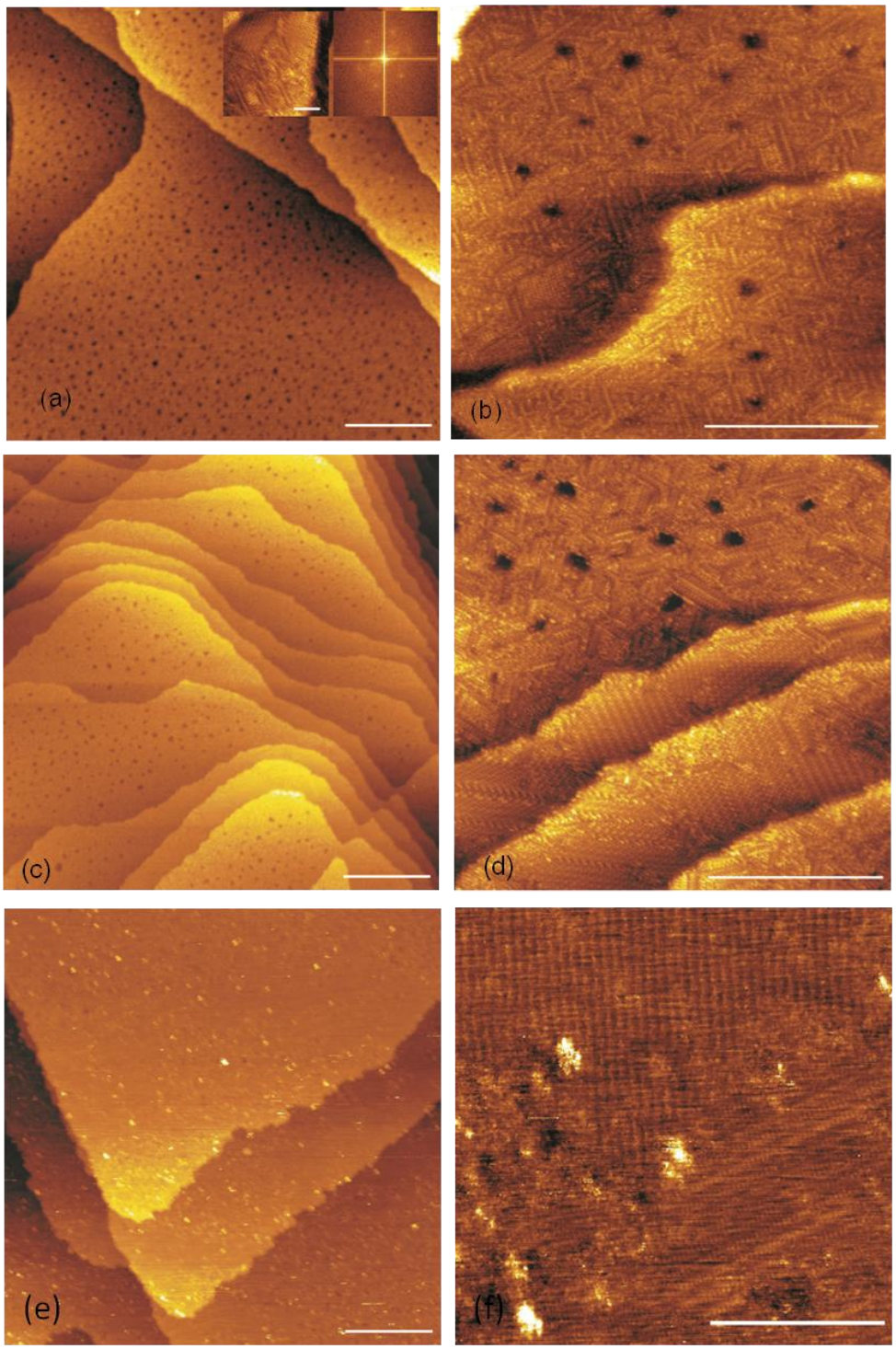

Figure 4.7: Large scale (250 nm × 250 nm) images of : (a) a freshly prepared C_6H_{13}-SAM; (c) a C_6H_{13}-SAM following 10 min NO_2 exposure; (e) a C_6H_{13}-SAM following 1 hr NO_2 exposure; scale bar = 50 nm. **High resolution (50 nm × 50 nm) images** of: (b) a freshly prepared C_6H_{13}-SAM; (d) a C_6H_{13}-SAM following 10 min NO_2 exposure; (f) a C_6H_{13}-SAM following 1 hr NO_2 exposure; scale bar = 20 nm. Inset in (a) is Fourier transform of a high resolution image showing the hexagonal packing of the alkyl chains.

4.3.2 OH and OD appearance profiles from the reaction of $O(^3P)$ atoms and alkylthiol self-assembled monolayers

Having established a viable procedure, experiments were carried out on the C_6D_{13}-SAMs with OD detection in the first instance. The probe laser-surface distance was varied and the OD appearance was measured as a function of photolysis-probe laser time delay (figure 4.8). A constant underlying probe signal has been subtracted from all profiles, the source of the background is scattered light and a small contribution from probe-induced photolysis (and simultaneous probing) of an OH containing impurity in NO_2 (chapter 3, section 3.3.1). The background contributions were not fully discriminated against by the interference filter. As would be expected, the size of the OD signal decreases as distance is increased and the peak shifts to later time delays. The appearance profiles show the signal-to-noise achievable using the 10 minute (see previous section) data acquisition window. Given that it is reasonable to assume that there would be no spurious sources of OD in the chamber, these profiles are confirmation of reaction taking place at the monolayer surface.

Ideally, perdeuterated SAMs might have been used throughout but the cost of the isotopically labelled thiols required was prohibitive. Therefore, appearance profiles were subsequently measured for C_6H_{13}-SAMs and $C_{18}H_{36}$-SAMs with OH detection. The same stringent experimental time constraints were used as for the OD measurements. It can therefore reasonably be assumed that the OH signals do originate from the monolayer rather than any secondary contaminant that appears to opportunistically adsorb to the damaged surface. OH appearance profiles were measured on the $Q_1(1)$ and $R_1(5)$ transitions of the OH A-X (1,0) band and are shown in figure 4.9. The profiles are averages of approximately twelve individual scans from 4 individual SAM samples per rotational line. Great care was taken to ensure the probe laser-surface distance was constant for each measurement. There were no perceptible differences in overall OH yield from either chain length (the profiles recorded on a given rotational line have not been re-normalised with respect to each other) indicating that the SAM surfaces appear similar to the incoming $O(^3P)$ atoms regardless of their depth. The $R_1(5)$ profiles appear to peak slightly earlier than the $Q_1(1)$ profiles. However, these differences are marginally significant within the signal-to-noise ratio.

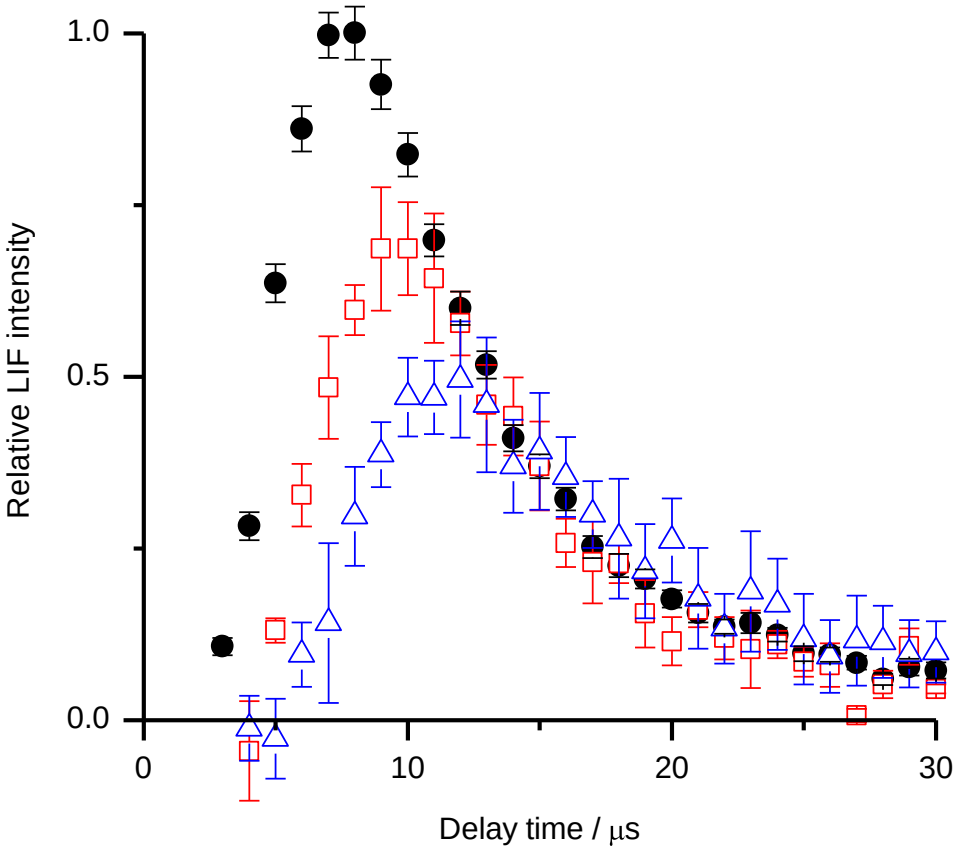

Figure 4.8: Measured appearance of the OD *A*-*X* (1,0) $Q_1(1)$ LIF signal as a function of photolysis-probe laser time delay from a C_6D_{13}-SAM. Nominal probe laser-surface distance of 4 mm (black closed circles), 5 mm (red open squares) and 6 mm (blue open triangles). $p(NO_2)$ ~ 1 mTorr.

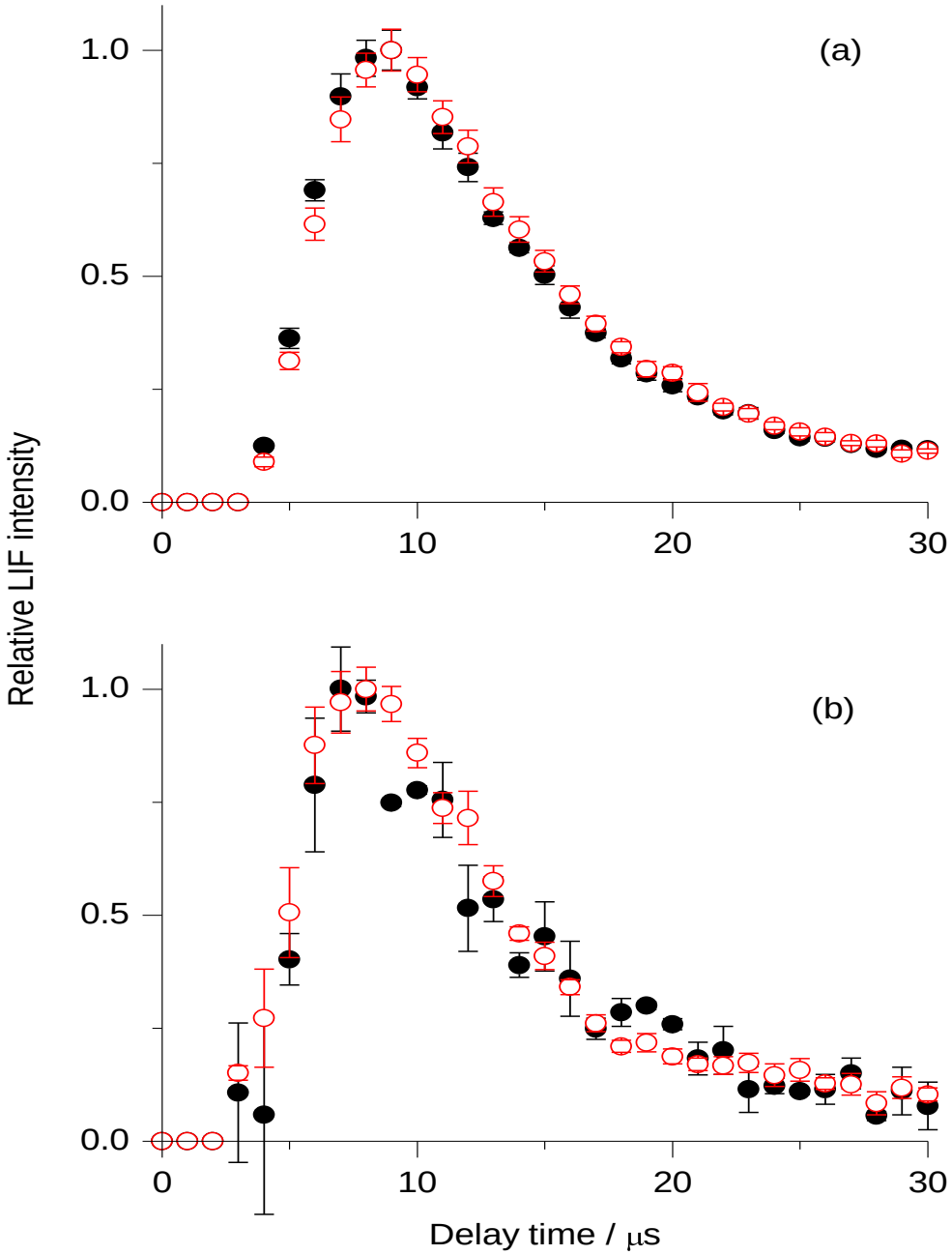

Figure 4.9: Measured appearance of OH (v' = 0), recorded on the (a) $Q_1(1)$ and (b) $R_1(5)$ transitions of the *A*-*X* (1,0) band from a C_6H_{13}-SAM (black filled circles) and a $C_{18}H_{36}$-SAM (red open circles). The relative signal heights from the two SAM types are shown as measured and have not been separately normalised. Probe laser-SAM distance = 4 mm; $p(NO_2)$ ~1 mTorr.

4.3.3 Rotational distribution of the OH/OD reaction products

The 10 minute data acquisition window made the recording of excitation spectra more problematic than for the ionic liquids in chapter 3 (section 3.3.3). As a result individual spectroscopic branches were recorded separately. The limited NO_2 exposure time allowed for either the R_1 bandhead or Q_1 (up to $N' = 5$) branch to be recorded, at 20 laser shots per point. Several individual partial spectra were recorded for C_6D_{13}-, C_6H_{13}- and $C_{18}D_{37}$-SAMs. Representative spectra are shown in figure 4.10. As was described in chapter 2 (section 2.8.2), a thermal calibration spectrum was acquired to account for any saturation, detection sensitivity or energy variation with probe laser wavelength. Ideally the thermal spectra would have been recorded alongside the nascent spectrum by adjusting the data acquisition software to record two photolysis-probe laser time delays simultaneously. In practise this was not possible as it would have doubled the acquisition time. The thermal spectra were therefore recorded immediately after the nascent spectrum but with the addition of 0.5 Torr of N_2 to the chamber. The thermal spectra were recorded at a 10 μs photolysis-probe laser delay time. Assuming a typical gas-kinetic collision rate of 10^7 $Torr^{-1}s^{-1}$, this would result in OH having undergone approximately 50 collisions.

The populations from the nascent and thermal spectra were extracted from the partial spectra using LIFBASE[145]. The relative thermal populations for each N' (from the measured thermal spectra) were compared to those in the known 300 K statistical distribution (conveniently generated from LIFBASE[145]) simulation. The resulting ratio was a calibration factor which could be applied to the populations for each N' from the measured nascent spectrum. Typical calibration factors were in the range 0.8-1.1, showing that the measured distribution did not, in practice, vary substantially from the simulated distribution.

The corrected populations, P, were plotted as Boltzmann plots ($\ln(P/g)$ vs. energy, where g is the degeneracy) and the corresponding rotational temperatures were obtained from the gradient of the linear fit (table 4.1). There is excellent agreement between the two spectroscopic branches measured for the hydrogenated SAMs with rotational temperatures close to thermal in each case. Measurements were made only on the Q_1 branch for the per-deutero C_6D_{13}-SAM. This was a consequence of the R_1 branch in the OD spectrum being too blended to be analysed reliably. Nevertheless, this single branch gave temperatures that were similar, if perhaps marginally hotter.

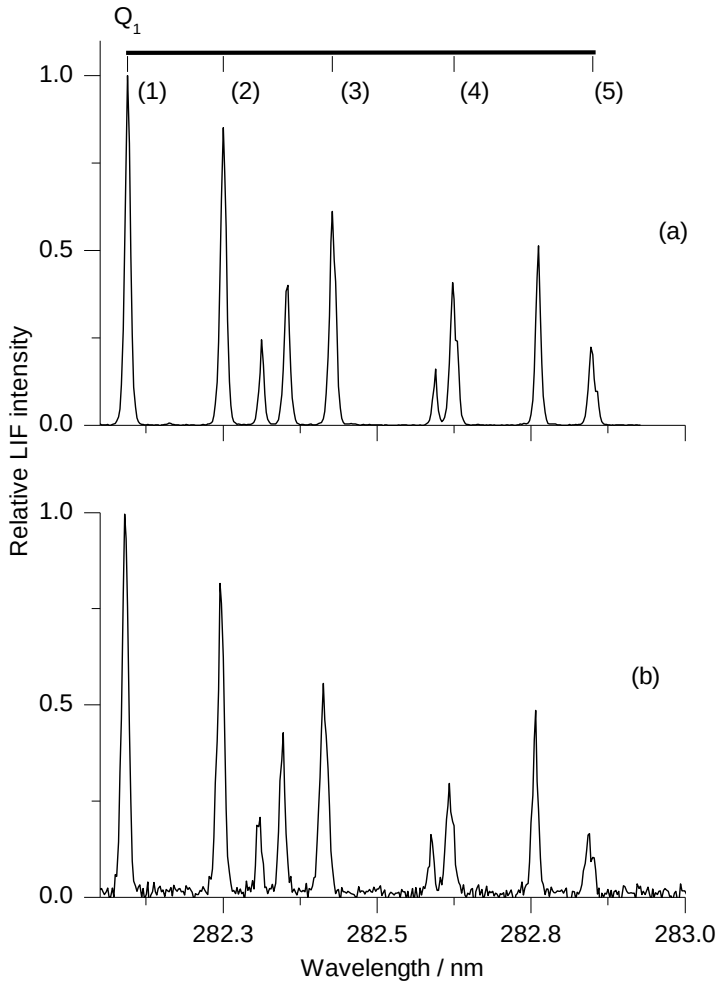

Figure 4.10: Representative OH *A*-*X* (1,0) excitation spectra. (a) Thermal spectrum recorded at a photolysis-probe laser delay of 10 μs, $p(NO_2)$ ~ 1 mTorr and $p(N_2)$ ~ 0.5 Torr. Q_1-branch line positions are indicated. (b) Nascent spectrum recorded at a photolysis-probe laser delay of 8 μs, probe laser-SAM (C_6H_{13}-SAM) distance = 4 mm $p(NO_2)$ ~ 1 mTorr.

$T_{rotation}$/K	C_6D_{13}-SAM	C_6H_{13}-SAM	$C_{18}H_{37}$-SAM
Q_1 branch average	—	283±5	286±2
R_1 branch average	320±8	280±4	287±7
weighted average	320±8	281±3K	286±4

Table 4.1: Rotational temperatures of nascent OH/OD (v' = 0), formed by reaction of O(^{3}P) atoms and perdeuterated and hydrogenated alkylthiol SAMs, measured at a photolysis-probe laser time delay of 8 μs. $T_{surface}$ ~298 K; Probe laser-SAM distance = 4 mm; $p(NO_2)$ ~ 1 mTorr.

4.3.4 Stability of SAMs towards NO_2 – SAM chain length dependence

In section 4.3.1, it was shown that that the C_6D_{13}-SAMs were unstable in the presence of NO_2. This was initially assumed to be the case for all chain lengths and both deuterated and hydrogenated samples. Following the initial experiments described above, a series of experiments was designed to investigate the penetration depth of $O(^3P)$ atoms at SAM surfaces (section 4.3.5). The first set of such experiments with the $C_{12}D_{25}$-SAMs revealed that the OD signal was, in fact, much more stable with respect to NO_2 exposure than the C_6D_{13}-SAM.

This conclusion was reached following the measurement of OD appearance profiles from the C_6D_{13}- and $C_{12}D_{25}$-SAMs as a function of NO_2 exposure time. The peak OD signal height was plotted as a function of NO_2 exposure time as shown in figure 4.11. The profiles show that for the $C_{12}D_{25}$-SAMs the OD signal is approximately stable for around 60 minutes. It then decays much more slowly than was observed for the shorter C_6- chain length. This was repeated several times for each SAM and the error bars at each point reflect the variation in the peak height of an appearance profile at a particular NO_2 exposure time.

The C_6D_{13}-SAM and $C_{12}D_{25}$-SAM surfaces were analysed by STM[135] following 10 minutes of NO_2 precursor exposure as had also been done previously (section 4.3.1). In contrast to the initial set of measurements for C_6D_{13}-SAMs, figure 4.7 (c) and (d), the C_6D_{13}-SAMs on this occasion showed some damage after only 10 minutes of exposure (figure 4.12). The low resolution, large image (figure 4.12 (a)) shows the characteristic Au vacancy islands indicative of full monolayer coverage (although they are low in density). On closer inspection however, the high resolution image reveals the presence of sub-monolayer coverage, illustrated by the striped features which are consistent with flat-lying molecules. The striped phase is particularly evident in the Fourier transform of the high resolution image (figure 4.12 (a)) where the hexagonal packing arrangement of the alkyl chains (characteristic of the full standing-up phase), is no longer present.

The $C_{12}D_{25}$-SAMs were found, in contrast, to be much more resilient. STM images of several independent samples having undergone NO_2 exposure were measured and each showed no signs of structural degradation (figure 4.12 (b)). The characteristic hexagonal packing of a high density SAM was always present.

The C_6D_{13}-SAMs have therefore proven to be unpredictable in terms of the amount of damage sustained within the 10-minute window; some samples appear undamaged (figure 4.7) while others are damaged (figure 4.12) on this timescale. This reflects the sudden onset of the destruction as shown in figure 4.11; some samples will inevitably be damaged earlier and others later. This is presumably a result of the extent to which the NO_2 pressure can be controlled. As a consequence it is clear that data collected from the long-chained SAMs are more reproducible than those from the short-chained SAMs. However, within the 10-minute window, providing sufficient independent measurements were made, the short chained C_6D_{13}-SAMs and C_6H_{13}-SAMs provided sufficiently reproducible data. In the majority of subsequent work on this system, the C_{12}-SAMs were used but the 10-minute window was maintained, to ensure the reactions were taking place at pristine SAM surfaces, unaffected by degradation or contamination.

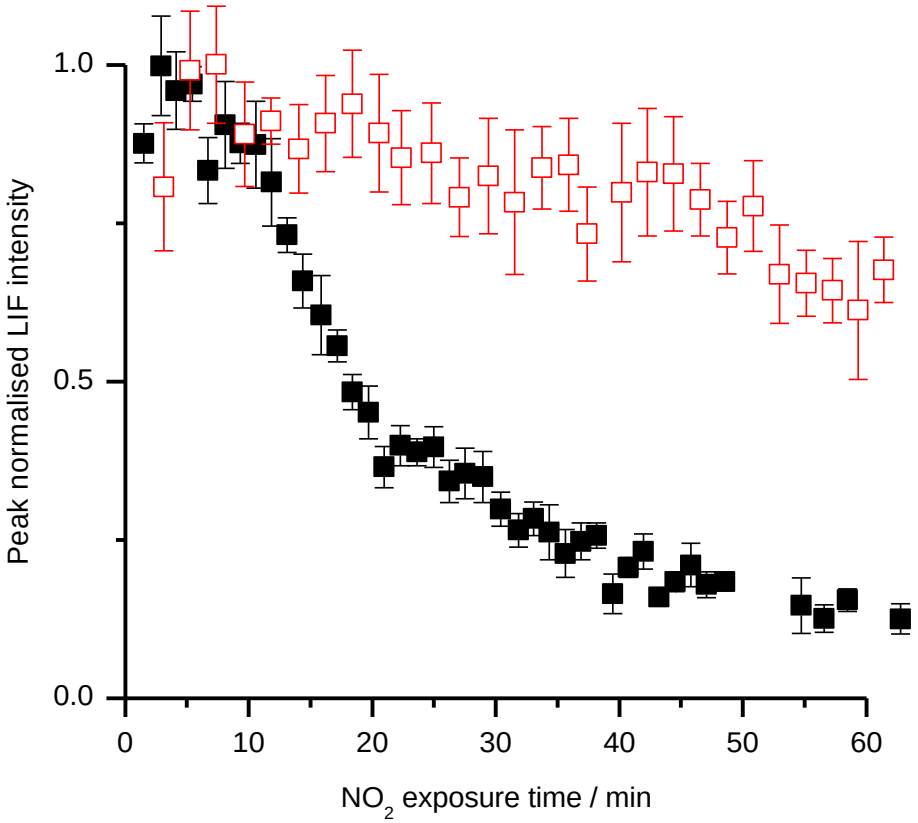

Figure 4.11: OD *A*-*X* (1,0) $Q_1(1)$ LIF signal decay as a function of exposure time to NO_2 (1 mTorr) from C_6D_{13}- (black filled squares) and $C_{12}D_{25}$-SAMs (red open squares). All traces have been normalised to their values at early times. $T_{surface}$ ~298 K; Probe laser-SAM distance = 4 mm.

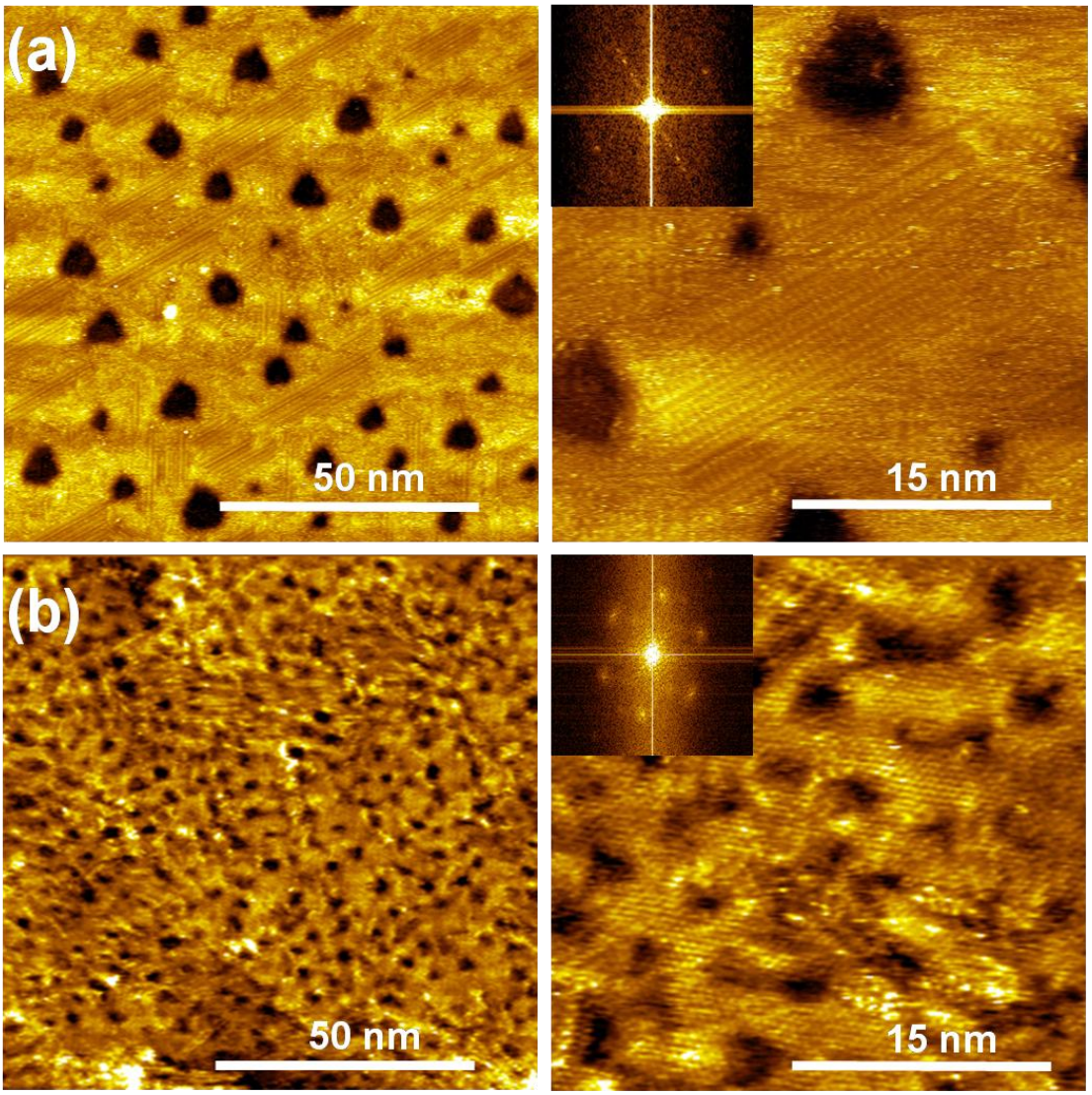

Figure 4.12: Low (left) and high (right) resolution STM images of thioalkyl SAMs of chain length (a) C_6 and (b) C_{12} following 10 min NO_2 exposure (1 mTorr). Insets are fast Fourier transforms of the high-resolution images, showing typical hexagonal packing for the C_{12} sample but a lack of symmetry indicative of partial destruction for the C_6 SAM.

4.3.5 OD detection - penetration depth of $O(^3P)$ atoms at dodecyl alkylthiol-SAM surfaces

The aim here was to investigate to what depth $O(^3P)$ atoms were able to abstract a hydrogen atom along a hydrocarbon chain and emerge as OH (or OD) without reacting further to form water. To achieve this, a series of isotopically labelled (deuterium) SAM surfaces were required. Fully-deuterated $C_6D_{13}SH$ and $C_{12}D_{25}SH$ thiols were purchased commercially (Cambridge Isotopes) while the partially-deuterated $CD_3(CH_2)_{11}SH$ and $CD_3CD_2(CH_2)_{10}SH$ thiols were custom-synthesised by a collaborator at Heriot-Watt University[208]. The structural integrity of the SAMs produced from the custom-synthesised thiols was established by LIF and STM measurements as described above for the C_6D_{13}-SAMs and the $C_{12}D_{25}$-SAMs. The dependence of the LIF signal height on NO_2 exposure time for the $CD_3CD_2(CH_2)_{10}$-SAM was measured and is shown alongside the previously presented (figure 4.11) data for the C_6- and $C_{12}D_{25}$-SAM in figure 4.13. The OD signals at short times from each of the SAMs has been normalised to aid comparison between the systems. It is clear that the partially deuterated $CD_3CD_2(CH_2)_{10}$-SAM behaves in an identical manner to the fully deuterated C_{12} analogue and is more stable than the shorter-chained SAM. The STM images of the $CD_3CD_2(CH_2)_{10}$-SAM were also indistinguishable from their fully-deuterated equivalents.

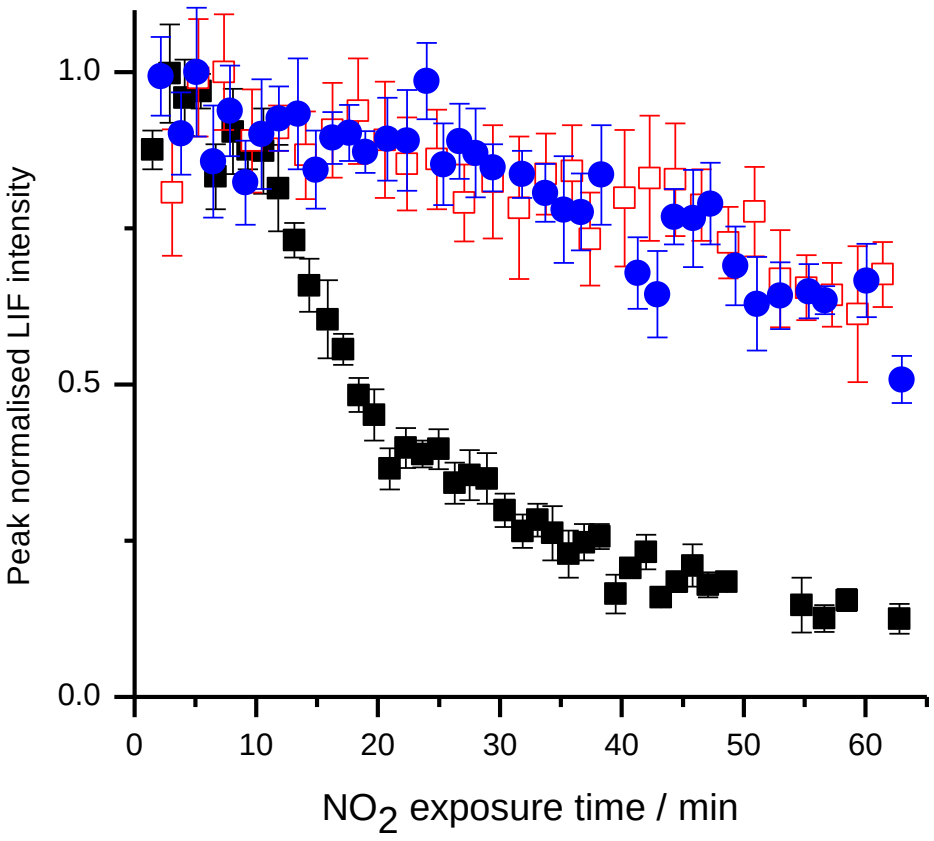

Figure 4.13: OD *A*-*X* (1,0) $Q_1(1)$ LIF signal decay as a function of exposure time to NO_2 (1 mTorr) from C_6D_{13}- (black filled squares), $C_{12}D_{25}$- (red open squares) and $CD_3CD_2(CH_2)_{10}$-SAMs (blue closed circles). All traces have been normalised to their values at early times. $T_{surface}$ ~298 K; Probe laser-SAM distance = 4 mm.

The conceptual basis of the experiment is shown in figure 4.14. By comparing the relative OD yield from a series of fully- and partially deuterated SAM surfaces, the penetration depth for hydrogen (or deuterium) abstraction at SAM surfaces could be established. As figure 4.14 shows, the convention for labelling of the carbon atoms in these systems begins with the terminal carbon at the air−monolayer interface being C_1. The chain is then labelled sequentially *down* the alkyl chain towards the sulphur atom. The OD yield from each of the fully- and partially deuterated samples was measured by fixing the photolysis-probe laser delay to that consistent with maximum signal height for a given SAM-laser distance (11 μs for 5 mm) and scanning the probe laser wavelength across the $Q_1(1)$ transition of the OD *A*-*X* (1,0) band. In practice this could have been carried out at any time delay and any transition as long as the conditions were identical for each SAM sample. The $Q_1(1)$ transition was the most intense signal in the

excitation spectrum so it was an obvious choice to achieve maximum signal-to-noise. The area under the resulting spectral line is proportional to the amount of OD (or OH in an equivalent experiment) present. The rotational distribution (and therefore fraction of the total population in a given *N'*) has been shown to be independent of alkyl chain length (section 4.3.3). This is, therefore, a suitable method for comparing the relative overall OD yields from each of the SAMs.

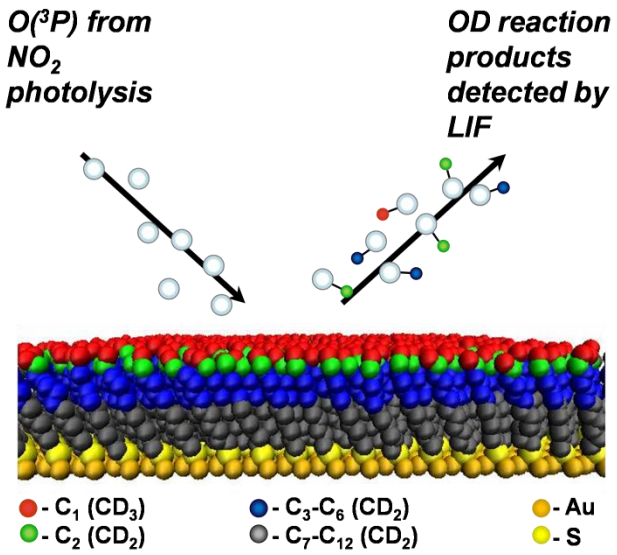

Figure 4.14: Schematic representation of the use of isotopic labelling to determine the penetration depth of O(^{3}P) atoms at SAM surfaces.

The resultant OD spectra are shown in figure 4.15. Three individual measurements were recorded per sample (within the 10-minute window). This was independently repeated four times per SAM type. The profiles shown are therefore the average of 12 individual scans. The order in which the different SAMs were measured was also scrambled to ensure that any trends detected were true representations of differences in reactivity. The absolute signal size from the C_6D_{13}-SAM was the same (within the associated errors) as that from the $C_{12}D_{25}$-SAM. This is a corroboration of what was observed in section 4.3.2 for fully-hydrogenated SAMs where the reactivity was found to be independent of alkyl chain length in the range C_6 to C_{18}.

The reactivity from the first carbon C_1, was measured directly using the OD yield from the $CD_3(CH_2)_{11}$-SAM. The C_1 position is the only methyl (CH_3) environment and therefore reactivity at this site provides information on the reactivity of O(^{3}P) towards methyl groups at this collision energy. The contribution from C_7-C_{12} is quantified using the difference in OD yield between the C_6- and C_{12}- fully deuterated SAMs. This difference was negligible. The signal intensity from the C_6- SAM is actually marginally

larger than the C_{12}-SAM. As a result, an upper limit on the C_7-C_{12} reactivity was established using the relative uncertainties in the C_6- and C_{12}- measurements. The contribution from C_2 corresponds to the difference in the relative yields from the $CD_3(CH_2)_{11}$-SAM and the $CD_3CD_2(CH_2)_{10}$-SAM. The C_3-C_6 contribution is derived from the difference between the $CD_3CD_2(CH_2)_{10}$-SAM and $C_{12}D_{25}$-SAM. The final contributions to OD yield from each carbon along the alkyl chain are provided in table 4.2 along with those from the conceptually similar measurements made by Jacobs and co-workers[88-90] introduced in chapter 1 (section 1.3.4).

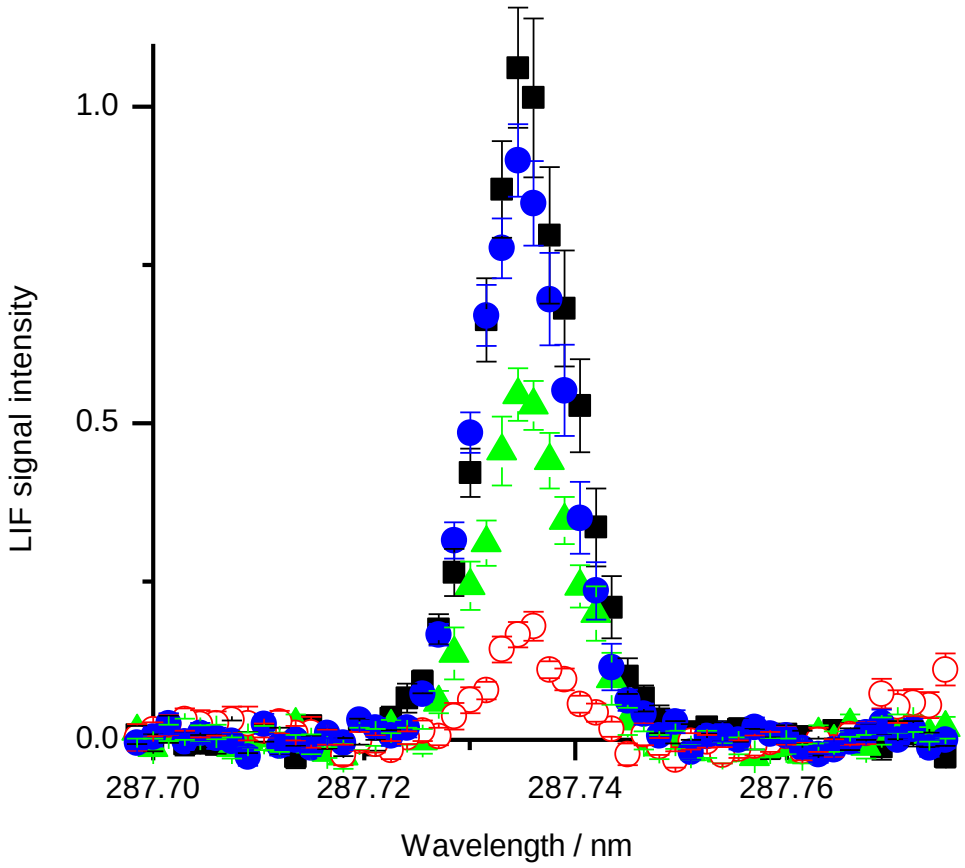

Figure 4.15: Early exposure (NO_2 < 10 min) OD *A*-*X* (1,0) $Q_1(1)$ LIF signals from $O(^3P)$ and a C_6D_{13}-(black filled squares), $C_{12}D_{25}$-(blue closed circles), $CD_3CD_2(CH_2)_{10}$-(green closed triangles) and $CD_3(CH_2)_{11}$-SAMs (red open circles). $T_{surface}$ ~298 K; Probe laser-SAM distance = 5 mm.

Carbon[a]	Contribution to OD detected	
	this work[b]	Jacobs[c]
C_1	(16 ± 3) %	>75%
C_2	(42 ± 5) %	~20%
C_3-C_6	(42 ± 4) %	<2.5%[d]
C_6-C_{12}	<4 %[e]	-

Table 4.2: OD production from different sites in dodecyl SAMs. [a] Numbered from terminal CD_3 group. [b] 2σ uncertainties from repeated measurements. [c] On the basis of OD^- anion yield as reported in reference[88]. [d] C_3 only. [e] Upper bound based on uncertainties in the difference between the C_6D_{13}- and $C_{12}D_{25}$- SAM signals.

4.3.6 OH detection - reactivity comparison between alkylthiol SAMs and the liquid hydrocarbon squalane

In theory, the reverse measurement to that described in section 4.3.5 with detection of the OH reaction products should yield the same penetration-depth information on the contribution from each carbon along the chain. This was attempted by recording the relative signal sizes of the $Q_1(1)$ transition of the OH A-X (1,0) band from the $C_{12}D_{25}$-, $CD_3(CH_2)_{11}$- and $CD_3CD_2(CH_2)_{10}$-SAM surfaces.

Figure 4.16 shows that the OH signal detected from the $CD_3CD_2(CH_2)_{10}$-SAM is consistently smaller than that from the $CD_3(CH_2)_{11}$-SAM as would be expected. This is in qualitative agreement with the OD measurements in section 4.3.5. The magnitude of the difference is also reassuringly close to that for OD. The ratio of the integrals of the curves in figure 4.15 for the $CD_3CD_2(CH_2)_{10}$-SAM and the $CD_3(CH_2)_{11}$-SAM gives a contribution from C_2 of ~47% compared to 42 ± 5% in the OD measurements. Despite this apparent consistency, a more major discrepancy was observed when looking at the OH detected from a fully-hydrogenated $C_{12}H_{25}$-SAM. As shown in figure 4.16, the overall signal height from the $C_{12}H_{25}$-SAM was consistently smaller than that from the $CD_3(CH_2)_{11}$-SAM.

Three independent measurements were made and the same trend was observed on each occasion. Time and experimental constraints, in addition to the knowledge that the OH measurements were less accurate than the OD measurements resulted in no further

investigation into this anomaly. It was also found that there was a contribution from OH at the fully deuterated $C_{12}D_{25}$-SAM surface. This is similar to the problem in section 4.3.1 where small OH signals were observed from a variety of surfaces. This spurious OH is presumably underlying every OH measurement and speculatively it could come from a variety of sources such as the mica border surrounding the SAM (0.5 mm), or the stainless steel holder on which the SAM is held. The source of the OH is unclear and experimental adaptations (such as the use of hydrocarbon traps and a turbomolecular pump (chapter 2, section 2.4)) aimed at reducing it were unsuccessful, this highlights the benefit of the isotopic labelling and OD detection.

Regardless of the difficulties associated with the detection of OH, it was still interesting to attempt to roughly quantify the difference in reactivity between the SAM surfaces and liquid hydrocarbon squalane studied extensively by McKendrick and co-workers previously[63,66-69,124]. The SAM surface was removed from the vacuum chamber and replaced with the liquid wheel assembly described in chapters 2 (section 2.3) and 3. The bath was filled with squalane and set at a 5 mm surface-laser distance to replicate the SAMs experiments. The liquid wheel and SAM surfaces have similar surface areas (8×10^{-4} m^2 and 6×10^{-4} m^2 respectively) although Monte Carlo simulations (chapter 2, section 2.8.3) suggest that the laser beam diameters and angular distribution of the $O(^3P)$ atoms have more influence than target size on the amount of OH products detected. Both of these were equivalent in the SAMs and liquid experiments.

The signal intensity from the liquid hydrocarbon squalane was found to be 4.5 times larger than that from the $C_{12}H_{25}$-SAM and 3 times larger than that from the $CD_3(CH_2)_{11}$-SAM. Despite the problems associated with the OH measurement from the SAM surfaces, this, at least approximately, provides information on the relative reactivity of the two systems. Spurious OH is not regarded as being an issue from the liquid experiments as the rotation of the wheel leads to a continually refreshed liquid surface and the entire surface is covered in squalane during the experiments. In all cases the OH detected from the liquid surface is in excess of that from any of the SAM surfaces by as quantified in section 4.4.3.

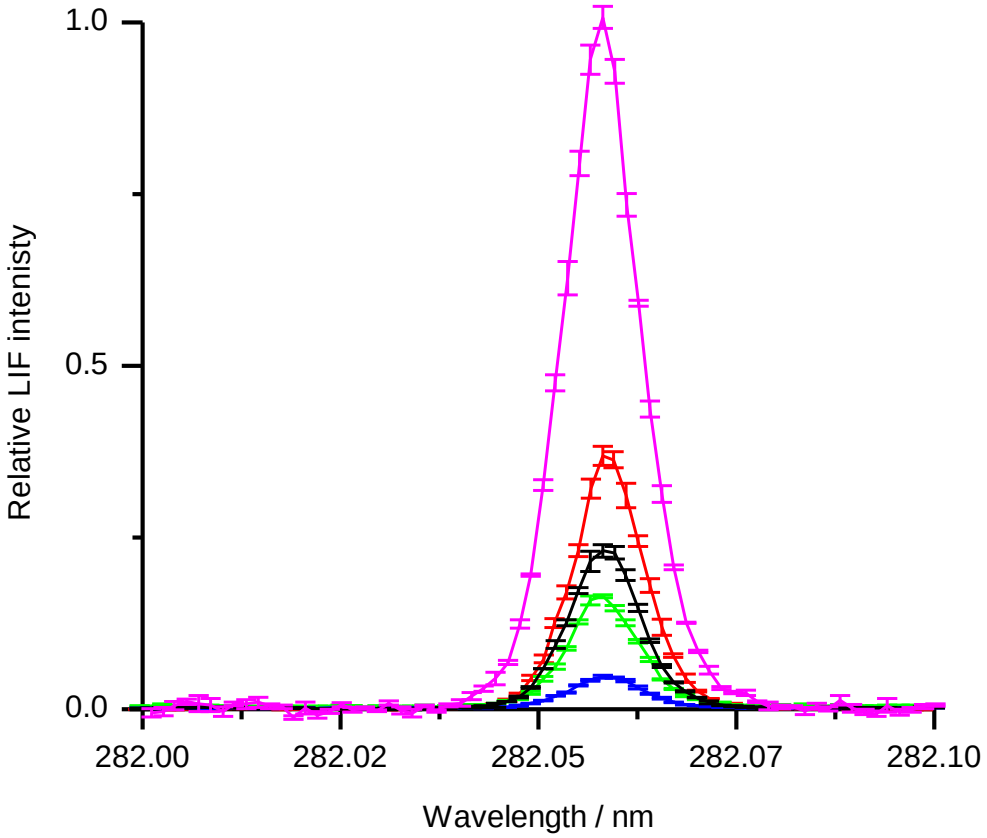

Figure 4.16: Early exposure (NO_2<10 min) OH *A*-*X* (1,0) $Q_1(1)$ LIF signals from $O(^3P)$ and a $C_{12}D_{25}$-(blue line), $CD_3CD_2(CH_2)_{10}$-(green line), $CD_3(CH_2)_{11}$-(red line), $C_{12}H_{25}$-SAM (black line) and squalane (magenta line) surface. $T_{surface}$ ~298 K; Probe laser-SAM distance = 5 mm.

4.4 Discussion

4.4.1 SAM structural integrity

In comparison to the closely related experiments carried out at the gas-liquid interface by McKendrick and co-workers[63,66-69,124], reactive studies at the gas—SAM interface are subject to additional experimental challenges. A major contributor to this is the inability to continually refresh the surface. As a consequence, the structural integrity of the SAMs during the experiments was a major concern. As described in sections 4.3.1 and 4.3.4, this was established by a combination of LIF, XPS and STM measurements. The STM imaging revealed that the SAM preparation methods used were sufficient to reproducibly form SAMs with full monolayer coverage. The XPS measurements showed that the SAMs were unaffected by their being held in a vacuum chamber (figure 4.5 (a)) for prolonged periods but that exposure to NO_2 caused damage to the monolayers (figure 4.5 (b)). This was echoed and quantified in the LIF measurements (figure 4.6 (a) and (b)), where the OD decay (and related OH growth) was measured from a series of SAMs of different chain lengths. On the basis of this, NO_2 exposure times and data acquisition was limited to 10 minutes for all samples to ensure their structural integrity.

Previous studies have shown that atomic oxygen or ozone in ambient air[193,194] can damage SAMs but this is the first identification that NO_2 is also capable of causing damage. The STM results support the conclusion from the OD LIF decays (figure 4.6 (b), figure 4.11 and figure 4.13), that the mechanism for SAM destruction is stripping of the surface by detachment of entire chains through breaking of the Au-S bond. The STM images show that NO_2 exposure leads to a reduction in monolayer coverage and the striped features (figures 4.7 (f) and 4.12 (a)) observed in the high resolution images for a C_6-SAM are suggestive of flat lying alkyl chains. The 'stripping' process has been found to be more facile for shorter chains (C_6-SAMs) which may be the result of the NO_2 having a higher probability of reaching the substrate in the C_6-SAMs.

The LIF decays (figures 4.6 (b) and 4.13) may also show subtle evidence for this stripping mechanism. The OD signal height from the C_6D_{13}-SAM, although approximately stable over the 10 minute NO_2 exposure time, increased slightly over the first few minutes. This was a consistent feature and is therefore unlikely to be the result

of experimental variables such as precursor pressure. It could be argued that as the monolayer coverage initially decreases, the remaining alkyl chains begin to collapse towards lying flat on the surface. This would presumably result in an increase in OD yield initially, as the 'shielding' by the less reactive primary groups is reduced. Further stripping of the chains would ultimately result in a reduction of OD yield as the number of available reaction sites decreases as was observed in the LIF decays (figures 4.6 (b) and 4.13).

Fairbrother and co-workers[84], when investigating the reaction of thermal $O(^3P)$ with C_{12}- and C_{16}- SAMs, proposed a destruction mechanism where the carbon atoms were etched sequentially from the gas—SAM interface. The extent of this damage was particularly obvious after ~100 minutes of exposure at 6×10^{-7} Torr. The overall $O(^3P)$ exposures in the two experiments will be different and are difficult to quantify. Fairbrother and co-workers had a constant source of $O(^3P)$ atoms operating at a lower pressure (6×10^{-7} Torr vs. 1×10^{-3} Torr). The work presented here was carried out using a pulsed source operating at 10 Hz. As a result the surface would be exposed to $O(^3P)$ atoms for much less of the exposure time quoted but the overall pressure was higher. The exposure would also be dependent on the NO_2 quantum yield, the laser fluence, the geometry of the beam relative to the surface and the expansion of the photodissociation products following the laser pulse.

Nevertheless, this etching mechanism was presumed not to be an issue as figure 4.13 shows minimal change in the OD signal height (for C_{12}-SAMs) over the timescales of the experiment. This would not be the case if significant carbon chain erosion was taking place. The stripping of the alkyl chains found in this work as opposed to the sequential loss of carbon observed by Fairbrother supports the proposition that it is the NO_2 causing any structural damage here, rather than $O(^3P)$. The results show that valuable and reproducible data can be acquired by limiting NO_2 exposure, using longer chain lengths where possible and using multiple techniques to ensure that the structural integrity of the surfaces is maintained.

4.4.2 Reaction mechanism

These results provide the first direct experimental evidence that alkylthiol-SAM layers undergo elementary hydrogen abstraction reactions with superthermal ground state O(^{3}P) atoms to produce OH (or OD) radicals. To probe the mechanistic details of this reaction, Monte Carlo simulations similar to those used previously by McKendrick and co-workers[66,67] have been carried out for both limiting mechanisms: *direct*; and *thermal* (trapping desorption), to model the shapes of the appearance profiles observed in the experiment. The simulation procedure was carried out as described in chapter 2, section 2.8.3, with the modification of the target shape to match the SAM surface rather than that of the wheel.

The thermal simulation is shown alongside the experimental OH appearance profiles from the $C_{18}H_{37}$-SAM and liquid hydrocarbon squalane surfaces in figure 4.17. The speed scale shown was generated by adapting the simulation code[147] to provide as an output the corresponding Maxwell-Boltzmann speed of the OH products at a given delay. The mean speed for thermal OH leaving the surface would be ~600 m s^{-1}, peaking at a time delay of 13 μs. The experimental appearance profiles from the $C_{18}H_{37}$-SAM peak at a photolysis-probe laser time delay of 9 μs. This shows that the majority of the OH molecules produced are travelling too fast to have been thermalised at the surface, i.e., to have undergone a TD-type reaction mechanism, and therefore are predominantly direct reaction products. Those detected at the very earliest time delays must, by definition, have undergone a direct mechanism. There are however, OH products travelling at speeds consistent with OH having undergone a thermal (TD) mechanism.

The direct simulation much more closely reproduces the shape of the profiles, particularly at the rising edge as is shown in figure 4.18(a). A χ^2-minimising fitting routine was used to fit the observed appearance profiles to a weighted sum of the simulated profiles. The resulting fits are shown alongside the correctly weighted direct and thermal contributions in figure 4.18 (a) and (b) for the $C_{18}H_{37}$-SAMs (OH detection) and $C_{12}D_{25}$-SAMs (OD detection) respectively. Note that the profiles for the $C_{18}H_{37}$-SAM were measured at a photolysis-probe laser distance of 4 mm but those for the $C_{12}D_{25}$-SAMs at 6 mm.

The corresponding direct:thermal ratio was found to be 0.86:14 for the $C_{18}H_{37}$-SAMs and 0.87:13 for the $C_{12}D_{25}$-SAMs. This reveals that the shapes of the appearance profiles are essentially identical for OH and OD detection, and also illustrates the accuracy with which the direct simulation replicates the rising edge of the profiles at a range of distances. Comparable experiments of Ne (collision energy ~60 kJ mol^{-1}) scattering from alkylthiol SAMs have been found to have a larger Boltzmann-type thermal contribution (~40%)[43]. However, unlike for Ne, the OH products in this case are also reactive. As a result, some of the trapped (slow) OH will presumably react further to form water, resulting in a comparatively small thermal fraction of OH escaping.

This analysis was also applied to the squalane profiles also and the ratio in that case was found to be 0.83:17, reflecting the fact that the profiles from squalane are noticeably broader and therefore require a slightly larger thermal component. As was discussed in chapter 1, the binary separation into direct and thermal components is an oversimplification, but this nevertheless shows that the appearance profiles can be reasonably well approximated by the sum of the two limiting distributions. The breadth of the squalane signals compared to that from the SAMs may reflect the enhanced roughness of liquid surfaces compared to SAMs; with rougher surfaces promoting multiple collisions and leading to enhanced accommodation. This is in agreement with scattering studies of Ne from liquid[9] and SAM[32] surfaces, where the fraction of atoms assigned to the TD channel (or the fraction of slow Ne atoms) was higher in the liquid than the SAMs.

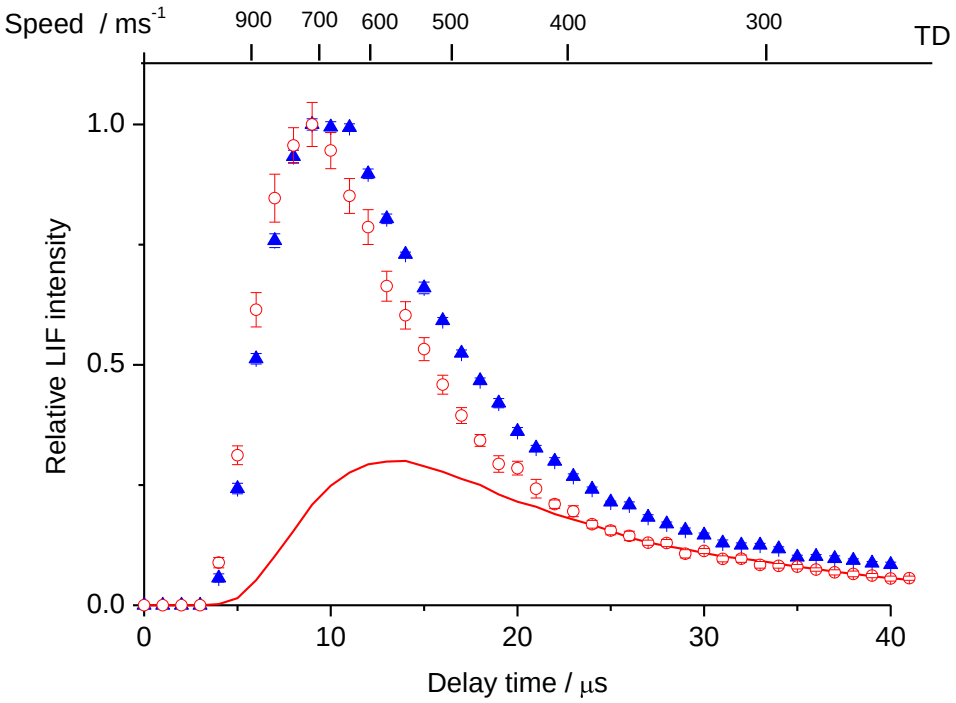

Figure 4.17: Peak normalised appearance profiles of OH (v' = 0), recorded on the $Q_1(1)$ transition of the *A*-*X* (1,0) band from a $C_{18}H_{37}$-SAM (red open circles) and liquid squalane (blue filled triangles). Background signals due to the probe and photolysis lasers have been subtracted. Probe laser-surface distance = 4 mm; pNO$_2$ ~1 mTorr. Superimposed is the MC simulation of a 300 K thermal component from a SAM.

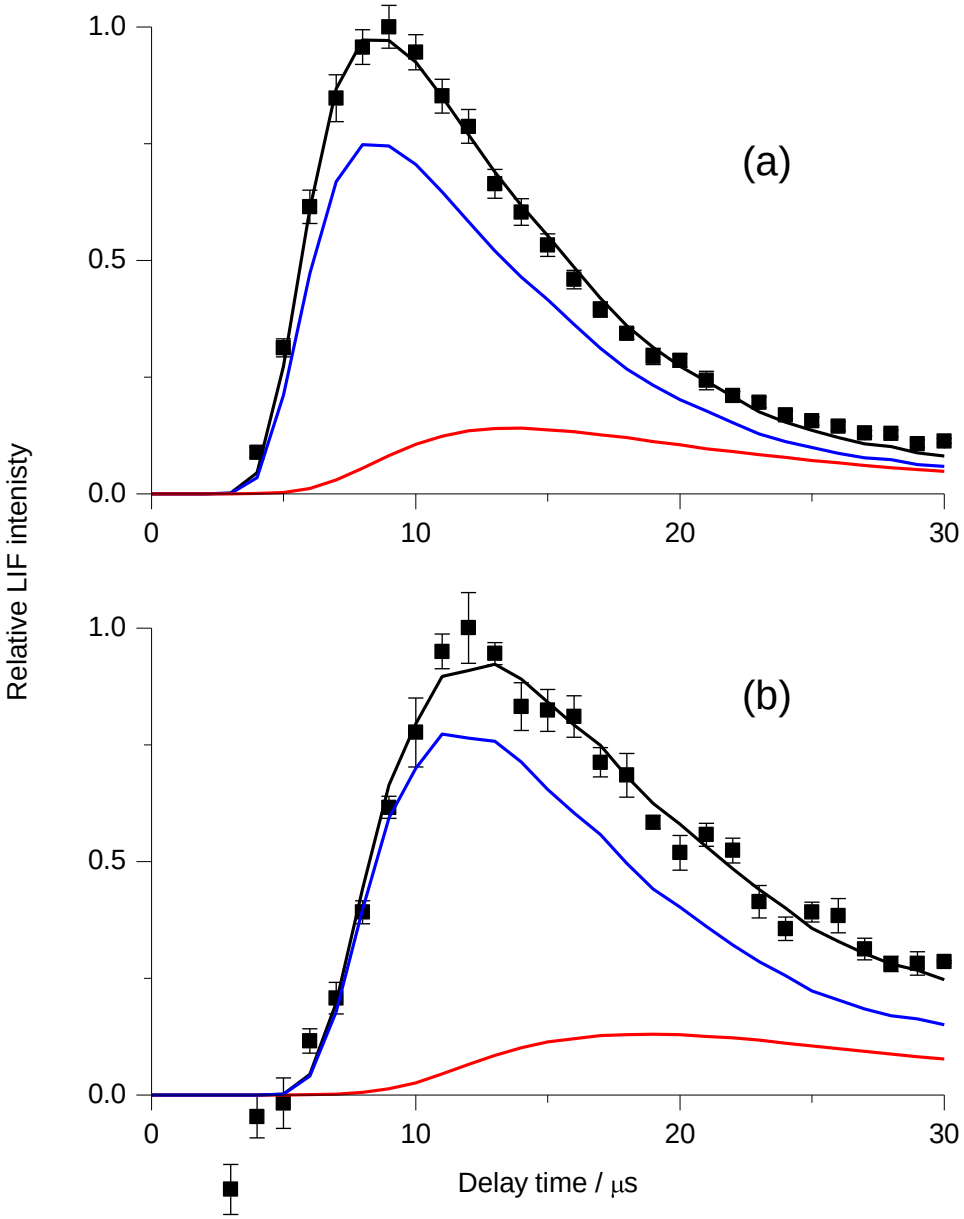

Figure 4.18: Peak normalised appearance profiles of OH/OD (v' = 0) recorded on the $Q_1(1)$ transition of the *A*-*X* (1,0) band from an (a) $C_{18}H_{37}$-SAM and (b) $C_{12}D_{25}$-SAM (black filled squares). Background signals due to the probe and photolysis lasers have been subtracted. Probe laser-surface distance (a) = 4 mm and (b) = 6 mm; pNO$_2$ ~1 mTorr. Superimposed is the MC simulation of a direct (blue line) and 300 K thermal component (red line) and from a SAM and the corresponding χ^2-minimising weighted fits to the experimental data (black line).

The translational distributions indicated that the OH/OD reaction products are predominantly products of direct abstraction reactions and as such emerge on average with superthermal speeds. The rotational temperatures provided in section 4.3.3 (table 4.1) were recorded at time delays corresponding to the peak of the appearance profiles and should therefore reflect a similar mechanistic interpretation as any thermal contribution at these time delays should be minor. However, approximately thermal rotational distributions were observed. This is in contrast to what has previously been observed in gas-phase[47,51] and gas-liquid studies[66-69] of O(^{3}P) and hydrocarbons.

The closely related work of McKendrick and co-workers on liquid hydrocarbons revealed a (moderately) superthermal rotational distribution at the peak of the appearance profiles, moving towards thermal as the time delay between the two lasers was increased. Hase and co-workers[209] and Troya and Schatz[112] found in their theoretical scattering simulations that direct reaction would lead to superthermal rotational temperatures, although their simulations were at much higher collision energy (5eV). Also, as was described in the introduction (chapter 1, section 1.4.2) the semi-empirical Hamiltonians used in the calculations have a tendency to over predict the internal energy of the products. The slightly hotter rotational distribution for the OD products (table 4.1) would fit in with this picture (moderately superthermal products). Although given that the OD rotational temperatures are based on fewer independent measurements with larger associated errors, it is difficult to argue that the difference between the measured OH and OD rotational temperatures is statistically meaningful. Previous gas-phase work has shown a similar rotational temperature in OH and OD products[52].

The only evidence that the rotational temperature varies with delay time in this work comes from the appearance profiles in figure 4.9 where the $N' = 5$ ($R_1(5)$) profiles peak slightly before the $N' = 1$ ($Q_1(1)$) profiles. The suggestion that there is a translational-rotational correlation (that the fastest products are also the most rotationally excited) is interesting, and was predicted by Troya and co-workers in their simulations of F atoms reacting at alkylthiol SAMs[132]. The rotational temperatures derived from the spectra shown in figure 4.10, could be subject to an un-quantified systematic error resulting from, for example, the limited 10 minute data acquisition time, or that only five independent lines were used to construct the Boltzmann plots from which the rotational temperatures were derived.

However, it is also possible that the direct reaction with SAMs produces, for some dynamical reason, colder OH than for its gas-phase or gas-liquid counterparts. Possible (cautious, given the limited data available) explanations for this could include, an entrance channel effect, whereby the order of the SAM surface could restrict the geometries through which the O atom reacts, resulting in lower rotational energy release in the OH.

Another possibility is that the apparently cold rotational distribution observed is a consequence of the post-reaction fate of the OH formed at the SAMs surface compared to that from a liquid hydrocarbon. As will be discussed in greater detail in the following section, the majority of the OH products formed by reaction with a SAM *must* originate from within the chain, at least below the terminal methyl group. This would be consistent with more of the *direct* OH from SAMs suffering at least one secondary collision within the chain. These restricted encounters would cause some, but incomplete, moderation of the rotational and translational distribution. This is consistent with the trajectory simulations of inelastic scattering by Hase and co-workers[209], where some of the O atoms that penetrate the surface escape with superthermal velocities. In contrast, the more open structure of squalane allows for more direct attack and subsequent escape of the OH products. This need not be a contradiction of the broader appearance profiles observed from squalane (figure 4.17) as the more open structure of squalane may also allow a higher escape probability (after a few secondary encounters) of these slow OH products. Conversely, from the SAM surfaces, those OH molecules formed deeper in the inter-chain channels of the SAMs, or recoil forward to reach there, could reasonably be expected to undergo more secondary encounters and therefore are more likely to react further to form H_2O and escape detection - apparently suppressing any observed thermal (TD) component; given that the barrier to reaction for OH to form H_2O is relatively low, at 3-10 kJ mol^{-1}[184].

A similar argument could explain the observed differences in the rotational temperatures of OH and OD reaction products formed at SAM surfaces. If, for example, the efficiency of secondary rotational energy loss were to be higher for the lighter rotor (OH) than for the heavier rotor (OD), then the apparent rotational temperature of OD would be higher than that of OH. More exotic possibilities may also exist, the mechanism *directed ejection* observed for Xe at SAM surfaces[31] for example, could generate reaction products with superthermal speeds and thermal rotational distributions; having first been rotationally thermalised before being

repulsively ejected. This was thought to be a consequence of the size of the Xe atoms and was not observed in the smaller, lighter noble gases making it unlikely in the case of OH. Clearly further experimental work and realistic complementary simulations would be needed to resolve the interesting internal state distributions observed in this, the first, quantum state resolved study of reactions at the gas-SAM interface.

4.4.3 How penetrable are alkylthiol self-assembled monolayers?

Using isotopic labelling, the penetration depth of $O(^3P)$ atoms undergoing hydrogen abstraction reactions to form OD products has been established for dodecyl SAMs. There was found to be little if any contribution beyond C_6. This suggests that up to six carbon atoms are involved in the reaction; a conclusion that is also corroborated by the lack of any chain length dependence in the OH detected from C_6- and C_{18}- fully hydrogenated SAMs (section 4.3.2, figure 4.9). The same conclusion was reached by Morris and co-workers investigating the inelastic scattering of Ar atoms from alkylthiol SAMs of varying alkyl chain lengths[36]. Morris found that the dynamics were altered as chain length was increased from 2 to 6 carbon atoms, but were chain length independent beyond C_6.

The $O(^3P)$ translational energy distribution is known to be broad around the average value of 16 kJ mol^{-1} (FWHM =26 kJ mol^{-1})[141] but the extent to which there are sufficiently high energy O atoms to surmount the predicted barrier for abstraction of a primary H atom was unknown. This was previously assumed by McKendrick and co-workers to be a minor contribution to any OH detected. It has been found, in the course of this work that ~17% of the OD detected originates from reaction at the primary C_1 position in alkyl SAMs.

The translational energy distribution for $O(^3P)$ atoms formed by photolysis of NO_2 at 355 nm is shown in figure 4.19. The integrated area between certain energy limits, as a fraction of the total area, represents the fraction of the total distribution within that energy range. Using this simple method, the fraction of $O(^3P)$ atoms which are potentially reactive at secondary sites (above 21 kJ mol^{-1}) was found to be ~40%. Of those, potentially reactive $O(^3P)$ atoms ~17% are above the barrier for abstraction at a primary site. This is obviously a simple treatment, neglecting the excitation function (i.e. reactivity as a function of collision energy). Although this appears to be a significant contribution, an important consideration is that, in this work, the primary C_1

position is the most probable position an O atom will strike. This will be explored in more detail below through comparison with independent trajectory calculations, but the qualitative conclusion is that the reactivity at the terminal group is therefore clearly suppressed by energetic constraints.

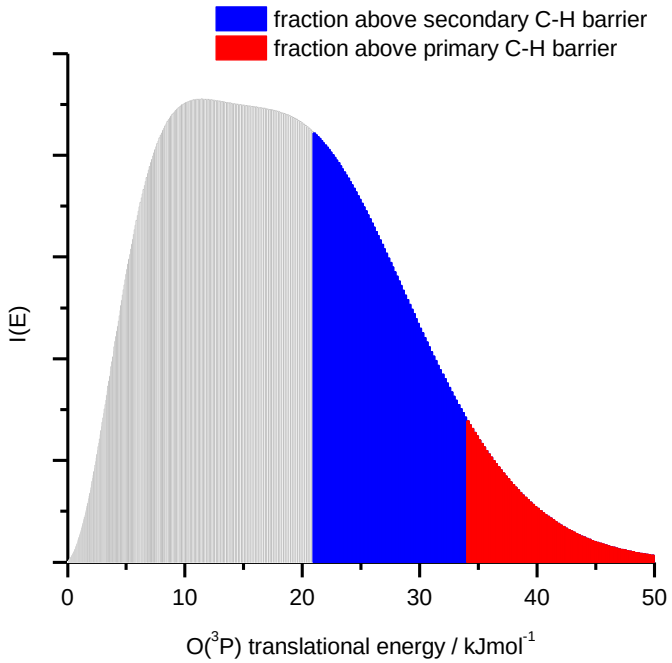

Figure 4.19: O(^{3}P) speed distribution from NO_2 photolysis at 355 nm[141] with the fraction of atoms (proportional to area) above the barrier for abstraction at a secondary (blue + red) and primary (red) C-H bond highlighted. The remaining fraction below the abstraction barrier (grey) is assumed to be unreactive.

The reduced reactivity of primary CH_3 groups (compared to secondary) observed in this work supports the *surface-freezing* phenomenon proposed by McKendrick and co-workers to explain the apparent reduced reactivity of a series of linear hydrocarbons compared to branched ones[68]. On the basis of relative reactivity of primary, secondary and tertiary groups it would be expected that linear liquid hydrocarbons would be more reactive than branched ones as they have fewer of the least reactive primary groups per molecule. In contrast, McKendrick and co-workers observed reduced reactivity in linear hydrocarbons compared with the branched molecules squalane and pristane. There was also an interesting decrease in reactivity as linear chain length decreased; the magnitude of the decrease was too large to be due to modest changes in the primary-to-secondary C-H groups present.

The contribution from the terminal CH_3 group (C_1), and the relative reactivity compared to the liquid hydrocarbon squalane, were important to quantify in the context of the previous work of McKendrick and co-workers[63,66-69,121,124]. The authors had previously assumed the primary groups in squalane to be essentially unreactive on the basis of bond strengths. The reduced reactivity at primary sites was proposed by McKendrick and co-workers as an explanation of the observed reduced reactivity of linear with respect to branched hydrocarbons[68] (chapter 1, section 1.3.3). It was proposed that surface freezing of linear hydrocarbons (where the molecules spontaneously align at the interface) would preferentially expose the least reactive CH_3 groups, resulting in reduced reactivity over branched molecules.

Surface freezing is the spontaneous freezing (into monolayer-type structures) of linear liquid hydrocarbons, at the interface, at temperatures close to their bulk freezing points. As a result of experimental constraints due to vapour pressure, this was the temperature range at which the experiments had to be carried out. It was proposed on the basis of the experimental observations that this effect is more prevalent in the shorter chain length hydrocarbons. In this surface frozen phase, the linear hydrocarbons would mimic SAM surfaces and the interface would be dominated by the less reactive primary groups, explaining the observed reduced reactivity. The magnitude of the difference in reactivity between liquid squalane ($C_{30}H_{62}$, branched) and the shortest linear hydrocarbon studied was a factor of ~3. This is very similar to the difference in reactivity between squalane and the alkylthiol SAMs observed in this work (~3-4.5 times higher reactivity for the liquid compared with the SAM).

The overall single largest contribution comes from the first available secondary group (C_2), contributing 42% of the overall yield. This reflects the lower barrier at this position compared to that at C_1 and that the structure is sufficiently open at this site for direct hydrogen abstraction. The contribution from C_3 to C_6 is equally important; it is reasonable to assume that the majority of this would come from C_3 but that C_4-C_6 may also contribute. Ideally, individually labelled thiols might have been synthesised to label each carbon along the chain explicitly, but this was not attempted in this preliminary study.

The fact that direct OD reaction products are observed from deep within the chain presents a picture of a surface which is relatively open to direct attack. The barrier for a second hydrogen abstraction is relatively low at 3-10 kJ mol^{-1} to form water[184] (or

HOD). The observation that OD products are able to escape without undergoing significant secondary collisions and ultimately reaction, is suggestive of reactive trajectories that allow for relatively unhindered attack and release from within the chain (certainly as deep as C_3).

There is only one other conceptually related experimental study that has been carried out to date, that reported by Jacobs and co-workers[88-90]. Selectively deuterated dodecyl (C_{12}) SAMs were bombarded with O^+ ions (believed to neutralise to $O(^3P)$ on impact) at much higher collision energies than were used here (~500-4000 kJ mol^{-1}). They detected OH^- reaction products by mass spectrometry. It was observed that hydrogen abstraction was confined to the outermost carbon atoms (at 500 kJ mol^{-1} collision energy) with contributions of 75%, 22.5% and < 2.5% for positions C_1, C_2 and C_3 respectively (table 4.2).

This gives a very different picture of the penetrability of O atoms at SAM surfaces than was found in this work. Jacobs and co-workers observed the majority of reaction taking place at the terminal group. The experiments presented in this chapter resulted in a much smaller fraction emanating from this position. Their much higher collision energy allows for unhindered (on energetic grounds) abstraction from the terminal C_1 position, in contrast to the suppression at this position observed in this work. It is much less obvious why Jacobs and co-workers observed minimal reactivity from C_3 and below. This could result from the much higher reactivity of the high-energy O atoms, resulting in them reacting with the first group they encounter. This shielding of the deeper positions is therefore likely to be a general feature of highly reactive probes, and is in agreement with a closely related theoretical investigation of high-energy, low barrier, reactions of F atoms with octyl (C_8) SAMs[132]. In those simulations, reactivity was predicted to occur primarily at the terminal C_1 position.

Alternatively, the difference could be a consequence of differences in the escape probability of the OH^- products compared to the neutral OH/OD in this work. Jacobs and co-workers reflected that escape of OH^- ions is likely to be biased to the outer regions of the monolayer as ions formed at greater depths are unlikely to escape without neutralising or reacting[88]. Neutral OD (or OH), on the other hand, has been shown in this work, to be able to escape from at least as deep as C_3.

The closest available theoretical work is that of $O(^3P)$ reacting with model SAMs[112] at energies more consistent with the work of Jacobs (5 eV) (chapter 1, section 1.4.2). Their choice of initial conditions biased reaction at chain ends rather than between chains, and they did not fully explore initial polar and azimuthal angles of the incoming atoms relative to the chains. The relationship between these angles and the alkyl chains of the SAMs are defined in figure 4.20. In the experimental work presented here, the azimuthal angles sampled are essentially random, and the initial polar angles would be wide ranging. As a result of the photodissociation anisotropy (chapter 2, section 2.6.2) and the surface-laser axis distance.

The contribution from each carbon for specific combinations of initial and azimuthal angle is summarised in table 4.3. It is clear that the depth at which reaction occurs has a strong correlation to the angles used. Nevertheless, the simulations[112] demonstrated that C_1 and C_2 are exposed to direct attack. In addition, certain initial conditions result in significant contributions from C_3, and even C_4, typically following a non-reactive deflection from C_1. There are a number of reasons why the simulations would not be expected to agree quantitatively with this work. The higher collision energy, angular factors and the biasing of the simulations to 'hit' the chains rather than penetrate between them are three examples of sources of the differences. Qualitatively though, the simulations show that penetration and subsequent abstraction from the surface interior are probable. The simulations therefore, are in better agreement with the lower energy (~16 kJ mol^{-1}) experimental work presented here, rather than that of Jacobs and co-workers at similar collision energy (~500 kJ mol^{-1}).

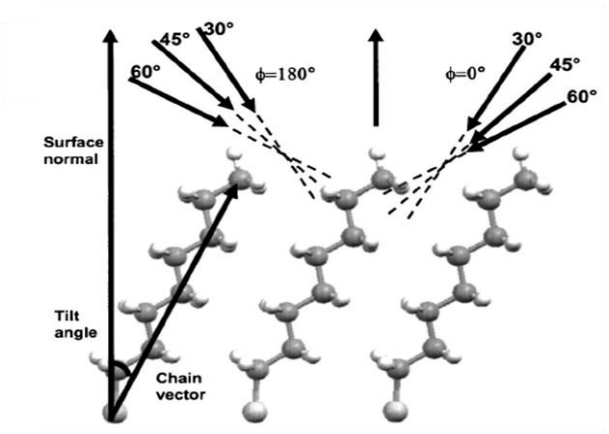

Figure 4.20: Schematic representation of the regions of the SAM that are directly exposed to O(^{3}P) in the simulations at different incident angles for dihedral angles φ0° and φ180°. Adapted from reference [112].

θ, ϕ	30°, 0°	30°, 180°	45°, 0°	45°, 180°	60°, 0°	60°, 180°
C_1	0.46 (0.18)	0.10 (0.04)	0.49 (0.18)	0.20 (0.06)	0.38 (0.09)	0.48 (0.10)
C_2	0.24 (0.09)	0.60 (0.24)	0.17 (0.06)	0.80 (0.23)	0.04 (0.01)	0.52 (0.11)
C_3	0.27 (0.10)	0.10 (0.04)	0.34 (0.13)		0.58 (0.14)	
C_4	0.03 (0.01)	0.20 (0.08)				

Table 4.3: OH fractional reactivity taking into account the H abstraction site as a function of initial conditions for 5 eV O(^{3}P) collisions with an octyl-thiolate SAM. Re-printed from reference [112].

Hase and co-workers[209], explored the *inelastic* scattering of O(^{3}P) from C_{10}-SAMs sampled over a wide range of energies and incident angles. Importantly, they extended beyond previous simulations by randomising the azimuthal angle and removing any bias for hitting the alkyl chains. The penetration depth was defined by the quantity h_{min}. This is the average minimum height reached by the O(^{3}P) atoms above the Au substrate. The results are summarised in figure 4.21 and the lower the value of h_{min}, the deeper the penetration. A h_{mim} value of 12.2 Å is equivalent to reaching C_3.

The simulations show that at the lower collision energies, the O(^{3}P) atoms are typically located between C_1 and C_3 (according to their h_{min} values). The authors speculate that abstraction is likely to occur from the surface interior even at low collision energy, and that a more complete reactive model (compared to that used by Troya and Schatz[112]) might show enhanced abstraction at greater depths. The penetration depth was predicted to increase at higher collision energy, an effect that was not observed experimentally, if the experimental work presented here is comparable with that of Jacobs and co-workers. These non-reactive simulations show, in agreement with the reactive work of Troya and Schatz, that the penetration depth is a sensitive function of

incident and azimuthal angle. Direct comparison between experiment and theory require equivalent angular sampling in both. The simulations however, both intimate that surface penetration followed by reaction is likely to occur (in the surface interior), in agreement with the experimental results presented in this chapter.

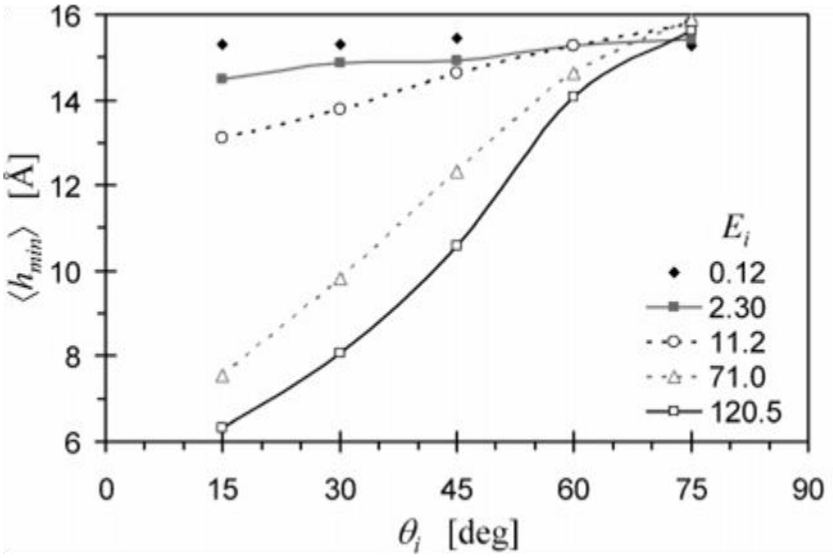

Figure 4.21: Plots of the average minimum height $\langle h_{min} \rangle$ vs the incident polar angle θ_i for different collision energies E_i in kcal mol^{-1}. Re-printed from reference[209].

An important consequence of this experimental work is its relevance for the design of theoretical scattering simulations. The QM/MM model developed for simulating reactive and inelastic scattering at SAM surfaces described in chapter 1 (sections 1.3.2 and 1.4.2) contains inherent assumptions about penetration depth. In such simulations, a decision is made on where the QM/MM boundary should lie. For example, Troya and co-workers simulated collisions of Ar at SAM surfaces[38] and only the outer two carbon atoms (C_1 and C_2) were treated quantum mechanically. Troya and Schatz later collaborated on the simulated reaction of hyperthermal (~5eV) O(^{3}P) atoms and alkylthiol SAMs[114]. They developed a (QM/MM) interaction potential where the outer 4 atoms were defined as being reactively active. The work presented here suggests that at least four atoms, but possibly up to six, should be considered as contributing towards OH formation. This work, in addition to that of Jacobs, suggests that penetration depth may also be collision energy and chemical species dependent. As a consequence it is necessary that more experimental work is carried out to test the theoretical models and vice versa.

4.5 Conclusions

- The dynamics of reactions at the gas-SAM interface have, for the first time, been investigated with quantum-state resolution. The translational and rotational distribution of the OH (OD) products following a hydrogen abstraction reaction by an $O(^3P)$ atom at alkylthiol SAM surfaces has been measured.
- The dominant reaction mechanism is found to be direct, with a minor contribution from slower OH(OD) consistent with thermalisation also being present. The translational distribution has been compared to that of the liquid hydrocarbon squalane and was found to be somewhat narrower, with less slow OH from the SAMs. This is consistent with the liquid squalane surface being rougher on a macroscopic scale, promoting multiple collisions and enhanced energy transfer.
- The provisional rotational distributions appear to be colder than those from equivalent gas-liquid and gas-phase experiments. This, if a genuine effect, is discussed in terms of possible entrance and post-reaction channels unique to the gas-SAM reaction.
- The fraction of the overall reactivity originating from the primary groups has been established using isotopic labelling. The reactivity at this site was found to be suppressed on account of its relatively high barrier compared to the average available collision energy.
- Up to six carbon atoms are proposed to be reactively active. There is significant penetration of $O(^3P)$ atoms at least as deep as C_3, resulting in OH products that are subsequently able to escape for detection without reacting further to form water. The penetration depth is far deeper than was observed in the only other related experimental measurement. Possible reasons for the observed differences between the two studies have been discussed and its consequence in the field of theoretical scattering simulations noted.

4.6 Future work

Following this proof of concept study, there are a vast number of further possibilities. Using the existing experimental procedure, a larger series of isotopically labelled thiols could be used to establish the definitive contribution from each carbon. The rotational distribution also could be investigated further. The use of longer alkyl chains and OD detection could allow possible experimental data acquisition times of greater than the 10 minutes used in this work. This would of course require further surface characterisation to establish the exposure time where the onset of damage occurs in the C_{12}- surfaces.

A considerable drawback of this work is that the NO_2 damages the SAMs, meaning that multiple samples are required for each experiment. Also, deuterium labelling is required to ensure no contamination from spurious sources is present. Both of these contribute to what is a very resource-intensive experiment to carry out, in terms of experimental time and purchase of consumables. To significantly improve upon the work described here would require a re-design of the experiment. As a starting point, a molecular beam source could be used. This would not only allow for the influence of collision energy to be investigated, but would also allow for overall lower gas dosage and elimination of the present requirement for NO_2 exposure.

A molecular beam source would also introduce the possibility for the investigation of impact angle, making for a closer comparison with theoretical work. The LIF detection method would be essential to allow for quantum-state resolution. A further improvement would be the integration of *in situ* STM imaging. This has been employed by other groups monitoring SAM structures in vacuum environments[27,28] and would be useful not only as an on-line check on structural integrity but would also hold the possibility of elucidating SAM degradation mechanisms following extensive bombardment by O atoms.

Chapter 5

Collision dynamics of OH radicals with liquids of atmospheric interest

5.1 Introduction

This chapter describes an experimental study investigating the inelastic scattering dynamics and reactivity of the hydroxyl radical at liquid surfaces. The work is primarily rooted in dynamics; therefore the general introduction (chapter 1) and relevant concepts are applicable here. What follows is an introduction to the role of the hydroxyl radical in the atmosphere and a summary of previous experimental work on its oxidation of liquid surfaces representative of organic atmospheric aerosols.

5.1.1 The role of the hydroxyl radical in the troposphere

Hydroxyl radical formation

Oxidation chemistry in the troposphere is dominated by the hydroxyl radical, formed primarily from secondary reactions of the $O(^1D)$ radical produced in the photodissociation of ozone. As a result of solar shielding by ozone in the stratosphere, the wavelengths of light available in the troposphere are limited to $\lambda > 280$ nm[210]. Ozone is photochemically active across a wide range of wavelengths from 200 – 850 nm. As OH formation is dependent on the reaction of electronically excited oxygen ($O(^1D)$) with water (reactions 1 and 2), the dominant wavelengths required are in the Hartley bands 200-320 nm[139].

$$O_3 + h\nu\ (\lambda < 320\ nm) \rightarrow O_2(^1\Delta) + O(^1D) \qquad (1)$$

$$O(^1D) + H_2O \rightarrow 2OH \qquad (2)$$

The barrier to reaction 2 is substantial at 119 kJ mol^{-1}[210]. Electronically excited oxygen atoms possesses 190 kJ mol^{-1} in electronic energy making the process exothermic overall. The measurement of the concentration of the OH radical in the atmosphere is extremely difficult. It varies according to season in urban, rural and marine environments. The OH radical also has a very short lifetime of ~1 s, as reviewed comprehensively by Heard and Pilling[211]. A number of research groups have carried out field studies measuring OH levels using a wide variety of sophisticated techniques including: LIF; differential optical absorption spectroscopy (DOAS); and chemical ionisation mass spectrometry (CIMS)[211]. The levels measured varied according to geography and season, but a typical global average is in the 10^6 cm^{-3} region. At atmospheric pressure and temperature the number density is ~3×10^{19} cm^{-3}, putting into context the low concentration of trace species such as the OH radical. Despite its mixing ratio of less than one part per trillion (ppt) in the troposphere the chemistry of the hydroxyl radical is of critical importance.

Reactions of hydroxyl radicals with organic matter in the troposphere

OH is the most potent oxidant in the troposphere. It is thought of as tropospheric detergent, cleansing the air through homogeneous reactions with CO, CH_4 and a wide variety of volatile organic compounds (VOCs). To put the oxidising power of the OH radical into context, the atmospheric lifetime is a useful concept. Isoprene for example, has lifetime, in rural environments of 1.7 hours with respect to OH, and 1.2 days with respect to ozone[210]. Of the three major tropospheric oxidants, OH, O_3 and NO_3[211] it is only the OH radical that reacts efficiently with alkanes, alkenes and aromatic VOCs. O_3 is only reactive towards alkenes and NO_3 reacts very slowly with all except alkenes. There are a huge variety of VOCs in the troposphere originating from biogenic and anthropogenic sources, ranging from the most prolific, methane, to relatively large mono- and sesquiterpenes.

The oxidation of VOCs by OH and other atmospheric oxidants is complex[212,213]. Generally the mechanism can be expected to follow one of two paths (figure 5.1). First the oxidation mechanism leads to the formation of smaller, volatile, oxidised organics (decomposition pathway). Examples of these include formaldehyde (HCHO) and methyl vinyl ketone ($CH_3COCH=CH_2$). The second path is the formation of secondary organic aerosols (SOA), where oxidation of a VOC leads to products with lower vapour pressure and greater polarity than their precursors (via an isomerism/polymerisation

pathway). Subsequent reactions lead to gas-to-particle transformation and a SOA particle is formed. The vast array of VOC precursors to SOA is indicative of their highly complex chemical nature. There are also primary sources. These primary organic aerosols (POA) can originate from emission from vegetation, combustion, biomass burning or sea spray[3]. Organic aerosols are then oxidised further by OH (as well as NO_3 and halogen atoms) which will in turn affect their chemical and physical composition.

The variety of sources, and constant physical and chemical alteration, leads to the organic constituents of atmospheric aerosols being present in a variety of phases such as liquids, waxes and solids. The organic material can form a coating on an inorganic core or be internally mixed with inorganic components[3]. The formation and processing of organic aerosols also leads to a wide variety of functional groups being present including alkyl, unsaturated, aromatic, and acid, as well as highly oxidized multifunctional compounds[3]. The general structural consensus is that the organic (hydrophobic) matter coats an inorganic/aqueous (hydrophilic) core in an inverted micelle structure[4,5] (chapter 1, section 1.2). Atmospheric aerosols (organic and inorganic) are thought to affect the Earth's energy budget and influence cloud formation. Establishing the direct and indirect effects aerosols have on climate are 'amongst the largest uncertainties in the current understanding of regional and global environmental change'[6].

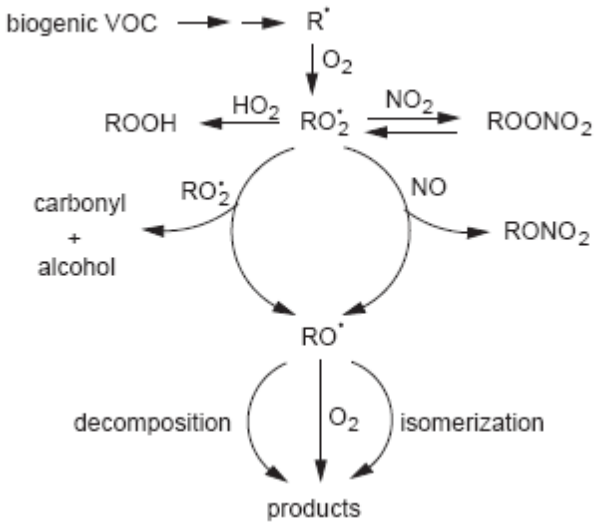

Figure 5.1: Schematic representation of the oxidation of VOC's in the atmosphere following the initial hydrogen abstraction by an OH radical. Figure re-printed from reference[213].

5.1.2 Laboratory measurements of radical uptake at atmospherically relevant surfaces

It is clear that to understand the composition and reactive processing of organic aerosols is highly complex task, and requires a multidisciplinary approach between field measurements and a wide range of laboratory studies. In the laboratory, simplified proxies are often used to mimic atmospheric aerosols. These take a wide variety of different forms, including organic liquids in droplets or continuous flow, waxes, surface films and self-assembled monolayers[214]. The self-assembled monolayer is an attractive proxy as it replicates an inverted micelle structure. Typical measurements include the reactive uptake coefficient, γ, defined as the reactivity per collision, and hygroscopicity (the ability of the surface to take up water). This is particularly important in studies looking at the cloud condensation abilities of certain aerosols. The majority of experiments are carried out under thermal conditions to mimic the ambient atmosphere.

There have been a number of gas-liquid/gas-particle kinetic studies carried out in recent years looking at reactions of a variety of inorganic and organic surfaces with many atmospherically relevant gases. A number of reviews have summarised the progress in the field[3,4,78,215,216]. The experiments which are most relevant here are those which measure OH uptake coefficients at organic surfaces. Typically, gaseous uptake measurements are carried out either by monitoring the loss of the gas-phase species (OH in this case), or by monitoring the rate of the removal of the particle phase. Flow tube experiments are widely utilised (where the liquid or solid coats the surface of a tube through which the gas is flowed and measured). An alternative is the use of an aerosol generator and subsequent mixing of the gas and particle phases in a stirred-tank reactor. The typical detection method, whether monitoring gas or particle loss, is mass spectrometry.

McNeil and co-workers measured OH uptake values of γ = 0.8 to 1 on submicron palmitic acid ($C_{16}H_{32}O_2$) aerosol particles by monitoring the loss of palmitic acid by CIMS. This was extended to measuring OH uptake at palmitic acid thin films coating NaCl particles, intended to represent sea-salt aerosols. They found that the uptake coefficient decreased (compared to bare palmitic acid particles) to 0.3 (+0.1/-0.5) but that the presence of the film led to a significant increase over uptake on bare NaCl

particles, where $\gamma = 0.05$ (±0.01). Robinson, in collaboration with Donahue and co-workers, exposed OH radicals to aerosolised motor oil consisting of a mixture of hopanes (penta-cyclic compounds with unsaturated groups), steranes (buta-cyclic compounds) and n-alkanes in a smog chamber and reported uptake coefficients in the range $\gamma = 0.1$ to 8[217]. A similar study on OH with n-hexacosane aerosol particles yielded an uptake coefficient of $\gamma = 1.04 \pm 0.21$[218].

A comprehensive study of OH uptake at a variety of surfaces was carried out by Molina and co-workers[79,80]. They completed a series of flow tube experiments on a range of organic and inorganic surfaces at low and high relative humidity. The reported coefficients at organic surfaces were as follows: halocarbon wax $\gamma = 6 \times 10^{-4}$; paraffin wax $\gamma = 0.34$; methyl terminated monolayer $\gamma = 0.29$; palmitic acid ($C_{16}H_{32}O_2$) $\gamma = 0.32$; vinyl terminated monolayer $\gamma = 0.60$; and pyrene ($C_{16}H_{10}$) $\gamma = 0.32$[79]. The results show some interesting trends; OH uptake at unsaturated surfaces is more facile than at saturated hydrocarbon surfaces; the presence of an acid group has little or no effect on the uptake coefficient compared with a hydrocarbon (palmitic acid vs. paraffin wax), and SAMs display similar uptake propensities to more disordered surfaces.

In contrast, aqueous inorganic salts resulted in considerably lower coefficients[80] (~$3-6 \times 10^{-3}$). These were more influenced by relative humidity than the organic surfaces. In agreement with Molina and co-workers, the experiments of D'Andrea *et al*.,[214] investigating the reaction of thermal OH with methyl and vinyl-terminated monolayers, found that the reaction at the unsaturated monolayer was more facile than that at the saturated monolayer (although uptake coefficients were not measured). D'Andrea *et al*.[214] also observed facile degradation of the unsaturated surfaces on very short timescales, proposed to be the result of a radical chain polymerisation reaction initiated by the initial insertion of OH into the vinyl unit.

Wilson and co-workers have carried out recent experiments using a flow tube[219] (high OH concentration, ~1×10^{10} molecules cm^{-3}) and a continuous flow stirred tank reactor[220] (lower OH concentrations, ~1×10^{8} molecules cm^{-3}) to investigate OH uptake at squalane aerosol surfaces. These sophisticated experiments allowed a reaction mechanism to be identified where the squalane molecule is sequentially oxidised in the presence of OH and O_2. This was deduced through the detection of a series of oxidised squalane molecules in the series Sq (parent peak), SqO, SqO_2, SqO_3, SqO_4 and so on. A fragmentation reaction, leading to the detection of volatile reaction products, was also

identified as being important in the more highly oxidised squalane particles. The atmospheric implication of this fragmentation reaction is that it may be a significant loss process for organic material in aerosols as they are aged (oxidized). The OH uptake coefficients measured were 0.3±0.07[219] in the flow tube experiments and 0.51±0.10[220] in the tank reactor. The differences, although not particularly vast considering the systematic differences between the experiments, were attributed to the differences in OH concentration. At lower OH concentration the squalane loss appeared to accelerate. This was justified as the measured uptake coefficient being influenced by the primary abstraction process *and* secondary loss processes. At the lower concentration, the secondary loss processes were postulated to have a greater influence.

Abbatt and co-workers used bis-(2-ethylhexyl)sebacate (BES) particles as a SOA mimic and exposed them to OH radicals (from ozone photolysis) and monitored their loss with an Aerodyne aerosol mass spectrometer (AMS)[221,222]. BES ($C_{26}H_{50}O_4$) is a saturated long chain di-ester representative of organic matter which has already undergone some atmospheric aging. The measured OH uptake coefficient was γ = 1.3±0.4, indicative of a very efficient process with an influence from secondary chemistry resulting in a coefficient higher than unity. Reminiscent of the experiments of Wilson and co-workers[219,220], the secondary reaction mechanism was found to involve volatilization of the oxidised products leading to a mass loss of up to 10%[221]. They also found that the hygroscopicity increased after OH exposure, which suggests a greater ability for oxidised organics to act as cloud condensation nuclei (CCN). An uptake coefficient of $\gamma = 2$ was measured for the same reaction by Smith and co-workers in a flow tube experiment, using HONO as a precursor to OH and monitoring BES particle loss by mass spectrometry. Recently, Smith and co-workers have also measured OH uptake coefficients at particle surfaces in flow-tube experiments, monitoring particle loss as a function of OH exposure, finding uptake coefficients of 0.28±0.04 for squalane, 0.4±0.03 for oleic acid and >1 for squalene[223].

The experimental approach described in the current chapter has an advantage over the work highlighted above in that what has been measured here is the *primary abstraction* process alone. This work is designed to complement the previous measurements, providing information on the structure of the interface and how it influences reactive uptake.

5.2 Experimental summary

The work presented in this chapter was carried out in two stages. The first (experiment 1) was a proof-of-concept study and the second (experiment 2) was more comprehensive, carried out 24 months later. The broader experimental details are provided throughout chapter 2 and a brief summary, highlighting in particular any differences between the two experiments, is provided here.

The inert liquid perfluoropolyether (PFPE) Krytox® 1506 (F-[$CF(CF_3)CF_2O]_{14ave}$-CF_2CF_3,) and the liquid hydrocarbon squalane ($C_{30}H_{62}$, 2,6,10,15,19,23-hexamethyltetracosane) were used in both experiments. For experiment 2, the work was extended to include the potentially reactive liquid squalene ($C_{30}H_{50}$, trans-2,6,10,15,19,23-hexamethyltetracosa-2,6,10,14,18,22-hexaene) and the organic acid, oleic acid ($C_{18}H_{34}O_2$, cis-9-octadecanoic acid). The structures of the liquids are provided in figure 5.1. The OH radicals were generated from a continuous flow of a gaseous nitrous acid (HONO) precursor[224] (in a N_2 carrier gas stream) prepared by adding sodium nitrite ($NaNO_2$, 2M, 200 ml) at a drop-rate of ~1 $mlmin^{-1}$ to a stirred volume of sulphuric acid (H_2SO_4, 2M, 100 ml) at 0 °C (experiment 1) or room temperature (experiment 2). The drop-rate and nitrogen flow rate were specifically chosen to minimize the formation of NO_2 while maximising the amount of OH formed.

A carefully controlled pressure (1 mTorr) of the HONO precursor mixture was photolysed (355 nm) at a fixed distance of 9 mm above the liquid surface. The photolysis beam (5 mm diameter) counter-propagated the probe beam, passing at the same carefully controlled distance from the surface. The spatial distribution of the OH produced in this manner is described by an anisotropy parameter, $\beta = -0.9$[140]. A λ/2 waveplate was therefore placed in the photolysis laser path to rotate the linear polarization to vertical. This optimised, as far as possible, the recoil of the OH towards the liquid surface. Following collision, a fraction of the OH radicals that escape from the surface returned to the laser axis, and were detected by LIF. The OH radicals were detected in their vibrational ground state by probing the $A^2\Sigma^+$—$X^2\Pi$ (1,0) (experiment 1) and the $A^2\Sigma^+$—$X^2\Pi$ (0,0) (experiment 2) bands.

Experiment 1 was carried out using the first generation wheel design and experiment 2 involved the second generation design (chapter 2, section 2.1). The second generation wheel was designed so that the distance was set and the wheel assembly was fixed

permanently in place, whilst three interchangeable wheels and their baths could be removed easily and quickly via the front access port. This resulted in increased efficiency when changing liquids and improvement in reproducibility in terms of wheel-to-laser-axis distance.

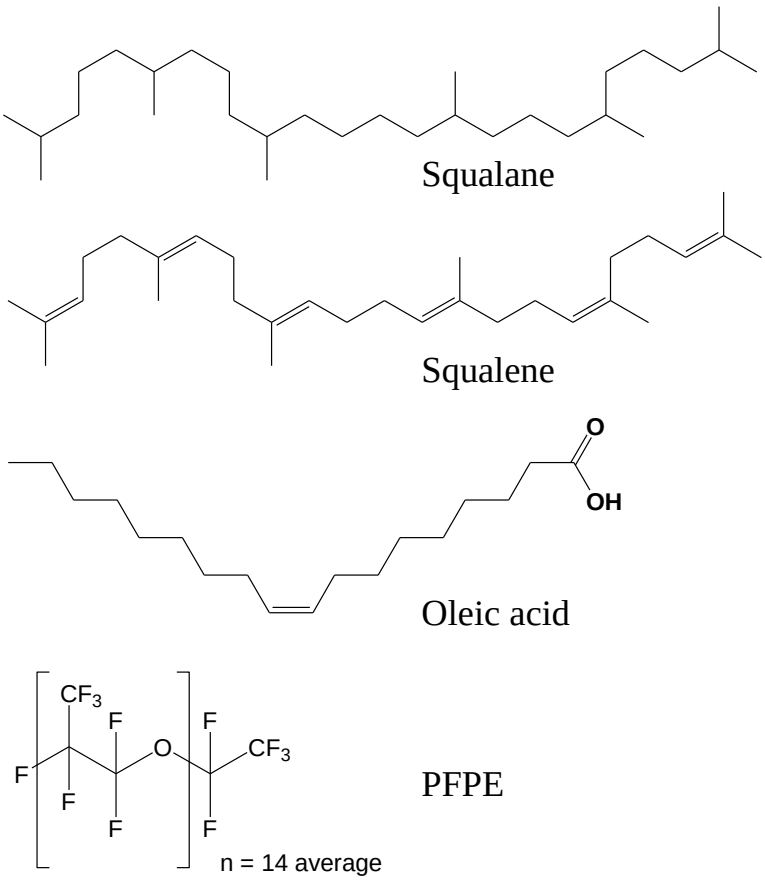

Figure 5.2: Chemical structures of the liquids used.

5.3 Experimental results

5.3.1 HONO source stability and purity

Nitrous acid, HONO, is not available commercially as it is highly unstable and readily dissociates on the walls of containers, and equilibrates in the presence of water to form oxides of nitrogen. As a result, a HONO generator was used to give a continuous supply of HONO for the duration of the experiments. A number of experimental parameters were investigated to optimise this process: the drop-rate of $NaNO_2$, the temperature of the reaction, and the flow-rate of the nitrogen carrier gas. Factors which were considered when optimizing the reaction were the concentrations of HONO and NO_2 formed and the stability of the HONO over time.

It was necessary to maximise as much as possible the formation of HONO in the generator. The HONO formed was quantified indirectly by observing how the OH LIF signal (proportional to HONO number density) was affected by different conditions. The amount of HONO formed increased with increasing $NaNO_2$ drop-rate, with increased temperature and with lower N_2 carrier gas flow rates, all as would be expected. The experimental conditions selected though, had to be a compromise between maximising HONO (OH) formation and minimising, as far as possible, the formation of NO_2. As described in chapter 2 (section 2.5.2) the formation of NO_2, through equilibrium 3, needed to be avoided as far as possible. NO_2 is photolysed at 355 nm to give $O(^3P)$ atoms which may react with the (potentially reactive) liquid surfaces. This could result in an undesired additional source of OH which would be difficult to distinguish from the scattered OH.

$$NO_2(g) + NO(g) + H_2O(l) \rightleftharpoons 2HONO(g) \qquad (3)$$

The third consideration was to investigate how the HONO concentration varied with time. It was necessary to establish how long it takes for a steady-state HONO concentration to be achieved, and also whether this could be maintained for the time periods required for data acquisition. An excitation spectrum, for example, recorded at only 20 laser shots per point, would take over an hour to record.

The time and source-temperature variation of the OH formed from HONO photolysis is shown in figure 5.3 (a) and (b). As would be expected, there was negligible OH formed initially. Over time (t = 0 defined as when the $NaNO_2$ was first added) the amount of OH formed increased, reaching a maximum after approximately 50 minutes. After this time a reasonably constant OH concentration was measured over a time period of over 1 hour. Figure 5.3 (a) shows that the rate of initial OH formation (t = 0 to t = 50 min) leading to the steady state concentration was faster at the higher temperature (implied by a steeper gradient for the room temperature measurement) and that the overall amount of OH formed was greater. Figure 5.3 (b) illustrates the reproducibility of the time-dependent behaviour. At both temperatures, when the profiles were peak normalised, the two time traces overlap almost exactly. This demonstrates that providing the $NaNO_2$ drop-rate, the temperature and the N_2 flow rate are constant, the OH concentration will remain relatively stable for a period of over 1 hour, after an initial equilibration period of greater than 50 minutes.

The first sets of experiments (experiment 1) were carried out at 0 °C. This temperature was chosen initially for safety concerns. As the reaction product (HONO) was gaseous the first attempt was carried out at low temperature to limit pressure build-up in the reaction vessel. It was found that this low temperature yielded a sufficiently large OH signal from HONO photolysis to complete the experiments. In the second set (experiment 2), the temperature dependence was investigated as shown in figure 5.2. This was required as a move from the off diagonal ($\Delta v \neq 0$) to the diagonal ($\Delta v = 0$) excitation band, and corresponding changes in the optical set-up (chapter 2, section 2.7.3) had resulted in a net decrease in OH detection sensitivity. It was therefore necessary to identify ways to increase OH production without affecting the HONO stability or NO_2 production. The final conditions were chosen as: a drop-rate of ~1 ml min^{-1}, a nitrogen carrier gas flow rate of 70 sccm, reagent concentrations of 2 mol $L^{-1}$and temperatures of 0 °C (experiment 1) and room temperature (experiment 2).

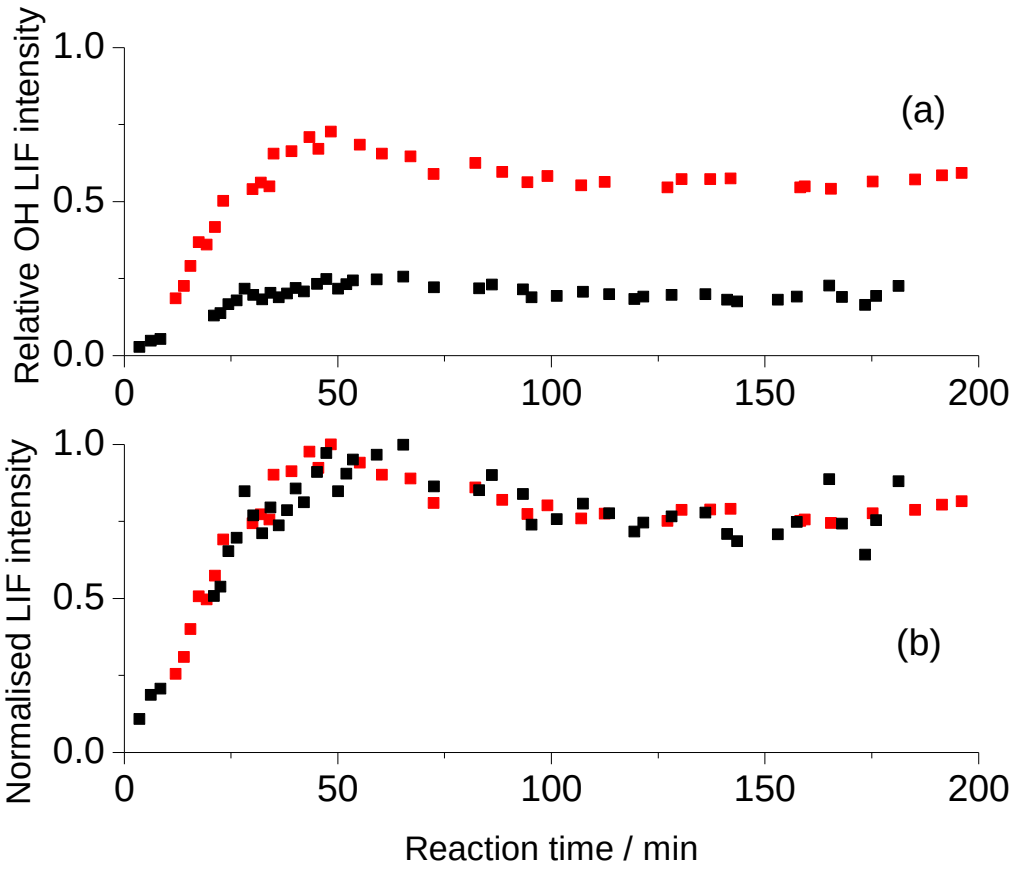

Figure 5.3: Figure showing the time and source-temperature dependence of the OH LIF signal from the photolysis of HONO. Each point represents the peak height of the OH $v' = 0$, $Q_1(1)$ transition measured at a photolysis-probe laser time delay of 3 μs. Results shown are for a fixed $NaNO_2$ drop-rate of ~1 mL min^{-1}, at a reaction temperature of 0 °C (black squares) and 25 °C (red squares). Panel (a) includes the measured relative OH signal heights for both temperatures. In panel (b) the data have been peak normalised.

As discussed in chapter 2 (section 2.5.2) and mentioned in the experimental summary above, a critical condition was that the experimental parameters chosen for the HONO generator, minimised, as far as possible the formation of NO_2 via equilibrium (3). In practice, when optimising the system, this could be done crudely by eye. NO_2 (or strictly speaking the N_2O_4 dimer) has a characteristic brown colour, making any significant quantities obvious in the otherwise colourless reaction vessel. Certain experimental parameters, such as increased $NaNO_2$ drop-rate, and slow N_2 flow rates, led to the obvious formation of NO_2. The conditions above were selected by this crude method, and a quantitative method of NO_2 detection was then necessary to establish how this would impact as an additional (undesired) source of OH radicals in the chamber.

The NO_2 content in the gaseous output from the HONO generator was quantified by measuring the OD formed following the reaction of $O(^3P)$ atoms with a per-deuterated liquid hydrocarbon ($C_{30}D_{62}$). The source of the $O(^3P)$ atoms was NO_2 photolysed at 355 nm, from either 'pure' NO_2 (98%, BOC) or the HONO precursor gas mixture. Appearance profiles ($Q_1(1)$ transition, A-X (1,0) band) were recorded using 1 mTorr of each of the gaseous precursors, and are shown in figure 5.4. A significant OD signal was observed from the 'pure' NO_2. The HONO precursor however, resulted in no observable OD within the signal-to-noise limits of the experiment. This was confirmed over several attempts and as a result only an upper limit on the maximum potential NO_2 content could be established. The comparative areas under both curves result in a maximum NO_2 fraction of 3±1% in the HONO mixture.

An NO_2 contribution at this upper limit in the HONO generator could have serious implications on interpreting whether the signals observed result from inelastically scattered OH (from HONO photolysis), or OH formed at the surface through reaction of $O(^3P)$ atoms (from NO_2 photolysis). Although the absorption cross sections of NO_2 and HONO at 355 nm are comparable[139], there are several other factors that, fortunately in this context, heavily favour the detection of inelastically scattered OH over that from $O(^3P)$ reaction. Most notably, Minton and co-workers[62,64,110] have shown that a large majority of $O(^3P)$ atoms scatter inelastically from squalane, even at much higher collision energies than used here. There is also a modest geometric bias in this work as a result of the vertical photolysis laser polarization because, in contrast to HONO, NO_2 has a positive anisotropy parameter ($\beta = +0.7$). It can therefore be reasonably

anticipated that any background OH from O(^{3}P) reaction with the hydrocarbon liquids will be minimal in comparison to the desired inelastically scattered OH.

To establish any possible contribution from an O(^{3}P) contamination absolutely, the experiment with perdeuterated squalane could be repeated with the aim of improving the signal-to-noise. However, the expense of the perdeuterated liquid hydrocarbon makes this prohibitive, particularly as the experiment (figure 5.4) was repeated multiple times so an increase in achievable signal-to-noise may not be possible. The most complete practical solution would be to use a different precursor altogether, that produces OH with a similar energy distribution, but without any possibility for NO_2 formation. The results could then be compared to those presented here.

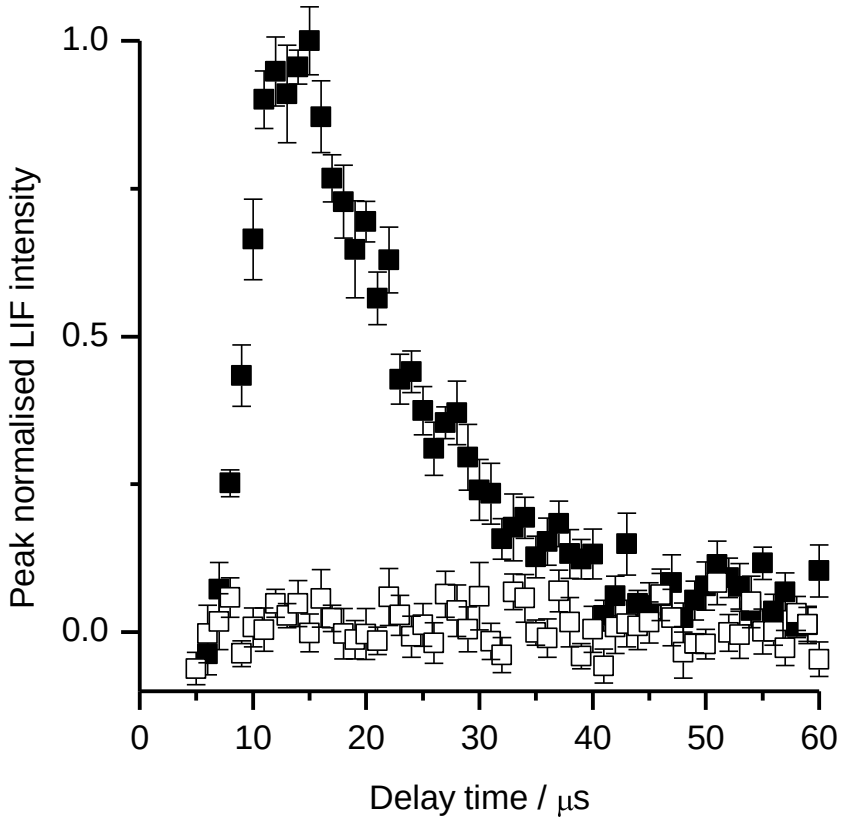

Figure 5.4: Measured appearance profiles of the OD ($v' = 0$) LIF signal following photolysis of the 'pure' NO_2 (black closed squares) and HONO gas mixture (black open squares). Background probe and photolysis laser signals have been subtracted. Profiles were recorded on the $Q_1(1)$ transition of the OD *A*-*X* (1,0) band. Bath temperature = 298 K; *p*(HONO or NO_2) ~ 1 mTorr; surface-probe laser distance = 5 mm.

5.3.2 OH signal verification

Following the optimisation of the experimental procedure for the generation of HONO, it was necessary to measure the photolysis-probe laser time delay dependence of the photolytically generated OH. Characterisation of the photolytically generated OH was vital to establish the background OH signal, before any scattered OH could be identified. This was achieved by fixing the probe laser wavelength on a specific rovibronic line of the OH spectrum, and varying the delay between the photolysis and probe lasers. This was carried out in the absence of the liquid-covered wheel. All other components of the liquid bath assembly remained in the chamber so that any influence they exerted would be measured.

Figure 5.5 clearly shows that the photolytically generated OH has its maximum at the earliest delay times. The OH signals between 0 and 4 μs are omitted as they are too large for the other more important details in the figure to be visible. The OH signal decays monotonically with an increase in delay, as the OH radicals formed 'fly out' of the probe region. The photolytically generated OH reaches a baseline value by 20 μs and is then reasonably constant out to 100 μs. A sum of three exponentials with a constant positive offset to reflect the 20-100 μs behaviour was fit to the profiles. An average of approximately twenty profiles, recorded over several days is shown in figure 5.5. The error bars are the 1σ standard error in the mean of these individual profiles. The profiles recorded on different days have been peak normalised at a time delay of 4 μs to account for any day-to-day fluctuations in the amount of OH detected. The data shown in figure 5.5 were recorded during the second sets of experiments (experiment 2). Equivalent profiles were recorded for the first set (experiment 1). Experiment 1 was a less comprehensive study, and although several profiles (~8 individual scans) were averaged, these were all recorded on the same day.

The photolytically generated OH profile contains all the contributions to a background signal, upon which any scattered OH signal would sit. The background consists of contributions from the photolytically generated OH, any scattered light from either laser pulse and the formation of OH from probe-induced photolysis of HONO. The absorption cross section of HONO in the probe region (~282 nm in experiment 1 and ~308 nm in experiment 2) is considerably smaller ($<1 \times 10^{-20}$ cm^2) than its value of ~7 $\times 10^{-19}$ cm^2 at 355 nm[139]. The fluence from the probe beam was also very much

lower than the photolysis beam, indicating that this would be only a very minor contribution. The most dominant contributor to the constant underlying background was found to be scatter from the probe laser, particularly in experiment 2. The OH in this case was probed on a diagonal transition and the probe laser could not be discriminated against using an interference filter. This was minimised by careful alignment of the beam. It was found that even very minor alterations, resulted in large changes in the scattered light contribution.

Having established the components of the background signal and measured the appropriate OH LIF profiles, the key goal was to unambiguously identify OH molecules that had collided with the liquid surface. This was achieved by repeating the process above in the presence of the liquid-covered wheel. The liquid used was the inert PFPE, and the resulting profile is shown in figure 5.5. The profiles recorded in the presence of the liquid surface clearly show a distinct secondary peak, followed by a slowly decaying tail. As only the liquid covered wheel is missing in the background profiles, this secondary peak *must* result from OH radicals that have collided with the liquid surface.

Further corroboration that the profiles reflect the scattered (post-collision) OH is that the peak arrival time is consistent with a reasonable round-trip time from the laser axis to the surface and back. The mean laboratory-frame collision energy of the OH radicals formed from HONO photolysis is 53.7 kJ mol^{-1}; equivalent to an average speed of 2500 m s^{-1}[140]. The photolytically generated OH would take on average 3.6 μs to travel the 9 mm to the surface, leaving 7.4 μs for the return journey, implying a speed of ~1200 m s^{-1}. The relationship between scattered OH signal and wheel—laser axes distance is represented in figure 5.6. Despite being a very early result (experiment 1) with lower than ideal signal-to-noise, it is obvious that as the distance is increased, the scattered OH signal peaks later and decreases in magnitude; as would be expected for a longer round-trip time and geometric factors associated with detection.

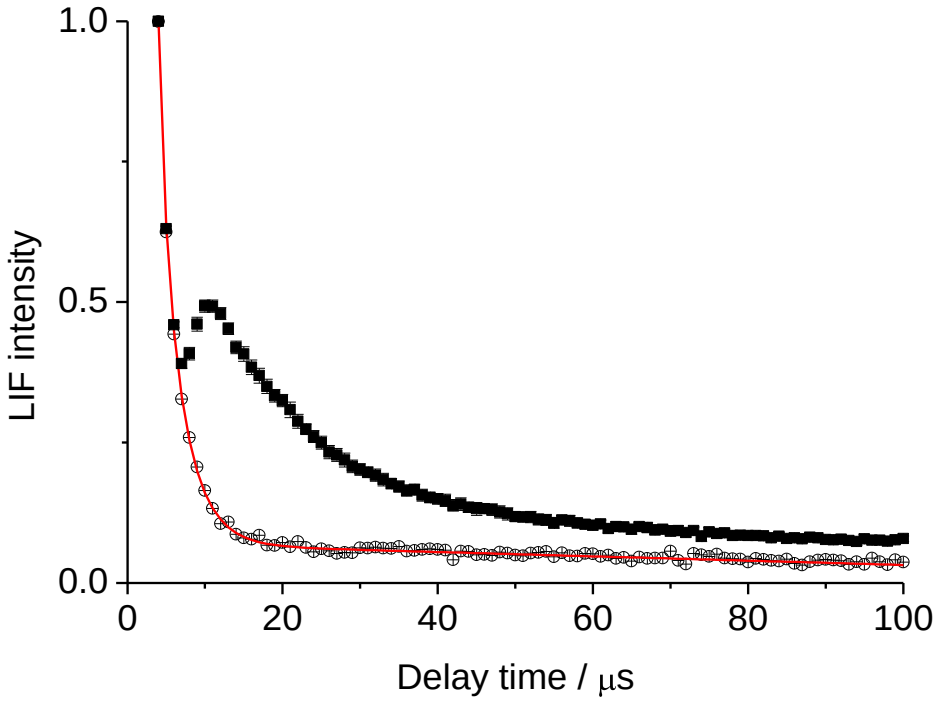

Figure 5.5: Photolysis-probe laser time delay dependence of the OH ($v' = 0$) LIF signal; recorded in the absence of a liquid covered wheel (black open circles) and in the presence of a PFPE covered wheel (black closed squares). Profiles were recorded on the $Q_1(1)$ transition of the OH A-X (0,0) band (experiment 2). Bath temperature = 298 K; *p*(HONO) ~1 mTorr; surface-probe laser distance = 9 mm.

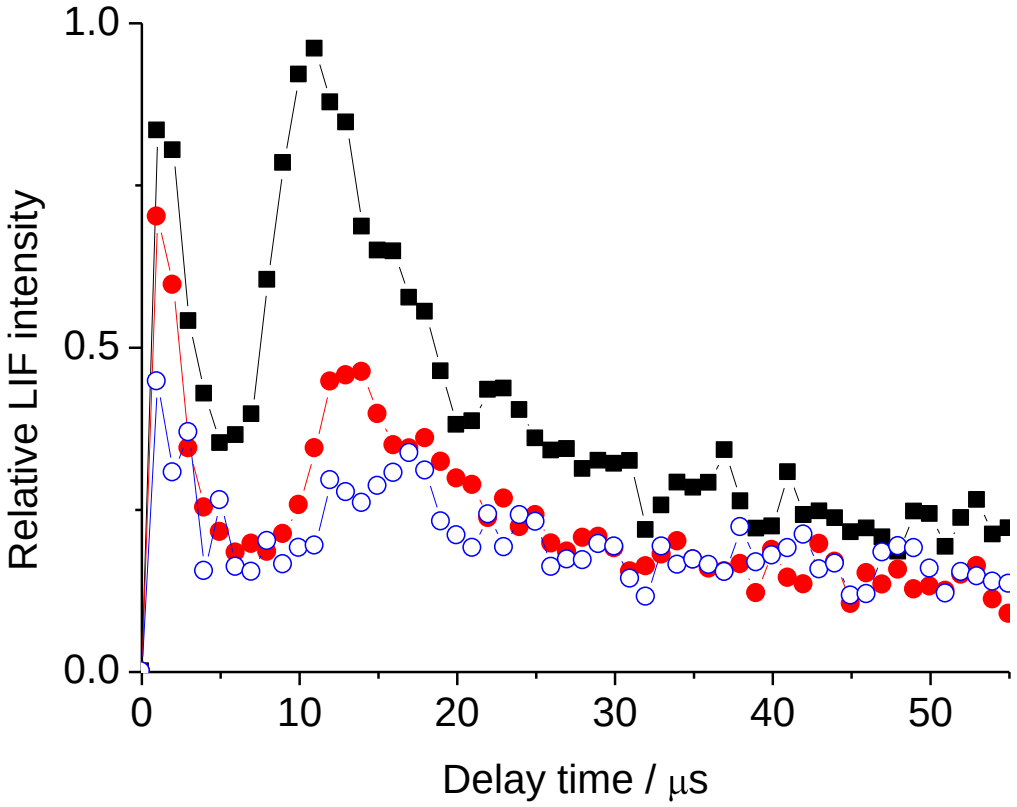

Figure 5.6: Photolysis-probe laser time delay dependence of the OH (v' = 0) LIF signal; recorded at a wheel—laser axes distance of 9 mm (black filled squares), 11 mm (red filled circles) and 13 mm (blue open circles). Profiles were recorded on the $Q_1(1)$ transition of the OH A-X (1,0) band (experiment 1). Bath temperature = 298 K; p(HONO) ~ 1 mTorr, liquid = PFPE.

5.3.3 OH appearance profiles

Sections 5.3.1 and 5.3.2 provide validation that OH radicals can be generated from HONO in a stable (over the appropriate timescales for data acquisition) and reproducible manner, and that OH formed photolytically can be distinguished from OH that has been scattered from a liquid surface. At this point it is important to introduce some terminology for the following sections: *Pre-collision OH* refers to nascent OH formed from the photolysis of HONO; *post-collision OH* refers to those OH radicals that have collided with a liquid surface; and *appearance profiles* refer to the appearance of OH as a function of photolysis-probe laser time delay for the post-collision OH.

The data handling procedure for both experiments 1 and 2 was essentially the same. Multiple profiles ($5 > n < 10$) were recorded on the $Q_1(1)$ and $Q_1(5)$ transitions in the presence and absence of a liquid covered wheel. This was carried out once per liquid for experiment 1 and repeated at least 5 times per liquid during experiment 2. The resulting profiles from each day were averaged and peak normalised at a time delay of 4 μs. This time delay was chosen as the signal intensity at this point reflects purely the pre-collision OH and is therefore a measure of the amount of photolytic OH formed on a given day (proportional to the HONO concentration and other factors). Following the application of this correction for day-to-day OH fluctuations, the resulting profiles were averaged again (experiment 2 only).

The profiles obtained during experiment 2 are shown in figure 5.7. This was the more comprehensive study, involving four liquids and significantly more repeat measurements. As a result the majority of the work presented in this chapter refers to this latter set of experiments, with comparisons between the two being highlighted as necessary. The appearance profiles shown inset in figure 5.7 were generated by subtracting the exponential fit to the background profile recorded in the absence of a wheel from the profile recorded in the presence of the wheel. The result is the appearance of post-collision, scattered OH, as a function of photolysis-probe laser delay.

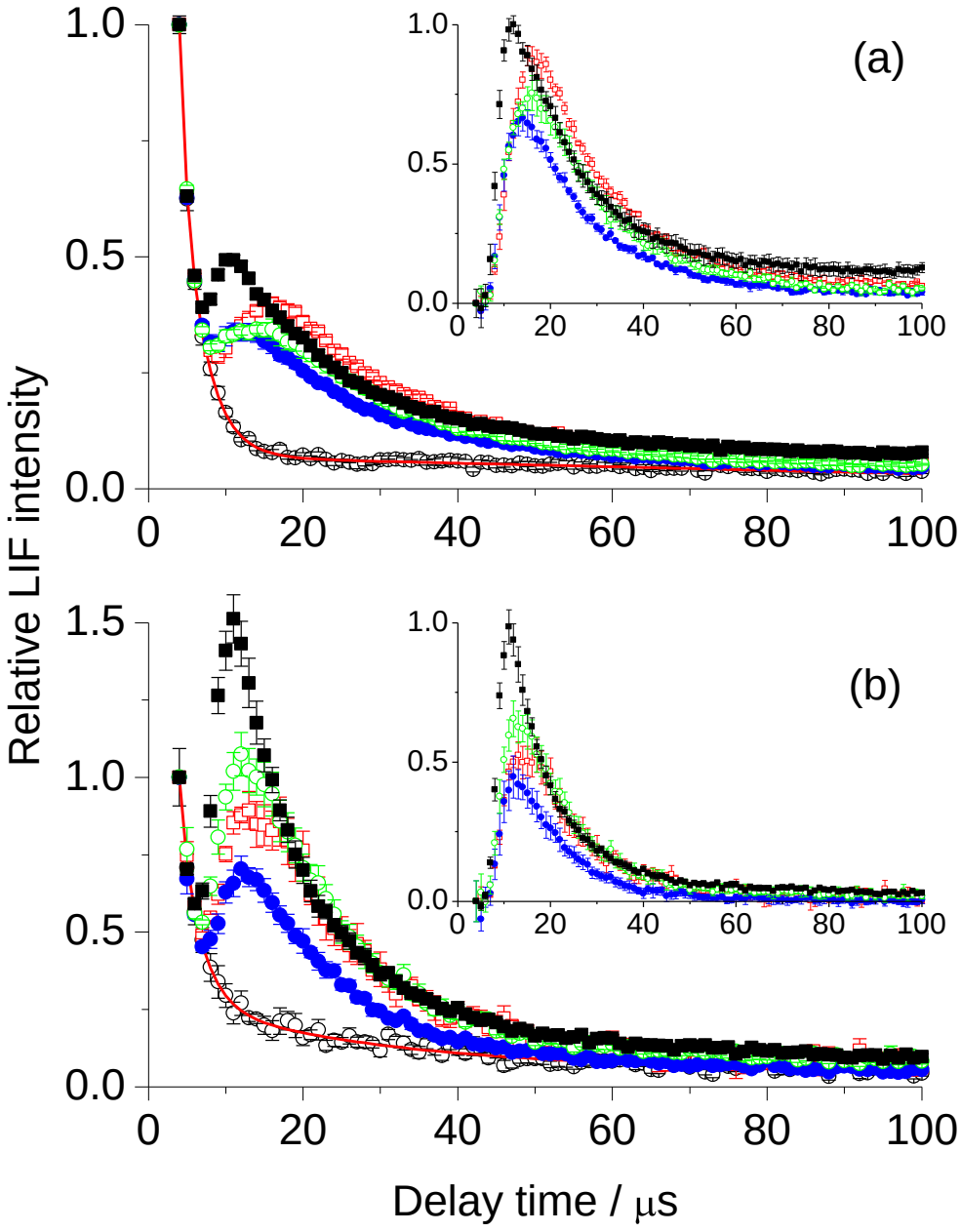

Figure 5.7: Measured photolysis-probe laser time delay dependence of the OH A-X (0,0) radical. Measured on the (a) $Q_1(1)$ and (b) $Q_1(5)$ transitions, recorded in the absence of a liquid covered wheel (black open circles), in the presence of a liquid wheel coated in PFPE (black closed squares), squalane (red open squares), squalene (blue closed circles) and oleic acid (green open circles). Red line represents a sum of three exponentials (with a constant offset) fit to the background profiles recorded in the absence of a liquid covered wheel. Insets show OH appearance profiles following subtraction of the background. Error bars are the 1σ standard error in the mean of the measured data points. *p*(HONO) ~1 mTorr, wheel-laser axes distance = 9 mm. Data from experiment 2.

Figure 5.7 shows that there are obvious differences between the OH scattered from the four liquids. These are evident in the shape of the profiles, representative of differences in the translational and internal energy of the scattered OH, and in the absolute signal heights. The normalization at 4 μs in the main figure (5.7) has been re-normalised in the insets by setting the $N' = 1$: $N' = 5$ ratio at 4 μs to that representative of the rotational distribution of the pre-collision OH (1:0.29) (section 5.3.6). The subsequent background subtraction (from main figure to insets) results in relative $N' = 1$: $N' = 5$ ratios reflecting the real rotational distribution of the scattered OH from each liquid. This makes it possible to compare the relative yield in each rotational state, for each liquid, directly from the profiles. It is evident that the OH rotational distribution from each liquid is different, and that it is significantly hotter than thermal in all cases. A $N' = 1$: $N' = 5$ ratio of 1:0.2 would be characteristic of a thermal distribution (300 K) while a $N' = 1$: $N' = 5$ ratio of approximately 1:1 for PFPE is indicative of a substantially hotter distribution.

Close inspection of the appearance profiles inset in figure 5.7 reveals that they do not decay to zero at long times. This is most noticeable for PFPE in $N' = 1$. This is likely to be a result of random diffusion of a minor thermal OH contaminant that grows in at long time delays. This contaminant is most likely OH that has scattered from the liquid surface and then has undergone further collisions with gas-phase molecules or other parts of the wheel assembly. It is reasonable that this would be most obvious in the PFPE profiles, as it is assumed that there are no loss mechanisms for OH at the PFPE surfaces. The reactive liquids, on the other hand, would presumably act as a sink for OH radicals, hence the effect is less pronounced for these liquids. The inference that this contaminant is thermalised is also reasonable, since this effect is more obvious in the $N' = 1$ profiles than the $N' = 5$ profiles. As was shown in chapter 2 (section 2.8.1) for the reaction between $O(^3P)$ and squalane, at time delays as early as 30 μs the effects of secondary collisions become evident at these pressures. As a result, to limit any possible misinterpretation, mechanistic conclusions are only inferred from profiles truncated at 30 μs.

Figure 5.8 re-presents the appearance profiles inset in figure 5.7, following an approximate density-flux transformation. The transformation corrects for the fact that the fastest OH (earliest arrival time) spend the least time in the probe region. This allows for quantitative comparison of the OH yield from the four liquids, by dividing

the relative OH intensity at each point (which is proportional to OH number density) by its appearance time.

It is clear from figure 5.8 that more OH scatters from PFPE than the other liquids. Despite this, a significant fraction still escapes the potentially reactive squalane, squalene, and oleic acid surfaces. This OH survival probability, σ, is related to the uptake coefficient, γ, according to equation 5.1.

$$\gamma = 1 - \sigma \qquad \text{Equation 5.1}$$

The survival probability can be quantified only when the internal energy distribution of the scattered OH is defined. A comparison of figures 5.8 (a) and (b) show that more OH is scattered into $N' = 1$ for squalane while more is scattered into $N' = 5$ for oleic acid. As well as differences in the amount of OH scattered from each liquid the appearance profiles also show more subtle effects, particularly in $N' = 1$.

Profiles from PFPE are comparatively narrow, squalane and oleic acid profiles are broader, whilst squalene is intermediate. The peak arrival time (inversely proportional to the speed of the scattered OH) is liquid and rotational-quantum-state dependent: for $N' = 1$ PFPE peaks earliest at ~11 μs; squalene at ~12 μs; oleic acid at ~14 μs; and squalane at ~15 μs. In $N' = 5$ the differences are less clear, while PFPE peaks earliest, the peak arrival times of the remaining liquids are more nearly coincident.

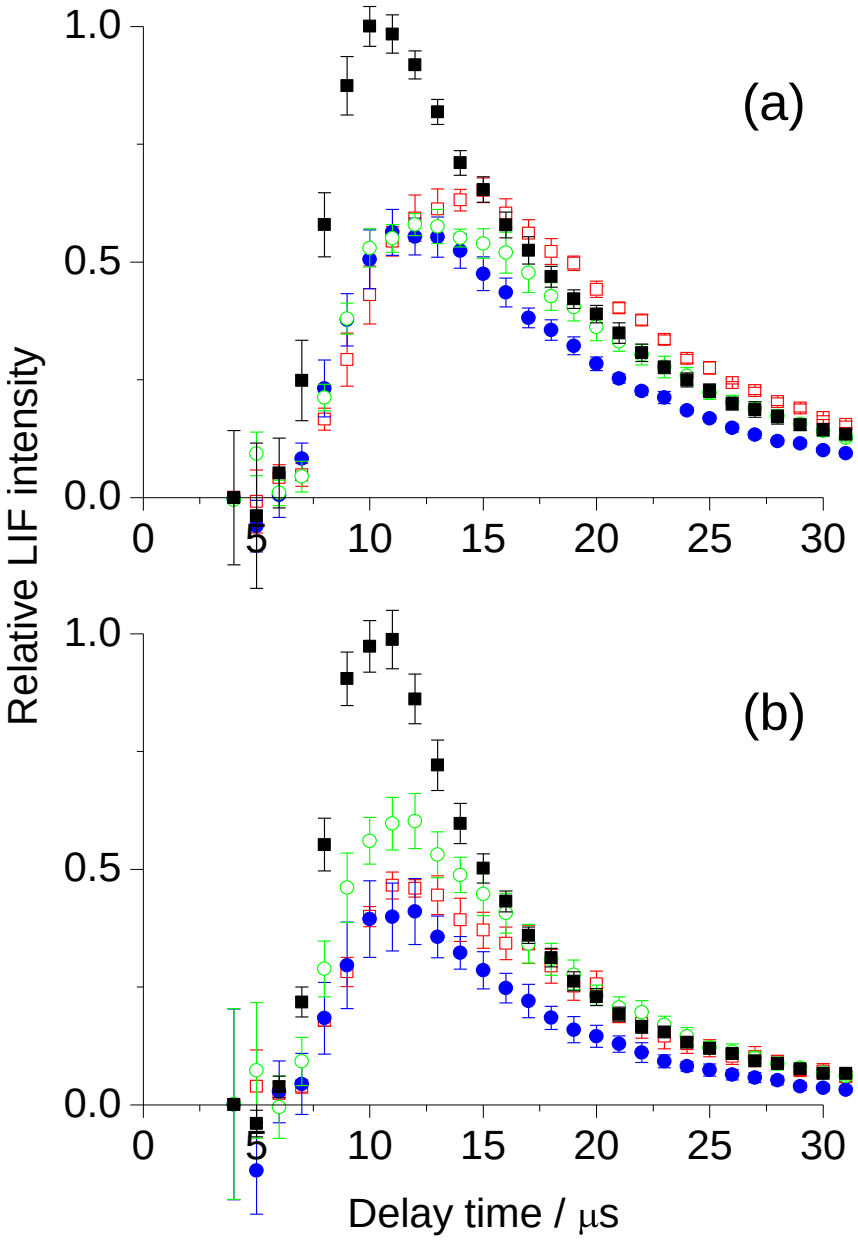

Figure 5.8: Appearance profiles of the OH radical recorded on the *A*-*X* (0,0) (a) $Q_1(1)$ and (b) $Q_1(5)$ transitions scattered from: PFPE (black filled squares); squalane (red open squares); squalene (blue closed circles); and oleic acid (green open circles). Signals have been inversely time-weighted to reflect fluxes and the respective background signals have been subtracted. Error bars are the 1σ standard error in the mean of the measured data points. *p*(HONO) ~1 mTorr, wheel-laser axes distance = 9 mm. Data from experiment 2.

5.3.4 Appearance profiles – rotational quantum state dependence

The rotational state dependence of the appearance profiles for each liquid is shown in figure 5.9. It is clear that the rising edges for $N' = 1$ and $N' = 5$ are essentially coincident in all cases. The differences are most obvious at long times where $N' = 1$ gains over $N' = 5$ for all four liquids. This reflects a rotational distribution that is dependent on photolysis-probe laser delay. There are a number of possible rationales for this behaviour: a dynamical effect, whereby the fastest molecules are also the most rotationally excited; evidence for a TD mechanism; or the effect of multiple collisions at longer time delays. These will be addressed in the subsequent sections, where the internal state distribution is probed in greater detail, and in the discussion (section 5.4).

Included in figure 5.9 is a Monte Carlo simulation of a thermal Boltzmann component as described in chapter 2 (section 2.8.3) and in the previous work of the McKendrick group[147]. The Maxwell-Boltzmann most probable speed at 300 K for OH is ~540 m s^{-1}. The appearance profiles in figure 5.9 show that for all 4 liquids the peaks occur at times that are much too early to be compatible with thermally desorbed (TD) OH speed distributions. This can be illustrated by a simple calculation of most-probable speeds. The average speed of the incoming OH is known to be 2500 m s^{-1}, so for direct travel over the minimum distance (1.8 mm) from the photolysis beam to the surface the time taken would be around 3.6 μs. A typical peak arrival time in figure 5.9 is around 14 μs. The difference of 10.4 μs would correspond to an average speed of ~900 m s^{-1} for the return leg of OH from the surface to the probe volume. Although a significant fraction of the incoming speed is therefore absorbed in the collision with the liquid, the residual speed is still significantly in excess of the most probable speed of 540 m s^{-1} in a 300 K sample of OH.

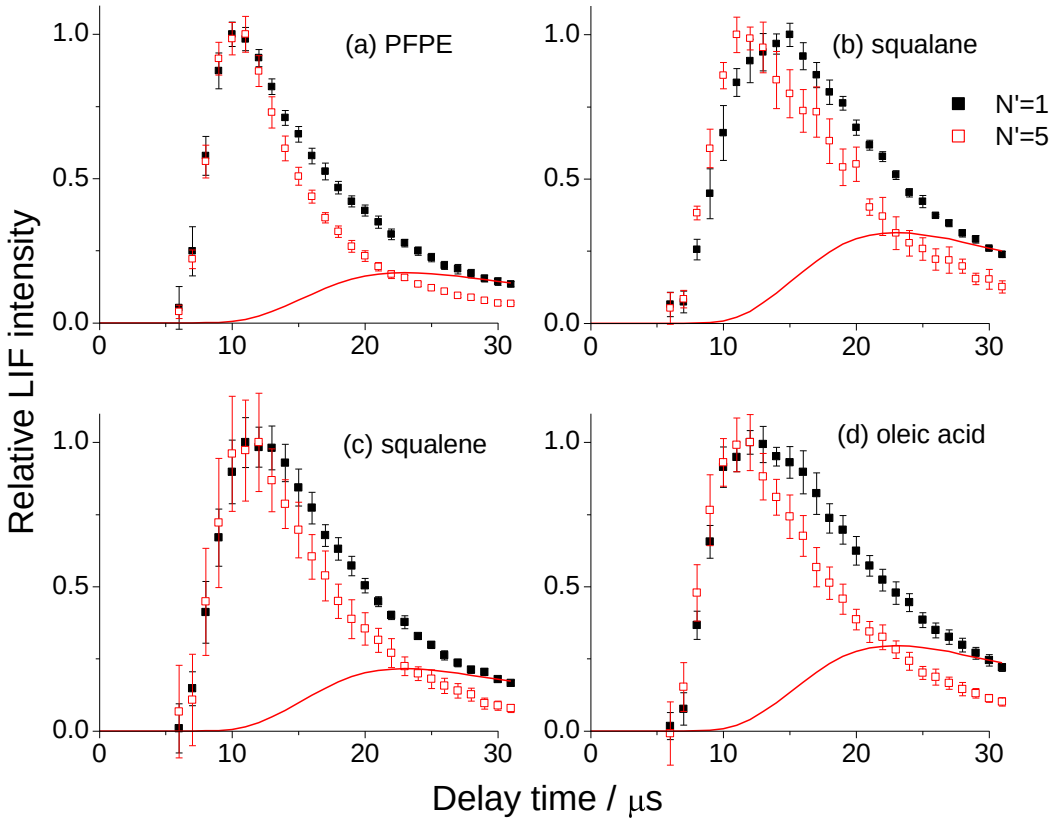

Figure 5.9: Appearance profiles of the OH radical recorded on the *A*-*X* (0,0) $Q_1(1)$ (black closed squares) and $Q_1(5)$ (red open squares) transitions scattered from: (a) PFPE, (b) squalane, (c) squalene and (d) oleic acid. Red lines are a Monte Carlo simulation of a 300 K thermal distribution. Signals have been inversely time-weighted to reflect fluxes and the respective background signals have been subtracted. Error bars are the 1σ standard error in the mean of the measured data points. *p*(HONO) ~1 mTorr, wheel-laser axes distance = 9 mm. Data from experiment 2.

5.3.5 Measured excitation spectra – rotational energy distribution of the pre- and post-collision OH

The appearance profiles provide some information on the rotational distribution of the scattered OH. However, in order to gain a fuller picture of rotational energy transfer in the scattering process, excitation spectra were recorded. Rotational spectra of OH in the ground vibrational state were recorded pre- and post-collision with each of the liquids at a photolysis-probe time delay corresponding to the peak in the appearance profiles for the scattered OH. The time delays chosen were: 4 μs (pre-collision), 12 μs (PFPE), 16 μs (squalane), 14 μs (squalene) and 16 μs (oleic acid). Representative spectra are shown in figure 5.10.

In experiment 1, the *thermal calibration* method was used (as described in chapter 2) to extract rotational populations and assign Boltzmann temperatures to them. The thermal calibration was used to correct for issues such as saturation and variation of probe laser energy and detection sensitivity with wavelength. Experiment 2 was carried out on a diagonal band ($\Delta v = 0$), at lower probe laser energies and hence a linear regime. To test whether a thermal calibration spectrum was necessary a spectrum of collisionally thermalised OH was recorded at a pressure of 120 mTorr (1 mTorr HONO, 120 mTorr N_2) and photolysis-probe delay of 100 μs. Assuming a typical gas-kinetic collision rate of 1×10^7 $Torr^{-1}s^{-1}$, the OH radicals would have undergone approximately 120 collisions on average under these conditions. Populations were extracted from the thermal spectrum using the LIFBASE[145] spectral simulation program and a Boltzmann temperature was assigned to them. An average of three such spectra resulted in a rotational temperature (with a 1σ associated error) of 304±21 K. As a result, for experiment 2 the rotational populations were extracted directly from the spectra in all cases, both pre- and post-collision.

The raw spectra in figure 5.10 were recorded during experiment 2 and are illustrative of the signal-to-noise level achieved for OH scattering from the liquid surfaces. On first inspection it is clear that the OH is more rotationally excited post-collision than it was pre-collision. This is particularly evident in the R_1 and Q_1 branches where the higher N' levels are comparatively more populated post-collision. The spectra also suggest that there are differences in the rotational distributions from the different liquids, as is particularly evident when comparing squalane and PFPE in the Q_1 branch.

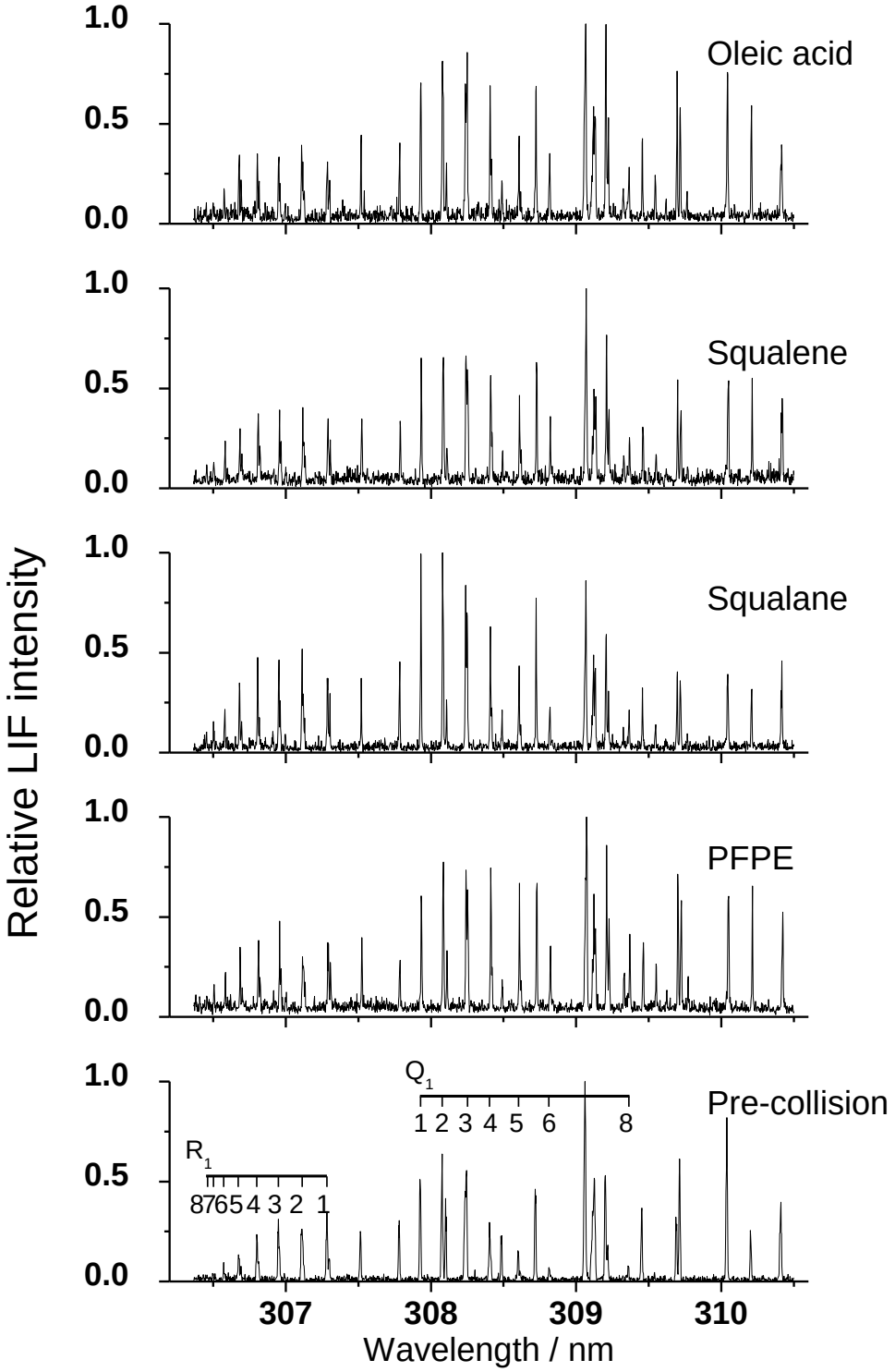

Figure 5.10: Representative peak normalized excitation spectra recorded on the OH *A*-*X* (0,0) band, recorded at a photolysis-probe time delay of 4 μs (pre-collision), 12 μs (PFPE), 16 μs (squalane), 14 μs (squalene) and 16 μs (oleic acid). Post-collision spectra contain an underlying cooling contribution of photolytically generated (pre-collision) OH. Bath temperature ~298 K, *p*(HONO) ~1 mTorr, wheel-laser axes distance = 9 mm.

5.3.6 Rotational energy distribution – pre-collision OH

The rotational population distribution for the R_1, Q_1 and R_2 rotational branches and associated Boltzmann plots for the pre-collision OH is shown in figure 5.11. The error bars are the 1σ standard error in the mean of four independent measurements. The rotational populations (figure 5.10 (a)) and the Boltzmann plots (figure 5.10 (b)) show a non-statistical population distribution. The rotational temperatures (table 5.1) are similar in each of the three branches, although the R_2 branch is slightly colder (as evidenced by the change in gradient in figure 5.10 (b)) when the final $N' = 8$ point is ignored). The F_2 ($^2\Pi_{1/2}$) spin-orbit manifold is preferentially populated when energy and degeneracy are accounted for, visible as the R_2 branch points lying above the R_1 branch points in the Boltzmann plot. This is also evident in the raw spectra when compared to a thermal spectrum with a statistically populated rotational distribution.

T_{Rot}/K (R_1)	T_{Rot} /K (Q_1)	T_{Rot} /K (R_2)	T_{Rot} /K (R_2)[a]
355±24	368±31	367±25	306±19

Table 5.1: Rotational temperature of the pre-collision OH form HONO photolysis, detected at 4 μs photolysis-probe laser time delay, for the R_1, Q_1 and R_2 spectroscopic branches. [a] the rotational temperature on the R_2 branch if the $N' = 8$ point is ignored as described in the text.

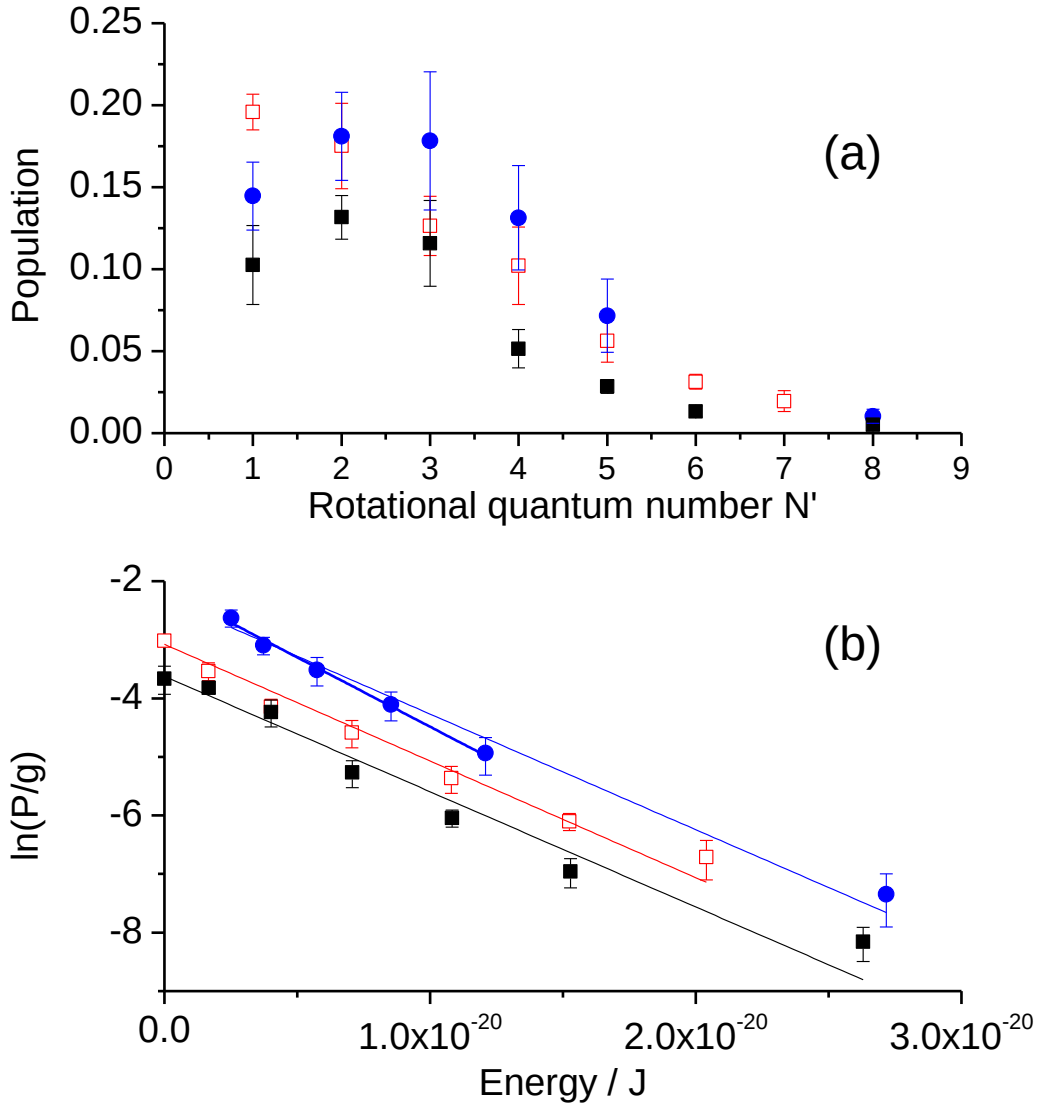

Figure 5.11: (a) Rotational population distributions for OH formed from HONO photolysis at 355 nm. Measured on the R_1 (red open squares), Q_1 (black closed squares) and R_2 (blue closed circles) spectroscopic branches. Extracted from LIF excitation spectra recorded on the OH *A*-*X* (0,0) band. Error bars reflect the standard error in the mean of repeated independent measurements (4 per liquid). (b) The associated Boltzmann plots for the three branches, from which the rotational temperature is established.

5.3.7 Rotational energy distributions of the isolated scattered OH

As was established in section 5.3.2, the measured spectra (figure 5.10) contain an underlying component resulting from a contribution from the pre-collision OH. The extent to which this will influence the population distributions extracted from the measured spectra can be quantified using the appearance profiles in figure 5.7. The appearance profiles provide a pre-collision to post-collision ratio for each delay. This was quantified by comparing the relative intensities of a given transition, recorded with and without a liquid covered wheel. This pre-:post-collision ratio, in addition to the knowledge of the rotational distribution of the pre-collision OH, was used to subtract the underlying photolytic component, hence isolating the rotational distribution of the scattered OH.

Figure 5.12 shows the rotational population distributions extracted from the Q_1 branch of the excitation spectra (labelled post-collision extracted) recorded at the peak of the appearance profiles for oleic acid (16 μs). The pre-collision rotational distribution is included also, having been scaled to the appropriate pre-:post-collision ratio determined from the appearance profiles in figure 5.7(a). Subtraction of the pre-collision populations from the post-collision extracted gives the populations from the post-collision *scattered* OH in isolation. This was repeated for each of the four liquids from both the $Q_1(1)$ (figure 5.6 (a)) and $Q_1(5)$ (figure 5.7(b)) appearance profiles. Rotational temperatures for the purely scattered OH were then established from Boltzmann plots and are summarised in table 5.2.

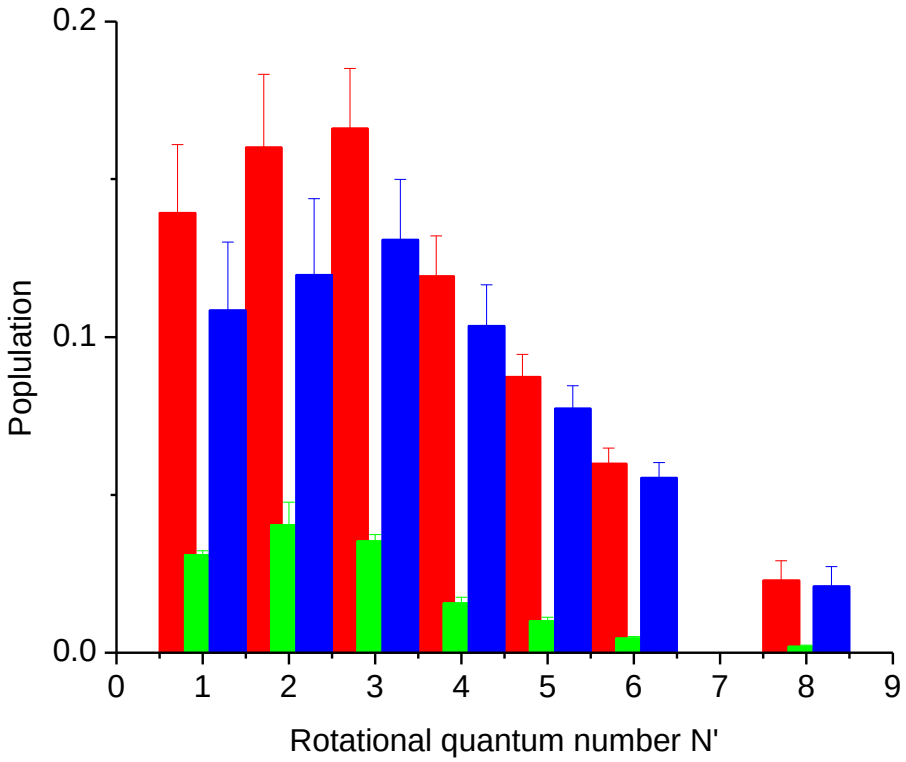

Figure 5.12: Rotational populations extracted from the excitation spectra of pre- (green) and post-collision (red) with oleic acid scaled to the appropriate pre-:post-collision ratios determined from figure 5.6(a). The subtraction of the pre-collision populations from the measured post-collision populations gives the post-collision distribution due to purely scattered OH (blue), without an underlying fraction of pre-collision OH.

	Pre-collision	PFPE	Squalane	Squalene	Oleic acid
Extracted rotational temperature / K	355±24	598±11	473±33	587±15	552±25
Scattered OH temperature / K (scaled at N'=1)		652±11	494±33	634±15	592±25
Scattered OH temperature / K (scaled at N'=5)		706±33	521±35	734±44	661±16
Experiment 1 scattered OH temperature / K (scaled at N'=1)	329±35	655±56	473±27		

Table 5.2: Rotational temperatures of nascent OH (v' = 0) extracted from excitation spectra recorded pre- (4 μs) and post-collision with a liquid surface (12 μs (PFPE), 16 μs (squalane), 14 μs (squalene) and 16 μs (oleic acid). Scattered OH temperatures refer to the rotational temperatures of the scattered OH without any contribution from an underlying photolytic component. Pre- :post-collision scaling applied at both N' = 1 and N' = 5 as described in the text. Errors quoted are the 1σ error in the exponent obtained from a χ^2-minimizing fitting routine applied to an exponential fit to the extracted populations (/degeneracy), weighted by the appropriate error (standard error in the mean of multiple measurements) at each point.

The rotational temperatures in table 5.2 show that the result of subtracting out the photolytic pre-collision component is a modest increase in rotational temperature compared with those extracted directly from the spectra. Close inspection of the rotational temperatures show excellent agreement between the two studies, experiment 1 and the more comprehensive experiment 2. The rotational temperatures generated following pre-:post-collision scaling at N' = 5 agree qualitatively with those scaled at N' = 1. The rotational temperature is higher post-collision with all liquids and OH scattered from squalane is colder than from the other liquids. There is however a quantitative disparity in that the N' = 5 temperatures are consistently hotter than the N' = 1 temperatures, particularly so for squalene.

The two analysis methods, scaling to N' = 1 and N' = 5, should yield the same temperatures. It is likely that the origin of the discrepancy is a result of poorer signal to noise in the excitation spectra and appearance profiles for N' = 5 compared with N' = 1.

This effect is worse for squalene than the other liquids as squalene gives the smallest scattered OH signal. This error is not reflected in the error quoted in table 5.2, as it is a systematic rather than a statistical error. On the assumption that the $N' = 5$ temperatures contain an additional source of un-quantified systematic error, they will be used only for qualitative observations. The $N' = 1$ temperatures in contrast are in much better agreement with the rotational temperatures recorded during experiment 1. They are also in agreement with the temperature derived from a simple two-point extrapolation from the relative intensities of the appearance profiles at a delay consistent with that at which the original spectra were measured (as described further in section 5.3.9).

5.3.8 Λ- Doublet and spin-orbit propensity comparison for the pre- and post-collision OH

In section 5.3.6 it was established that the OH formed from HONO photolysis preferentially populates the F_2 spin-orbit manifold, as evidenced by comparison of the relative intensities of the R_1 and R_2 spectroscopic branches. It also indicates the preferred population of the A' Λ-doublet over the A" Λ-doublet (table 5.3). The rotational temperature of the OH formed was also found to vary depending on the spin-orbit manifold, being generally cooler in the F_2 manifold (table 5.1), the extent to which depends on the range of rotational quantum states included in the Boltzmann fit.

The spin-orbit and Λ-doublet propensities were also probed post-collision. The Boltzmann plots (figure 5.13) clearly show that for the case of OH scattering from PFPE and squalene, the spin-orbit and Λ-doublet preferences of the pre-collision OH are lost. The Boltzmann plots are collapsed to a common line (within errors) for the three spectroscopic branches probed. The rotational temperature (illustrated by the gradient of the linear fits) and hence rotational distribution in the F_1 and F_2 spin-orbit manifolds have also equilibrated post-collision.

The rotational populations and hence Boltzmann plots for OH scattered from squalane and oleic acid show larger statistical fluctuation. This is most likely a result of the pre-collision contribution subtraction procedure. Despite this, they show that any spin-orbit and Λ-doublet preference is also reduced post-collision with these liquids. The plots imply that some of the spin-orbit and Λ-doublet preference may be retained with these liquids. However, within the limits of the uncertainties in the populations, it is impossible to conclude this with certainty.

N'	$P_{A'}(R_1)$	$P_{A''}(Q_1)$	$P_{A'}$:$P_{A''}$	$I_{A'}$:$I_{A''}$ linestrength	A'/ A''	Previous work[a]
2	0.1751	0.1316	1:0.7517	1:1.00	1.33	<1.58
4	0.1020	0.0515	1:0.5049	1:1.01	2.00	1.93
5	0.0561	0.0285	1:0.0508	1:1.01	1.99	2

Table 5.3: The Λ-doublet population ratios for OH formed from HONO photolysis. [a] from Vasudev *et al.*[140].

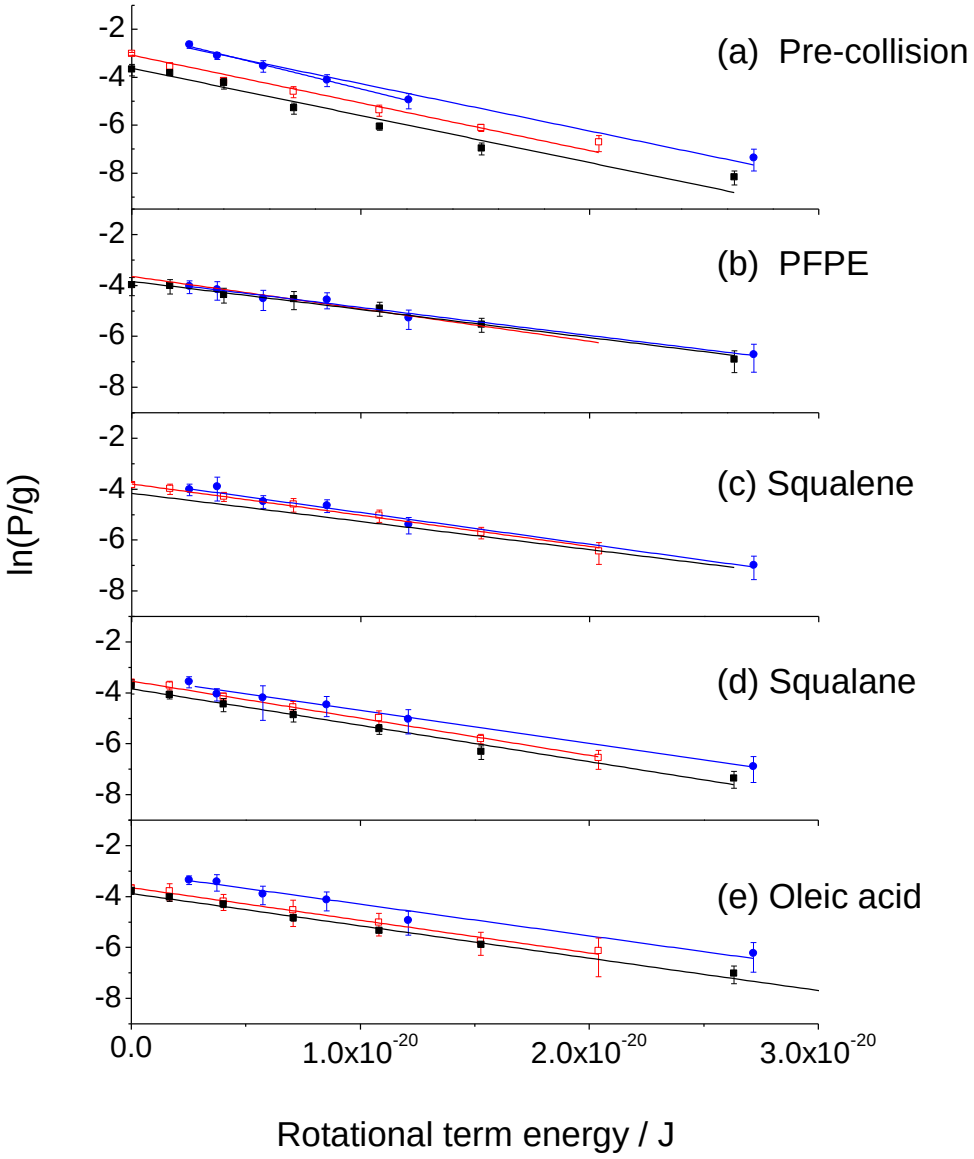

Figure 5.13: Boltzmann plots for OH (a) pre- collision and post-collision with (b) PFPE, (c) squalene, (d) squalane and (e) oleic acid liquid surfaces. Populations from the R_1 (red open squares), Q_1 (black closed squares) and R_2 (blue closed circles) spectroscopic branches are included. Pre-collision populations are extracted directly from the measured spectra, post-collision spectra are the populations extracted from the relevant spectra, minus the appropriate pre-collision population distribution as determined by the pre-:post-collision ratio.

5.3.9 Two-point and global rotational temperatures

In section 5.3.4 the appearance profiles (figure 5.9) measured on different rotational lines provided an indication that the rotational temperature is dependent on the photolysis-probe laser time delay at which it was measured. A rotational temperature that was independent of time delay would result in profiles identical in shape for the two transitions. An idealised experiment would be one where an excitation spectrum could be measured at each time delay along the appearance profile, giving a full picture of how the rotational distribution varies with delay. In practice this could not be achieved as a single excitation spectrum at one time delay required at least 3 hours of experimental time. As a best alternative *two-point temperatures* were extracted from the measured appearance profiles as a function of photolysis-probe delay.

The two-point temperatures were deduced by using the relative intensity of the $N' = 1$ ($Q_1(1)$) and $N' = 5$ ($Q_1(5)$) lines (figure 5.7 insets) at a given delay time and assuming they were in a Boltzmann ratio. The resulting rotational temperatures at each delay are shown in figure 5.14. The error in the two-point rotational temperature is the combination of the errors in the intensity at each time delay in the measured appearance profiles for each rotational line.

The vertical lines in figure 5.14 are to illustrate the time delays at which the excitation spectra (figure 5.10) were measured. The two-point rotational temperatures at a given delay should, in principle, replicate the rotational temperatures extracted from the measured excitation spectra. The approximate two-point temperatures at these times are provided in table 5.4. Overall there is excellent agreement between these crude two-point temperatures and the scattered OH rotational temperatures in section 5.3.7. The exception is squalene, whose two-point rotational temperature is consistently colder than the other liquids and colder than that extracted from the excitation spectra (634±15 K). There is no physical basis to believe that this is anything other than an experimental error in the squalene appearance profiles. The appearance profiles and excitation spectra at a common delay must contain the same information. This experimental error can be isolated to the squalene $N' = 5$ appearance profiles being slightly smaller than they should be.

This would explain an apparently colder rotational temperature and is also behind the systematic error described for the squalene $N' = 5$ scattered OH rotational temperature

in table 5.2. The most likely source of this error would have been in fixing the laser wavelength on the $Q_1(5)$ transition when measuring the appearance profiles. The appropriate wavelength was selected by scanning the probe wavelength across the peak of the transition and determining the wavelength at which the OH signal was at a maximum. This was required as the wavelength output of the probe laser would vary by very small amounts day-to-day due to fluctuations in temperature. Identifying the exact wavelength at which the OH signal is at a maximum was influenced by many factors such as shot-to-shot fluctuations in laser power, HONO concentration and background noise. It is plausible that the squalene $N' = 5$ profiles were the most likely to contain this error as the $N' = 5$ profiles contained the most background noise and the squalene profiles give the smallest scattered OH signals.

Having established that there is most likely a systematic error resulting in the squalene $N' = 5$ profiles being smaller than expected, a correction factor was applied to the two-point temperatures for squalene as shown in figure 5.14. This was achieved by effectively forcing the two-point temperature at 14 μs to agree with the rotational temperatures extracted from the measured excitation spectra (634 K). To replicate this temperature would be the equivalent of the squalene $N' = 5$ profiles being a factor of 1.28 larger than the measured profiles. This factor, in essence, is the amount by which the systematic error has affected the squalene $N' = 5$ profiles and has been applied to the data for analysis in the following sections when explicitly stated. Otherwise the assumption should be that the squalene data being used are as they were measured.

The two-point temperatures for all liquids, including the corrected and uncorrected temperatures for squalene, show similar delay-time-dependent behaviour. The rotational temperatures decrease rapidly over the first 20 μs, before beginning to level off and decline more slowly towards more thermal temperatures at longer delays. This echoes what was seen in the appearance profiles measured on different rotational lines for a given liquid (figure 5.9), where the $N' = 1$ profiles become more dominant at longer times. To account for this effect and quantify it for the different liquids, the concept of a *global rotational temperature* was introduced.

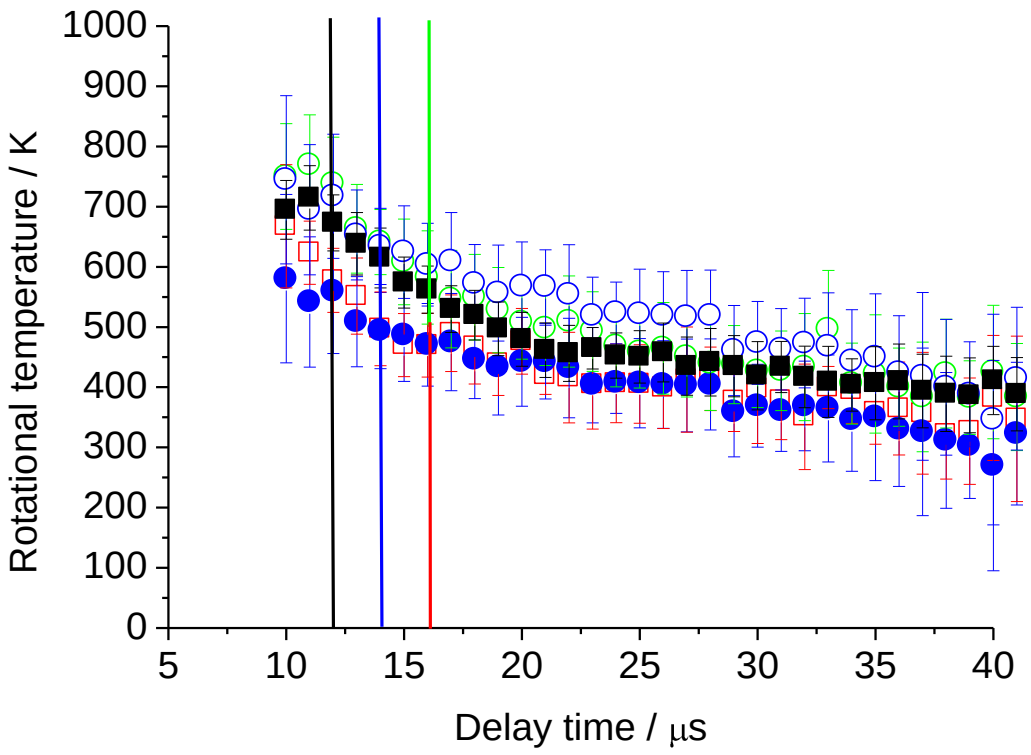

Figure 5.14: Two-point rotational temperatures as a function of photolysis-probe delay time for PFPE (black closed squares), squalane (red open squares), squalene (blue closed circles) and oleic acid (green open circles). Temperatures assigned by using the relative intensity of the N' = 1 ($Q_1(1)$) and N' = 5 ($Q_1(5)$) lines at a given delay time, assuming they were in a Boltzmann ratio. The error bars are the resultant combined 1σ errors from the standard error in the mean at each time delay in the appearance profiles used. Included is the 'corrected' squalene two-point temperatures (blue open circles) generated by forcing the two-point temperature for squalene at 14 μs to 634 K. The vertical lines are illustrative of the time delays at which the excitation spectra were measured for each liquid.

The global temperature is an overall average rotational temperature for OH scattered from a given liquid over a defined range of delay times (in this case 4-30 μs). The global temperatures were calculated by using the flux-weighted integrals (figure 5.8) of the $N' = 1$ and $N' = 5$ OH appearance profiles for a given liquid (area is proportional to OH yield) as two-points in a Boltzmann plot. The method is similar to that for the two-point temperatures but area rather than intensity at a single point was used. The global temperatures are shown in table 5.4. The errors reflect the 1σ statistical uncertainty associated with the integrated fluxes used to calculate the global temperatures.

The global temperatures are related to those extracted from the excitation spectra. The exception being squalene for the reasons described above. Following the application of the correction factor to the squalene $N' = 5$ area, the corrected global temperature for OH scattered from squalene is 574 K. The global temperatures will be used in section 5.3.11 to calculate the OH survival probability following collision with the four liquids.

	PFPE	Squalane	Squalene	Oleic acid
Extracted rotational temperature / K	598±11	473±33	587±15	552±25
Scattered OH temperature / K (scaled at N'=1)	652±11	494±33	634±15	592±25
Two-point temperature / K	670	470	500	600
Global temperature / K	598±41	500±20	479±22 574±26[a]	606±30

Table 5.4: Re-presented from table 5.2 are the rotational temperatures of nascent OH ($v' = 0$) extracted from excitation spectra. 'Scattered OH' refers to the rotational temperatures of the scattered OH without any contribution from an underlying photolytic component. Also included are the two-point and global temperatures. [a] the global temperature after the correction factor had been applied for squalene (as described in the text).

5.3.10 Quantification of a possible thermal component

The broader shape of the appearance profiles from squalane and oleic acid could be indicative of a more significant TD component. The simulations shown in figure 5.8 (section 5.3.4) were fit to the appearance profiles at 25-30 μs. Comparison of the relative integral of the measured and simulated appearance profiles (as fluxes) gives a maximum TD or thermal component scattered from each liquid. This is quoted as a maximum TD component as it has been established in theoretical treatments of similar systems that 'slow' products can also be the result of single-hard collisions. This was described in detail in chapter 1 (section 1.4).

The simulations were fit to both the $N' = 1$ and $N' = 5$ profiles for each of the four liquids. These both should, in principle, yield the same TD component after correction for the different rotational temperatures of the direct IS ('scattered' OH temperatures, table 5.4) and TD (assumed 300 K) components. This correction was necessary to account for the different fractions of each population in a given rotational quantum state for a particular rotational temperature. The overall maximum (average of that determined from the $N' = 1$ and $N' = 5$ profiles) TD components for experiment 2 are: PFPE (13±2%), squalane (23±5%), squalene (14±2%) and oleic acid (17±3%). The PFPE and squalane TD components compare quite favourably with the earlier preliminary measurements (experiment 1) of PFPE (9±1%) and squalane (22±2%). The shape of the appearance profiles from experiment 1 and 2 are essentially identical when overlaid.

5.3.11 OH survival probability

The OH survival probability (σ) (equation 5.2) is inferred by assuming the observed integrated flux from PFPE represents 100% survival probability of OH molecules that impact the surface. The relative observed integrated fluxes for the other liquids can then be compared with that from PFPE. This requires the respective global temperatures (section 5.3.9), which compensate for the amount of OH scattered into each quantum state to be taken into account. This is achieved using the relationship highlighted in equation 5.2. σ is defined to be the ratio of the integrated product flux from a given liquid, $f(N')_{liq}$, to that from PFPE, $f(N')_{PFPE}$, following an adjustment for the relative fractions of the total rotational population, $p(N')_{liq}$ and $p(N')_{PFPE}$, respectively, that reside in the level for which the profiles were measured.

This method is reliant on: (a) there being no other unrecognised sources of OH at any of the surfaces, such as through the reaction of $O(^3P)$ (from any significant amounts of NO_2 being present) as discussed in section 5.3.1; (b) any differences in angular scattering distributions between the liquids being safely neglected; and (c) the introduction of a finite upper limit on the range of integration (i.e. 30 μs) does not create a bias between the liquids.

The resulting survival probabilities are given in table 5.5. The trend in OH survival is oleic acid>squalane>squalene. The survival probability of σ = 0.52±0.05 for squalene is likely to be an underestimation, directly resulting from the error in the N' = 5 squalene appearance profile (sections 5.3.7 and 5.3.9) which consequently affects the global temperature used. This can be accounted for by using the corrected global temperature provided in table 5.4. The correction factor of 1.28 was applied to the N' = 5 profiles from squalene, and the result was an OH survival probability of 0.61±0.06.

$$\sigma = \frac{\int_0^{max} f(N')_{PFPE}\, dt}{\int_0^{max} f(N')_{liq}\, dt} \times \frac{p(N')_{liq}}{p(N')_{PFPE}} \qquad \text{Equation 5.2}$$

Regardless of the analysis method for squalene, whether the correction factor is applied or not, the amount of OH returning from the squalene surface is less than that from squalane. The OH survival probabilities measured are the complement of the reactive uptake coefficients (γ) discussed in the introduction (section 5.1.2) as expressed in

equation 5.1. The estimated OH reactive uptake coefficients are therefore ~0.30 for squalane, ~0.48 (without correction) or ~0.39 (with correction) for squalene and ~0.24 for oleic acid liquid surfaces.

Experiment 1 yielded an OH survival probability of 0.51±0.04 for squalane, where the error reflects the statistical error in the measurement. The differences between the OH survival probabilities in the two experiments are due to a number of factors, the most significant of which is the number of repeat measurements made. In the first set (experiment 1) only one set of results, recorded on two rotational lines were used per liquid. In the second set, at least five independent measurements were made (on both rotational lines) per liquid. There were also a number of experimental improvements introduced following the preliminary proof-of-concept study (experiment 1). These included the use of the second generation wheel which resulted in greater distance reproducibility and a more precise dropping funnel for $NaNO_2$ addition. As a result of these factors, the measurements made during the second set of experiments (experiment 2) summarised in table 5.5, can be considered the most accurate.

	PFPE	Squalane	Squalene	Oleic acid
OH survival probability	1.00	0.70±0.06	0.52±0.05/**0.61±0.06**	0.76±0.07

Table 5.5: Measured OH survival probabilities from the four liquids. The value in bold is the corrected squalene value and the errors reflect the 1σ errors in the integrated appearance profiles used.

5.4 Discussion

5.4.1 OH survival probability and reaction mechanism

The inherent assumption here is that the PFPE liquid is unreactive, and that the integrated flux from PFPE represents 100% scattered OH. The relative OH fluxes from the other liquids were then used to deduce the OH survival probability at each liquid surface (section 5.3.11). This also assumes that there are no differences in the angular scattering distributions from the different liquids, these cannot be established in the current set-up. Despite this, the Monte Carlo simulations which take into account the geometry of the experiment suggest that the OH signal observed would be largely insensitive to the direct IS scattering angular distribution.

Starting with the liquid hydrocarbon squalane, the survival probability (from experiment 2) was found to be 0.7±0.06, meaning that around 30% of the OH radicals hitting the surface are *lost*. The fate of the OH lost at the squalane surface is presumably to undergo a hydrogen abstraction reaction to form water. Typical barriers for these reactions are in the region of 3-10 kJ mol^{-1}[184], well below the average energy of the incoming OH in these experiments and close to thermal energies. The fact that the majority of OH radicals survive collision at the squalane surface is an important corroboration of the previous work of McKendrick and co-workers on O(^{3}P) and liquid hydrocarbons[63,66,69,124]. They found that slow moving, potentially thermalised, OH radicals are able to escape the surface without reacting further to form H_2O.

The reaction probability at the squalane surface of approximately 0.3 is a significant enhancement over the per-collision gas-phase reaction probability between OH and an alkane. These reactions typically have Arrhenius A-factors in the region of ~10^{-11} cm^3 s^{-1}[184]. This, compared with a gas-kinetic rate constant of ~3×10^{-10} cm^3 s^{-1} gives an estimated reaction probability of 0.03. This estimate assumes that all collisions take place with energies above the barrier. In the work described in this chapter the majority of the OH formed in the photolysis have energies well above the barrier making this a reasonable analogy. Comparison to a gas-phase reaction probability is an obvious oversimplification and an increased reaction probability for a gas-liquid reaction is expected. A significant contributory factor to this reactive enhancement is that in the gas phase, a large fraction of non-reactive encounters are forward scattered, after which

the scattering event is over. In gas—liquid interfacial collisions, however, that forward-scattered non-reactive encounter will inevitably lead to a secondary collision with another part of the surface. If this then leads to trapping and multiple additional encounters, the rate will be increased by a corresponding multiplicative factor.

The results reveal that more OH reacts at the squalene surface than at the squalane surface. This has been shown to be true with and without a correction factor applied to the squalene profiles (section 5.3.11). The same hydrogen abstraction reaction channel (equation 4) is available in squalane and squalene. There is also a second channel for squalene, proposed to be a capture mechanism (equation 5).

$$OH + R\text{-}CH(R')\text{-}R'' \rightarrow R\text{-}C^{\bullet}R'\text{-}R'' + H_2O \qquad (4)$$

$$OH + R\text{-}CH{=}C(CH_3)\text{-}R'' \rightarrow R\text{-}C^{\bullet}H\text{-}COH(CH_3)\text{-}R'' \text{ or } R\text{-}CH(OH)\text{-}C^{\bullet}(CH_3)\text{-}R'' \qquad (5)$$

The appearance profiles (figure 5.8) are re-presented in figure 5.15 alongside a Monte Carlo simulation of a 300 K thermal distribution. The profiles from squalene peak earlier and are narrower than those from squalane. The OH molecules from squalene appear to be travelling faster and are more rotationally excited than those from squalane. The dynamical implications of this will be discussed in sections 5.4.2 and 5.4.3. However, within the context of reactivity at the liquid surfaces, it appears that some of the slow-moving OH molecules returning from squalane are missing from squalene.

To test this hypothesis, for each of the levels, $N' = 1$ and 5, a least-squares fit of the composite of the observed squalene profile plus a weighted multiple of the TD prediction to the observed squalane profile was carried out. Figure 5.15 shows that the shape of the squalane appearance profile can be effectively reproduced by adding a thermal (TD) component to the squalene profile. The fact that a smaller multiple of the TD component is required to replicate the $N' = 5$ profiles also supports the hypothesis that it is the slower, rotationally colder OH molecules which are missing. It is proposed that the slow, rotationally cold OH preferentially reacts via the capture mechanism. This is consistent with the gas-phase behaviour of OH reacting with alkenes, where the reaction rate is known to have a negative temperature dependence[212]; the reaction is faster for low energy OH. For this reason it could be anticipated that this effect could be even more pronounced under atmospherically realistic collision energies.

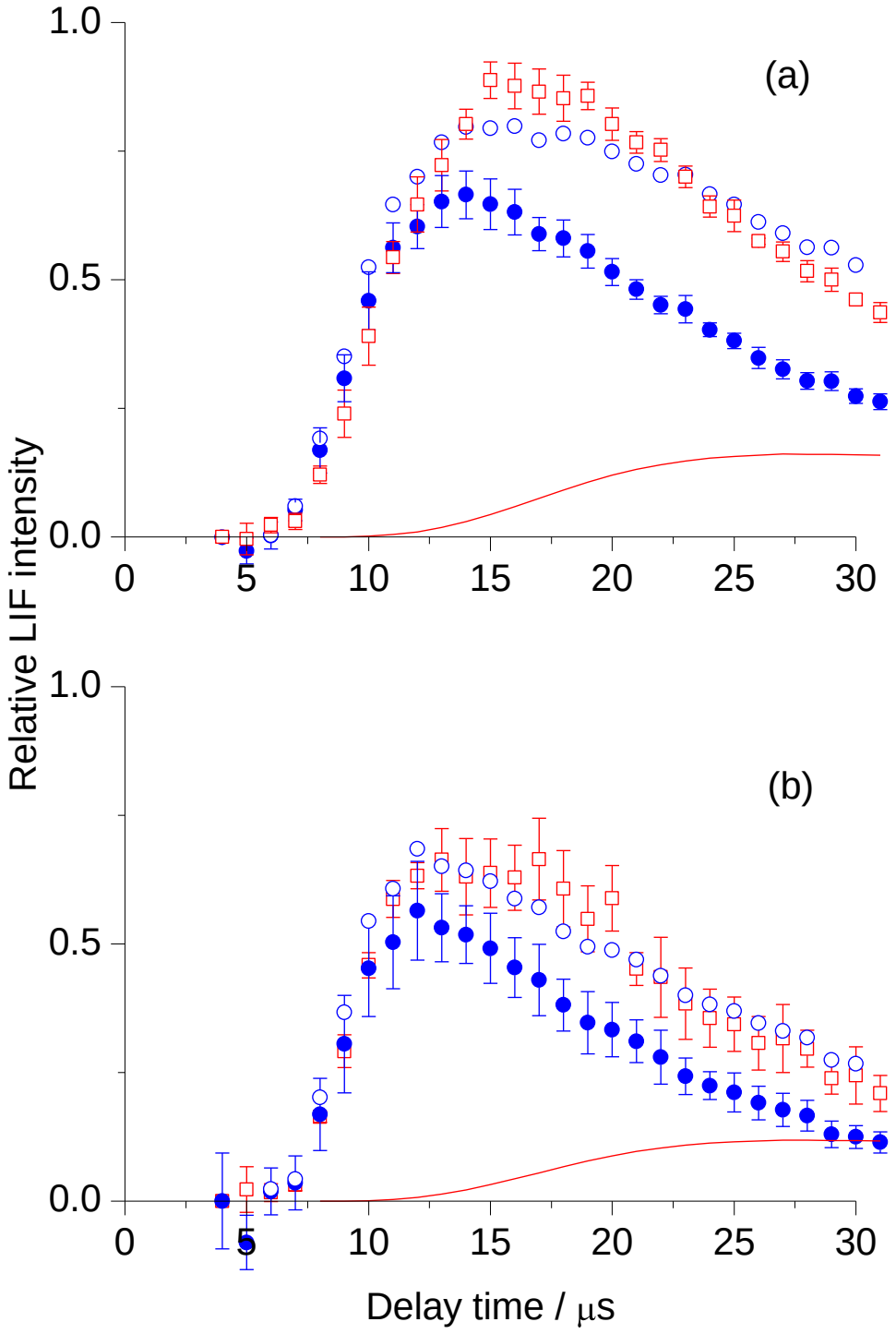

Figure 5.15: OH A-X (0,0) appearance profiles recorded on the (a) $Q_1(1)$ and (b) $Q_1(5)$ transition, following subtraction of the fit to the profiles recorded in the absence of a liquid covered wheel, from squalane (red open squares) and squalene (blue closed circles). Included is a Monte Carlo simulation of a thermal component, addition of this thermal component to the squalene data is also shown (blue open circles).

The survival probability from oleic acid was found to be 0.76±0.07. This is slightly higher than that measured from squalane, although both measurements lie within each other's uncertainty limits. A higher survival probability and therefore lower reactive uptake for oleic acid could be explained as a result of OH radicals colliding with the unreactive COOH head-groups which are absent in the squalane structure. What is certain is that the double bond in oleic acid plays no significant role in enhancing reactivity at the oleic acid surface. This could suggest that the double bonds are either not available at the interface or are simply too dilute to make an observable difference.

The reactive uptake measurements will now be discussed in the context of those described in the introduction (section 5.1.2). An interesting comparison is with Molina and co-workers[79,80], who also measured OH loss. Their uptake coefficients were, $\gamma = 0.34$ for paraffin wax and $\gamma = 0.29$ for a methyl terminated monolayer. Both are effectively hydrocarbon surfaces and are in excellent agreement with the squalane measurement reported here ($\gamma = 0.30$). Palmitic acid ($C_{16}H_{32}O_2$) gave a coefficient, of 0.32, which is comparable to the oleic acid measurement here of $\gamma = 0.24$.

Molina and co-workers reported a reactive uptake at a vinyl terminated monolayer of $\gamma = 0.60$, higher than that reported here for squalene ($\gamma = 0.4$). The two studies have reasonable quantitative agreement for some cases but agree qualitatively on all levels. They show that there is very little difference in reactivity between a hydrocarbon and an organic acid and that alkenes are more reactive towards OH than the alkanes. The difference between that measured at the vinyl monolayer and the squalene measurement could be the result of their use of thermal OH. As was described above, the reaction of OH and an alkene has a negative rate dependence. As a result enhanced reactive uptake under ambient conditions (over the superthermal energies used here) would be reasonable.

The flow-tube results of Wilson and Leone[219] are in particularly good agreement with the value for squalane reported here ($\gamma = 0.3\pm0.07$). Smith and co-workers report uptake coefficients of 0.28±0.04 (squalane), >1 (squalene) and 0.4±0.03 (oleic acid)[223]. The differences in this case are more extreme. The squalane measurement agrees almost exactly. Smith and co-workers report however, that oleic acid is more reactive than the hydrocarbon. This may be a consequence of the double bond playing more of a role when thermal OH is used rather than superthermal OH.

In general OH uptake has been found to be an efficient process at a wide range of surfaces and coefficients greater than unity are reasonably common (section 5.1.2). Clearly, any values of $\gamma > 1$ imply that some secondary chemistry must be taking place. It is also possible that this contributes to some of the apparently high efficiencies close to unity. This may explain the disagreement with the lower values for related surfaces above. However, there are also other possible interesting potential explanations, relating to bulk-versus-particle properties, pressure effects and the higher collision-energy regime used here. Given its atmospheric significance, this area would clearly warrant further experimental investigation to disentangle these factors for both single-component liquids and, ultimately, multi-component systems representative of real aerosol surfaces at different stages of aging.

5.4.2 Scattering dynamics and mechanistic interpretation

The shape of the appearance profiles provides some valuable information on the inelastic scattering mechanism. There is however a certain degree of geometric blurring inherent in the experiment. As a result the profiles observed are influenced by: the breadth of the incoming OH translational energy distribution; the incoming and scattered angles; and the inelastic scattering mechanism itself. The factors leading to geometric blurring in the experiment will be discussed first before considering what the profiles are able to reveal about the scattering mechanism.

The incoming OH velocity distribution is fairly narrow at 2500±165 m s^{-1} as determined from the Doppler profiles measured by Zare and co-workers[140]. The angular distribution of the incoming OH is controlled to an extent by the anisotropy parameter β = -0.9. The photolysis of an isotropic gas sample with a strongly negative anisotropy parameter, above the liquid surface will preferentially direct gas towards the surface (and half away from it) as was described in chapter 2 (section 2.6.2). This will however lead to a wide variety of incident angles relative to the surface normal and acts as an additional source of blurring. The incoming OH approaching the surface at wide impact angles will have travelled further before hitting the surface than those approaching at more normal angles. This is echoed with the scattered OH, those detected at a given delay are not necessarily travelling at the same speed. They may have simply travelled different distances.

The experimental set-up also preferentially detects OH scattered at more normal scattering angles, simply because these are more likely to enter the probe region. As a consequence any thermal components would be preferentially detected as they are known to have a $\cos\theta$ angular dependence. These geometric blurring effects make the translational energies extracted from the appearance profiles less well defined than their molecular beam based counterparts (TOF), which have fixed incidence and detection angles and near monoenergetic beams. The appearance profiles can, however, provide valuable translational energy and mechanistic information on the differences between the four liquids, as the geometric blurring effects apply to all cases equally.

The OH appearance profiles provide information on the translational energy of the scattered OH. The peak of the appearance profiles represents the photolysis-probe delay at which the majority of the OH radicals are detected. In sections 5.3.2 and 5.3.4,

crude average recoil speeds have been estimated for OH scattering from the four liquids. In all cases, the average recoil speed is estimated to be less than 1300 m s^{-1}, compared to an average incoming speed of 2500 m s^{-1}. It is clear therefore that the scattered OH has lost a significant fraction of its original translational energy following collision with each of the liquid surfaces. However, the majority of the scattered OH radicals are travelling at speeds well in excess of thermal from each liquid. The most probable speed for thermalised OH at 300 K leaving the surface would be ~540 m s^{-1}. It can therefore be concluded that the majority of OH scattered from each of the four liquids is simply travelling too fast to have undergone a true TD mechanism. They can reasonably be assumed to have undergone one or a limited number of direct or impulsive collisions with the surface.

The missing initial translational energy has either been transferred to scattered product internal energy or is transferred to the liquid surface. Ignoring the scattered OH internal state distribution for the moment (which will be discussed in section 5.4.3), the translational energy distribution from each liquid can provide information on the ability of the surface to accept energy from the incoming OH. This energy would then partition itself amongst 'translation' and internal modes of the liquid molecules.

Comparing PFPE and squalane in the first instance, the appearance profiles show that OH recoiling from squalane is travelling slower than that from PFPE; as shown in the differences in peak arrival time (figure 5.7). This reflects the relative *stiffness* of the two liquid surfaces, where stiffness represents the reluctance of a surface to accept energy from the incoming OH. PFPE, according to this definition, is stiffer than squalane as it behaves more elastically. The most probable reason for the differences between the ability of squalane and PFPE to dissipate the initial energy of the incoming OH is a result of the kinematic differences between the two liquids. The effective mass of the 'collision partner' for OH hitting either surface is unknown. It is however indisputable that the CF_x groups in PFPE are much more massive than any CH_x groups in squalane. The consequence of this is that, constrained by conservation of momentum, OH recoiling from a more massive collision partner must do so at higher velocity than that from a lighter partner.

The effective mass of squalane colliding with $O(^3P)$ atoms was found to be ~76 mu in the molecular beam experiments of Minton and co-workers[61]. Although this is not directly comparable to the work described here, it is reasonable to assume that the

kinematics of OH colliding with squalane would be similar. A mass of 71 mu would equate approximately to collision with a C_5H_{11} portion of a squalane chain. An equivalent portion from PFPE would be far more massive (269 mu) resulting in a more elastic collision. As a result the recoiling OH must travel faster from PFPE than squalane.

A further consequence of the kinematic differences between PFPE and squalane is the shape of the appearance profiles. The profiles from squalane are considerably broader than those from PFPE. This may also reflect the differences in the effective surface masses of squalane and PFPE. The reduced mass of the collision pair is likely to vary more substantially between different CH_x than CF_x fragments. The breadth of the profiles could therefore be regarded as a measure of the *homogeneity* of the surface on a molecular level.

The breadth of appearance and TOF profiles is more typically assigned to the *roughness* of a surface. Within this description the squalane surface is rougher, whereas the PFPE surface can be considered as a smoother, more solid-like, collision partner. These trends echo those in the molecular beam experiments of Nathanson and co-workers[8], comparing collisions of noble gases with squalane and PFPE surfaces. The time-of-flight spectra were similar to these appearance profiles. PFPE gave a sharp peak and rapidly decaying tail, while squalane profiles are broader and peak later.

A recent study by Morris and co-workers on the dynamics of Ar scattering from OH-, CH_3- and fluorinated CF_x- SAMs[46] found that Ar transfers less energy to the OH- and CF_x-SAMs than the alkyl CH_3-SAMs. In the OH-SAMs this is due to cooperative motion, as a result of H-bonding impeding energy transfer. The effect in the CF_x-SAMs is similar to that found in this work for PFPE. It is a result of the high effective mass of the CF_x groups.

In addition to molecular scale roughness, the appearance profiles also reflect the relative ability of the surfaces to accommodate (temporarily) the OH molecules at the surface, as influenced by the intermolecular interactions between the OH radicals and the liquid surfaces. The TD components in section 5.3.10 are a convenient way to quantify this. Squalane was found to have a larger potential TD component than PFPE with TD fractions of 23±5% and 13±2% respectively. This agrees qualitatively and reasonably quantitatively with the work of Nathanson and co-workers with the kinematically

similar Ne. They found, that (for PFPE) at comparable incident energies to those used here the TD fraction for a range of projectiles along the sequence Ne, CH_4, NH_3 and D_2O increased from ~10% to ~20% for PFPE. The same series gave TD fractions between 20% and 40% from squalane[8]. In contrast, Neon has been found to scatter almost exclusively via a direct, impulsive mechanism from alkylthiol SAMs[32,43]. In this case slow trajectories were assigned to 'hard' single-bounce encounters rather than any degree of accommodation at the surface[32]. It is a possibility that this conclusion may also apply to the liquids work of Nathanson and co-workers. The differences observed could be the result of varying proportions of collisions that efficiently absorb momentum without necessarily resulting in accommodation. Their raw TOF profiles for Ne from PFPE[10], squalane and glycerol[8] contain much less evidence of a true TD component than more polarisable gases such as NH_3[8] and Xe[10].

The polar projectiles were found to accommodate more readily on the squalane surface, this was more extreme when a polar liquid (glycerol) was used. Similar trends were observed in the experiments of Morris and co-workers where polar HCl accommodated more readily on a hydrogen bonded OH terminated SAM than an alkyl SAM[37]. Translational energy transfer reflects the interplay between kinematics and the influence of attractive intermolecular forces between the gas-phase species and the surface. Within this framework, it might be expected that polar OH radicals would be more likely to accommodate on a squalane surface than the kinematically similar Ne. This however neglects the fact that trapped OH radicals can proceed to react at a squalane surface; a channel which for obvious reasons would not be available to closed shell species.

In this work the polar and non-polar liquids (oleic acid and squalane) display similar trends in translational energy transfer. The peak is very slightly earlier (15 μs compared with 16 μs) but the two liquids are comparably broad. This suggests that oleic acid appears much like a liquid hydrocarbon to the incoming OH molecules. The translational energy of the scattered OH is largely unaffected by the presence of either the double bond or acid (COOH) head-groups present in oleic acid. Any differences between oleic acid and squalane are subtle, if present at all. The TD component from oleic acid is smaller than that from squalane at 17±3%. This value however is the same as that from squalane when their respective errors are taken into account.

The apparent similarities between the squalane and oleic acid surfaces may suggest that on average the OH molecules colliding with the oleic acid surface come into contact with the hydrocarbon tail, rather than the COOH head-group. An interesting question is whether this is a consequence of the COOH head-groups preferentially occupying the bulk, exposing the hydrocarbon tail-groups, or if the COOH to alkyl fraction at the surface is purely statistical and based on stoichiometry. This could in principle be investigated by molecular dynamics simulations, which could determine what groups are most predominant at the interface, and how this compares with the stoichiometry of the bulk liquid.

Perhaps the most interesting differences in the appearance profiles are those between squalane and squalene as highlighted in section 5.4.1. The profiles from squalene peak earlier and are narrower than those from squalane. Using the rationale described above to explain the differences between PFPE and squalane this could be interpreted as the squalene surface being stiffer than the squalane surface. There is however no objective reason for believing this to be the case. Squalene and squalane have similar kinematic properties, and arguments of stiffness are not reflected in the bulk density of the two liquids (squalane bulk density = 0.82 g cm^{-3}, squalene = 0.86 g cm^{-3}). This is to be expected since their structures are identical, except for the presence of six double bonds in squalene which are not present in squalane (figure 5.2).

The difference therefore is not likely to be due to the inelastic scattering mechanism but the reaction mechanism. It was proposed in section 5.4.1 that some of the slower, rotationally colder OH radicals that scatter from squalane are missing from squalene. As a consequence, there is an apparently smaller TD component (section 5.3.10) for squalene compared with squalane (squalane (23±5%), squalene (14±2%)). The missing TD fraction is due to those OH radicals that have undergone the additional ‘capture’ mechanism with squalene.

Further confirmation of the differences being a result of reactivity rather than inelastic scattering dynamics is observed in figure 5.7. The rising edge of the appearance profiles from squalane and squalene are coincident, whereas for PFPE it is steeper. This shows that the fastest OH molecules (defined by the rising edge) are travelling at the same speeds from squalane, oleic acid and squalene. From PFPE however, the directly scattered OH molecules are travelling faster than those from the hydrocarbons.

5.4.3 Internal energy distribution of the pre- and post- collision OH

Spin-orbit and Λ-doublet propensities

The rotational distributions of the pre- and post-collision OH were established by measuring LIF excitation spectra at a photolysis-probe delay of 4 μs for the pre-collision OH, and at delays consistent with the peaks of the appearance profiles for each of the liquids. The OH excitation spectra were recorded in the vibrational ground state ($v' = 0$) only. OH formed from HONO photolysis is formed almost exclusively in the vibrational ground state[140]. This in turn leads to the presumption that only OH in $v' = 0$ need be considered, as upward scattering from the vibrational ground state to higher levels is very inefficient. This is due to weak coupling between initial translational energy and the vibrational modes (T→V).

Considering the pre-collision OH in the first instance, OH formed from HONO photolysis displays some interesting dynamical phenomena. The OH formed has a non-statistical rotational population distribution. The F_2 ($^2\Pi_{1/2}$) spin-orbit manifold is preferentially populated meaning that the R_2 branch is more intense than it would be (when energy and degeneracy is accounted for) in a statistical distribution. The F_1:F_2 ratio at $N' = 1$ extracted from the spectra was found to be 1.35, in a statistically populated sample at 355 K this ratio would be 3.34[145]. This preferential population of the F_2 manifold has been observed previously by Zare and co-workers, who reported a slightly larger ratio of 1.66[140].

Zare and co-workers also reported that rotational population distribution is different in the two spin-orbit manifolds; expressed as differences in the Boltzmann rotational temperature. They report a colder temperature in the F_2 manifold than in the F_1 manifold (253±5 K and 364±20 K respectively). The rotational distributions shown in figure 5.10 show a similar, although less extreme, difference when the first 8 rotational quantum states are considered (306±19 K and 355±24 K). Figure 5.11 and table 5.1 however show that this is not the case when higher rotational quantum states are ignored (up to $N' = 5$). The fact that the Boltzmann rotational temperature changes depending on the range of rotational quantum states considered suggests that the distribution in the F_2 spin-orbit manifold is not well characterised by a Boltzmann temperature.

The Λ-doublet propensities were also measured and quantified (table 5.3). Preferential population of the Λ-doublets is determined by the relative intensities of the P/R branches compared to their Q branch counterparts, after their relative linestrengths are considered. There is a clear preference for the A' (probed by the P and R branches) Λ-doublet over the A" (probed by the Q branch). However, it is important to consider whether this difference might arise from rotational alignment, rather than Λ-doublet preferences. An alignment effect is the result of the experimental geometry favouring detection of one Λ-doublet over another.

The planar HONO molecule was photolysed using vertically polarised light. The negative anisotropy parameter for HONO photolysis means that the OH and NO photo-fragments preferentially recoil perpendicular to the electric vector of the photolysis beam. The resulting OH fragment will therefore have its internuclear axis preferentially perpendicular to the electric vector of the photolysis beam. It will, by definition, be rotating with the rotational vector perpendicular (in the limit of high $\boldsymbol{J}$) to the internuclear axis. The transition dipole moment ($\boldsymbol{\mu}$) for this $^2\Pi$-$^2\Sigma$ transition must always lie perpendicular to the internuclear axis. It may lie either parallel to, or perpendicular to, $\boldsymbol{J}$. $\boldsymbol{\mu}$ is perpendicular to $\boldsymbol{J}$ for the R and P branches and parallel to $\boldsymbol{J}$ for the Q branches. As a result $\boldsymbol{J}$ can be expected to lie preferentially parallel to the electric vector of the photolysis beam. The probe beam was horizontally polarised and will therefore preferentially interact where $\boldsymbol{\mu}$ is perpendicular to $\boldsymbol{J}$, artificially enhancing the R and P branches over the Q branch.

The extent to which the lab-frame polarisation of the photolysis and probe lasers can influence the observed spectrum is quantified by the photofragment alignment parameter (A_0^2) conventionally defined as having limits from +2 to -1. This was determined by Zare and co-workers as having a value of ~0.2. This relatively small alignment suggests that there will be little influence on the observed Λ-doublet preference by ignoring alignment effects. Indeed, neglecting any alignment effects, it was found that the observed Λ-doublet ratios were consistent with those from the full alignment-included analysis of Zare and co-workers (table 5.3), justifying this approximation.

On the basis of any alignment effects being negligible, the observed Λ-doublet preference must be genuine. In the A' case the unpaired electron in the molecular plane

is symmetric with respect to inversion (figure 5.16). The alternative, where the unpaired electron is perpendicular to the molecular plane, would be asymmetric with respect to inversion and is therefore labelled A". The favouring of the A' Λ-doublet indicates that the unpaired electron remains in the molecular plane after photolysis. As a result the final plane of rotation of the OH fragment is in the plane of the HONO parent molecule. This would break down if there was out-of-plane rotation of the parent and the Λ-doublet preference would be lifted.

The use of HONO as a photolytic precursor was interesting because it allowed for a starting position of preferential population of the $^2\Pi_{1/2}$ spin orbit manifold and the A' Λ-doublet. Having established that the majority of the OH detected must have undergone direct IS-type collisions, an interesting consideration is whether these preferences remain after collision. The results show that the spin-orbit and Λ-doublet labels have been essentially scrambled for PFPE and squalene (figure 5.13). These are the first fine structure resolved measurements of OH scattering with any condensed phase partner.

For squalane and oleic acid, there appears to be some fine-structure conservation post-collision; although, within the certainties of the experiment, this is difficult to state conclusively and would warrant further investigation. This discrepancy is more likely due to the extent to which the underlying pre-collision contribution has been correctly subtracted. The excitation spectra from squalane and oleic acid were recorded at longer delay times than the other liquids. At longer delays, the pre-:post-collision ratio was smaller (figure 5.6). The underestimation of a pre-collision component could result in the propensities observed (figure 5.13) as opposed to genuine fine-structure conservation post-collision.

Previous, related, gas-phase measurements for OH have been confined to relatively simple partners, in particular the noble gases and a few small molecules[225-228]. There is also an extensive theoretical literature[229,230]. Theoretical treatments are founded on the key concept of the breakdown of the cylindrical symmetry of the $^2\Pi$ diatomic on approach to a collision partner, giving rise to two surfaces of A′ and A″ symmetry, respectively. Interferences then give rise to the detailed Λ-doublet and spin-orbit propensities. As discussed extensively by Alexander and co-workers[229,230], the collision dynamics can conveniently be represented in terms of the sum and difference of the A′ and A″ potentials. In the Hund's case (a) limit, to which the low *N* levels of OH most closely approximate, spin–orbit conserving collisions are governed

by the sum potential. Spin-orbit changing is induced by the difference potential which, being smaller in magnitude in the relevant range generally sampled at accessible energies, results in a propensity for spin-orbit conservation.

Therefore, there is a basis for expecting a degree of OH fine-structure conservation for small-partner systems. However, there are no existing predictions for the corresponding OH interactions with condensed phases. Probably the closest large-scale systems for which some information is known involve the scattering of the related open-shell diatomic, NO($X^2\Pi$). Its collisions with solid surfaces have been studied extensively [231-234]. Perhaps most relevant here is the more restricted work on molecular adlayers[30,235]. For both types of surface, scattering out of the lowest $^2\Pi_{1/2}$ state, typically present almost exclusively in cold beam sources, into higher $^2\Pi_{3/2}$ levels is in fact found to be efficient. This is broadly consistent with the strong mixing seen here, but clearly this aspect of OH scattering from condensed surfaces remains to be fully explored.

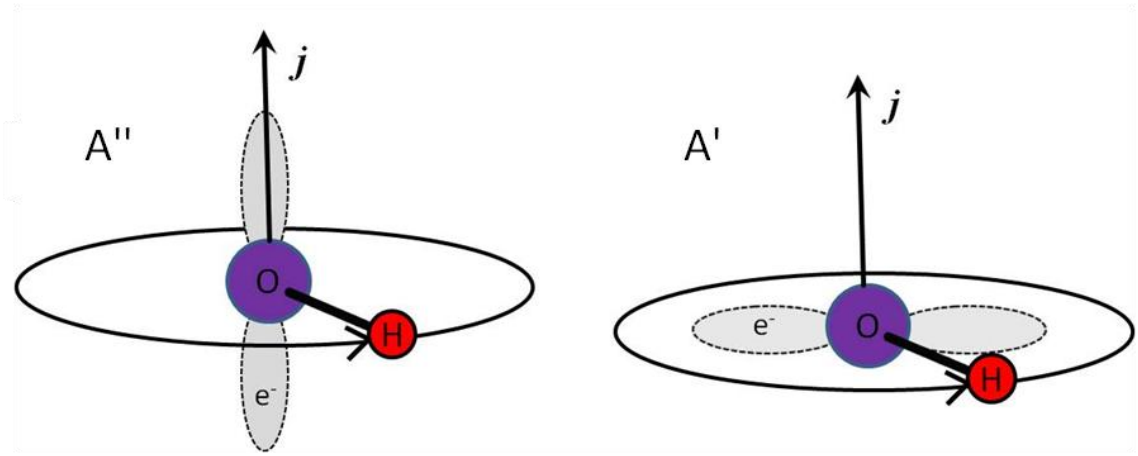

Figure 5.16: Schematic representation of the Λ-doublet symmetry in the high J limit.

Rotational distribution of the scattered OH

The excitation spectra from which the rotational temperatures originate were measured at delays corresponding to the peak in the appearance profiles from a given liquid. As the appearance profiles in figure 5.9 show, OH molecules detected at the peak are travelling too fast to have undergone any significant thermalisation. The rotational distributions therefore, are representative of the direct or impulsively scattered OH. Rotational excitation following collision is a dynamical property of the scattered products. The liquid surfaces have exerted a torque on the OH molecules such that they emerge rotating faster on the return journey than they were on the way in. The extent to which this occurs is dependent on the scattering mechanism and how well the liquid surface promotes T→R energy transfer.

The rotational excitation of the scattered OH follows the trend PFPE>squalene>oleic acid>squalane. The differences in rotational excitation between PFPE and squalane are consistent with the liquid properties described in section 5.4.2 for translational energy transfer. The PFPE surface is stiffer, more massive, impeding energy transfer to the surface and promoting T→R. Squalane also results in rotational excitation post collision. It is however less efficient at promoting T→R energy transfer than PFPE. The softer squalane surface absorbs more of the initial translational energy making less available for (scattered) product rotational excitement. The degree of rotational excitation is also dependent on the anisotropy of the interaction potential. From this point of view it could be argued that squalane has weaker anisotropic interactions with OH than PFPE.

The rotational temperature from oleic acid is higher than that from squalane. This is in contrast to the translational energy distributions which are similar for these two liquids. The implication is that there are structural differences between the two liquids that influence OH rotation but not translation. This suggests that the incoming OH does not simply ‘see’ oleic acid as a liquid hydrocarbon as proposed in section 5.4.2 for the translational energy distribution. Instead the functional groups, presumably the COOH head-groups, exert an influence that is only apparent in the rotational distribution of the scattered OH. This is not a result of kinematics as this would be present in the translational distribution. It could be the result of local structural features in oleic acid that are absent in squalane. In addition, there could be more strongly anisotropic interactions between OH and oleic acid than between OH and squalane.

The difference in the rotational distribution of OH rebounding from squalene and squalane echoes what was observed in the translational energy distributions (section 5.4.2). Those from squalene appear to be more rotationally excited than those from squalane which would suggest that squalene presents a stiffer surface more like PFPE. As was the case for translational energy transfer, the difference is not likely to be due to the inelastic scattering mechanism or surface stiffness but the *reaction* mechanism (section 5.4.1). It is proposed that the rotationally colder OH molecules are subject to additional reactive channels in squalene. This gives the illusion of a hotter rotational distribution as the underlying colder contribution (which leads to a later peak in the appearance profiles in squalane) is missing.

A key conclusion is that in all cases the post-collision OH are more rotationally excited than their pre-collision counterparts. As the excitation spectra were measured at the peak of the appearance profiles, where direct (IS) scattering dominates, this superthermal, yet reasonably Boltzmann-like, rotational distribution can be regarded as a signature for direct processes. This can be compared to the very limited number of previous studies of inelastic scattering at liquid surfaces with rotational resolution. Nesbitt and co-workers, investigating CO_2 scattering from PFPE surfaces, also observed rotational excitation in the IS products[21,22]. In this case a wide range of final $\boldsymbol{J}$ states were detected ($J > 17$) and the IS channel was characterised by rotational temperatures of 600-800 K depending on the liquid surface temperature[21]. Quantitative agreement between the IS rotational temperatures of CO_2 and OH from a PFPE surface would not be expected as they are very different rotors. The fact that they are similar is therefore presumably a coincidence. What is important is the qualitative agreement that direct IS leads to rotational excitation, which can be described by a superthermal Boltzmann rotational temperature in both cases.

When comparing the dynamics of CO_2 scattering from PFPE and squalane surfaces, Nesbitt and co-workers found that the rotational temperature of the IS CO_2 was not influenced by the chemical nature of the liquid[26]. This is in contrast to what was observed here in the case of OH scattering from the two liquids. This could be a result of experimental differences. Nesbitt and co-workers were able to isolate the IS component completely. As the two-point temperatures show (section 5.3.9), the measurement of OH at different arrival times in this work will influence the rotational temperature extracted.

Theoretical simulations on SAM surfaces on the other hand suggest that a difference in rotational excitation *would* exist between the different liquids[45]. There is predicted to be an overall rotational warming (T→R energy transfer) post-collision for CO at SAM surfaces, and this would be more extreme for a CF_3-SAM than a CH_3-SAM. This echoes what was observed by McCaffery and co-workers in their early work scattering I_2 from PFPE and squalane surfaces[18-20]. McCaffery and co-workers, in agreement with what was observed here, saw an increase in the rotational temperature of I_2 scattered from PFPE over that from squalane. The difficulty is in comparing different systems (liquids and SAMs) and different projectiles (closed-shell and open-shell, triatomics and diatomics), which shows the necessity of expanding the current field to include more quantum-state-resolved experimental studies at gas−liquid and gas−SAM surfaces.

5.5 Conclusions

- The collision dynamics of an open-shell, potentially reactive radical (OH) scattering from a liquid surface has been established for the first time. This work is also the first measurement of OH rotational fine-structure post-collision with any condensed phase.
- The dominant scattering mechanism was found to be direct, impulsive scattering from each of the liquids studied (PFPE, squalane, squalene and oleic acid). A minor component consistent with a trapping-desorption (TD) mechanism was observed in all four cases and increased along the series PFPE~squalene<oleic acid<squalane.
- The translational distributions revealed that in all cases, a large fraction of the initial collision energy is transferred to the liquid surfaces. The efficiency of the energy transfer follows the trend squalane~oleic acid>squalene>PFPE. This trend was interpreted in terms of the properties of the liquids (roughness, elasticity and homogeneity) and the intermolecular interactions.
- There was efficient translational-to-rotational energy transfer in all cases with the OH being more rotationally excited post-collision. This followed the trend PFPE~squalene>oleic acid>squalane, and was proposed to be the result of kinematics, molecular scale roughness and in the case of squalene, preferential removal of cold OH by reaction.
- The spin-orbit and Λ-doublet propensities present pre-collision were effectively collisionally removed, resulting in statistical distributions from PFPE and squalene. This also appears to the case for squalane and oleic acid, within the uncertainties of the measurements.
- The reactive uptake for the primary process of OH colliding with squalane, squalene and oleic acid has been established. The OH removal was found to be efficient at all the potentially reactive surfaces, as compared to equivalent gas-phase measurements. Oleic acid has a lower reactive uptake coefficient than squalane, revealing that the double bond does not enhance reactivity, and suggesting that non-reactive collisions with the acid headgroup (COOH) could result in the reduced reactivity compared with squalane.
- Squalene is more reactive than squalane, and it has been proposed that the increased reactivity is the result of a secondary (to the primary H-abstraction

reaction) reaction channel at the double bonds. It has also been inferred that it is the slower, rotationally colder, OH molecules that preferentially react here, consistent with this proposed additional reaction channel.

- For each of the four liquids the reactive uptake was below unity which is in good quantitative agreement with some, but not all, previous related observations of OH uptake on related bulk or particulate surfaces at ambient temperatures and pressure.

5.6 Future work

There are a number of possible interesting extensions to the work described in this chapter. In the first instance, and most simple to implement, would be to vary the photolytic precursor to investigate how the dynamics are affected by different initial translational and internal energies of the OH projectile. This would also, as described in section 5.3.2, be a useful experiment to determine absolutely whether the results presented here are free from any contribution from OH formed by reactions of $O(^3P)$ (from NO_2 photolysis).

The liquid surfaces investigated could be extended to include other functional groups representative of organic aerosols such as aldehydes, ketones and esters. Once the effect of individual functional groups is established it would be interesting to see how the collision dynamics is affected when looking at multi-component, mixed surfaces which are more atmospherically realistic. Realistic molecular dynamics simulations could also be beneficial to predict the availability of functional groups present at the interface and to correlate this to the measured reaction probabilities. The ultimate experimental development would be a molecular beam source of OH, giving narrow, tuneable, speed and internal energy distributions and coupling this with internal-state detection.

Chapter 6

Concluding remarks

There were two primary objectives of the work presented in this thesis. The first was to improve the current understanding of collision dynamics at the gas−liquid and related interfaces. The second was to use collision dynamics as a chemical probe of such interfaces. This chapter summarises the extent to which these goals were met.

A summary was provided in chapter 1 (section 1.5, table 1.1) of the current 'state of the art' of collision dynamics at the gas−liquid and gas−SAM interfaces. It is clear that there were certain disparities in the amount of work carried out in each of the sub-fields. In particular there was a clear requirement for advancements in experimental work utilising spectroscopic detection across the board, and in reactive studies at the gas−SAM interface.

This thesis presents the first dynamical investigation of an open-shell molecule at a gas−liquid interface (chapter 5). Although there is room for experimental improvements, this comparatively simple method has uncovered a number of previous unknowns: the OH radicals do not *all* react at potentially reactive surfaces; a significant amount of translational energy is transferred to the surface in all cases, even for the most direct of collisions; the dominant collision mechanism is direct-impulsive scattering; these collisions lead to efficient T→R energy transfer; the degree of translational and T→R energy transfer is the result of kinematics and gas−surface intermolecular interactions; any spin-orbit or Λ-doublet propensities present in OH are effectively scrambled following collision with a liquid surface.

Reactions at the gas−SAM interface have also been investigated for the first time with quantum-state resolution. The translational and rotational distribution of the OH (OD) products following a hydrogen abstraction reaction by an O(^{3}P) atom at alkylthiol SAM surfaces has been measured. The abstraction mechanism was found to be

predominantly direct, with the majority of OH products being translationally too hot to have been thermalised at the surface. The experiments proved more challenging than their liquid counterparts on account of the inability to continually refresh the surface. As a result the SAM surfaces were prone to damage. The source of the damage was established and as a result reproducible data could be extracted. The lessons learned as a result of this work would provide a valuable platform for future developments in experiments of this type.

The second major objective of the work was to use collision dynamics as a *probe* of the gas−liquid and related interfaces. The aim was to use the gas-phase radicals to interrogate the interfacial structure. In all three cases, the results have been able to provide unique information about the interface, with varying degrees of success.

First, the OH inelastic scattering work (chapter 5) has suggested very strongly that in the case of squalene, there are double bonds located at the interface. This is implied by the increased reactive loss of OH at a squalene surface relative to that of squalane. In addition, the results from oleic acid hint at some interesting interfacial properties. On account of the reactive loss of OH not being enhanced (over squalane) it could be concluded that the vinyl unit is not available at the interface. The slightly reduced reactive uptake coefficient and the rotational distribution of the scattered OH from oleic acid are suggestive of acid headgroups (COOH) occupying the interface. These effects may be partially cancelling. The results cannot yet be untangled to conclude whether there is an excess of either group at the interface beyond the molecular stoichiometry of the liquid. This would be an interesting future development and could be complemented by molecular dynamics simulations.

The reactivity of $O(^3P)$ atoms towards alkylthiol SAMs was investigated in chapter 4. It was found that there is significant penetration of $O(^3P)$ atoms at least as deep as C_3 resulting in OH products that are subsequently able to escape for detection without reacting further to form water. The penetration depth is far deeper than was observed in the only other (higher energy) experimental measurement of penetration depth[88,90]. These results suggest that, in contrast to the higher energy work, the interface of the monolayers is open to direct attack and is not completely shielded by the outer terminal (CH_3) canopy. In principle this work could be extended further by sequential isotopic labelling to identify the contribution from each methylene unit along the chain

specifically. This would, however, require non-trivial input from a synthetic collaborator.

It has been shown that $O(^3P)$ atoms are a functional-group-selective chemical probe for ionic liquid interfaces (chapter 3). The energetics of the $O(^3P)$ atoms formed by 355 nm photolysis of NO_2 allows them to specifically target the secondary CH_2 units. The abstraction of H atoms by $O(^3P)$ could obviously be applied to other ionic liquids. The method could be extended to site as well as overall group or atom-type specificity by the simple (at least in principle) expedient of site-specific isotopic labelling.

There is a potentially much wider range of other suitable projectiles that could, in principle, be used as probes of the availability of specific atoms or groups at liquid surfaces. Interfacial reaction of Cl has already been demonstrated with squalane[61] but not pursued beyond that in an analytical sense, as is similarly the case with F atoms.[73]. Electronically excited species such as $O(^1D)$ provide an interesting alternative, being known to be much more reactive, but via very distinct mechanisms, than $O(^3P)$.

There is a clear requirement for further advancements to be made in the field of gas−liquid/SAM scattering with quantum-state resolution, particularly in potentially reactive systems. The work presented in this thesis goes someway to rectify the imbalances in the field of scattering dynamics and forms a foundation from which numerous developments could be made.

References

[1] Grossman, E.; Gouzman, I. *Nucl. Instrum. Methods Phys. Res., Sect. B* **2003**, *208*, 48.

[2] Reddy, M. R. *J. Mater. Sci.* **1995**, *30*, 281.

[3] Rudich, Y. *Chem. Rev.* **2003**, *103*, 5097.

[4] Donaldson, D. J.; Vaida, V. *Chem. Rev.* **2006**, *106*, 1445.

[5] Ellison, G. B.; Tuck, A. F.; Vaida, V. *J. Geophys. Res. Atmos.* **1999**, *104*, 11633.

[6] Poschl, U.; Martin, S. T.; Sinha, B.; Chen, Q.; Gunthe, S. S.; Huffman, J. A.; Borrmann, S.; Farmer, D. K.; Garland, R. M.; Helas, G.; Jimenez, J. L.; King, S. M.; Manzi, A.; Mikhailov, E.; Pauliquevis, T.; Petters, M. D.; Prenni, A. J.; Roldin, P.; Rose, D.; Schneider, J.; Su, H.; Zorn, S. R.; Artaxo, P.; Andreae, M. O. *Science* **2010**, *329*, 1513.

[7] Saecker, M. E.; Govoni, S. T.; Kowalski, D. V.; King, M. E.; Nathanson, G. M. *Science* **1991**, *252*, 1421.

[8] Saecker, M. E.; Nathanson, G. M. *J. Chem. Phys.* **1993**, *99*, 7056.

[9] King, M. E.; Nathanson, G. M.; Hanning-Lee, M.; Minton, T. K. *Phys. Rev. Lett.* **1993**, *70*, 1026.

[10] King, M. E.; Saecker, M. E.; Nathanson, G. M. *J. Chem. Phys.* **1994**, *101*, 2539.

[11] Ronk, W. R.; Kowalski, D. V.; Manning, M.; Nathanson, G. M. *J. Chem. Phys.* **1996**, *104*, 4842.

[12] Nathanson, G. M.; Davidovits, P.; Worsnop, D. R.; Kolb, C. E. *J. Phys. Chem.* **1996**, *100*, 13007.

[13] King, M. E.; Fiehrer, K. M.; Nathanson, G. M.; Minton, T. K. *J. Phys. Chem. A.* **1997**, *101*, 6556.

[14] Muenter, A. H.; DeZwaan, J. L.; Nathanson, G. M. *J. Phys. Chem. B.* **2006**, *110*, 4881.

[15] Nathanson, G. M. *Annu. Rev. Phys. Chem.* **2004**, *55*, 231.

[16] Lipkin, N.; Gerber, R. B.; Moiseyev, N.; Nathanson, G. M. *J. Chem. Phys.* **1994**, *100*, 8408.

[17] Klassen, J. K.; Fiehrer, K. M.; Nathanson, G. M. *J. Phys. Chem. B.* **1997**, *101*, 9098.

[18] Kenyon, A. J.; McCaffery, A. J.; Quintella, C. M.; Zidan, M. D. *J. Chem. Soc., Faraday Trans.* **1993**, *89*, 3877.

[19] Kenyon, A. J.; McCaffery, A. J.; Quintella, C. M.; Zidan, M. D. *Faraday Discuss* **1993**, *96*, 245.

[20] Kenyon, A. J.; McCaffery, A. J.; Quintella, C. M.; Zidan, M. D. *Chem. Phys. Lett.* **1992**, *190*, 55.

[21] Perkins; Nesbitt, D. J. *J. Phys. Chem. B.* **2007**, *112*, 507.

[22] Perkins, B. G.; Haber, T.; Nesbitt, D. J. *J. Phys. Chem. B.* **2005**, *109*, 16396.

[23] Perkins, B. G.; Nesbitt, D. J. *J. Phys. Chem. A.* **2009**, *114*, 1398.

[24] Nogueira, J. J.; Vazquez, S. A.; Mazyar, O. A.; Hase, W. L.; Perkins, B. G.; Nesbitt, D. J.; Martinez-Nunez, E. *J. Phys. Chem. A.* **2009**, *113*, 3850.

[25] Perkins, B. G.; Nesbitt, D. J. *J. Phys. Chem. A.* **2009**, *113*, 4613.

[26] Perkins, B. G.; Nesbitt, D. J. *J. Phys. Chem. B.* **2006**, *110*, 17126.

[27] Kautz, N. A.; Kandel, S. A. *J. Am. Chem. Soc.* **2008**, *130*, 6908.

[28] Fogarty, D. P.; Kandel, S. A. *J. Chem. Phys.* **2006**, *124*.

[29] Camillone, N.; Chidsey, C. E. D.; Eisenberger, P.; Fenter, P.; Li, J.; Liang, K. S.; Liu, G. Y.; Scoles, G. *J. Chem. Phys.* **1993**, *99*, 744.

[30] Cohen, S. R.; Naaman, R.; Sagiv, J. *Phys. Rev. Lett.* **1987**, *58*, 1208.

[31] Gibson, K. D.; Isa, N.; Sibener, S. J. *J. Phys. Chem. A.* **2006**, *110*, 1469.

[32] Isa, N.; Gibson, K. D.; Yan, T.; Hase, W.; Sibener, S. J. *J. Chem. Phys.* **2004**, *120*, 2417.

[33] Gibson, K. D.; Isa, N.; Sibener, S. J. *J. Chem. Phys.* **2003**, *119*, 13083.

[34] Day, B. S.; Shelby, F. S.; Adonis, D.; John, R. M. *J. Chem. Phys.* **2003**, *119*, 8084.

[35] Day, B. S.; Morris, J. R. *J. Chem. Phys.* **2005**, *122*, 234714.

[36] Day, B. S.; Morris, J. R. *J. Phys. Chem. B.* **2003**, *107*, 7120.

[37] Lohr, J. R.; Day, B. S.; Morris, J. R. *J. Phys. Chem. B.* **2005**, *109*, 15469.

[38] Day, B. S.; Morris, J. R.; Alexander, W. A.; Troya, D. *J. Phys. Chem. A.* **2005**, *110*, 1319.

[39] Tasic, U.; Day, B. S.; Yan, T.; Morris, J. R.; Hase, W. L. *J. Phys. Chem. C.* **2007**, *112*, 476.

[40] Scott Day, B.; Davis, G. M.; Morris, J. R. *Anal. Chim. Acta.* **2003**, *496*, 249.

[41] Vazquez, S. A.; Morris, J. R.; Rahaman, A.; Mazyar, O. A.; Vayner, G.; Addepalli, S. V.; Hase, W. L.; Martinez-Nunez, E. *J. Phys. Chem. A.* **2007**, *111*, 12785.

[42] Alexander, W. A.; Morris, J. R.; Troya, D. *J. Phys. Chem. A.* **2009**, *113*, 4155.

[43] Bennett, M. E.; Alexander, W. A.; Lu, J. W.; Troya, D.; Morris, J. R. *J. Phys. Chem. C.* **2008**, *112*, 17272.

[44] Lohr, J. R.; Day, B. S.; Morris, J. R. *J. Phys. Chem. A.* **2006**, *110*, 1645.

[45] Alexander, W. A.; Morris, J. R.; Troya, D. *J. Chem. Phys.* **2009**, *130*, 084702.

[46] Lu, J. W.; Alexander, W. A.; Morris, J. R. *Phys. Chem. Chem. Phys.* **2010**, *12*, 12533.

[47] Ausfelder, F.; McKendrick, K. G. *Prog. React. Kinet. Mec.* **2000**, *25*, 299.

[48] Andresen, P.; Luntz, A. C. *J. Chem. Phys.* **1980**, *72*, 5842.

[49] Dutton, N. J.; Fletcher, I. W.; Whitehead, J. C. *Mol. Phys.* **1984**, *52*, 475.

[50] Whitehead, J. C.; Winterbottom, F. *Chem. Phys. Lett.* **1991**, *177*, 207.

[51] Sweeney, G. M.; Watson, A.; McKendrick, K. G. *J. Chem. Phys.* **1997**, *106*, 9172.

[52] Ausfelder, F.; Kelso, H.; McKendrick, K. G. *Phys. Chem. Chem. Phys.* **2002**, *4*, 473.

[53] Tsurumaki, H.; Fujimura, Y.; Kajimoto, O. *J. Chem. Phys.* **2000**, *112*, 8338.

[54] Liu, X. H.; Gross, R. L.; Suits, A. G. *J. Chem. Phys.* **2002**, *116*, 5341.

[55] Liu, X. H.; Gross, R. L.; Hall, G. E.; Muckerman, J. T.; Suits, A. G. *J. Chem. Phys.* **2002**, *117*, 7947.

[56] Garton, D. J.; Minton, T. K.; Troya, D.; Pascual, R.; Schatz, G. C. *J. Phys. Chem. A.* **2003**, *107*, 4583.

[57] Garton, D. J.; Minton, T. K.; Hu, W. F.; Schatz, G. C. *J. Phys. Chem. A.* **2009**, *113*, 4722.

[58] Zhang, B.; Liu, K. *J. Phys. Chem. A.* **2005**, *109*, 6791.

[59] Hori, A.; Takmuku, S.; Sakurai, H. *J. Org. Chem.* **1977**, *42*, 2318.

[60] Zadok, E.; Mazur, Y. *J. Org. Chem.* **1982**, *47*, 2223.

[61] Garton, D. J.; Minton, T. K.; Alagia, M.; Balucani, N.; Casavecchia, P.; Volpi, G. G. *J. Chem. Phys.* **2000**, *112*, 5975.

[62] Garton, D. J.; Minton, T. K.; Alagia, M.; Balucani, N.; Casavecchia, P.; Volpi, G. G. *Faraday Discuss* **1997**, *108*, 387.

[63] Kelso, H.; Kohler, S. P. K.; Henderson, D. A.; McKendrick, K. G. *J. Chem. Phys.* **2003**, *119*, 9985.

[64] Zhang, J.; Upadhyaya, H. P.; Brunsvold, A. L.; Minton, T. K. *J. Phys. Chem. B.* **2006**, *110*, 12500.

[65] Zhang, J.; Garton, D. J.; Minton, T. K. *J. Chem. Phys.* **2002**, *117*, 6239.

[66] Kohler, S. P. K.; Allan, M.; Costen, M. L.; McKendrick, K. G. *J. Phys. Chem. B.* **2006**, *110*, 2771.

[67] Allan, M.; Bagot, P. A. J.; Costen, M. L.; McKendrick, K. G. *J. Phys. Chem. C.* **2007**, *111*, 14833.

[68] Allan, M.; Bagot, P. A. J.; Westacott, R. E.; Costen, M. L.; McKendrick, K. G. *J. Phys. Chem. C.* **2008**, *112*, 1524.

[69] Kohler, S. P. K.; Allan, M.; Kelso, H.; Henderson, D. A.; McKendrick, K. G. *J. Chem. Phys.* **2005**, *122*.

[70] Allan, M.; Bagot, P. A. J.; Kohler, S. P. K.; Reed, S. K.; Westacott, R. E.; Costen, M. L.; McKendrick, K. G. *Physica Scripta* **2007**, *76*, C42.

[71] Hong Zhen, L.; Takashi, Y. *J. Chem. Phys.* **2001**, *114*, 5774.

[72] Thoru, S.; Takashi, Y. *J. Chem. Phys.* **2000**, *113*, 3351.

[73] Zolot, A. M.; Harper, W. W.; Perkins, B. G.; Dagdigian, P. J.; Nesbitt, D. J. *J. Chem. Phys.* **2006**, *125*.

[74] Moussa, S. G.; Finlayson-Pitts, B. J. *Phys Chem Chem Phys* **2010**, *12*, 9419.

[75] Dubowski, Y.; Vieceli, J.; Tobias, D. J.; Gomez, A.; Lin, A.; Nizkorodov, S. A.; McIntire, T. M.; Finlayson-Pitts, B. J. *J. Phys. Chem. A.* **2004**, *108*, 10473.

[76] McIntire, T. M.; Scott Lea, A.; Gaspar, D. J.; Jaitly, N.; Dubowski, Y.; Li, Q.; Finlayson-Pitts, B. J. *Phys. Chem. Chem. Phys.* **2005**, *7*, 3605.

[77] McIntire, T. M.; Ryder, O.; Finlayson-Pitts, B. J. *J. Phys. Chem. C.* **2009**, *113*, 11060.

[78] Finlayson-Pitts, B. J. *Phys. Chem. Chem. Phys.* **2009**, *11*, 7760.

[79] Bertram, A. K.; Ivanov, A. V.; Hunter, M.; Molina, L. T.; Molina, M. J. *J. Phys. Chem. A.* **2001**, *105*, 9415.

[80] Park, J.-H.; Ivanov, A. V.; Molina, M. J. *J. Phys. Chem. A.* **2008**, *112*, 6968.

[81] Paz, Y.; Trakhtenberg, S.; Naaman, R. *J. Phys. Chem.* **1994**, *98*, 13517.

[82] Paz, Y.; Trakhtenberg, S.; Naaman, R. *J. Phys. Chem.* **1992**, *96*, 10964.

[83] Torres, J.; Perry, C. C.; Bransfield, S. J.; Fairbrother, D. H. *J. Phys. Chem. B.* **2002**, *106*, 6265.

[84] Wagner, A. J.; Wolfe, G. M.; Fairbrother, D. H. *J. Chem. Phys.* **2004**, *120*, 3799.

[85] Gorham, J.; Smith, B.; Fairbrother, D. H. *J. Phys. Chem. C.* **2006**, *111*, 374.

[86] Gorham, J. M.; Stover, A. K.; Fairbrother, D. H. *J. Phys. Chem. C.* **2007**, *111*, 18663.

[87] Berry, R. J.; Ehlers, C. J.; Burgess, D. R.; Zachariah, M. R.; Marshall, P. *Chem. Phys. Lett.* **1997**, *269*, 107.

[88] Qin, X.; Tzvetkov, T.; Liu, X.; Lee, D.-C.; Yu, L.; Jacobs, D. C. *J. Am. Chem. Soc.* **2004**, *126*, 13232.

[89] Qin, X.; Tzvetkov, T.; Jacobs, D. C. *J. Phys. Chem. A.* **2005**, *110*, 1408.

[90] Qin, X.; Tzvetkov, T.; Jacobs, D. C. *Nucl. Instrum. Methods Phys. Res., Sect. B* **2003**, *203*, 130.

[91] Bosio, S. B. M.; Hase, W. L. *J. Chem. Phys.* **1997**, *107*, 9677.

[92] Yan, T. Y.; Isa, N.; Gibson, K. D.; Sibener, S. J.; Hase, W. L. *J. Phys. Chem. A.* **2003**, *107*, 10600.

[93] Yan, T.; Hase, W. L. *J. Phys. Chem. B.* **2002**, *106*, 8029.

[94] Vazquez, S. A.; Morris, J. R.; Rahaman, A.; Mazyar, O. A.; Vayner, G.; Addepalli, S. V.; Hase, W. L.; Martinez-Nunez, E. *J. Phys. Chem. A.* **2007**, *111*, 12785.

[95] Luntz, A. C.; Andresen, P. *J. Chem. Phys.* **1980**, *72*, 5851.

[96] Clary, D. C.; Connor, J. N. L.; Southall, W. J. E. *J. Chem. Phys.* **1986**, *84*, 2620.

[97] Walch, S. P.; Dunning, J. T. H. *J. Chem. Phys.* **1980**, *72*, 3221.

[98] Gonzalez, C.; McDouall, J. J. W.; Schlegel, H. B. *J. Phys. Chem.* **1990**, *94*, 7467.

[99] Corchado, J. C.; Espinosa-Garcia, J.; Roberto-Neto, O.; Chuang, Y.-Y.; Truhlar, D. G. *J. Phys. Chem. A.* **1998**, *102*, 4899.

[100] Espinosa-Garcia, J.; Garcia-Bernaldez, J. C. *Phys. Chem. Chem. Phys.* **2000**, *2*, 2345.

[101] Clary, D. C. *Phys. Chem. Chem. Phys.* **1999**, *1*, 1173.

[102] Juliana, P.; David, C. C. *J. Chem. Phys.* **2000**, *112*, 1859.

[103] Palma, J.; Clary, D. C. *Phys. Chem. Chem. Phys.* **2000**, *2*, 4105.

[104] Troya, D.; Pascual, R. Z.; Schatz, G. C. *J. Phys. Chem. A.* **2003**, *107*, 10497.

[105] Troya, D.; Pascual, R. Z.; Garton, D. J.; Minton, T. K.; Schatz, G. C. *J. Phys. Chem. A.* **2003**, *107*, 7161.

[106] Yan, T.; Hase, W. L.; Doubleday, C. *J. Chem. Phys.* **2004**, *120*, 9253.

[107] Yan, T. Y.; Doubleday, C.; Hase, W. L. *J. Phys. Chem. A.* **2004**, *108*, 9863.

[108] Troya, D. *J. Phys. Chem. A.* **2007**, *111*, 10745.

[109] Li, G.; Bosio, S. B. M.; Hase, W. L. *Journal of Molecular Structure* **2000**, *556*, 43.

[110] Jianming, Z.; Donna, J. G.; Timothy, K. M. *The Journal of Chemical Physics* **2002**, *117*, 6239.

[111] Tasic, U.; Yan, T.; Hase, W. L. *J. Phys. Chem. B.* **2006**, *110*, 11863.

[112] Troya, D.; Schatz, G. C. *J. Chem. Phys.* **2004**, *120*, 7696.

[113] Iimori, T.; Iwahashi, T.; Kanai, K.; Seki, K.; Sung, J.; Kim, D.; Hamaguchi, H.-o.; Ouchi, Y. *J. Phys. Chem. B.* **2007**, *111*, 4860.

[114] Troya, D., Schatz, G. C. *J. Chem. Phys.* **2004**, *120*, 7696.

[115] Layfield, J. P.; Troya, D. *J. Chem. Phys.* **2010**, *132*, 134307.

[116] Harris, J. G. *J. Phys. Chem.* **1992**, *96*, 5077.

[117] Mondello, M.; Grest, G., S. *J. Chem. Phys.* **1995**, *103*, 7156.

[118] Zhuravlev, N. D.; Ilja Siepmann, J. *Fluid Phase Equilib.* **1997**, *134*, 55.

[119] Zhuravlev, N. D.; Martin, M. G.; Ilja Siepmann, J. *Fluid Phase Equilib.* **2002**, *202*, 307.

[120] Wick, C. D.; Siepmann, J. I.; Schure, M. R. *Anal. Chem.* **2002**, *74*, 3518.

[121] Kohler, S. P. K.; Reed, S. K.; Westacott, R. E.; McKendrick, K. G. *J. Phys. Chem. B.* **2006**, *110*, 11717.

[122] Peng, Y.; Liu, L.; Cao, Z.; Li, S.; Mazyar, O. A.; Hase, W. L.; Yan, T. *J. Phys. Chem. C.* **2008**, *112*, 20340.

[123] Radak, B. K.; Yockel, S.; Kim, D.; Schatz, G. C. *J. Phys. Chem. A.* **2009**, *113*, 7218.

[124] Allan, M.; Bagot, P. A. J.; Costen, M. L.; McKendrick, K. G.; . *Physica Scripta* **2007**, *76*, C42.

[125] Wu, B.; Zhang, J.; Minton, T. K.; McKendrick, K. G.; Slattery, J. M.; Yockel, S.; Schatz, G. C. *J. Phys. Chem. C.* **2010**, *114*, 4015.

[126] Govoni, S. T.; Nathanson, G. M. *J. Am. Chem. Soc.* **1994**, *116*, 779.

[127] Darling, S. B.; Rosenbaum, A. M.; Sibener, S. J. *Surf. Sci.* **2001**, *478*, L313.

[128] Paz, Y.; Naaman, R. *J. Chem. Phys.* **1991**, *94*, 4921.

[129] Sylvie, B. M. B.; William, L. H. *J. Chem. Phys.* **1997**, *107*, 9677.

[130] Vazquez, S. A.; Morris, J. R.; Rahaman, A.; Mazyar, O. A.; Vayner, G.; Addepalli, S. V.; Hase, W. L.; Martinez-Nunez, E. *J. Phys. Chem. A.* **2007**, *111*, 12785.

[131] Martinez-Nunez, E.; Rahaman, A.; Hase, W. L. *J. Phys. Chem. C.* **2007**, *111*, 354.

[132] Layfield, J. P.; Troya, D. *J. Chem. Phys.* **2010**, *132*, 134307.

[133] Lednovich, S. L.; Fenn, J. B. *AIChE J.* **1977**, *23*, 454.

[134] Slattery, J. M. Ionic liquid custom synthesis; Department of Chemistry, University of York, Heslington, York, YO10 5DD. UK, 2009.

[135] Raisanen, M. T.; Buck, M. STM analysis University of St Andrews, Scotland, UK. KY16 9AJ 2009/2010.

[136] Brown, R. XPS analysis; School of Chemistry, University of Edinburgh, Edinburgh EH9 3JJ, 2008.

[137] Johnston, R. A. W.; Loureiro, R. M. S.; Cristiano, M. L. S.; Labat, G. *ARKIVOC* **2010**, 142.

[138] Szalay, V.; Kovács, L.; Wöhlecke, M.; Libowitzky, E. *Chem. Phys. Lett.* **2002**, *354*, 56.

[139] Okabe, H. *Photochemistry of Small Molecules*; John Wiley & Sons, 1978.

[140] Vasudev, R.; Zare, R. N.; Dixon, R. N. *J. Chem. Phys.* **1984**, *80*, 4863.

[141] Baker, R. P.; Costen, M. L.; Hancock, G.; Ritchie, G. A. D.; Summerfield, D. *Phys. Chem. Chem. Phys.* **2000**, *2*, 661.

[142] Levine, R. D. *Molecular Reaction Dynamics*, 1 ed.; Cambridge University Press, 2005.

[143] Schultz, A.; Cruse, H. W.; Zare, R. N. *The Journal of Chemical Physics* **1972**, *57*, 1354.

[144] Andrews, D. L. *Applied Laser Spectroscopy*; VCH Publishers Inc., 1992.

[145] Luque, J.; Crosely, D. R. *Database and spectral simulation program (version 2.0.63).* ; SRI international, 1999.

[146] Paterson, G. PhD thesis: Collisional Depolarisation of Rotational Angular Momentum in the OH Radical Heriot-Watt University, Edinburgh, 2010.

[147] Costen, M. L. Monte Carlo simulations for direct and thermal components; Heriot-Watt University, Edinburgh, EH14 4AS., 2002/2009/2010.

[148] Waring, C.; Bagot, P. A. J.; Raisanen, M. T.; Costen, M. L.; McKendrick, K. G. *J. Phys. Chem. A.* **2009**, *113*, 4320.

[149] Parvulescu, V. I.; Hardacre, C. *Chem. Rev.* **2007**, *107*, 2615.

[150] Cho, E.; Park, J. S.; Sekhon, S. S.; Park, G. G.; Yang, T. H.; Lee, W. Y.; Kim, C. S.; Park, S. B. *J. Electrochem. Soc.* **2009**, *156*, B197.

[151] Chiu, Y. H.; Gaeta, G.; Levandier, D. J.; Dressler, R. A.; Boatz, J. A. *Int. J. Mass spectrom.* **2007**, *265*, 146.

[152] Romero-Sanz, I.; Bocanegra, R.; Mora, J. F. d. l.; Gamero-Castano, M. *J. Appl. Phys.* **2003**, *94*, 3599.

[153] Dupont, J.; Fonseca, G. S.; Umpierre, A. P.; Fichtner, P. F. P.; Teixeira, S. R. *J. Am. Chem. Soc.* **2002**, *124*, 4228.

[154] Liang, C.; Yuan, C.-Y.; Warmack, R. J.; Barnes, C. E.; Dai, S. *Anal. Chem.* **2002**, *74*, 2172.

[155] Rogers, R. D.; Seddon, K. R. *Science* **2003**, *302*, 792.

[156] Law, G.; Watson, P. R.; Carmichael, A. J.; Seddon, K. R. *Phys. Chem. Chem. Phys.* **2001**, *3*, 2879.

[157] Gannon, T. J.; Law, G.; Watson, P. R.; Carmichael, A. J.; Seddon, K. R. *Langmuir* **1999**, *15*, 8429.

[158] Martinez, I. S.; Baldelli, S. *J. Phys. Chem. C.* **2010**, *114*, 11564.

[159] Atsushi, O.; Hiroki, H.; Kaoru, N.; Motofumi, S.; Kenji, K. *J. Chem. Phys.* **2009**, *130*, 204705.

[160] Smith, E. F.; Villar Garcia, I. J.; Briggs, D.; Licence, P. *Chem. Commun.* **2005**, 5633.

[161] Lovelock, K. R. J.; Kolbeck, C.; Cremer, T.; Paape, N.; Schulz, P. S.; Wasserscheid, P.; Maier, F.; SteinruÌˆck, H. P. *J. Phys. Chem. B.* **2009**, *113*, 2854.

[162] Kolbeck, C.; Cremer, T.; Lovelock, K. R. J.; Paape, N.; Schulz, P. S.; Wasserscheid, P.; Maier, F.; Steinruck, H. P. *J. Phys. Chem. B.* **2009**, *113*, 8682.

[163] Bowers, J.; Vergara-Gutierrez, M. C.; Webster, J. R. P. *Langmuir* **2003**, *20*, 309.

[164] Morrow, T. I.; Maginn, E. J. *J. Phys. Chem. B.* **2002**, *106*, 12807.

[165] Wang, Y.; Voth, G. A. *J. Phys. Chem. B.* **2006**, *110*, 18601.

[166] Wang, Y.; Jiang, W.; Yan, T.; Voth, G. A. *Acc. Chem. Res.* **2007**, *40*, 1193.

[167] Yan, T.; Burnham, C. J.; Del Popolo, M. G.; Voth, G. A. *J. Phys. Chem. B.* **2004**, *108*, 11877.

[168] Yan, T.; Li, S.; Jiang, W.; Gao, X.; Xiang, B.; Voth, G. A. *J. Phys. Chem. B.* **2006**, *110*, 1800.

[169] Jiang, W.; Wang, Y.; Yan, T.; Voth, G. A. *J. Phys. Chem. C.* **2008**, *112*, 1132.

[170] Picálek, J.; Kolafa, J. *J. Mol. Liq.* **2007**, *134*, 29.

[171] Mohammad Hadi, G.; Younes, A. *J. Chem. Phys.* **2007**, *126*, 154502.

[172] Lynden-Bell, R. M.; Kohanoff, J.; Del Popolo, M. G. *Faraday Discuss* **2005**, *129*, 57.

[173] Bhargava, B. L.; Balasubramanian, S. *J. Am. Chem. Soc.* **2006**, *128*, 10073.

[174] Sergio, M. U.; Mauro, C. C. R. *J. Chem. Phys.* **2004**, *120*, 1855.

[175] Sloutskin, E.; Lynden-Bell, R. M.; Balasubramanian, S.; Deutsch, M. *J. Chem. Phys.* **2006**, *125*, 174715.

[176] Canongia Lopes, J. N. A.; Padua, A. A. H. *J. Phys. Chem. B.* **2006**, *110*, 3330.

[177] Santos, C. S.; Baldelli, S. *J. Phys. Chem. B.* **2007**, *111*, 4715.

[178] Iimori, T.; Iwahashi, T.; Ishii, H.; Seki, K.; Ouchi, Y.; Ozawa, R.; Hamaguchi, H.-o.; Kim, D. *Chem. Phys. Lett.* **2004**, *389*, 321.

[179] Lockett, V.; Sedev, R.; Bassell, C.; Ralston, J. *Phys. Chem. Chem. Phys.* **2008**, *10*, 1330.

[180] Sung, J.; Jeon, Y.; Kim, D.; Iwahashi, T.; Iimori, T.; Seki, K.; Ouchi, Y. *Chem. Phys. Lett.* **2005**, *406*, 495.

[181] Goebel D. M, K. I. *Fundamentals of electric propulsion: Ion and Hall thrusters*; JPL Space Science and Technology Series, 2008.

[182] Bonhote, P.; Dias, A.-P.; Papageorgiou, N.; Kalyanasundaram, K.; Gratzel, M. *Inorg. Chem.* **1996**, *35*, 1168.

[183] Berkowitz, J.; Ellison, G. B.; Gutman, D. *J. Phys. Chem.* **1994**, *98*, 2744.

[184] Wilson, E. W.; Hamilton, W. A.; Kennington, H. R.; Evans, B.; Scott, N. W.; DeMore, W. B. *J. Phys. Chem. A.* **2006**, *110*, 3593.

[185] Chailapakul, O.; Sun, L.; Xu, C. J.; Crooks, R. M. *J. Am. Chem. Soc.* **1993**, *115*, 12459.

[186] Poirier, G. E. *Chem. Rev.* **1997**, *97*, 1117.

[187] Han, S. M.; Ashurst, W. R.; Carraro, C.; Maboudian, R. *J. Am. Chem. Soc.* **2001**, *123*, 2422.

[188] Revell, D. J.; Knight, J. R.; Blyth, D. J.; Haines, A. H.; Russell, D. A. *Langmuir* **1998**, *14*, 4517.

[189] Soja, G. R.; Watson, D. F. *Langmuir* **2009**, *25*, 5398.

[190] Mrksich, M.; Whitesides, G. M. *Annu. Rev. Biophys. Biomolec. Struct.* **1996**, *25*, 55.

[191] Lavrich, D. J.; Wetterer, S. M.; Bernasek, S. L.; Scoles, G. *J. Phys. Chem. B.* **1998**, *102*, 3456.

[192] Subramanian, S.; Sampath, S. *PRAMANA-J PHYS* **2005**, *65*, 753.

[193] Schoenfisch, M. H.; Pemberton, J. E. *J. Am. Chem. Soc.* **1998**, *120*, 4502.

[194] Willey, T. M.; Vance, A. L.; van Buuren, T.; Bostedt, C.; Terminello, L. J.; Fadley, C. S. *Surf. Sci.* **2005**, *576*, 188.

[195] De Renzi, V.; Di Felice, R.; Marchetto, D.; Biagi, R.; del Pennino, U.; Selloni, A. *J. Phys. Chem. B.* **2003**, *108*, 16.

[196] Vericat, C.; Vela, M. E.; Andreasen, G.; Salvarezza, R. C.; VAzquez, L.; MartIn-Gago, J. A. *Langmuir* **2001**, *17*, 4919.

[197] Barrena, E.; Palacios-Lidan, E.; Munuera, C.; Torrelles, X.; Ferrer, S.; Jonas, U.; Salmeron, M.; Ocal, C. *J. Am. Chem. Soc.* **2003**, *126*, 385.

[198] Schreiber, F. *Prog. Surf. Sci.* **2000**, *65*, 151.

[199] Schreiber, F.; Eberhardt, A.; Leung, T. Y. B.; Schwartz, P.; Wetterer, S. M.; Lavrich, D. J.; Berman, L.; Fenter, P.; Eisenberger, P.; Scoles, G. *Phys. Rev. B.* **1998**, *57*, 12476.

[200] Ulman, A. *Chem. Rev.* **1996**, *96*, 1533.

[201] Woodruff, D. P. *Phys. Chem. Chem. Phys.* **2008**, *10*, 7211.

[202] Nuzzo, R. G.; Dubois, L. H.; Allara, D. L. *J. Am. Chem. Soc.* **1990**, *112*, 558.

[203] Camillone, N.; Leung, T. Y. B.; Schwartz, P.; Eisenberger, P.; Scoles, G. *Langmuir* **1996**, *12*, 2737.

[204] Schwartz, D. K. *Annu. Rev. Phys. Chem.* **2001**, *52*, 107.

[205] Day, B. S. PhD Thesis: The Dynamics of Gas-Surface Energy Transfer in Collisions of Rare Gases with Organic Thin Films, Virginia Polytechnic Institute and State University, 2005.

[206] Schoenenberger, C.; Sondag-Huethorst, J. A. M.; Jorritsma, J.; Fokkink, L. G. J. *Langmuir* **1994**, *10*, 611.

[207] Kondoh, H.; Kodama, C.; Sumida, H.; Nozoye, H. *J. Chem. Phys.* **1999**, *111*, 1175.

[208] Bebbington, M. W. P. Custom synthesis Heriot-Watt University, Edinburgh, EH14 4AS, 2009.

[209] TasiÄ‡, U. S.; Yan, T.; Hase, W. L. *The Journal of Physical Chemistry B* **2006**, *110*, 11863.

[210] Wayne, R. P. *Chemistry of Atmospheres*, Third ed.; Oxford University Press, 2000.

[211] Heard, D. E.; Pilling, M. J. *Chem. Rev.* **2003**, *103*, 5163.

[212] Atkinson, R.; Arey, J. *Chem. Rev.* **2003**, *103*, 4605.

[213] Atkinson, R.; Arey, J. *Atmospheric Environment* **2003**, *37*, 197.

[214] D'Andrea, T. M.; Zhang, X.; Jochnowitz, E. B.; Lindeman, T. G.; Simpson, C. J. S. M.; David, D. E.; Curtiss, T. J.; Morris, J. R.; Ellison, G. B. *J. Phys. Chem. B.* **2007**, *112*, 535.

[215] Davidovits, P.; Kolb, C. E.; Williams, L. R.; Jayne, J. T.; Worsnop, D. R. *Chem. Rev.* **2006**, *106*, 1323.

[216] George, I. J.; Abbatt, J. P. D. *Nature Chem.* **2010**, *2*, 713.

[217] Weitkamp, E. A.; Lambe, A. T.; Donahue, N. M.; Robinson, A. L. *Environ. Sci. Tech.* **2008**, *42*, 7950.

[218] Lambe, A. T.; Zhang, J.; Sage, A. M.; Donahue, N. M. *Environ. Sci. Tech.* **2007**, *41*, 2357.

[219] Smith, J. D.; Kroll, J. H.; Cappa, C. D.; Che, D. L.; Liu, C. L.; Ahmed, M.; Leone, S. R.; Worsnop, D. R.; Wilson, K. R. *Atmos. Chem. Phys.* **2009**, *9*, 3209.

[220] Che, D. L.; Smith, J. D.; Leone, S. R.; Ahmed, M.; Wilson, K. R. *Phys. Chem. Chem. Phys.* **2009**, *11*, 7885.

[221] George, I. J.; Abbatt, J. P. D. *Atmos. Chem. Phys.* **2010**, *10*, 5551.

[222] George, I. J.; Vlasenko, A.; Slowik, J. G.; Broekhuizen, K.; Abbatt, J. P. D. *Atmos. Chem. Phys.* **2007**, *7*, 4187.

[223] Renbaum, L. H.; Smith, G. D. Unpublished results; Department of Chemistry, University of Georgia, Athens, GA 30602, 2010.

[224] Ning, C. L.; Pfab, J. *J. Phys. Chem. A.* **1997**, *101*, 6008.

[225] Hickson, K. M.; Sadowski, C. M.; Smith, I. W. M. *J. Phys. Chem. A.* **2002**, *106*, 8442.

[226] Hickson, K. M.; Sadowski, C. M.; Smith, I. W. M. *Phys. Chem. Chem. Phys.* **2002**, *4*, 5613.

[227] Beek, M. C. v.; Meulen, J. J. t.; Alexander, M. H. *J. Chem. Phys.* **2000**, *113*, 628.

[228] Grant, P.; Sarantos, M.; Matthew, L. C.; Kenneth, G. M.; Jacek, K.; Robert, T. *J. Chem. Phys.* **2008**, *129*, 074304.

[229] Alexander, M. H. *J. Chem. Phys.* **1982**, *76*, 5974.

[230] Alexander, M. H. *Chem. Phys.* **1985**, *92*, 337.

[231] Jacobs, D. C.; Kolasinski, K. W.; Madix, R. J.; Zare, R. N. *J. Chem. Soc., Faraday Trans.II* **1989**, *85*, 1325.

[232] Budde, F.; Gritsch, T.; Mödl, A.; Chuang, T. J.; Ertl, G. *Surf. Sci.* **1986**, *178*, 798.

[233] Segner, J.; Robota, H.; Vielhaber, W.; Ertl, G.; Frenkel, F.; Häger, J.; Krieger, W.; Walther, H. *Surf. Sci.* **1983**, *131*, 273.

[234] Frenkel, F.; Häger, J.; Krieger, W.; Walther, H.; Ertl, G.; Segner, J.; Vielhaber, W. *Chem. Phys. Lett.* **1982**, *90*, 225.

[235] Ainsworth, M. K.; Fiorin, V.; McCoustra, M. R. S.; Chesters, M. A. *Surf. Sci.* **1999**, *433-435*, 790.

Appendix I - Publications

1. Carla Waring, Kerry L. King, Matthew L. Costen, and Kenneth G. McKendrick.
Dynamics of the gas-liquid interfacial reaction of O(^{1}D) with a liquid hydrocarbon.
The Journal of Physical Chemistry A (ACS, accepted April 2011).

2. Carla Waring, Kerry L. King, Paul A. J. Bagot, Matthew L. Costen, and Kenneth G. McKendrick.
Collision dynamics and reactive uptake of OH radicals at liquid surfaces of atmospheric interest
Physical Chemistry Chemical Physics, Volume 13, Page 8457, (2011).

3. Carla Waring, Paul A. J. Bagot, Matthew L. Costen, and Kenneth G. McKendrick.
Reactive scattering as a chemically specific analytical probe of liquid surfaces
The Journal of Physical Chemistry Letters, Volume 2, Page 12, (2011) Perspectives article

4. Carla Waring, Paul A. J. Bagot, Magnus W. P. Bebbington, Minna T. Raisannen, Manfred Buck, Matthew L. Costen, and Kenneth G. McKendrick.
'How penetrable are thioalkyl self-assembled monolayers?'
The Journal of Physical Chemistry Letters, Volume 1, Page 1917, (2010)

5. Carla Waring, Paul A. J. Bagot, John M. Slattery, Matthew L. Costen, and Kenneth G. McKendrick.
O(^{3}P) atoms as a chemical probe of surface ordering in ionic liquids
The Journal of Physical Chemistry A, Volume 114, Page 4896, (2010)

6. Carla Waring, Paul A. J. Bagot, John M. Slattery, Matthew L. Costen, and Kenneth G. McKendrick.
O(^{3}P) atoms as a probe of the surface ordering in 1-alkyl-3-methylimidazolium based ionic liquids
The Journal of Physical Chemistry Letters, Volume 1, Page 429, (2010)

7. Carla Waring, Paul A. J. Bagot, Matthew L. Costen, and Kenneth G. McKendrick.
Dynamics of the Reaction of O(^{3}P) Atoms with Alkylthiol Self-Assembled Monolayers
The Journal of Physical Chemistry A, Volume 113, Page 4320, (2009)

8. Paul A. J. Bagot, Carla Waring, Matthew L. Costen, and Kenneth G. McKendrick.
Dynamics of inelastic scattering of OH radicals from reactive and inert liquid surfaces
The Journal of Physical Chemistry A, Volume 112 Page 10868, (2008)

Appendix II – Conferences attended

1. **Carla Waring**, Paul A. J. Bagot, Matthew L. Costen, and Kenneth G. McKendrick.
Collision dynamics as a probe of interfacial structure
Oral presentation at the American Chemical Society Fall National Meeting, Boston (August 2010).

2. **Carla Waring**, Paul A. J. Bagot, Minna T. Raisannen, Manfred Buck, Matthew L. Costen, and Kenneth G. McKendrick.
Interfacial dynamics of $O(^3P)$ atoms with selectively deuterated self-assembled monolayers
Oral presentation at the 21st International Symposium on Gas Kinetics, Leuven, Belgium (Jul 2010).

3. **Carla Waring**, Paul A. J. Bagot, Matthew L. Costen, and Kenneth G. McKendrick.
Dynamics of reactions between $O(^3P)$ atoms and selectively deuterated self-assembled monolayers
Oral presentation at the Annual Meeting of the RSC Spectroscopy and Dynamics Interest Group, University of Birmingham (Jan 2010).

4. **Carla Waring**, Paul A. J. Bagot, Matthew L. Costen, and Kenneth G. McKendrick.
Dynamics of reactive and inelastic scattering at soft surfaces
Oral presentation at the Annual Meeting of the RSC Spectroscopy and Dynamics Interest Group, University of Nottingham (Jan 2009).

5. **Carla Waring**, Paul A. J. Bagot, Matthew L. Costen, and Kenneth G. McKendrick.
Dynamics of inelastic scattering of OH radicals from reactive and inert liquid surfaces
Oral presentation at the 20th International Symposium on Gas Kinetics (July 2008) at the University of Manchester.

6. **Carla Waring**, Paul A. J. Bagot, Matthew L. Costen, and Kenneth G. McKendrick.
Dynamics of inelastic scattering of OH radicals from reactive and inert liquid surfaces
Oral presentation at the Annual Northern Universities Meeting on Chemical Physics (June 2008) at the University of Sheffield.